Institute of Low Temperature and Structure Research
Polish Academy of Sciences

DOCTORAL DISSERTATION

Standardization of the photothermal conversion efficiency methodology and quantitative evaluation of colloidal nanoheaters

In the form of thematically coherent series of articles published in scientific journals

---

M.Sc. Agnieszka Paściak

Supervisor

Prof. Artur Bednarkiewicz

WROCŁAW 2022

Acknowledgements

I would like to gratefully acknowledge:

My supervisor, prof. Artur Bednarkiewicz – for inspiration, discussions in a great atmosphere, priceless support in good and bad times and valuable suggestions

My parents – for instilling a passion for science in me and constant support

Marcin Białas - for continuous support and help with the advanced technical solutions

My colleagues from LUNASI group – for the great atmosphere at work

Table of Contents

1 THE AIM OF THE THESIS

The aim of the thesis was to propose and develop a novel measurement system and methodology to evaluate the colloidal nanoparticles for photothermal therapy. The motivation for this research originated from a few reasons: various existing measurement systems required relatively high sample volumes and provided diverse results in demanding and time-consuming measurements, while the most popular model and analysis method led to numerous understatements, making comparisons of photothermal conversion efficiency in different materials unreliable.

Subsequently, the goal was to evaluate numerous light-to-heat converting nanomaterials and determine which ones have the greatest application potential. So far, only a limited number of studies had been conducted in which some nanomaterials have been compared on a single system, while such a comparison was urgent, desirable and prerequisite to rank the nanoheaters suitable for photothermal therapy application. Therefore, the studies described in this thesis included materials belonging to different classes: plasmonic, semiconductor, carbon, iron oxide-based, and nanocrystals doped with lanthanide ions. Of the latter, the aim was also to determine if the selection of dopant ion, doping level and the choice of matrix have a significant impact on the photothermal efficiency, which has not been systematically studied yet. On the other hand, expanding the knowledge of the mechanisms and photothermal conversion efficiency of nanomaterials, as well as the ability to compare different nanomaterials directly and quantitatively, contribute not only to a better understanding of the phenomena taking place, but also to determination of further directions for the design of materials for biomedical or technology applications.

2.1 Projects

03/2022 – 05/2022	NCN PRELUDIUM 19 2020/37/N/ST5/00536 Biocompatible $NaRE_xTM_{1-x}F_4$ nanoparticles combining the functions of luminescent nanothermometers and nanoheaters for photothermal therapy applications. Position: project contractor Main responsibilities: Evaluation of photothermal conversion efficiency of colloidal nanomaterials.
10/2018 – 02/2022	FET OPEN NanoTBtech Nanoparticles-based 2D thermal bioimaging technologies Position: project contractor Main responsibilities: Designing, developing, optimization and evaluation of a novel measurement system for determining the photothermal conversion efficiency of nanomaterials. Performing the measurements of photothermal conversion efficiency of nanomaterials delivered by consortium members. Developing LabVIEW software for automated measurement of luminescence intensity as a function of temperature. Preparing interim and final project reports.

2.2 Full list of publications

1. **Agnieszka Paściak**, Aleksandra Pilch-Wróbel, Łukasz Marciniak, P. James Schuck, Artur Bednarkiewicz; Standardization of Methodology of Light-to-Heat Conversion Efficiency Determination for Colloidal Nanoheaters; ACS Applied Materials and Interfaces 2021, 13, 44556-44567; DOI: 10.1021/acsami.1c12409.

2. **Agnieszka Paściak**, Riccardo Marin, Lise Abiven, Aleksandra Pilch-Wróbel, Małgorzata Misiak, Wujun Xu, Katarzyna Prorok, Oleksii Bezkrovnyi, Łukasz Marciniak, Corinne Chanéac, Florence Gazeau, Rana Bazzi, Stéphane Roux, Bruno Viana, Vesa-Pekka Lehto, Daniel Jaque, Artur Bednarkiewicz; Quantitative Comparison of the Light-to-Heat Conversion Efficiency in Nanomaterials Suitable for Photothermal Therapy; ACS Appl. Mater. Interfaces 2022, 14, 33555–33566. DOI: 10.1021/acsami.2c08013.
3. **Agnieszka Paściak**, Małgorzata Misiak, Karolina Trejgis, Karolina Elżbieciak-Piecka, Oleksii Bezkrovnyi, Łukasz Marciniak, Artur Bednarkiewicz; Highly-doped lanthanide nanomaterials for efficient photothermal conversion – selection of the most promising ions and matrices; J. Alloys Compd. 2023, 934, 167900.
   DOI: 10.1016/j.jallcom.2022.167900

2.3 Patents granted

1. **Agnieszka Paściak**; Artur Bednarkiewicz; Łukasz Marciniak, PL: „Układ pomiarowy oraz sposób do wyznaczania sprawności konwersji światła z zakresu VIS i NIR na ciepło w nanomateriałach koloidalnych" (EN: „Experimental system and method for determining the photothermal efficiency of colloidal nanomaterials in VIS and NIR range").

Application filed on March 17, 2021, published in the Bulletin of the Patent Office of the Republic of Poland on September 19, 2022 (Bulletin No. 38/2022, Physics section). On October 18, 2022, the Polish Patent Office granted a patent for the invention with the number P-437330.

2.4 Conferences and science schools

1. **Agnieszka Paściak**, Aleksandra Pilch-Wróbel, Łukasz Marciniak, Artur Bednarkiewicz, "Evaluation of light to heat conversion efficiency of colloidal

nanoparticles", 8th International Symposium on Optical Materials, 9-14.06.2019, Wroclaw, Poland (poster presentation).

2. **Agnieszka Paściak**, Aleksandra Pilch-Wróbel, Łukasz Marciniak, Artur Bednarkiewicz, "How to measure the light-to-heat conversion efficiency of colloidal nanoparticles? The comparison of different experimental setups" - Three Wise Men Winter School on Luminescent Nanothermometry for Biomedical Applications, 8-11.01.2020 (poster presentation).
3. **Agnieszka Paściak**, Aleksandra Pilch-Wróbel, Łukasz Marciniak, Artur Bednarkiewicz, "Development and evaluation of experimental methodology for light-to-heat conversion efficiency determination in colloidal nanoheaters" – PhoBiA Annual Nanophotonics International Conference (PANIC) 12-14.10.2020 (online, oral presentation).
4. **Agnieszka Paściak**, Aleksandra Pilch-Wróbel, Łukasz Marciniak, Artur Bednarkiewicz, "Light-to-heat conversion efficiency of different nanomaterials obtained with droplet-base experimental setup", 3rd Conference on Properties, Design, and Applications of Upconversion Nanomaterials (UPCONline) 6-9.04.2021, (online, poster presentation).
5. **Agnieszka Paściak**, Riccardo Marin, Lise Abiven, Aleksandra Pilch-Wróbel, Małgorzata Misiak, Wujun Xu, Katarzyna Prorok, Oleksii Bezkrovnyi, Łukasz Marciniak, Corinne Chaneac, Florence Gazeau, Bruno Viana, Vesa-Pekka Lehto, Daniel Jaque, Artur Bednarkiewicz, "Comparison of light-to-heat converting nanomaterials suitable for photothermal therapy", 1st International Conference on Advanced Materials for Bio-Related Applications (AMBRA), 16–19.05.2022, Wrocław, Poland (poster presentation).

2.5 Seminars

1. **Agnieszka Paściak**, „Pomiary sprawności konwersji światła na ciepło w nanomateriałach", Optical Spectroscopy Division seminar, Institute

of Low Temperature and Structure Research, Polish Academy of Sciences, 6.06.2019

2. **Agnieszka Paściak**, Aleksandra Pilch-Wróbel, Łukasz Marciniak, Artur Bednarkiewicz, "Standardization of light-to-heat conversion efficiency of colloidal nanoheaters" – NanoTBTech webinars (online 16.10.2020)

2.6 Scientific awards

04.2021	Best poster award, 3rd Conference on Properties, Design, and Applications of Upconversion Nanomaterials (UPCONline)

3 ABSTRACT

Nanomaterials that convert light energy into heat have been known for many years and have found applications in various fields such as renewable energy and medicine. In particular, high hopes are related to their possible use in photothermal therapy. However, even though a large number of materials have been already demonstrated and many studies have been conducted on the subject, a quantitative comparison of nanoheaters has not yet been carried out in a way that allows for creating an unambiguous ranking of them. In addition, photothermal conversion efficiencies for similar materials were significantly different in publications from different research groups, which calls into question the methodology used. Moreover, the measurement systems known so far required large sample volumes and time-consuming measurement, or did not allow routine measurement of a larger number of diversified samples.

To overcome these flaws, within the scope of the dissertation, a novel measurement system was designed and constructed that enables rapid, reproducible and accurate measurement of small sample volumes. Furthermore, existing models used to analyze photothermal conversion efficiency results were compared and a model was selected that leads to consistent results regardless of the measurement conditions. Moreover, the methodology was proposed that enables quantitative comparison of nanomaterials belonging to different classes. In particular, the figure of merit proposed by the author, i.e. external light-to-heat conversion efficiency (eHCE), allowed for quantitative comparison of various materials in terms of their applicability. Then, materials characterized by different physicochemical properties were compared, including plasmonic, semiconductor, carbon, iron oxide-based, and nanocrystals doped with lanthanide ions using exactly the same methodology and the same optical setup. For the latter class, it was also examined how the choice of dopant ion affect the photothermal conversion efficiency. Analysis of the results showed that the parameter which was previously considered as the major indicator of the suitability of nanoheaters for application, did not actually vary strongly for most

of the samples examined, however, with the newly proposed eHCE parameter, logarithmic differences were observed between samples. The most promising class of materials for photothermal therapy was found to be plasmonic materials, with copper sulfide nanoparticles taking a lead.

Moreover, a systematic study of a group of materials doped with different rare earth ions and in different matrices has been conducted and the significant impact of these factors on photothermal properties was observed. While significant cross-relaxation (known as concentration quenching) takes place in lanthanide doped materials, their modest or weak absorption cross section hinders their application in photothermal therapies. Nevertheless, among materials doped with rare earth ions, $NdVO_4$ deserves special attention for photothermal application due to its superior absorption properties and proven non-toxicity.

The presented methodology and achieved results contribute to the systematization of knowledge on the efficiency and suitability of nanoheaters, help to better understand the phenomenon of photothermal conversion of nanomaterials, and may be useful to rank and select the most promising photothermal materials for medical applications.

Nanomateriały przekształcające energię świetlną w ciepło są znane od wielu lat i znajdują zastosowanie w różnych dziedzinach, takich jak odnawialne źródła energii, czy medycyna. Szczególnie duże nadzieje związane są z możliwością ich wykorzystania w terapii fototermicznej. Jednak pomimo tego, że zaprezentowano i scharakteryzowano już dużą liczbę materiałów, nie przeprowadzono dotychczas ilościowego porównania nanogrzałek w sposób pozwalający na stworzenie ich jednoznacznego rankingu. Co więcej, efektywności konwersji światła na ciepło dla podobnych materiałów były istotnie różne w pracach różnych grup badawczych, co poddaje w wątpliwość stosowaną metodologię. Ponadto znane dotychczas systemy pomiarowe wymagały dużych objętości próbek i czasochłonnego pomiaru lub nie pozwalały na rutynowy pomiar większej liczby różnorodnych próbek.

W celu wyeliminowania tych problemów, w ramach rozprawy doktorskiej, zaprojektowano i skonstruowano nowatorski układ pomiarowy, który umożliwia szybki, powtarzalny i dokładny pomiar małych objętości próbek. Ponadto porównano istniejące modele stosowane do analizy wyników efektywności konwersji światła na ciepło i wybrano model, który niezależnie od warunków pomiarowych prowadzi do spójnych wyników. Zaproponowano metodologię umożliwiającą ilościowe porównanie nanomateriałów należących do różnych klas. W szczególności, zaproponowana przez autorkę miara, tj. zewnętrzna sprawność konwersji światła na ciepło (eHCE), pozwoliła na ilościowe porównanie różnych materiałów pod względem możliwości ich zastosowania. Następnie porównano materiały charakteryzujące się różnymi właściwościami fizykochemicznymi, w tym materiały plazmoniczne, półprzewodnikowe, węglowe, materiały na bazie tlenku żelaza oraz nanokryształy domieszkowane jonami lantanowców przy użyciu tej samej metodologii i zaprezentowanego układu optycznego. Dla ostatniej z tych klas sprawdzono również, jak wybór jonu domieszki wpływa na wydajność konwersji fototermicznej. Analiza uzyskanych wyników pokazała, że parametr,

który wcześniej był uważany za najważniejszy wskaźnik przydatności nanogrzałek, w rzeczywistości nie różnił się znacznie dla większości badanych próbek, jednak w przypadku nowo zaproponowanego parametru eHCE zaobserwowano różnice rzędów wielkości pomiędzy próbkami. Najbardziej obiecującą klasą materiałów do terapii fototermicznej okazały się materiały plazmoniczne, spośród których najlepszy okazał się siarczek miedzi.

Przeprowadzono także systematyczne badania grupy materiałów domieszkowanych różnymi jonami metali ziem rzadkich oraz w różnych matrycach i zaobserwowano istotny wpływ tych czynników na właściwości fototermiczne. Podczas gdy w materiałach domieszkowanych jonami lantanowców zachodzi relaksacja krzyżowa (znana jako wygaszanie koncentracyjne), ich niewielki lub średni przekrój absorpcyjny utrudnia ich zastosowanie w terapiach fototermicznych. Niemniej jednak, spośród materiałów domieszkowanych jonami metali ziem rzadkich, $NdVO_4$ zasługuje na szczególną uwagę w zastosowaniu fototermicznym ze względu na swoje wyróżniające się właściwości absorpcyjne i udowodnioną nietoksyczność.

Przedstawiona metodologia oraz uzyskane wyniki przyczyniają się do usystematyzowania wiedzy na temat sprawności i przydatności nanogrzałek, pomagają w lepszym zrozumieniu zjawiska konwersji fototermicznej nanomateriałów, a także mogą być przydatne do uszeregowania i wyboru najbardziej obiecujących materiałów fototermicznych do zastosowań w medycynie.

5.1 Nanomaterials

Nanoparticles have been gaining increasing attention over time. A nanoparticle is defined as a "particle of any shape with dimensions in the 1×10^{-9} and 1×10^{-7} m range" (IUPAC). The upper limit results from the fact that the novel (relative to bulk materials) properties of these materials typically occur at a critical length scale below 100 nm. With such small dimensions, the surface-to-volume ratio increases, which often translates into novel properties that are not observed for larger counterpart materials. The field of nanotechnology is currently one of the fastest growing fields, thanks to the powerful tools available for their characterization, as well as modern synthesis methods that make it possible to precisely produce nanomaterials with predetermined characteristics such as composition, size, shape and structure to provide unique or unprecedented properties of nanoparticles.

Nanoparticles can be applied in e.g. UV filtering [1], water purification [2], exhibit antibacterial activity [3] or enable enhancement of parameters such as durability [4], fluorescence brightness [5] etc. Moreover, they can ensure unique optical or magnetic properties as well as offer the possibility to selectively deliver (by proper surface biofunctionalization), controllably release, monitor and encapsulate cytotoxic drugs [6].

Nanoparticles which demonstrate the ability to generate heat, called nanoheaters, are another class of functional nanoparticles that are promising for numerous technologies and medical treatment applications. Nanoheaters are used in renewable energy, e.g. solar vapor generation and storage [7], in photocatalyst [8] or photo-actuators [9], i.e. for 3D printing [10]. In medicine, heat generation might be applied in cancer therapy [11], dentin hypersensitivity treatment [12], retinal degenerative diseases therapy [13], hair removal [14], acne treatment [15], antibacterial therapy [16,17] or sterilization [18].

Efficient localized heat generation in nanomaterials can be induced by a non-contact manner, i.e. by optical excitation or applying alternative magnetic field, thus providing greater capabilities than conventional heaters, which is critical especially in medicine. Nanoheaters, which generate heat under optical excitation, due to the conversion of light into heat, are the main focus of this dissertation. The therapeutic use of nanoheaters stems from the various effects of temperature on tissues, which are described in the following subsection.

5.2 Hyperthermia and photothermal therapy

The hyperthermia (HT) refers to raising the temperature of a part (local HT) of or the whole-body (systemic HT) above normal for a defined period of time [19]. Typically applied thermal therapies are in the following temperature ranges [20]:

- 40-41 °C – low-temperature hyperthermia / diathermia (DT)
- 42-45 °C – moderate hyperthermia (mHT)
- > 50 °C – thermal ablation (TA)

In DT range [21], no significant modifications at cellular level occur and homeostasis can be maintained. Nevertheless, the blood flow is enhanced and ion diffusion rate across cellular membranes increases, which leads to positive health effects, such as accelerated tissue repair. DT is usually a long-term (6-72 h) treatment [20] and is primarily used in physiotherapy.

In 43-45 °C range the biochemical reactions rate notably increases, which cause oxidative stress, results in proteins, lipids and nucleic acids degradation [22]. mHT find application especially in cancer therapy. Even though in general there is no significant difference in thermal sensitivity of tumor and healthy cells, the tumor has different architecture of the vasculature, which cause increased susceptibility to mHT [23]. On the other hand, the research on hepatoma cells has proven that at 43 °C in aerobic conditions, protein synthesis [24] and cellular respiration [25] have been suppressed. Furthermore, the divergences in cell membranes lability in cancer and healthy cells has been speculated [25]. The cell death due to mHT occurs in the apoptosis path [23]. Clinical trials using mHT show strong evidence of the effectiveness of this therapy [26], but it is recommended for mHT to be used synergistically with other therapies such as chemo- or radiotherapy, because of raised therapeutic effect in increased temperatures. mHT treatment usually last 15-60 min [20].

Above 50 °C DNA become damaged, protein undergoes denaturation and subsequent cell death occurs [27]. Tissues undergo coagulation, and ablation, when the temperature exceed 60 °C. At the temperature above 100 °C, vaporization of the tissues takes place. The method is therefore effective to destroy malignant tissues, but it does not provide selectivity for cancer treatment. Moreover, there is a strong risk of the damage of adjacent tissues. Typically in TA treatment the exposure time is short, lasting 4-6 minutes [20].

In terms of area of effect HT can be divided into 3 categories: localized hyperthermia, regional hyperthermia and whole body hyperthermia [19]. Of these, localized hyperthermia is the most beneficial as it allows for a limited negative impact on healthy tissues or limited side effects typically observed in a whole body hyperthermia. Depending on the type of heat induction, the most common approach is to use ultrasound, radiofrequency or microwave applicators [19].

Localized HT usually requires mediators to convert one form of energy into heat and confine this activity to limited tissue volume. This is usually performed with nanoparticles capable to efficiently convert alternating magnetic field of electromagnetic radiation from NIR spectral region to heat. So far, only few nano-drugs for cancer therapies have been approved by the FDA [28]. I.e., in dentistry, indocyanine green dye is allowed for photothermal antibacterial therapy. Therapeutic nanoparticles raise more and more attention, because of the advantages - in particular their high selectivity and confinement of action (i.e. localization), that they offer over the other methods. Nanoparticle-based thermal therapies include photothermal therapy (PTT) and magnetothermal therapy (MT).

PTT is usually conducted in mHT or TA temperature range, often synergically with other methods, e.g. chemotherapy [29,30] or photodynamic therapy [31]. The major advantage of PTT is its minimal invasiveness and low risk of patient complications [32]. Moreover, this therapy can prevent cancer recurrence [33]. The light source in PTT is usually a laser operating in the NIR range.

5.3 Materials for photothermal therapy

Nanoparticles that are dedicated to PTT, called nanoheaters (NHs) must meet a number of requirements and should be comprehensively examined before being introduced for clinical studies. These requirements should include following factors:

- Physical (small size [34], high absorption cross-section at NIR region, high photostability, high light-to-heat conversion efficiency)
- Biological (nontoxicity [5,35,36], biodegradability [37], bio-excretion [38], biocompatibility, circulation time and clearance [35])
- Chemical (chemical stability, coating type)
- Economical (low synthesis costs and preparation time)
- Functional (selective targeting of tumor tissues, multifunctionality, e.g. drug carriers, MRI agents, nanothermometry)

Size of NHs should not exceed 200 nm to prevent issues such as occlusions, kidney blocks or thrombus [34]. On the other hand, other studies put more stringent conditions, as they show that less side effects are provided by nanoparticles that are smaller than 50 nm [39]. The selection of stimulation wavelength is referred to water and tissue absorption. Because of strong absorption of water at ~1000 nm, and strong absorption of tissues components at

UV and VIS, the use of radiation from biological spectral windows in NIR is the most beneficial. First biological window (NIR-I) falls within the wavelength range: 700-980 nm, and second (NIR-II): 1000-1400 nm [21]. Among these, NIR-I is characterized by lower water absorption, making this range preferable. NIR spectral region is also beneficial for biomedical and theranostic (therapeutic and diagnostic) procedures for one another reason. Some of the therapies gain from feedback control – either drug release or heat deposition can be spectroscopically monitored and the choice of NIR excitation wavelength prevents the strong autofluorescence of tissues. In this case it is recommended that the absorption and emission bands of fluorescence agents are spectrally narrow to provide a reliable monitoring of the treatment progress [40].

To achieve better stability and biocompatibility, nanomaterials are covered with an inert or functional coating. For example, a silica coating enhances thermal stability [41], stabilizes NPs shape and surface, and improves colloidal stability [42]. Anyway, further surface biofunctionalization is required to target required sites in tissues and cells. One of the most effective methods to create a targeted delivery system is the use of antigen-antibody bonding in tumor tissues. Specific antigens are expressed on the surface of affected cells and suitable antibody-nanomaterial conjugate can bond with them. Functionalization of nanoparticles is achieved by adsorption, covalent linkage, or using adaptor molecules [6].

To date, numerous light-to-heat converting structures have been proposed. Among them, the most popular are organic agents [43–57]. Extensive research is also being conducted on inorganic materials, of which the most popular are metallic nanoparticles that exhibit plasmonic properties [58–66]. Semiconductors [67–72], metal oxides (e.g. iron oxide [73–75]), lanthanide-doped nanocrystals [76–83], materials based on carbon [45,84,85], silicon [86] or titanium [87], etc., are also comprehensively studied.

The photothermal conversion is carried out through a variety of mechanisms that, in many cases, are not yet well understood. In general it could be claimed that multiphonon relaxation of the excited states is the origin of heat generation. When the material is illuminated with a laser beam of a strictly defined energy corresponding to the difference in energy levels between the ground and an excited state, an electron transition occurs. Then, a return of the excited electrons to the lowest level takes place through internal conversion and vibrational relaxation, e.g., to the excited singlet state (in the case of organic molecules), the valence band (in semiconductors) or the ground state (in lanthanides). In the following subsections, a main characterization of the most commonly mentioned classes of NHs and a brief description of the mechanisms of photothermal conversion in different classes of materials will be presented.

5.3.1 Plasmonic nanomaterials

Plasmonic nanoparticles are among the most extensively studied materials for their conversion of light to heat. They include metals such as gold [58–60,66], silver [61], platinum [62] and their derivatives, such as copper sulfide [69], titanium nitride [63], bismuth sulfide [64] and selenide [65], etc. The field that studies the thermal effects of plasmonic materials has been called thermoplasmonics [88]. The mechanism responsible for heat generation is called localized surface plasmon resonance. It relies on collective oscillations of electron density on the surface of nanostructures through coupling with electromagnetic waves [88]. The movement of conduction electrons is enhanced and increases the frequency of collisions with lattice atoms, causing the generation of Joule heat. When surface plasmons are in resonance with an incident electromagnetic wave, the maximum of the delivered energy is converted into heat. Absorption, and at the same time photothermal properties of plasmonic materials strongly depend on the morphology of nanoparticles. The heating properties of plasmonic nanomaterials can be evaluated theoretically, using Mie theory [89]. However, this theory requires the accurate information about material geometry and thermal conductivity as well as the light distribution on the nano scale, and these are often hard to determine. For this reason, more universal experimental methods are usually applied.

Many morphologically different materials with varying optical properties have been proposed (Figure 1), including: nanospheres [58] , nanorods [59], nanostars [60], nanohexapods and nanocages [66] and others. Spherical and rod-shape nanoparticles are the most commonly investigated nanostructures. They differ considerably in absorption properties: gold spherical nanoparticles have one absorption peak in the Vis range connected with the transverse mode and nanorods have also the NIR absorption band associated with the longitudinal mode [90].

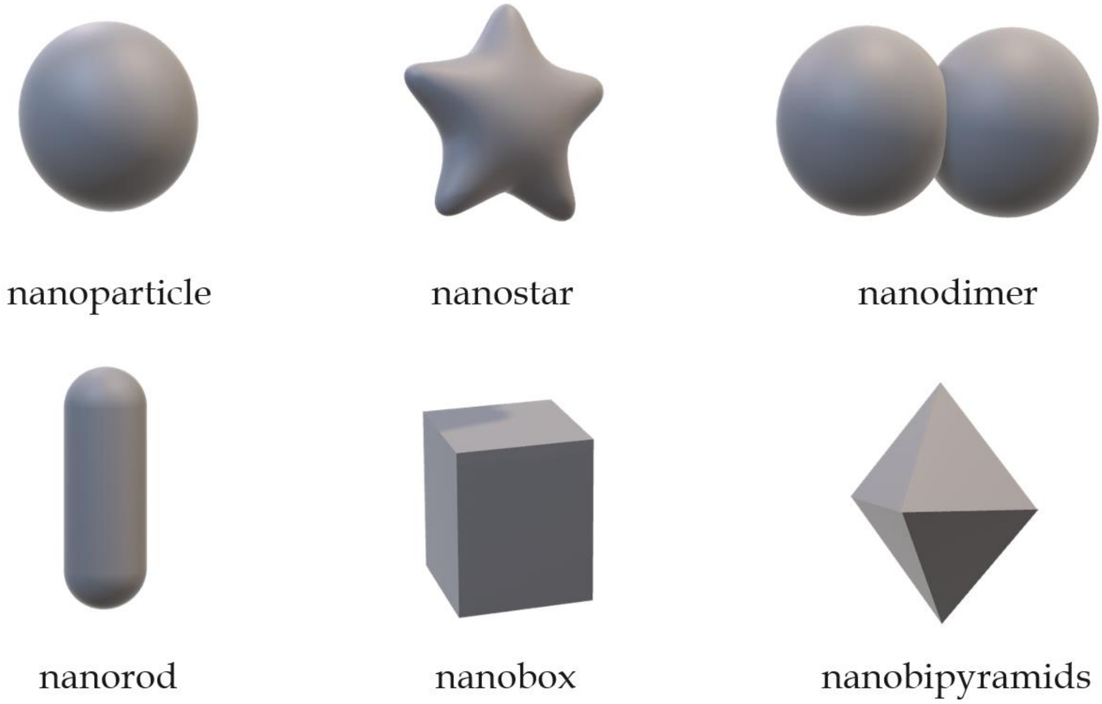

Figure 1. Example shapes of plasmonic nanomaterials.

5.3.2 Semiconductor and quantum dots nanomaterials

For non-plasmonic materials, heat generation is related to electron absorption. Intrinsic band gap absorption is associated with transitions from the valence state to the conduction state and the subsequent non-radiative relaxation. It occurs in nitrides, carbides, borides and sulfides of transition metals. In contrast, in the case of semiconductors with structure defect, absorption by surface free carriers occurs. This mechanism is similar to localized surface plasmon resonance in metals [91]. An example of a material in which absorption occurs by nonradiative carrier recombination is copper chalcogenide or silicon [92].

A special case of semiconductor materials are quantum dots (QDs), whose optical properties strictly depend on size due to quantum confinement. The most important advantages of semiconductor quantum dots are good photostability and chemical stability [67]. Disadvantages, on the other hand, can be the photo-blinking or cytotoxicity found for some of them [36]. Biosafety can be ensured by choosing Pb- or Cd-free compositions and by passivation and biofunctionalization of the nanomaterial surface [93]. Different quantum dots have already been proposed for photothermal purpose, including Ag_2S [68], $Cu_{2-x}S$ [69,70], $Cu_{2-x}Se$ [71] and germanium quantum dots [72].

5.3.3 Organic nanomaterials

Organic nanomaterials are the most diverse class of the nanomaterials used in PTT, so it is difficult to unequivocally attribute any specific properties to them [81]. Examples of these materials are dyes [45–47], organic conductive polymers [48], polymer dots [49], nanogels [51], amino acids [52], polydopamine [44], polyaniline [53,54], lignin [55] or organic supramolecular assemblies [56,57]. For example, polymers can have good stability and good absorption capabilities in the NIR [81]. In the case of dyes, they are characterized by unique absorption properties and also free radical generation, which may allow the combination of photothermal and photodynamic therapy [46]. However, they often suffer from photostability issues, which depend on the type of dye and bio-chemical environment. Next generation dyes exhibit improved photostability [47]. In organic materials the non-radiative transitions are mainly responsible for the photothermal conversion mechanism [94].

5.3.4 Carbon-based nanomaterials

Carbon nanomaterials raise special interest for PTT due to the high absorption cross-section at visible and NIR range. In example, carbon nanotubes exhibit absorption cross-section of 7.6×10^{-18} cm^2 [95]. Among the carbon materials for applications in PTT the most commonly mentioned nanomaterials are [81]: graphene-based materials: graphene, graphene oxide, reduced graphene oxide, as well as single and multi-wall carbon nanotubes and carbon dots. It was shown that using graphene nanoheaters the side effects of therapy can be reduced [96]. The toxicity of graphene oxide is considered to be less than reduced graphene oxide, because of the presence of hydroxide and carboxyl groups in the material structure. However, both were investigated in *in vivo* studies [85,97]. Due to the complex structure of carbon materials, they are usually used in combination with other nanomaterials [81]. The mechanism for converting light to heat, the same as of organic materials, are usually non-radiative transitions [94].

Carbon dots (Cds) have special potential because of their small size. Importantly for photothermal therapy, CDs are characterized by good dispersibility, easy surface functionalization, low toxicity and high biocompatibility [98]. Furthermore, they also enable multifunctionality, because of their tunable emission. CQDs are characterized by a large number of mobile π-electrons. This results in relatively strong electron-electron scattering and weak electron-phonon interactions. Consequently, their optical properties are more similar to metallic QDs (nanoclusters) than semiconducting QDs [99].

5.3.5 Iron oxide nanomaterials

Iron oxide NHs are used in magnetic hyperthermia thanks to their ferromagnetic properties. However, it has also been shown that even higher temperature rise can be achieved using optical excitation [74] and the best results are obtained by synergizing the two types of therapy [73]. In terms of interaction with tissues, iron oxide has relatively good biocompatibility and biodegradability [100]. To date, the mechanisms of photothermal conversion of iron oxide nanoparticles have not yet been fully understood [75].

5.3.6 Lanthanide-doped nanomaterials

In lanthanides, *f-f* transitions are forbidden by Laporte rule, which implies that the absorption cross section of these materials is relatively low. That is a major drawback of these materials in the context of nanoheating, but on the other hand they are characterized by unique properties, i.e. narrow absorption and emission bands, long luminescence lifetimes, which enable their application in a variety of fields of science and technology such as e.g. light sources [101], nanothermometry [102], pressure [103] and pH [104] sensors, strip tests [105], super resolution microscopy [106] or single molecule sensing [107]. Importantly, in PTT, lanthanide-doped materials allow for combining different functionalities, such as luminescent thermometry [82,102], bioimaging [108], magnetic resonance/computer tomography (MRI/CT) [109]. A heater-thermometer based solely on lanthanide materials allows for easy spectral separation of excitation and emission bands [82].

The use of lanthanide-doped nanomaterials is also associated with advantages such as ease of synthesis, high stability (and especially photostability [78]) and low cytotoxicity [35]. However, more detailed research is still needed on the effects of lanthanides on the human body [110], as the effects depend on a number of factors such as the dose, coating, and the time and mode of exposure [111].

A pioneering paper on the use of materials doped with rare earth ions as the NHs was written in 2010 [77]. In subsequent years, the possibility of heating was also demonstrated *ex vivo* (by Rocha et al [79], in 2014), and later also *in vivo* [80,112–114]. Of the lanthanide ions used as NHs, Nd^{3+} [77,82,112–116], Yb^{3+} [117–119] and Er^{3+} [120,121] are primarily investigated, as they have distinct absorption bands within the biological window range. It was also shown that increased heating occurs for materials doped or co-doped with Ho^{3+} [122], Tm^{3+} [123], Sm^{3+} [124], Eu^{3+} [125], Dy^{3+} [126] or La^{3+} [127] ions.

The proposed heat generation mechanism takes into account non-radiative processes occurring in lanthanide ions such as e.g. non-radiative relaxation, or emission quenching [78]. These processes occur quite frequently, and to enhance luminescence, materials are usually designed to reduce them and at the same time increase the probability of luminescence. However, for materials with a high concentration of dopant, effective heat generation can be expected [115].

5.3.7 Other light-to-heat converting nanomaterials

In addition to nanoparticles that can be directly categorized into any of the above groups, a number of nanoplatforms have also been proposed that combine two or more types of nanomaterials into one with more versatile properties, thereby gaining an increase in light-to-heat conversion efficiency or additional functionality. An example is the combination of materials that allows to take advantages from their best features, e.g. lanthanide materials, with relatively low active cross-section but good stability and emitting properties for bioimaging, with dyes, with high absorption coefficient [116], polymer loaded with doxorubicin (chemotherapeutic agent) covered by polydopamine (photothermal agent) and folic acid (targeting agent) [128].

5.4 Photothermal conversion efficiency evaluation

Nanomaterials for PTT are very diverse, but efforts have been made to compare them with each other aiming to rank their heat generation abilities. A commonly determined parameter that characterizes photothermal properties is photothermal efficiency, also called light-to-heat conversion efficiency or transduction efficiency [129]. The commonly accepted literature models which allows for determining the photothermal efficiency will be presented below.

5.4.1 Models

Roper's model

The most popular model which allows to determine the photothermal conversion efficiency originates from the pioneering work of Roper et al. (2007) [129]. This work concerns modeling of laser beam continuous wave illumination of 20 nm gold nanoparticles suspension placed in the measurement cell under vacuum conditions. To determine photothermal efficiency, energy balance equations were proposed.

$$\sum_i m_i c_{p,i} \frac{dT}{dt} = \sum_j Q_j \qquad \text{(Eq. 1)}$$

$m_iC_{p,i}$ are the products of the mass and heat capacity of the components of the system, both sample and sample cell, T is the temperature of the system (aggregated). Term Q_j describes the source of energy induced by laser (by NPs: Q_I and by surroundings: Q_0) and energy outputs, from conduction and radiation. Q_I could be defined as:

$$Q_I = I(1 - 10^{-A_\lambda}) * \eta_T \qquad \text{(Eq. 2)}$$

I is the incident power of the laser, A_λ is the absorption of NPs at wavelength λ, defined by Beer-Lambert's law, η_T is the light-to-heat conversion efficiency. It was found that for small (<11°C) temperature increments, radiative heat transfer is of relatively minor importance and can be neglected. Hence, the heat released to the environment by the system can be described by the following formula:

$$Q_{ext} = hA(T - T_{amb}) \qquad \text{(Eq. 3)}$$

where T is the temperature of the system and T_{amb} is ambient temperature; h is a heat transfer coefficient and A is thermal exchange surface area. However, the latter values do not need to be known exactly, as they can be approximated from the cooling time constant τ_s:

$$\tau_s \equiv \frac{\sum_i m_i c_{p,i}}{hA} \qquad \text{(Eq. 4)}$$

After illuminating the sample with a laser beam and stabilizing the temperature, the following equality occurs:

$$Q_I + Q_0 = hA(T_{max} - T_{amb}) \qquad \text{(Eq. 5)}$$

After substituting Equation 2 and Equation 5, the following equation is obtained:

$$\eta_T = \frac{hA(T_{max} - T_{amb}) - Q_0}{I(1 - 10^{-A_\lambda})} = \frac{\frac{\sum_i m_i c_{p,i}(T_{max} - T_{amb})}{\tau_s} - Q_0}{I(1 - 10^{-A_\lambda})} \qquad \text{(Eq. 6)}$$

The Q_0 can be determined analogously to Q_I, basing on knowledge of the maximum temperature and time constant of the same system in which the nanoparticles are not suspended.

Chen's model

Chen et al. (2010) [130] proposed some modifications to the Roper model, which, however, were not very widely adopted. In Chen work, the sample was placed in a spectrophotometric cuvette. The reflection coefficient from the front of the cuvette was taken into account and Eq. 2 took the form:

$$Q_I = I(1-\xi)(1-10^{-A_\lambda}) * \eta_T \qquad \text{(Eq. 7)}$$

Herein, I is the laser power corrected for reflection, and ξ is the fraction of energy that is absorbed by the adjuvant medium and the holder. Furthermore, the energy dissipated from the system was represented by a Taylor series of ΔT:

$$Q_{ext} = B\Delta T + C\Delta T^2 \qquad \text{(Eq. 8)}$$

Where B and C are parameters determined from the cooling part of the temperature curve. The final equation allowing to determine efficiency from this model is as follows:

$$\eta = \frac{B(T_{max}-T_{amb})+C(T_{max}-T_{amb})^2-I\xi}{I(1-\xi)(1-10^{-A_\lambda})} \qquad \text{(Eq. 9)}$$

Wang's model

Wang et al. (2014) [60] demonstrated a different perspective on the light-to-heat conversion model. The energy balance equation was written in a simplified form:

$$\frac{d(T-T_0)}{dt} = a - b(T-T_0) \qquad \text{(Eq. 10)}$$

Of the parameters in this equation, a is the rate of energy absorption (K/s) and b (1/s) is the rate constant associated with heat loss.

$$\mathrm{a} = \frac{P\cdot(1-10^{-A_\lambda})\cdot\eta}{\sum m_i\cdot C_{p,i}} \qquad \text{(Eq. 11)}$$

$$\mathrm{b} = \frac{hS_A}{\sum m_i\cdot C_{p,i}} \qquad \text{(Eq. 12)}$$

Integrating of Eq. 10 results in the temperature change equation:

$$T(t) = T_0 + \frac{a}{b}[1-e^{-bt}] \qquad \text{(Eq. 13)}$$

The parameters a and b can be then evaluated from fitting of the experimental data from the heating part of heating-cooling equation and can be then substituted to the final photothermal conversion efficiency equation in which P is a laser power and remaining parameters are the same as in Roper model:

$$\eta = \frac{a\cdot\sum m_i\cdot C_{p,i}}{P\cdot\left(1-10^{-A_\lambda}\right)} \tag{Eq. 14}$$

Wang’s work also pointed out that in the case of a spectrophotometric cuvette which is a holder for liquid sample, not whole mass of the cuvette is involved in the thermal exchange and thus should not be included in the analysis. In order to determine how much of the mass should be included, an experiment was proposed in which the laser beam was replaced by a resistive heating wire, and it was assumed that such an element provides energy with 100% efficiency.

5.4.2 Experimental setups

One of the first proposed experimental system for photothermal conversion efficiency determination was demonstrated by Roper et al. (2007) [129] (Figure 2), who placed the suspension of nanoparticles in the micro cell (15.9 x 4.4 x 0.6 mm of which 9.9 x 4.0 x 0.2 mm was volume of sample). The solvent was distilled, deionized and vacuum degassed water. The sample cell was placed in the vacuum chamber during the measurements. The temperature was measured by K type thermocouple.

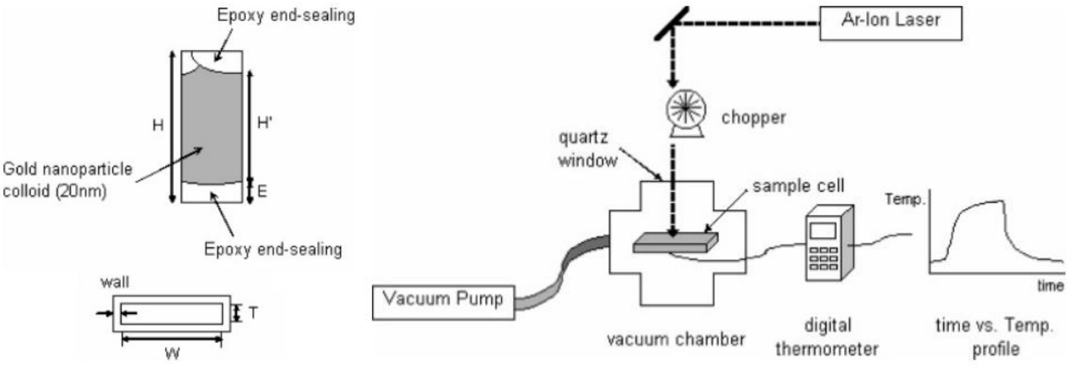

Figure 2. One of the first proposed experimental systems for light-to-heat conversion efficiency determination (Roper et al.) [129]: sample cell (left) and experimental system (right).

The other, simplified experimental system was proposed by Chen et al. (2010) [130] (Figure 3) , which turned out to be much simpler to reproduce, hence it has been adopted by many research groups. The sample was placed in a spectrophotometric cuvette, over a magnetic stirrer. The laser beam passed through the centre of the cuvette and the thermocouple was immersed in the suspension. The cuvette was covered from above with polystyrene.

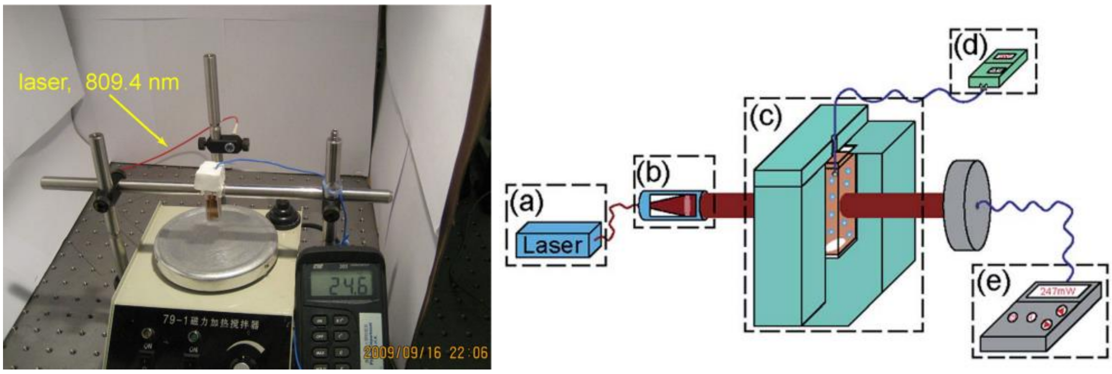

Figure 3. Experimental system presented by Chen et al. (left) [130] and by Wang et al. (right) [60].

Apart from the traditional thermocouple measurements, other techniques are applied, i.e. fluorescent thermometry [76,82,131], infrared camera measurements [132–134] (Figure 4) or magnetic resonance imaging [135].

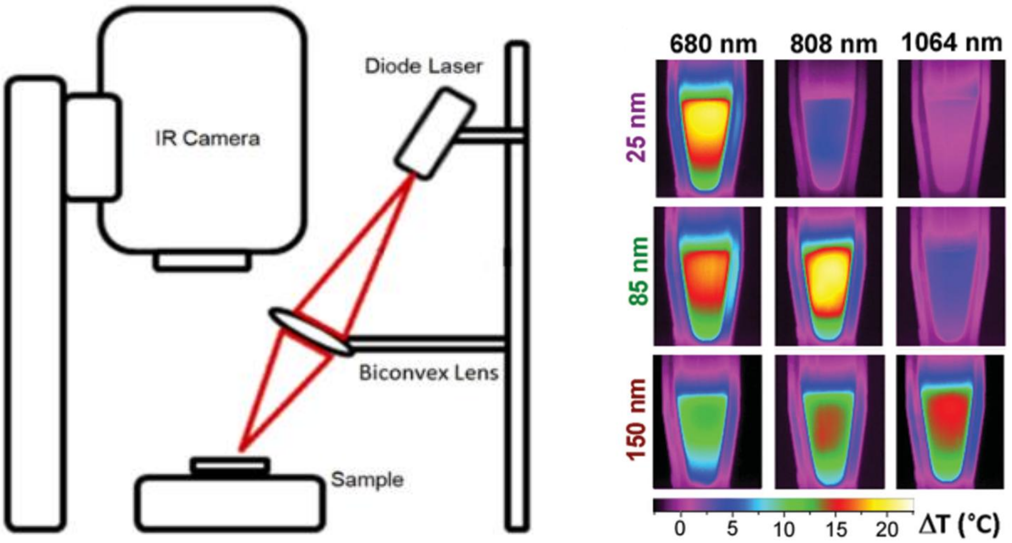

Figure 4. Experimental setup using thermal camera (left) [133] and example data obtained from thermal imaging camera (right) [134]

A different measurement system to the above was demonstrated by Richardson et al. (2009) [136] (Figure 5). Instead of placing the sample in a container, it was held on a syringe, in the form of a droplet. This solution allowed a clear reduction in measurement time and reduced the contact between the sample and the environment during measurement. Temperature was measured using a thermocouple, which clung to the drop. However, hanging the drop in the correct location relative to the laser beam was difficult to reproduce and evaporation of small droplets was found to disturb the reliable measurements, thus the system was very rarely replicated [137].

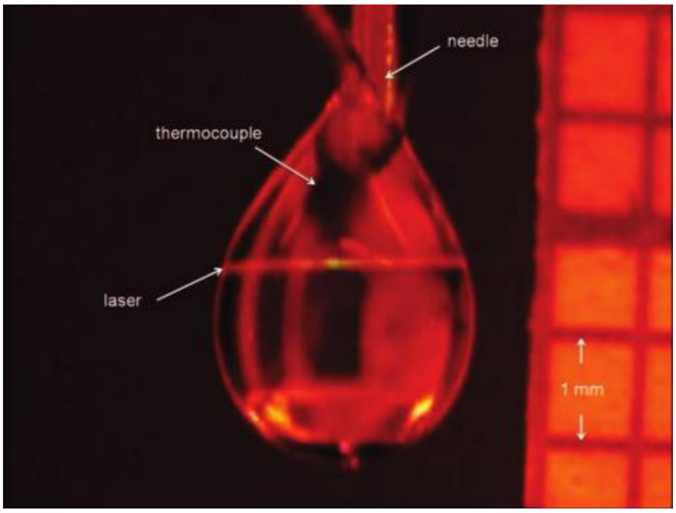

Figure 5. Droplet experimental system presented by Richardson et al. [136]

Another approach was also proposed in which gold nanoparticles were embedded in ice. The heat generated by the materials when illuminated caused the ice to melt, which was analyzed using a time-resolved Raman signal [138]. This approach appears complicated, so it is not considered a routine way to determine photothermal conversion efficiency.

The variety of measurement techniques proposed and used so far have indicated numerous issues and drawbacks. For example, in the case of infrared camera measurements, it is important to note that the camera only records the surface temperature and not the internal temperature of the system. Especially in larger measuring systems, thermal gradients can occur and the way how the temperature is measured can determine the result [132]. To date, there have been no clear guidelines on how temperature should be measured and the lack of consensus on which model should be chosen for data analysis when determining the light-to-heat conversion efficiency.

Bio-related studies

According to the recommendations from the European Upconversion Network [110] the introduction of a nanomaterial for therapeutic use should begin with verification that the material is effective and can be inserted inside the organ/tissue/cell. Cytotoxicity should then be determined. Based on this, the maximum dose is selected, and it is necessary to verify that it allows to obtain therapeutic effect. The next step, after verifying the photothermal conversion efficiency of nanomaterials and *in vitro* studies of cytotoxicity, is to test them under *in vivo* conditions [80,112–114]. Typically, such experiments are carried out on mice. They allow verification of whether the generated heat can cure the tumor, as well as checking the biocompatibility and the clearance mechanism.

Clinically applied PTT is based on the absorption properties of chromophores naturally occurring in tissues, which are illuminated by laser radiation [139]. The US Food and Drug Administration has approved the Indocyanine Green dye for use in photothermal therapy. Also, the use of 980 nm, 150 W (Visualase Thermal Therapy ®) and 1064 nm, 12 W (NeuroBlate ®) lasers has also been approved. The use of nanoparticles, on the other hand, still needs to be studied more thoroughly, because up to now only single clinical early-phase pilot studies have been conducted using nanomaterials [11].

It is also necessary to standardize the methods used so far, since the commonly determined photothermal conversion efficiency does not directly translate into photothermal effects achieved in the tissue.

5.4.3 Photothermal conversion efficiency of exemplary nanomaterials

Nanomaterials belonging to various classes are characterized by different photothermal capabilities. Representative examples of nanomaterials, along with their photothermal conversion efficiencies, are summarized in Table 1.

Table 1. Photothermal conversion efficiency **η** of exemplary colloidal nanoparticles measured at various sizes and excitation wavelengths λ.

	Material	Size [nm]	λ [nm]	**η [%]**	Ref
PLASMONIC	Au nanoparticles	20	532	**100**	136
	Bumpy Hollow Gold Nanospheres	56-90	790	**97-99**	58
	Au nanorods	44 x 13	815	**61**	140
	Au/AuS nanoshells	50	815	**59**	140
	Biodegradable Au nanovesicles	26	808	**37**	141
	Au nanoparticles	20	514	**3-10**	129
SEMICONDUCTOR	Si	8	808	**75**	92
	Si	4	808	**58**	92
	Ag_2S	9.8	785	**35.0**	142
	Black porous silicon	156	808	**33.6**	86
	Cu_9S_5	70 x 13	980	**26**	143
	$Cu_{2-x}Se$	16	800	**22**	71
ORGANIC	Conjugated polymer dots	30	808	**65**	49
	Porphyrin-containing conjugated polymer	39	808	**63.8**	144
	Dopamine-melanin	160	808	**40**	145
	Prussian blue	-	808	**19.8**	114
CARBON	Amido modified carbon dots	4.1	660	**77.6**	146
	Supra carbon dots	12	808	**53.2**	147
	Carbon dots (N-O-CDs)	1.2-3.3	808	**38.3**	148
	Carbon dots	6-10	635	**36.2**	148
	Glucose-derived carbonaceous nanospheres	30-100	808	**35.1**	149
IRON	Iron oxide functionalized with TAT	5	808	**43**	150
	Iron oxide functionalized with TAT	20	808	**37**	150
	Fe_3O_4 nanoclusters	21	1064	**20.8**	151
	$Fe@Fe_3O_4$	13.4	808	**20.3**	152
LANTHANIDE-DOPED	$NaNdF_4$	9-25	800	**85-74**	115
	$NdVO_{4,}$	2.4	808	**72**	112
	NaNdF4 @prussian blue	29	808	**60.8**	114
	NaDyF4:10%Nd-GA-Fe	9	808	**60.1**	126
	$NaDyF_4$:Yb@$NaLuF_4$:Yb,Er@PDA –Mn	48.3	808	**40.8**	153
	NdVO4/Au	21	808	**32.2**	113
	NaNdF4	19	808	**8.7**	114

The table shows quite striking results - both the highest (100%) but also the lowest (3%) photothermal conversion efficiency was obtained for plasmonic materials. Among semiconductor materials, values of 22-75% were obtained. Particularly noteworthy in this group are silicon-based materials with high photothermal conversion efficiencies. Organic and carbon-based materials also show widely varying photothermal conversion efficiencies (19.8-65% and 35.1-77.6%). Low photothermal conversion efficiencies compared to the other groups were obtained for iron-based materials. However, these materials, unlike all the others, allow additional heat generation under the influence of a magnetic field. On the other hand, in the group of nanocrystals doped with rare earth ions, very different results were obtained for very similar materials.

As is evident, it is difficult to assess unequivocally, basing solely on the literature data, which class of materials show greatest promise to become effective reliable nanoheaters. The matter is further strongly complicated by the experimental conditions. Most of the works listed in Table 1 used the Roper model for calculations, however, different experimental systems were used. In addition, variety of nanomaterials is characterized by different absorption cross sections, which further disturbs the interpretation of the results. Furthermore, factors such as size [60,115,150], morphology [58,60,154,155] or wavelength [69,92] were found to affect the photothermal conversion efficiency.

The difficulties in directly identifying the best nanoheaters basing on the literature were the direct motivation for the author's further research, described in the subsequent chapters of this dissertation.

6 EXPERIMENTAL

6.1 Materials

The studies were performed on variety of nanomaterials synthesized in different European laboratories. These nanomaterials were in the form of colloids. The main role of the author of the dissertation was to characterize and compare the mentioned nanomaterials in terms of their photothermal ability.

Au@SiO_2 and $NaNdF_4$@PAA doped with Dy^{3+} and Sm^{3+} (instead of Nd^{3+} ions) was synthesized by Aleksandra Pilch-Wróbel (Institute of Low Temperature and Structure Research, Polish Academy of Sciences, PAS). Gold nanorods (AuNRs) were synthesized by Katarzyna Prorok (Institute of Low Temperature and Structure Research, PAS). Ag-Ag_2S dimers and CuS covered by citrate and by glutathione was prepared by Riccardo Marin (Universidad Autónoma de Madrid). γ-Fe_2O_3 and Ag_2S nanoparticles covered by mercaptoundecanoic acid (MUA), polyethylene glycol (PEG) and dithiolated diethylenetriamine pentaacetic acid (DTDTPA) were synthesized by Lise Abiven (Sorbonne Université, CNRS). Black porous silicon was prepared by Wujun Xu (University of Eastern Finland). γ-Fe_2O_3@Au was synthesized by Rana Bazzi and Stephane Roux (Université Bourgogne Franche-Comté, CNRS). Carbon nanodots, NdF_3 and Nd_2O_3 nanoparticles were synthesized by Małgorzata Misiak (Institute of Low Temperature and Structure Research, PAS). $NaYF_4$ doped with Nd^{3+}, Yb^{3+} and Tm^{3+} and co-doped with Sm^{3+} and Dy^{3+} were prepared by Karolina Trejgis (Institute of Low Temperature and Structure Research, PAS). $NdVO_4$ and $NdAlO_3$ were prepared by Karolina Elżbieciak-Piecka (Institute of Low Temperature and Structure Research, PAS).

6.2 Methods

6.2.1 Structural and morphological properties

1. The X-ray diffraction profiles (XRD) of BPSi and γ-Fe_2O_3 were collected on a Bruker D8 Advance. XRD of Ag_2S was measured by diffractometer

Bruker D8 Discover equipped with a EIGER2 R 500K 2D detector. XRDs of CuS and Ag-Ag_2S nanoparticles were measured on a Rigaku D/max-γB diffractometer. A filtered Cu Kα radiation (λ = 1.5418 Å) was used. XRDs of AuNRs, $NaNdF_4$:Dy@PAA, $NaYF_4:Yb^{3+}$, $NaYF_4:Yb^{3+},Sm^{3+}$ $NaYF_4:Nd^{3+}$, $NaYF_4:Nd^{3+},Sm^{3+}$, $NaYF_4:Tm^{3+}$, $NaYF_4:Tm^{3+},Sm^{3+}$, $NaYF_4:Tm^{3+},Dy^{3+}$, $NaNdF_4$, NdF_3, $NdVO_4$, $NdAlO_3$ and C-dots were collected on an X'Pert PRO X-ray diffractometer equipped with a PIXcel ultrafast line detector, a focusing mirror, and soller slits for Cu Kα radiation.

The resulting data were plotted using OriginPro software and compared with the reference peaks corresponding to each sample.

2. Transmission electron microscope (TEM) images of AuNRs, NaNdF4:Dy@PAA nanoparticles and carbon dots were obtained using a Philips CM-20 Super-Twin instrument operating at 160 kV. TEM images of Ag_2S, γ-Fe_2O_3, and of γ-Fe_2O_3-Au were obtained by an FEI Tecnai Spirit G2 instrument operating at 120.0 kV. TEM images of CuS and Ag-Ag_2S nanoparticles were obtained by JEOL JEM1400 Flash at an acceleration voltage of 100 kV. BPSi was imaged with High-Resolution TEM, JEOL JEM2100F. TEM images of $NaNdF_4$, $NaYF_4:Yb^{3+}$, $NaYF_4:Yb^{3+},Sm^{3+}$, NdF_3 (synthesized in water and in $CHCl_3$,) Nd_2O_3, $NdVO_4$, $NdAlO_3$ were obtained using a Titan G2 (S)TEM 60-300 instrument at 80 kV. TEM images of $NaYF_4:Nd^{3+}$, $NaYF_4:Nd^{3+},Sm^{3+}$, $NaYF_4:Tm^{3+}$, $NaYF_4:Tm^{3+},Sm^{3+}$, $NaYF_4:Tm^{3+},Dy^{3+}$ were determined using a Philips CM-20 Super-Twin instrument operating at an acceleration voltage of 160 kV.

Nanoparticle sizes were determined by the author of this dissertation, by analyzing TEM images in ImageJ software.

6.2.2 Optical properties

1. The extinction spectra of CuS and Ag-Ag_2S nanoparticles were obtained by UV−Vis−NIR spectrophotometer (Perkin Elmer Lambda 1050). The extinction spectra of remaining samples were measured in the

transmission mode using a Cary Varian 5E UV-Vis-NIR spectrometer. A deuterium (for UV) and halogen (for Vis/NIR excitation) lamp were used as excitation sources. In the UV and Vis range, the R928 photomultiplier was used as a detector, and a cooled PbS detector was used for the NIR range.

2. The photoluminescence quantum yield (QY) of carbon dots (CDs) was evaluated using the FLS 980 spectrograph equipped with custom designed integrating sphere. The irradiation source was a 445 nm laser diode (1.5 W, Changhun New Industries). The Al_2O_3 powder was used as a reference. QY was evaluated using the following equation, where h_{em} is a number of photons emitted and h_{abs} is a number of photons absorbed, and I is an intensity obtained for CDs and reference:

$$QY = \frac{h_{em}}{h_{abs}} = \frac{I_{CDs} - I_{ref}}{I_{ref} - I_{CDs}} \quad \text{(Eq. 15)}$$

Absorption intensity was calculated in 435-453 nm range and emission intensity was calculated in 460-640 nm range.

6.2.3 Photothermal properties – cuvette measurement system

Evaluation of the photothermal properties of colloidal nanomaterials required the preparation of experimental systems from scratch basing on the available literature. The photothermal conversion efficiency of $Au@SiO_2$ nanoparticles was evaluated using the cuvette experimental system, which was constructed similarly to the system proposed by Chen et al. [130] presented in Figure 3. However, the temperature was measured with a thermal imaging camera (FLIR T540) in a position that allows direct measurement of the colloid temperature (Top), and in a position perpendicular to the cuvette (measurement through glass, Side). Measurement conditions were also modified by using a magnetic stirrer.

Laser diode (532 nm, 1 W, Changhun New Industries) was used as a light source and the excitation optical power was ~200 mW (power density ~1.6 W/cm^2). Beam shape was obtained using a beam shaping system consisting of an objective (45/0.65) and a pair of plano-convex lenses (f=150 and f=100, Thorlabs). Optical power meters were used to record optical power (photodiode S120C head and PM100USB power meter, Thorlabs). The measurements were conducted in an air-conditioned room, at a temperature of 23 °C, with constant humidity conditions. The system was additionally isolated from the impact of external interferences by a styrofoam cage.

6.2.4 Calibration of the experimental system for photothermal efficiency evaluation – Wang's method

The Wang model requires an accurate determination of the effective mass of the system. For this purpose, the laser beam was replaced by a resistance wire, so it was possible to assume that 100% of the supplied energy was converted to heat. When the sample holder is a quartz cuvette, a technical solution is needed that will not damage the cuvette. Hence, a heating element was prepared from scratch (Figure 6). This was an approximately 1 cm segment of 0.3 mm thick Kanthal wire which was welded on both edges with silver-plated copper wire, which acted as a current input. This element was placed inside a quartz cuvette in a position that corresponds to the position of the laser beam. Other components of the measurement system were in the same position as in the experiment. A current of 0.25-1.02 A was set on a regulated DC power supply (MCP M10-QS3020, Poland), while the voltage on the heating wire was registered with a multimeter (UNI-T UT39A). From these data, the resistance (R=380 Ω) of the heating element and delivered power (P) at different set currents were evaluated and used for further calculations.

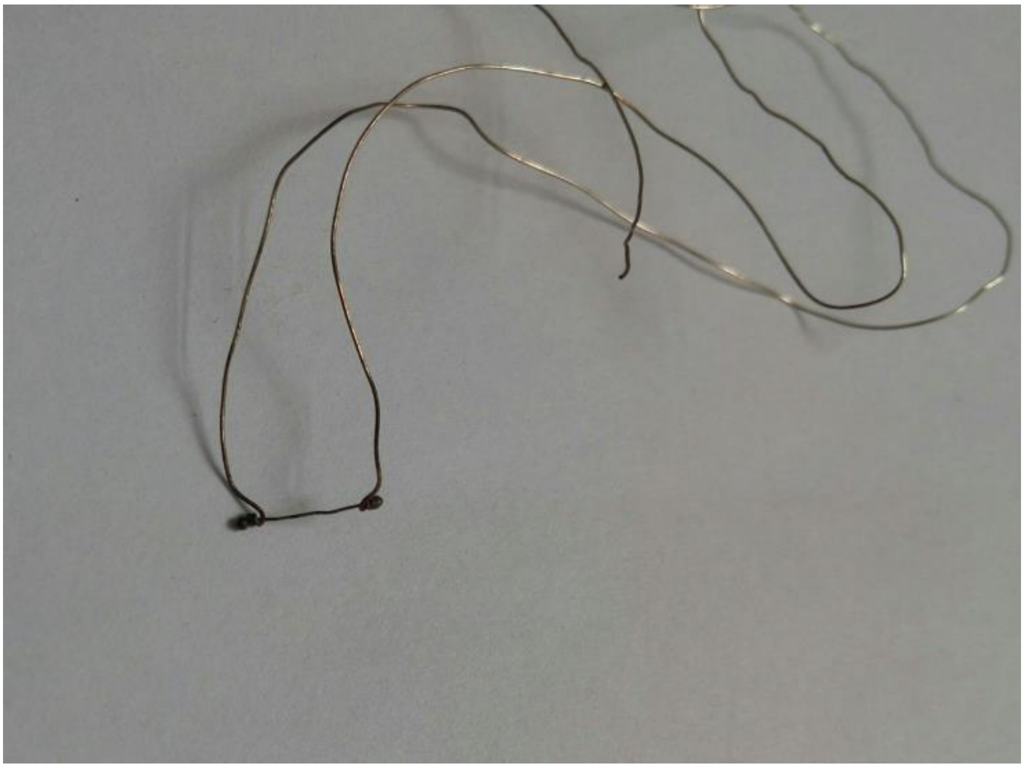

Figure 6. Heating element for Wang's calibration

6.2.5 Photothermal properties – droplet measurement system

The photothermal conversion efficiency of all the investigated samples was evaluated using the droplet measurement system designed by the author of this dissertation. Details of the system structure are presented in the patent described in Section 7.2. Various laser diodes were used during photothermal conversion studies (from Changchun New Industries Optoelectronics Technology Co., Ltd.): 400 nm (100 mW), 445 nm (1.5 W), 532 nm (1 W), 668 nm (1 W), 793 nm (3 W), 808 nm (2 W), 940 nm (2 W), 980 nm (10 W), and 1060 nm (2 W). Optical power was registered by power meters (photodiode S120C head and PM100USB power meter, Thorlabs). Typically, excitation laser power was 90 mW, and the optimal optical power was adjusted by moving the droplet in the optical axis to change the beam diameter.

6.2.6 Measurement procedure

The technical details of the measurement procedure are described in detail in publications [P1] and [P2], as well as in the patent. Briefly, after adjusting the measurement system and appropriate dilution of the sample, the optical power in the system and the reference power were recorded and the desired optical power was ensured. Then, in the case of the droplet system, the sample droplet was formed and its position was adjusted relative to the laser beam, or the sample was placed in a cuvette in the given position in the system. The humidity chamber was then sealed (in the case of the droplet system) and the system was covered with a polystyrene cover and was left to achieve thermal stabilization (~5 min for the droplet system and ~1 h for the cuvette system). The laser diode was then turned on to warm up, and the sample temperature and optical power recording was started. After recording of the initial temperature, the laser beam was attached to the system by unlocking the mechanical shutter and the temperature rise curve was recorded. After the temperature was stabilized (about 2 min for the droplet system and about 45 min for the cuvette system), the laser diode was turned off and the temperature decrease curve was recorded. At the end, to determine the mass of the sample, the photo of the droplet was registered or the cuvette containing the sample was weighed.

The procedure described above was carried out independently for the reference (water) and for the measured sample. Figure 7 schematically illustrates the droplet measurement system and the optical power and temperature profiles during the measurement.

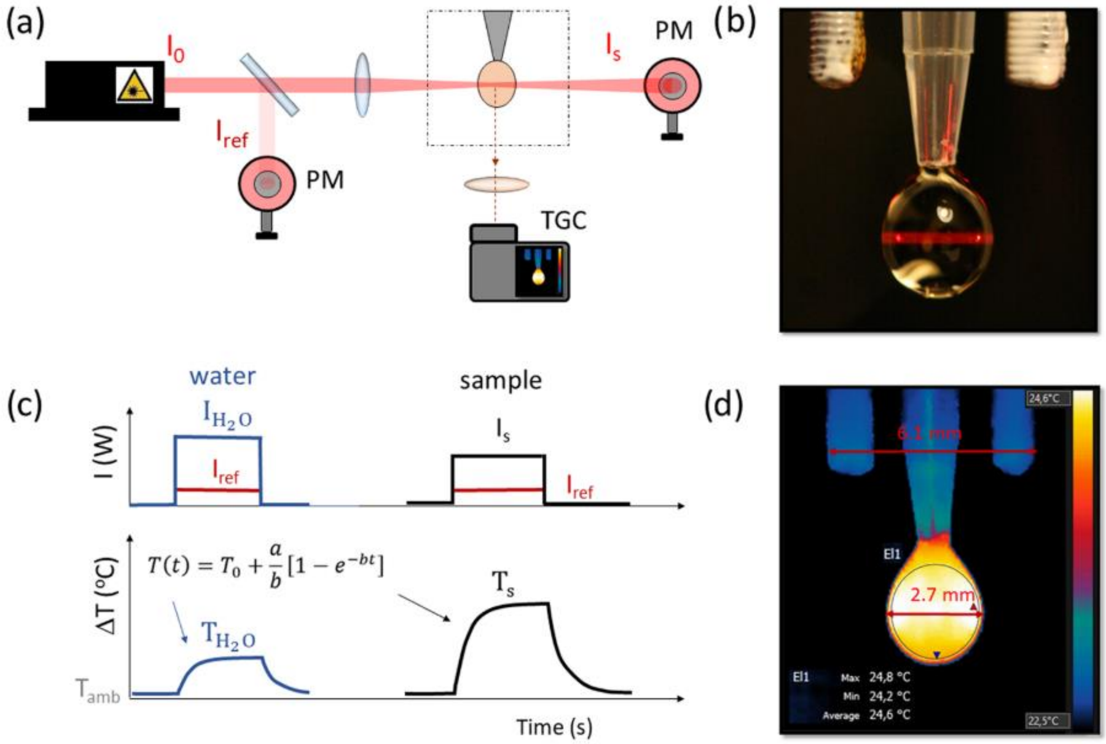

Figure 7. Droplet optical system: a) system scheme b,d) droplet image (optical and thermographic), c) registered profiles of optical power and temperature during measurement [P2].

Basing on the acquired data, i.e., temperature curve, optical power (reference and determined behind the sample) and sample mass, calculations were carried out according to the equations described in the Introduction (Eq. 6, Eq. 14) or the modified Wang equation proposed in the paper [P2]. The methodology used and example data were uploaded and made publicly available - the photothermal conversion efficiency calculations in Excel is posted as Supplementary material to the paper [P2] available online at the journal's website (https://pubs.acs.org/doi/10.1021/acsami.2c08013).

In the described series of publications, the photothermal conversion efficiency of nanomaterials belonging to different classes was studied. To compare the nanoheaters, it was necessary to develop and evaluate a new methodology, because the methodology most commonly applied in the literature led to inconsistent results. For this reason, the first part of this chapter includes a description of methodology and a patent on the droplet measurement system for determining the photothermal conversion efficiency, which were both proposed and evaluated by the author of this dissertation. The second part shortly describes publications in which different nanoheaters were examined and compared using the droplet system.

7.1 Development of the methodology of photothermal conversion efficiency evaluation

7.1.1 Standardization of Methodology of Light-to-Heat Conversion Efficiency Determination for Colloidal Nanoheaters [P1]

The P1 work was motivated by the author's observation that the literature has reported extremely different photothermal conversion efficiencies for very similar materials. Specifically, Roper et al. [129] showed that for gold (~20 nm) nanocrystals the determined efficiency is 3-10% (depending on the light modulation). In contrast, Richardson et al. [136] for similar materials (also ~20 nm gold nanocrystals) obtained the efficiency close to 100%. In addition, a numerous papers concerning nanoheaters were cited in which thermal kinetics were presented, but the photothermal conversion efficiency was not determined at all, which may indicate that it was problematic for some reason.

Moreover, it has been noticed that there was no single "gold standard" of photothermal conversion efficiency measurement, and the use of different measurement methods and models can cause large discrepancies in the results obtained by different researchers. In consequence, the reliable comparison of various NHs was not available at that stage. To prove that the existing methods were poorly reliable, a series of experiments were conducted in which one sample (the same batch of Au@SiO$_2$) was measured in five different measurement configurations (Figure P1.1), and then the results were calculated using two different models, including the most commonly used Roper model [129] and the less popular Wang model [60].

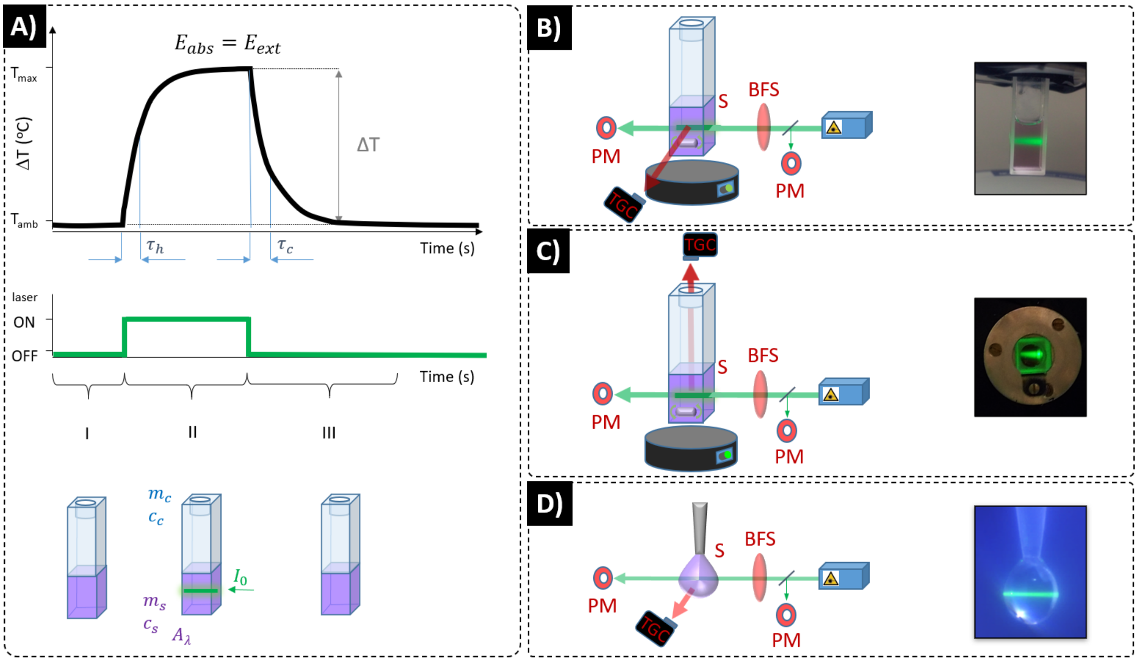

Figure P1.1 General scheme of methods and setups used to determine η_Q. (A) Schematic presentation of the elements and methods used in heat balance physical model (bottom row), photostimulation (middle row), and the exemplary results of typical η_Q measurements (top row); τ_h and τ_c denote inverse of heating and cooling rates, respectively, at saturation stage $E_{abs} = E_{ext}$, where E_{abs} and E_{ext} are absorbed and external energies, the ΔT is maximum temperature rise; m_x and c_x denote the mass and heat capacity of the cuvette (x = C) and of the sample (x = S), the sample is heated at stage II, while stabilizing at stage I and cooling down at stage III; schematic presentation and example photos of experimental setup variants: (B) Thermographic camera (TGC) records the temperature of side wall of the cuvette, (C) TGC records the temperature of colloidal nanoparticle solution directly from the top of the cuvette, (D) TGC records the temperature images of a small droplet of colloidal HTNPs. PM is optical power meter, BFS is a beam focusing system, S is a sample. Mild sample stirring may be applied in (B) and (C) setups.

Among the considered measurement configurations were: a sample placed in a cuvette with an optional magnetic stirrer whose temperature was measured with a thermal imaging camera in two ways (from the surface of the sample, and, as in some works, through a glass cuvette), and a sample in the form of a droplet. Measurements of the sample temperature in different configurations resulted in different rise and fall of temperature curves (Figure P1.2).

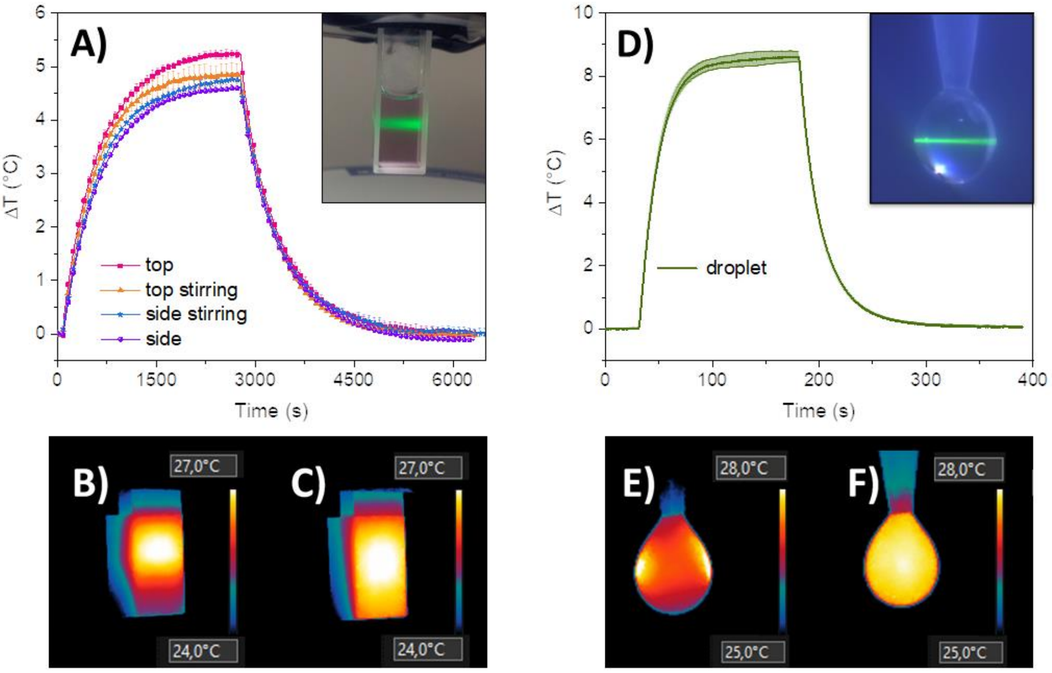

Figure P1.2. Heating and cooling of Au@SiO$_2$ sample in various experimental configurations. (A) Temperature curves in the "standard" setup with TGC in top and side view, with and without mechanical stirring. (B) Corresponding temperature images (obtained from the side view, in a setup without mechanical stirring) at heating (B) and cooling (C) stages. (D) Temperature heating–cooling curves obtained in a setup with droplet and corresponding temperature images of (E) heating and (F) cooling. Experimental variants are presented in Figure P1.1.

In the calculations according to the Roper model, it was assumed (as in the original work) that all the elements that make up the system take part in the heat exchange, including in particular the cuvette that acts as a sample holder. For the Wang model, on the other hand, a resistance wire experiment was performed to simulate a material with a 100% efficiency and determine the effective mass. The results showed that using of the Wang model leads to convergent results (81% for the tested Au@SiO$_2$ sample), regardless of the measurement system. In contrast, the most popular Roper model leads to divergent results (51-107%) and is highly dependent on the assumption which mass volume should be considered as participating in the heat exchange. It turns out that different effective mass of the same cuvette was determined by the Wang method for the different measurement configurations. Consequently, the Wang model has been shown to perform more reliable than any other previous model. This is also the most important conclusion from this publication.

In the case of the droplet system, because a sample holder is not present, 9the mass included in the calculation was assumed to be the mass of the droplet. This assumption led to the same photothermal efficiency as in the case of the most sophisticated systems with a spectrophotometric cuvette. This means that this system can also be successfully used to evaluate the photothermal conversion efficiency of colloids. The exact design and advantages of the author's measurement system, which enables the measurement of a sample as a droplet, are presented in the following patent.

7.1.2 Experimental system and method for determining the photothermal efficiency of colloidal nanomaterials in VIS and NIR range [Patent]

The inspiration for constructing of the measurement system came from the understanding of the drawbacks of measurement systems found in the literature. In particular, the standard system with a spectrophotometric cuvette requires a large sample volume, and the measurement is very time-consuming (a single measurement takes about 3h per sample). On the other hand, systems that allow the measurement of small sample volumes suspended in droplet form are characterized by a number of physical, metrological and technical problems that have not been solved yet. The following are the problems encountered, and the solutions proposed by the author of this dissertation, which were used in the measurement system and covered by the patent claims.

1. <u>The need to accurately measure the temperature of a small object such as a droplet</u>

   The use of a traditional thermocouple does not provide the required accuracy since the head of the thermocouple is of comparable size to the drop. On the other hand, the use of a standard thermal imaging camera does not allow for higher image magnification. In addition, the manufacturer of the thermal camera declares an accuracy of 2 °C, which is insufficient for such precise measurements. Thus, a solution was proposed in which a germanium lens was used for magnification, while to increase the accuracy of the measurement, it was based on a reference measurement.

2. The need to maintain a stable droplet of a set volume during the measurement

   Maintaining a drop of a fixed size is a difficult task. While solutions have been proposed in which the droplet was dispensed using a syringe [136] or one-end-sealed PTFE pipette [137], these solutions do not allow free modification of the droplet size and producing a droplet requires skill. The problem was solved by using an automatic pipette connected to a designed mechanical valve, with the help of which the access of air is cut off after the droplet is formed to prevent backflow.

3. The need to reduce sample evaporation

   Directly related to the aspect of maintaining a droplet of a set size is the reduction of evaporation, because a droplet of small volume (~10 µL) under average laboratory conditions evaporates very quickly. The proposed solution is to switch into conditions of increased humidity, in a sealed humidity chamber.

4. The need to precisely control the position of the droplet

   In the literature solutions, the position of the drop was not modified. Meanwhile, the ability to move the droplet in the optical axis allows to adjust the power of the beam, and in the plane perpendicular to the beam axis - to adjust the position of droplets of different sizes. This capability was provided by using an XYZ micrometric screw-controlled table to which the droplet dispensing part was mounted.

5. The need to provide easily accessible interchangeable components that are in direct contact with samples

   Replacement tips used as standard for 2-200 µL automatic pipettes are used to dispense the sample.

A scheme of the measurement system that allows for measuring of the photothermal conversion efficiency with the elimination of the above-mentioned problems is shown in Figure 8. The patent application includes claims regarding the design of the measurement system (e.g. the design of the droplet dispensing system and measurement chamber) and its specific methodology (e.g. the collection and positioning of the sample, method of providing increased humidity during measurement, determining the droplet volume).

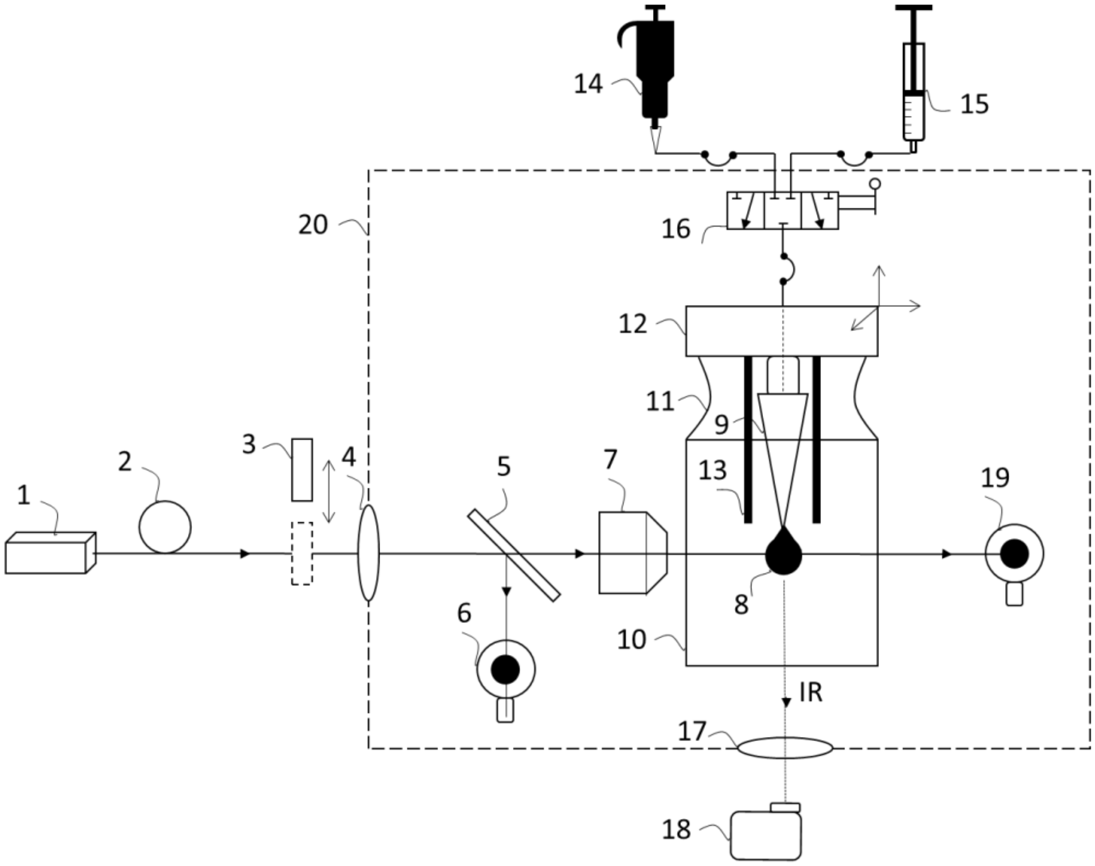

Figure 8. Scheme of the measurement system for measuring photothermal conversion efficiency of colloidal materials 1) light source (laser diode) 2) input optical fiber 3) adjustable shutter 4) focusing lens 5) semi-transparent element 6) optical power meter (reference measurement) 7) beam focusing system (focusing lens + objective) 8) sample in the form of a droplet 9) interchangeable tip (for automatic pipette) 10) sealed humidity chamber 11) flexible sealing of the upper part of the chamber 12) adapter between the tip and the flexible tube attached to the XYZ table providing mobility of the tip 13) scale for camera calibration and droplet size determination 14) precision dispenser (e.g. pipette) 15) dispenser (e.g. syringe) 16) three-way valve 17) transmission element for radiation from the working range of the thermal imaging camera (e.g., germanium lens) 18) thermal imaging camera 19) optical power meter (measuring transmission behind the sample) 20) thermal insulation.

7.2 Photothermal conversion efficiency evaluation of colloidal nanomaterials

7.2.1 Quantitative Comparison of the Light-to-Heat Conversion Efficiency in Nanomaterials Suitable for Photothermal Therapy [P2]

The P2 paper concerns the comparison of materials belonging to different classes in terms of their photothermal properties. It was motivated by three issues. First, there was a large discrepancy in the results obtained by different researchers for similar materials on different measurement systems, making their direct comparison difficult. Second, there is no direct translation of the parameter determined so far (*internal* light-to-Heat Conversion Efficiency, iHCE) into suitability for photothermal application. This is due to the fact that iHCE is a value that determines which fraction of the absorbed energy will be converted into useful heat. However, in the application it is also significant how much of the energy will be absorbed, as there are materials with very high photothermal conversion efficiency, but relatively low absorption cross-section. A third issue was the lack of works illustrating how photothermal conversion efficiency changes as a function of wavelength. Single papers have examined the material at 2-3 wavelengths [69,92], but no systematic study of the effect of wavelength on photothermal conversion efficiency has yet been conducted.

To address these issues, a new parameter, *external* light-to-heat conversion efficiency, eHCE, was proposed that considers both *internal* HCE and the mass absorption coefficient a determined for a specific wavelength. This parameter allows quantitative assessment of the suitability of the material for PTT in terms of their heating properties:

$$eHCE = HCE \cdot a(\lambda) \qquad \text{(Eq. 16)}$$

Wang model was also extended to include the heating of solvent. This was not necessary for the aqueous suspension of nanoparticles measured at 532 nm in the [P1] work, however, it was crucial for determination of *internal* HCEs at >700 nm excitation because then the heating of the solvent itself is becoming significant and non-negligible:

$$\mathrm{HCE} = \frac{a \cdot m_d \cdot C_{p,d} - \dot{Q}_0}{P \cdot (1 - 10^{-A_\lambda})} = \frac{(a_s - a_0) \cdot m_d \cdot C_{p,d}}{P \cdot (1 - 10^{-A_\lambda})} \qquad \text{(Eq. 17)}$$

Herein, parameters a_s and a_0 are fitting parameters corresponding to Eq. 13 of temperature increase of sample and water respectively, m_d, $C_{p,d}$ are mass and heat capacity of a sample droplet, and the other parameters are the same as explained in Section 5.4.1 in the description of the Wang model.

In the P2 publication seventeen materials belonging to five different classes were examined. For each of them, the photothermal conversion efficiency was determined, and for materials that showed absorption capabilities in a wider spectral range, iHCE and eHCE were determined for six wavelengths (445 nm, 668 nm, 794 nm, 806 nm, 980 nm, 1060 nm). Each measurement was repeated at least three times.

The iHCE analysis for various materials (Figure P2.1) led to surprising conclusions. For most materials, there was no clear trend in the change of iHCE as a function of wavelength. In addition, of the materials tested, the vast majority exhibited iHCE >80%, which is consistent with some work [60,130,136,137] but inconsistent with others [114,140,148,151]. The discrepancies may be related to the system used and the selected model, as described in [P1]. However, high iHCEs are expected, as this means that there is low scattering of the laser beam energy and negligible emission. This was also the case for these samples.

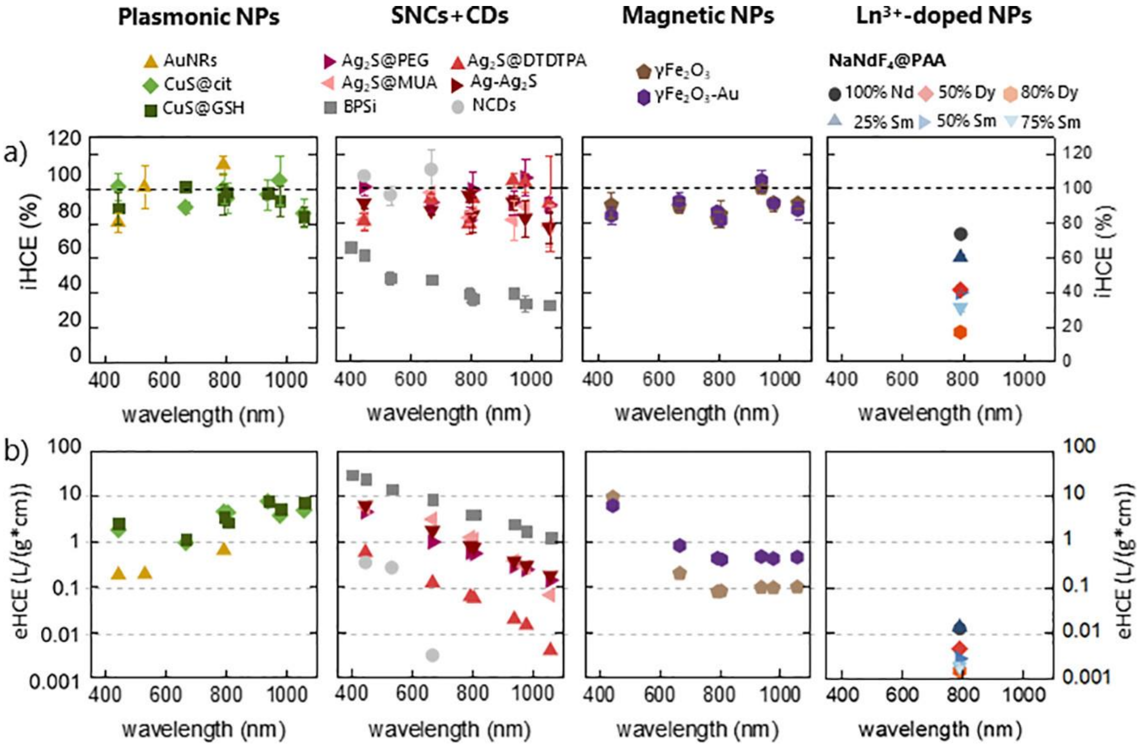

Figure P2.1 Ranking of the studied nanoheaters. Wavelength dependent (a) Internal and (b) External light-to-heat conversion efficiency.

The calculated eHCE values show that different materials exhibit eHCEs that vary by orders of magnitude. This makes it possible to explicitly select the best materials. In the visible range, the highest eHCE of >10 L/g · cm is achieved by black porous silicon. For PTT applications, however, the NIR range is of greatest importance. In this range, copper sulfide nanomaterials deserve special attention. The ranking of the tested materials at the optimal wavelength for PTT (794 nm) is shown in Figure P2.2.

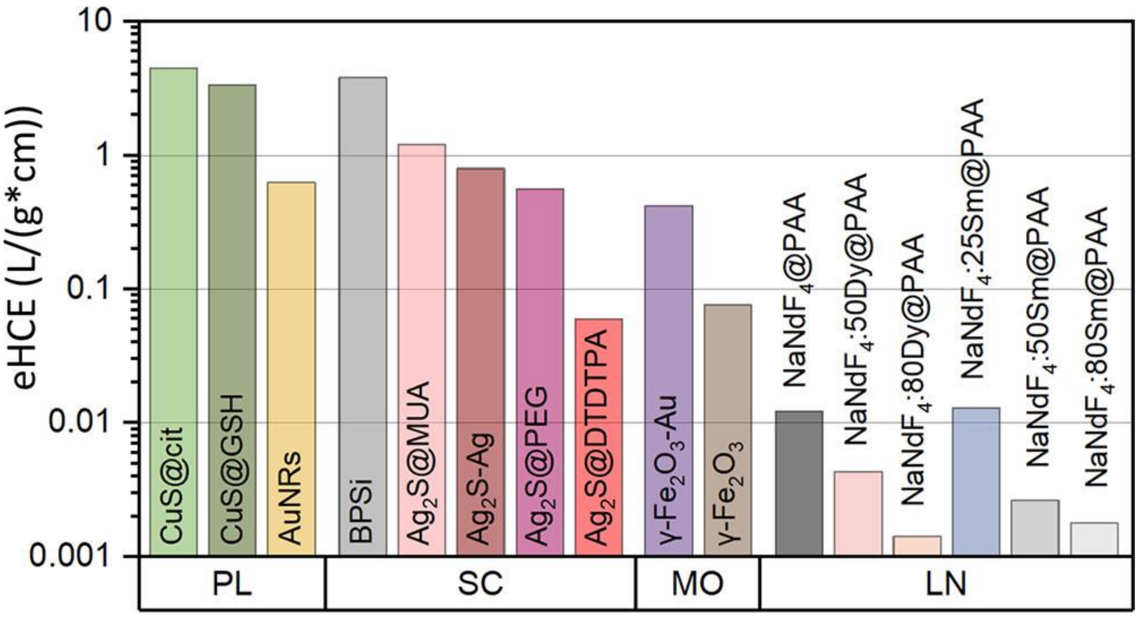

Figure P2.2. External light-to-heat conversion efficiency at 794 nm: ranking of the investigated nanoheaters (PL – plasmonic, SC – semiconductor, MO – metal oxide, LN – lanthanide-doped nanomaterials).

7.2.2 Highly-doped lanthanide nanomaterials for efficient photothermal conversion – selection of the most promising ions and matrices [P3]

The P3 work concerns the photothermal conversion efficiency of materials doped with lanthanide ions. These materials, although known as heaters for more than a decade [77], have not yet been comprehensively studied for their photothermal properties, as there are no comparisons in the literature of materials doped with different ions and no proven impact of matrix selection on photothermal properties. For this reason, the following dopant ions were chosen: neodymium, thulium and ytterbium ions, co-doped with samarium and dysprosium ions. Dysprosium ions have also been studied in the literature, but preliminary unpublished results indicated that these ions show exceptionally low absorption in the NIR range, and the heat generation was weak. Also, the photothermal conversion efficiency of five different matrices (two fluorides, oxide, vanadate and perovskite) was investigated.

Of the three ions studied (Figure P3.1), the material doped with neodymium ion achieves the highest iHCE (>90%). This is probably because in thulium ions, excitation with a wavelength of 794 nm can be followed by emission at ~1800 nm, while ytterbium is characterized by a large energy gap between the ground level $^4F_{7/2}$ and the first excited level $^4F_{5/2}$.

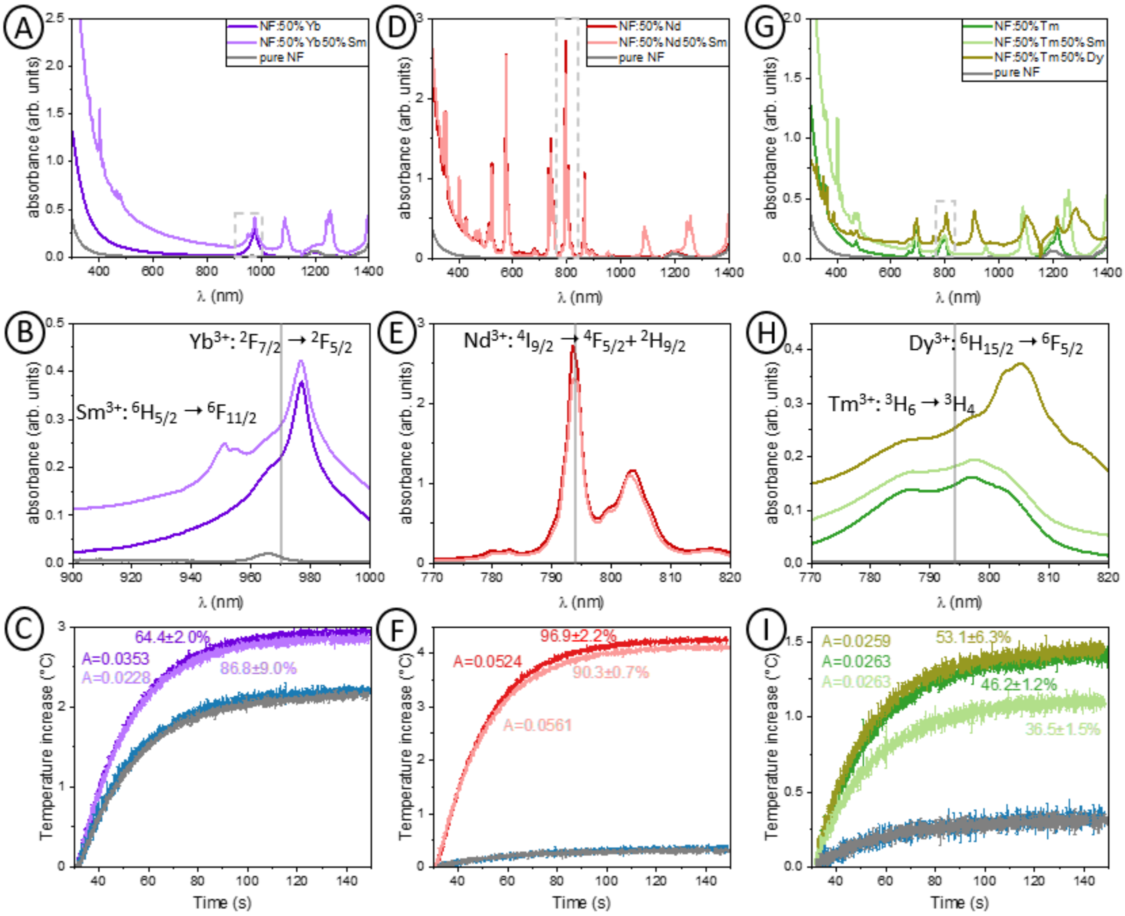

Figure P3.1. Absorption spectra in chloroform (A, C, E) and temperature increase in function of illumination time determined for samples dispersed in water and for the solvent (water - blue curve) itself: $NaYF_4$:Yb,Sm measured at 970 nm, $NaYF_4$:Nd,Sm measured at 794 nm, $NaYF_4$:Tm,Dy,Sm measured at 794 nm. The *A* parameter is the measured absorbance and numbers given in % are iHCEs with standard deviation.

The co-doping of samarium ions resulted in improved efficiency only when the absorbing ions were ytterbium ions, which was explained by a denser Sm^{3+} energy ladder and the possibility of non-radiative transitions. In contrast, for the other ions, samarium caused a slope in photothermal efficiency. The hypothesis explaining this dependence relates to the uneven location of these elements in the structure of the nanomaterial. On the other hand, co-doping with

Dy^{3+} of Tm^{3+} doped $NaYF_4$ resulted in improved efficiency, likely due to additional cross-relaxation capabilities.

Based on these results, it was concluded that the best efficiencies (both iHCE and eHCE) were obtained for samples containing neodymium, without co-doping of Sm^{3+}. Therefore, samples doped with 100% Nd^{3+} ions in different matrices were prepared and photothermal conversion efficiency was evaluated for 794 and 806 nm (Figure P3.2).

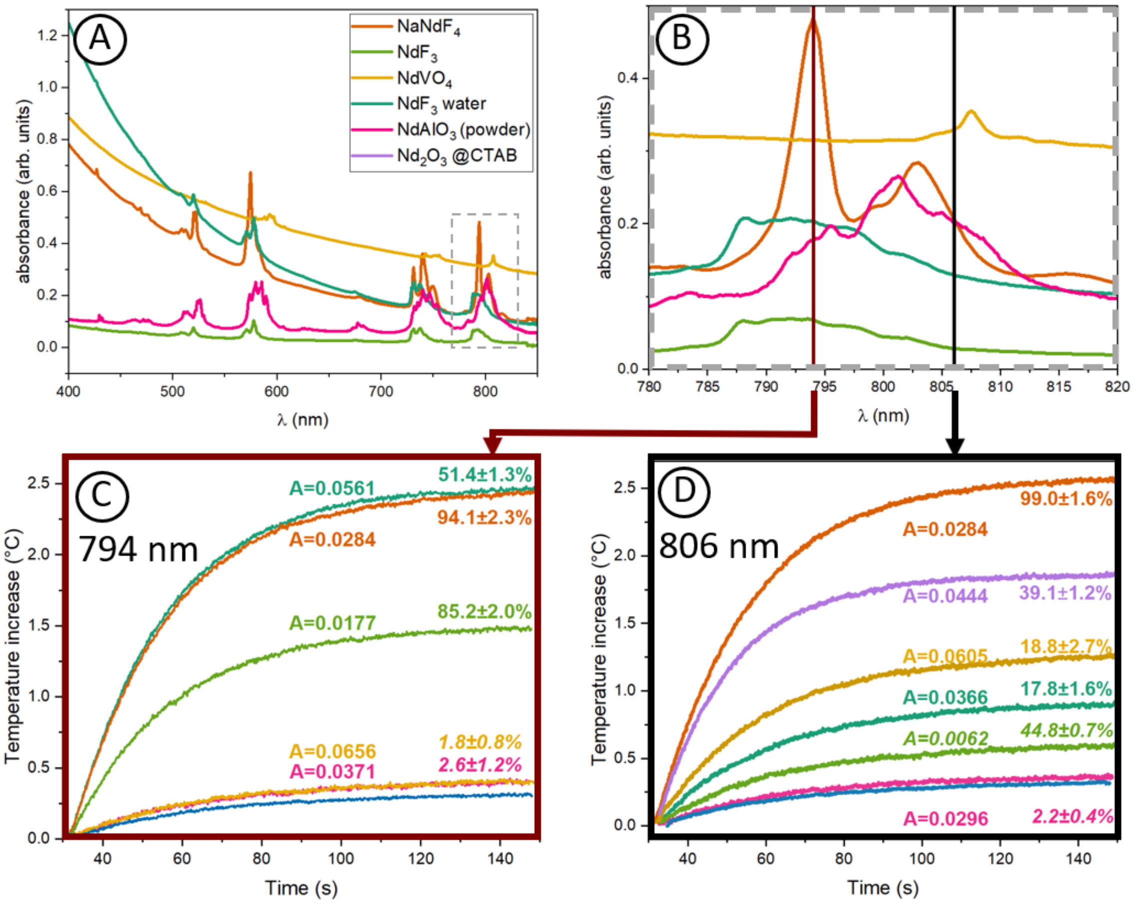

Figure P3.2. Absorption spectra (A,B) and temperature increase curves of fully concentrated Nd^{3+} doped samples under 794 (C), and 806 nm (D) laser beam excitation (90 mW), *A* is the measured absorbance and numbers given in % are iHCEs values with standard deviation.

The largest temperature rise was obtained for $NaNdF_4$ at both 794 and 806 nm. However, it should be kept in mind that these measurements were conducted at different concentrations (due to their different preparation methods), hence iHCE and eHCE are more authoritative values.

The morphology of the nanoparticles and the way they are suspended in water are also of significant importance. For example, NdF_3 synthesized in water with a larger size is characterized by a significantly lower iHCE (in comparison to the smaller NdF_3 transferred to water by HCl method) because of the scattering properties. However, in terms of eHCE, this material performs far better, as the more complex shape of the nanoparticles provides greater absorption capacity.

The highest iHCE was obtained for $NaNdF_4$. On the other hand, after considering the mass absorption coefficient, it turns out that the best eHCEs are achieved by $NdVO_4$ at 806 nm (0.08 L/g · cm) and $NaNdF_4$ at 794 nm (0.04 L/g · cm). $NdVO_4$, moreover, can find application in PTT due to its low cytotoxicity [156] and the possibility of being covered by additional coatings [113].

8 CONCLUSIONS

The conclusions of the work presented within this dissertation on the photothermal conversion efficiency can be divided into three areas: measurement systems, models, and ranking of nanomaterials.

Concerning the measurement systems, the standard cuvette system was evaluated in four different measurement configurations considering the effect of stirring and the choice of the area of which the temperature is measured. The system in which the sample is in the form of a droplet was also investigated. The droplet system was optimized to eliminate the drawbacks of the other existing systems, i.e., the measurement accuracy was improved, a solution was introduced to maintain a stable droplet of a given size for the duration of the measurement and its positioning, the effect of evaporation was reduced, and the possibility of using interchangeable tips was provided. The technical solutions used are described within the patent.

Concerning the models, the most commonly used Roper model and less known Wang model were evaluated experimentally. The research conducted as a part of the [P1] publication indicate that the former model is highly susceptible to assumptions about the effective mass of the system and can be strongly affected by measurement conditions. In contrast, the latter model leads to consistent results regardless of the measurement system used. This is a finding of particular importance to the photothermal conversion community, as it demonstrates an important reason, why the results obtained from the Roper model do not allow for a reliable comparison of materials between different laboratories. Thus, the Wang model was used to determine the photothermal conversion efficiency. To make the model more versatile, it was expanded to include a term related to the heating of the solvent itself, which is crucial for measurements at wavelengths above 700 nm, and therefore most of the analysis performed for PTT purposes. It was found that the photothermal conversion efficiency is not a sufficient parameter to determine the effectiveness of a nanoheater in an application use. For this reason, an eHCE parameter was proposed that is the product of the photothermal conversion efficiency and the mass absorption coefficient at a given wavelength. This parameter allowed for a quantitative comparison of different materials in terms of application, which is a novelty against the background of the works appearing in the field.

The proposed methodology allowed to verify the internal and external photothermal conversion efficiency of seventeen materials belonging to different classes [P2]. Plasmonic (gold, copper sulfide), semiconductor (silver sulfide, porous silicon), nanocrystals doped with lanthanide ions, iron oxides, and carbon dots samples were investigated. Most of these materials were found to exhibit high (80-100%) internal photothermal conversion efficiency, which would indicate relatively small variations between the samples. However, when the eHCE was compared, differences of orders of magnitude were obtained between various samples. This is an additional confirmation that the eHCE allows for a practical ranking of nanoheaters. Plasmonic copper sulfide proved to be the best among the materials evaluated in the NIR range. In contrast, black porous silicon was outstanding in the visible range. High eHCEs were also obtained for Ag_2S quantum dots. These results provide a preliminary ranking showing a perspective on which materials acting as nanoheaters are likely to be the focus of future attention, validated *in vitro* and then considered for PTT.

In the [P3] a particular attention was paid to materials doped with rare earth ions, due to the lack of systematic studies of this class of nanoheating materials in the literature. It was found that the choice of matrix and dopant ion significantly affects the photothermal conversion efficiency (both internal and external). Of the ions studied (Nd^{3+}, Yb^{3+} and Tm^{3+}), the Nd^{3+} ion shows the best photothermal properties. In turn, the most promising matrix in terms of application from the investigated matrices (fluorides, oxide, vanadate, perovskite) was vanadate. These results will contribute to a better understanding of the phenomenon of photothermal conversion in nanocrystals doped with lanthanide ions, as well as the other factors that influence it such as nanoparticle size or water conversion approach.

9 REFERENCES

(1) Deng, Y.; Ediriwickrema, A.; Yang, F.; Lewis, J.; Girardi, M.; Saltzman, W. M. A Sunblock Based on Bioadhesive Nanoparticles. *Nat. Mater.* **2015**, *14* (12), 1278–1285. https://doi.org/10.1038/nmat4422.

(2) Savage, N.; Diallo, M. S. Nanomaterials and Water Purification: Opportunities and Challenges. *J. Nanoparticle Res.* **2005**, *7* (4–5), 331–342. https://doi.org/10.1007/s11051-005-7523-5.

(3) Su, Z.; Sun, D.; Zhang, L.; He, M.; Jiang, Y.; Millar, B.; Douglas, P.; Mariotti, D.; Maguire, P.; Sun, D. Chitosan/Silver Nanoparticle/Graphene Oxide Nanocomposites with Multi-Drug Release, Antimicrobial, and Photothermal Conversion Functions. *Materials (Basel).* **2021**, *14* (9). https://doi.org/10.3390/ma14092351.

(4) Saloma; Nasution, A.; Imran, I.; Abdullah, M. Improvement of Concrete Durability by Nanomaterials. *Procedia Eng.* **2015**, *125*, 608–612. https://doi.org/10.1016/j.proeng.2015.11.078.

(5) Ximendes, E.; Benayas, A.; Jaque, D.; Marin, R. Quo Vadis, Nanoparticle-Enabled in Vivo Fluorescence Imaging? *ACS Nano* **2021**, *15* (2), 1917–1941. https://doi.org/10.1021/acsnano.0c08349.

(6) Farahavar, G.; Abolmaali, S. S.; Gholijani, N.; Nejatollahi, F. Antibody-Guided Nanomedicines as Novel Breakthrough Therapeutic, Diagnostic and Theranostic Tools. *Biomater. Sci.* **2019**, *7* (10), 4000–4016. https://doi.org/10.1039/c9bm00931k.

(7) Kim, J. U.; Lee, S.; Kang, S. J.; Kim, T. Il. Materials and Design of Nanostructured Broadband Light Absorbers for Advanced Light-to-Heat Conversion. *Nanoscale* **2018**, *10* (46), 21555–21574. https://doi.org/10.1039/c8nr06024j.

(8) Ng, C.; Yap, L. W.; Roberts, A.; Cheng, W.; Gómez, D. E. Black Gold: Broadband, High Absorption of Visible Light for Photochemical Systems. *Adv. Funct. Mater.* **2017**, *27* (2). https://doi.org/10.1002/adfm.201604080.

(9) Wang, T.; Torres, D.; Fernández, F. E.; Wang, C.; Sepúlveda, N. Maximizing the Performance of Photothermal Actuators by Combining Smart Materials with Supplementary Advantages. *Sci. Adv.* **2017**, *3* (4), 1–10. https://doi.org/10.1126/sciadv.1602697.

(10) Yang, H.; Leow, W. R.; Wang, T.; Wang, J.; Yu, J.; He, K.; Qi, D.; Wan, C.; Chen, X. 3D Printed Photoresponsive Devices Based on Shape Memory Composites. *Adv. Mater.* **2017**, *29* (33). https://doi.org/10.1002/adma.201701627.

(11) Rastinehad, A. R.; Anastos, H.; Wajswol, E.; Winoker, J. S.; Sfakianos, J. P.; Doppalapudi, S. K.; Carrick, M. R.; Knauer, C. J.; Taouli, B.; Lewis, S. C.; Tewari, A. K.; Schwartz, J. A.; Canfield, S. E.; George, A. K.; West, J. L.; Halas, N. J. Gold Nanoshell-Localized Photothermal Ablation of Prostate

Tumors in a Clinical Pilot Device Study. *Proc. Natl. Acad. Sci. U. S. A.* **2019**, *116* (37), 18590–18596. https://doi.org/10.1073/pnas.1906929116.

(12) Gao, H.; Zhang, L.; Lian, X.; Wang, Y.; Jiang, S.; Wang, G.; Dai, X.; Zou, H.; Ding, D. A Dentin Hypersensitivity Treatment Using Highly Stable Photothermal Conversion Nanoparticles. *Mater. Chem. Front.* **2021**, *5* (8), 3388–3395. https://doi.org/10.1039/d0qm01006e.

(13) Wilson, A. M.; Mazzaferri, J.; Bergeron, É.; Patskovsky, S.; Marcoux-Valiquette, P.; Costantino, S.; Sapieha, P.; Meunier, M. In Vivo Laser-Mediated Retinal Ganglion Cell Optoporation Using KV1.1 Conjugated Gold Nanoparticles. *Nano Lett.* **2018**, *18* (11), 6981–6988. https://doi.org/10.1021/acs.nanolett.8b02896.

(14) Todd, I.; Harris, J.; Clemente, S.; Us, C. A. Hair Removal with Coated Metal Nanoparticles, US Patent 9,421,259, 2016.

(15) Paithankar, D. Y.; Sakamoto, F. H.; Farinelli, W. A.; Kositratna, G.; Blomgren, R. D.; Meyer, T. J.; Faupel, L. J.; Kauvar, A. N. B.; Lloyd, J. R.; Cheung, W. L.; Owczarek, W. D.; Suwalska, A. M.; Kochanska, K. B.; Nawrocka, A. K.; Paluchowska, E. B.; Podolec, K. M.; Pirowska, M. M.; Wojas-Pelc, A. B.; Anderson, R. R. Acne Treatment Based on Selective Photothermolysis of Sebaceous Follicles with Topically Delivered Light-Absorbing Gold Microparticles. *J. Invest. Dermatol.* **2015**, *135* (7), 1727–1734. https://doi.org/10.1038/jid.2015.89.

(16) Zhang, S.; Lu, Q.; Wang, F.; Xiao, Z.; He, L.; He, D.; Deng, L. Gold-Platinum Nanodots with High-Peroxidase-like Activity and Photothermal Conversion Efficiency for Antibacterial Therapy. *ACS Appl. Mater. Interfaces* **2021**, *13* (31), 37535–37544. https://doi.org/10.1021/acsami.1c10600.

(17) Xiao, Y.; Xu, M.; Lv, N.; Cheng, C.; Huang, P.; Li, J.; Hu, Y.; Sun, M. Dual Stimuli-Responsive Metal-Organic Framework-Based Nanosystem for Synergistic Photothermal/Pharmacological Antibacterial Therapy. *Acta Biomater.* **2021**, *122*, 291–305. https://doi.org/10.1016/j.actbio.2020.12.045.

(18) Pihl, M.; Bruzell, E.; Andersson, M. Bacterial Biofilm Elimination Using Gold Nanorod Localised Surface Plasmon Resonance Generated Heat. *Mater. Sci. Eng. C* **2017**, *80*, 54–58. https://doi.org/10.1016/j.msec.2017.05.067.

(19) Habash, R. W. Y.; Bansal, R.; Krewski, D.; Alhafid, H. T. Thermal Therapy, Part 2: Hyperthermia Techniques. *Crit. Rev. Biomed. Eng.* **2006**, *34* (6), 491–542. https://doi.org/10.1615/CritRevBiomedEng.v34.i6.30.

(20) Habash, R. W. Y.; Bansal, R.; Krewski, D.; Alhafid, H. T. Thermal Therapy, Part 1: An Introduction to Thermal Therapy. *Crit. Rev. Biomed. Eng.* **2006**, *34* (6), 459–489. https://doi.org/10.1615/CritRevBiomedEng.v34.i6.20.

(21) Jaque, D.; Martínez Maestro, L.; Del Rosal, B.; Haro-Gonzalez, P.; Benayas, A.; Plaza, J. L.; Martín Rodríguez, E.; García Solé, J. Nanoparticles for

Photothermal Therapies. *Nanoscale* **2014**, *6* (16), 9494–9530. https://doi.org/10.1039/c4nr00708e.

(22) Sapareto, S. A.; Dewey, W. C. Thermal Dose Determination in Cancer Therapy. *Int. J. Radiat. Oncol.* **1984**, *10* (6), 787–800. https://doi.org/10.1016/0360-3016(84)90379-1.

(23) Ahmed, K.; Tabuchi, Y.; Kondo, T. Hyperthermia: An Effective Strategy to Induce Apoptosis in Cancer Cells. *Apoptosis* **2015**, *20* (11), 1411–1419. https://doi.org/10.1007/s10495-015-1168-3.

(24) Mondovi, B.; Finazzi Agro, A.; Rotilio, G.; Strom, R.; Morrica, G.; Rossi Fanelli, A. The Biochemical Mechanism of Selective Heat Sensitivity of Cancer Cells: II. Studies on Nucleic Acids and Protein Synthesis. *Eur. J. Cancer* **1969**, *5* (2), 137–146.

(25) Mondovi, B.; Strom, R.; Rotilio, G.; Agro, A. F.; Cavaliere, R.; Rossi Fanelli, A. The Biochemical Mechanism of Selective Heat Sensitivity of Cancer Cells: I. Studies on Cellular Respiration. *Eur. J. Cancer* **1969**, *5* (2), 129–136.

(26) van der Zee, J.; Vujaskovic, Z.; Kondo, M.; Sugahara, T. The Kadota Fund International Forum 2004-Clinical Group Consensus. *Int. J. Hyperth.* **2008**, *24* (2), 111–122. https://doi.org/10.1038/jid.2014.371.

(27) Lepock, J. R.; Cheng, K.-H.; Al-qysi, H.; Sim, I.; Koch, C. J.; Kruuv, J. Hyperthermia-Induced Inhibition of Respiration and Mitochondrial Protein Denaturation in CHL Cells. *Int. J. Hyperth.* **1987**, *3* (2), 123–132. https://doi.org/10.3109/02656738709140380.

(28) Wang, S.; Cheng, K.; Chen, K.; Xu, C.; Ma, P.; Dang, G.; Yang, Y.; Lei, Q.; Huang, H.; Yu, Y.; Fang, Y.; Tang, Q.; Jiang, N.; Miao, H.; Liu, F.; Zhao, X.; Li, N. Nanoparticle-Based Medicines in Clinical Cancer Therapy. *Nano Today* **2022**, *45*, 101512. https://doi.org/10.1016/j.nantod.2022.101512.

(29) Chen, S.; Lei, Q.; Qiu, W. X.; Liu, L. H.; Zheng, D. W.; Fan, J. X.; Rong, L.; Sun, Y. X.; Zhang, X. Z. Mitochondria-Targeting "Nanoheater" for Enhanced Photothermal/Chemo-Therapy. *Biomaterials* **2017**, *117*, 92–104. https://doi.org/10.1016/j.biomaterials.2016.11.056.

(30) Liu, T.; Wang, C.; Gu, X.; Gong, H.; Cheng, L.; Shi, X.; Feng, L.; Sun, B.; Liu, Z. Drug Delivery with PEGylated MoS2 Nano-Sheets for Combined Photothermal and Chemotherapy of Cancer. *Adv. Mater.* **2014**, *26* (21), 3433–3440. https://doi.org/10.1002/adma.201305256.

(31) Bucharskaya, A.; Maslyakova, G.; Terentyuk, G.; Yakunin, A.; Avetisyan, Y.; Bibikova, O.; Tuchina, E.; Khlebtsov, B.; Khlebtsov, N.; Tuchin, V. Towards Effective Photothermal/Photodynamic Treatment Using Plasmonic Gold Nanoparticles. *Int. J. Mol. Sci.* **2016**, *17* (8), 1–26. https://doi.org/10.3390/ijms17081295.

(32) Vines, J. B.; Yoon, J. H.; Ryu, N. E.; Lim, D. J.; Park, H. Gold Nanoparticles for Photothermal Cancer Therapy. *Front. Chem.* **2019**, *7* (APR), 1–16.

https://doi.org/10.3389/fchem.2019.00167.

(33) Wang, S.; Ma, X.; Hong, X.; Cheng, Y.; Tian, Y.; Zhao, S.; Liu, W.; Tang, Y.; Zhao, R.; Song, L.; Teng, Z.; Lu, G. Adjuvant Photothermal Therapy Inhibits Local Recurrences after Breast-Conserving Surgery with Little Skin Damage. *ACS Nano* **2018**, *12* (1), 662–670. https://doi.org/10.1021/acsnano.7b07757.

(34) Quarta, A.; Piccirillo, C.; Mandriota, G. Nanoheterostructures (NHS) and Their Applications in Nanomedicine : Focusing on In Vivo Studies. *Materials (Basel).* **2019**, *12* (139), 1–37. https://doi.org/10.3390/ma12010139.

(35) Gnach, A.; Lipinski, T.; Bednarkiewicz, A.; Rybka, J.; Capobianco, J. A. Upconverting Nanoparticles: Assessing the Toxicity. *Chem. Soc. Rev.* **2015**, *44* (6), 1561–1584. https://doi.org/10.1039/c4cs00177j.

(36) Hardman, R. A Toxicologic Review of Quantum Dots: Toxicity Depends on Physicochemical and Environmental Factors. *Environ. Health Perspect.* **2006**, *114* (2), 165–172. https://doi.org/10.1289/ehp.8284.

(37) Zhou, Z.; Wang, X.; Zhang, H.; Huang, H.; Sun, L.; Ma, L.; Du, Y.; Pei, C.; Zhang, Q.; Li, H.; Ma, L.; Gu, L.; Liu, Z.; Cheng, L.; Tan, C. Activating Layered Metal Oxide Nanomaterials via Structural Engineering as Biodegradable Nanoagents for Photothermal Cancer Therapy. *Small* **2021**, *17* (12), 1–12. https://doi.org/10.1002/smll.202007486.

(38) Li, Y.; Fan, X.; Li, Y.; Zhu, L.; Chen, R.; Zhang, Y.; Ni, H.; Xia, Q.; Feng, Z.; Tang, B. Z.; Qian, J.; Lin, H. Biologically Excretable AIE Nanoparticles Wear Tumor Cell-Derived "Exosome Caps" for Efficient NIR-II Fluorescence Imaging-Guided Photothermal Therapy. *Nano Today* **2021**, *41*, 101333. https://doi.org/10.1016/j.nantod.2021.101333.

(39) Yan, L.; Zhao, F.; Wang, J.; Zu, Y.; Gu, Z.; Zhao, Y. A Safe-by-Design Strategy towards Safer Nanomaterials in Nanomedicines. *Adv. Mater.* **2019**, *1805391*. https://doi.org/10.1002/adma.201805391.

(40) Liu, T. M.; Conde, J.; Lipiński, T.; Bednarkiewicz, A.; Huang, C. C. Revisiting the Classification of NIR-Absorbing/Emitting Nanomaterials for in Vivo Bioapplications. *NPG Asia Mater.* **2016**, *8* (8), 1–25. https://doi.org/10.1038/am.2016.106.

(41) Chen, Y.-S.; Frey, W.; Kim, S.; Homan, K.; Kruizinga, P.; Sokolov, K.; Emelianov, S. Enhanced Thermal Stability of Silica-Coated Gold Nanorods for Photoacoustic Imaging and Image-Guided Therapy. *Opt. Express* **2010**, *18* (9), 8867. https://doi.org/10.1364/oe.18.008867.

(42) Wu, Z.; Liang, J.; Ji, X.; Yang, W. Preparation of Uniform Au@SiO2 Particles by Direct Silica Coating on Citrate-Capped Au Nanoparticles. *Colloids Surfaces A Physicochem. Eng. Asp.* **2011**, *392* (1), 220–224. https://doi.org/10.1016/j.colsurfa.2011.09.059.

(43) Guo, L.; Liu, W.; Niu, G.; Zhang, P.; Zheng, X.; Jia, Q.; Zhang, H.; Ge, J.; Wang, P. Polymer Nanoparticles with High Photothermal Conversion Efficiency as Robust Photoacoustic and Thermal Theranostics. *J. Mater. Chem. B* **2017**, *5* (15), 2832–2839. https://doi.org/10.1039/c7tb00498b.

(44) Tas, C. E.; Berksun, E.; Koken, D.; Unal, S.; Unal, H. Photothermal Waterborne Polydopamine/Polyurethanes with Light-to-Heat Conversion Properties. *ACS Appl. Polym. Mater.* **2021**, *3* (8), 3929–3940. https://doi.org/10.1021/acsapm.1c00495.

(45) Jiang, R.; Cheng, S.; Shao, L.; Ruan, Q.; Wang, J. Mass-Based Photothermal Comparison among Gold Nanocrystals, PbS Nanocrystals, Organic Dyes, and Carbon Black. *J. Phys. Chem. C* **2013**, *117* (17), 8909–8915. https://doi.org/10.1021/jp400770x.

(46) Shirata, C.; Kaneko, J.; Inagaki, Y.; Kokudo, T.; Sato, M.; Kiritani, S.; Akamatsu, N.; Arita, J.; Sakamoto, Y.; Hasegawa, K.; Kokudo, N. Near-Infrared Photothermal/Photodynamic Therapy with Indocyanine Green Induces Apoptosis of Hepatocellular Carcinoma Cells through Oxidative Stress. *Sci. Rep.* **2017**, *7* (1), 1–8. https://doi.org/10.1038/s41598-017-14401-0.

(47) Gao, X.; Jiang, S.; Li, C.; Chen, Y.; Zhang, Y.; Huang, P.; Lin, J. Highly Photostable Croconium Dye-Anchored Cell Membrane Vesicle for Tumor PH-Responsive Duplex Imaging-Guided Photothermal Therapy. *Biomaterials* **2021**, *267* (September 2020), 120454. https://doi.org/10.1016/j.biomaterials.2020.120454.

(48) Cantu, T.; Walsh, K.; Pattani, V. P.; Moy, A. J.; Tunnell, J. W.; Irvin, J. A.; Betancourt, T. Conductive Polymer-Based Nanoparticles for Laser-Mediated Photothermal Ablation of Cancer: Synthesis, Characterization, and in Vitro Evaluation. *Int. J. Nanomedicine* **2017**, *12*, 615–632. https://doi.org/10.2147/IJN.S116583.

(49) Li, S.; Wang, X.; Hu, R.; Chen, H.; Li, M.; Wang, J.; Wang, Y.; Liu, L.; Lv, F.; Liang, X. J.; Wang, S. Near-Infrared (NIR)-Absorbing Conjugated Polymer Dots as Highly Effective Photothermal Materials for in Vivo Cancer Therapy. *Chem. Mater.* **2016**, *28* (23), 8669–8675. https://doi.org/10.1021/acs.chemmater.6b03738.

(50) Zhang, S.; Song, H. L.; Yang, X. L.; Yang, K. Y.; Wang, X. Y. Effect of Electrical Stimulation on the Fate of Sulfamethoxazole and Tetracycline with Their Corresponding Resistance Genes in Three-Dimensional Biofilm-Electrode Reactors. *Chemosphere* **2016**, *164*, 113–119. https://doi.org/10.1016/j.chemosphere.2016.08.076.

(51) Liu, D.; Ma, L.; An, Y.; Li, Y.; Liu, Y.; Wang, L.; Guo, J.; Wang, J.; Zhou, J. Thermoresponsive Nanogel-Encapsulated PEDOT and HSP70 Inhibitor for Improving the Depth of the Photothermal Therapeutic Effect. *Adv. Funct. Mater.* **2016**, *26* (26), 4749–4759. https://doi.org/10.1002/adfm.201600031.

(52) Chang, R.; Zou, Q.; Zhao, L.; Liu, Y.; Xing, R.; Yan, X. Amino-Acid-Encoded Supramolecular Photothermal Nanomedicine for Enhanced Cancer Therapy. *Adv. Mater.* **2022**, *34* (16). https://doi.org/10.1002/adma.202200139.

(53) Silva, J. S. F.; Silva, J. Y. R.; de Sá, G. F.; Araújo, S. S.; Filho, M. A. G.; Ronconi, C. M.; Santos, T. C.; Júnior, S. A. Multifunctional System Polyaniline-Decorated ZIF-8 Nanoparticles as a New Chemo-Photothermal Platform for Cancer Therapy. *ACS Omega* **2018**, *3* (9), 12147–12157. https://doi.org/10.1021/acsomega.8b01067.

(54) Chen, Y.; Li, C.; Hou, Z.; Huang, S.; Liu, B.; He, F.; Luo, L.; Lin, J. Polyaniline Electrospinning Composite Fibers for Orthotopic Photothermal Treatment of Tumors in Vivo. *New J. Chem.* **2015**, *39* (6), 4987–4993. https://doi.org/10.1039/c5nj00327j.

(55) Zhao, X.; Huang, C.; Xiao, D.; Wang, P.; Luo, X.; Liu, W.; Liu, S.; Li, J.; Li, S.; Chen, Z. Melanin-Inspired Design: Preparing Sustainable Photothermal Materials from Lignin for Energy Generation. *ACS Appl. Mater. Interfaces* **2021**, *13* (6), 7600–7607. https://doi.org/10.1021/acsami.0c21256.

(56) Liu, Y.; Shen, G.; Zhao, L.; Zou, Q.; Jiao, T.; Yan, X. Robust Photothermal Nanodrugs Based on Covalent Assembly of Nonpigmented Biomolecules for Antitumor Therapy. *ACS Appl. Mater. Interfaces* **2019**. https://doi.org/10.1021/acsami.9b13966.

(57) Zhao, L.; Liu, Y.; Xing, R.; Yan, X. Supramolecular Photothermal Effects: A Promising Mechanism for Efficient Thermal Conversion. *Angew. Chemie - Int. Ed.* **2020**, *59* (10), 3793–3801. https://doi.org/10.1002/anie.201909825.

(58) Lindley, S. A.; Zhang, J. Z. Bumpy Hollow Gold Nanospheres for Theranostic Applications: Effect of Surface Morphology on Photothermal Conversion Efficiency. *ACS Appl. Nano Mater.* **2019**, *2* (2), 1072–1081. https://doi.org/10.1021/acsanm.8b02331.

(59) Liao, Y.-T.; Liu, C.-H.; Chin, Y.; Chen, S.-Y.; Liu, S. H.; Hsu, Y.-C.; Wu, K. C.-W. Biocompatible and Multifunctional Gold Nanorods for Effective Photothermal Therapy of Oral Squamous Cell Carcinoma. *J. Mater. Chem. B* **2019**, *7* (28), 4451–4460. https://doi.org/10.1039/c9tb00574a.

(60) Wang, X.; Li, G.; Ding, Y.; Sun, S. Understanding the Photothermal Effect of Gold Nanostars and Nanorods for Biomedical Applications. *RSC Adv.* **2014**, *4* (57), 30375–30383. https://doi.org/10.1039/C4RA02978J.

(61) Wei, L.; Lu, J.; Xu, H.; Patel, A.; Chen, Z. S.; Chen, G. Silver Nanoparticles: Synthesis, Properties, and Therapeutic Applications. *Drug Discov. Today* **2015**, *20* (5), 595–601. https://doi.org/10.1016/j.drudis.2014.11.014.

(62) Zhu, X. M.; Wan, H. Y.; Jia, H.; Liu, L.; Wang, J. Porous Pt Nanoparticles with High Near-Infrared Photothermal Conversion Efficiencies for Photothermal Therapy. *Adv. Healthc. Mater.* **2016**, *5* (24), 3165–3172. https://doi.org/10.1002/adhm.201601058.

(63) Ishii, S.; Sugavaneshwar, R. P.; Nagao, T. Titanium Nitride Nanoparticles as Plasmonic Solar Heat Transducers. *J. Phys. Chem. C* **2016**, *120* (4), 2343–2348. https://doi.org/10.1021/acs.jpcc.5b09604.

(64) Jiang, J.; Che, X.; Qian, Y.; Wang, L.; Zhang, Y.; Wang, Z. Bismuth Sulfide Nanorods as Efficient Photothermal Theragnosis Agents for Cancer Treatment. *Front. Mater.* **2020**, *7* (August), 1–11. https://doi.org/10.3389/fmats.2020.00234.

(65) Guozhi, J.; Peng, W.; Yanbang, Z.; Kai, C. Localized Surface Plasmon Enhanced Photothermal Conversion in Bi 2 Se 3 Topological Insulator Nanoflowers. *Sci. Rep.* **2016**, *6* (May), 1–8. https://doi.org/10.1038/srep25884.

(66) Wang, Y.; Black, K. C. L.; Luehmann, H.; Li, W.; Zhang, Y.; Cai, X.; Wan, D.; Liu, S. Y.; Li, M.; Kim, P.; Li, Z. Y.; Wang, L. V.; Liu, Y.; Xia, Y. Comparison Study of Gold Nanohexapods, Nanorods, and Nanocages for Photothermal Cancer Treatment. *ACS Nano* **2013**, *7* (3), 2068–2077. https://doi.org/10.1021/nn304332s.

(67) Yang, J. M.; Yang, H.; Lin, L. Quantum Dot Nano Thermometers Reveal Heterogeneous Local Thermogenesis in Living Cells. *ACS Nano* **2011**, *5* (6), 5067–5071. https://doi.org/10.1021/nn201142f.

(68) Shen, Y.; Santos, H. D. A.; Ximendes, E. C.; Lifante, J.; Sanz-Portilla, A.; Monge, L.; Fernández, N.; Chaves-Coira, I.; Jacinto, C.; Brites, C. D. S.; Carlos, L. D.; Benayas, A.; Iglesias-de la Cruz, M. C.; Jaque, D. Ag2S Nanoheaters with Multiparameter Sensing for Reliable Thermal Feedback during In Vivo Tumor Therapy. *Adv. Funct. Mater.* **2020**, *30* (49). https://doi.org/10.1002/adfm.202002730.

(69) Marin, R.; Skripka, A.; Besteiro, L. V.; Benayas, A.; Wang, Z.; Govorov, A. O.; Canton, P.; Vetrone, F. Highly Efficient Copper Sulfide-Based Near-Infrared Photothermal Agents: Exploring the Limits of Macroscopic Heat Conversion. *Small* **2018**, *14* (49). https://doi.org/10.1002/smll.201803282.

(70) Li, Y.; Lu, W.; Huang, Q.; Li, C.; Chen, W. Copper Sulfide Nanoparticles for Photothermal Ablation of Tumor Cells. *Nanomedicine* **2010**, *5* (8), 1161–1171. https://doi.org/10.2217/nnm.10.85.

(71) Hessel, C. M.; P. Pattani, V.; Rasch, M.; Panthani, M. G.; Koo, B.; Tunnell, J. W.; Korgel, B. A. Copper Selenide Nanocrystals for Photothermal Therapy. *Nano Lett.* **2011**, *11* (6), 2560–2566. https://doi.org/10.1021/nl201400z.

(72) Lambert, T. N.; Andrews, N. L.; Gerung, H.; Boyle, T. J.; Oliver, J. M.; Wilson, B. S.; Han, S. M. Water-Soluble Germanium(0) Nanocrystals: Cell Recognition and near-Infrared Photothermal Conversion Properties. *Small* **2007**, *3* (4), 691–699. https://doi.org/10.1002/smll.200600529.

(73) Espinosa, A.; Di Corato, R.; Kolosnjaj-Tabi, J.; Flaud, P.; Pellegrino, T.; Wilhelm, C. Duality of Iron Oxide Nanoparticles in Cancer Therapy: Amplification of Heating Efficiency by Magnetic Hyperthermia and

Photothermal Bimodal Treatment. *ACS Nano* **2016**, *10* (2), 2436–2446. https://doi.org/10.1021/acsnano.5b07249.

(74) Cabana, S.; Curcio, A.; Michel, A.; Wilhelm, C.; Abou-Hassan, A. Iron Oxide Mediated Photothermal Therapy in the Second Biological Window: A Comparative Study between Magnetite/Maghemite Nanospheres and Nanoflowers. *Nanomaterials* **2020**, *10* (8), 1–17. https://doi.org/10.3390/nano10081548.

(75) Lozano-Pedraza, C.; Plaza-Mayoral, E.; Espinosa, A.; Sot, B.; Serrano, A.; Salas, G.; Blanco-Andujar, C.; Cotin, G.; Felder-Flesch, D.; Begin-Colin, S.; Teran, F. J. Assessing the Parameters Modulating Optical Losses of Iron Oxide Nanoparticles under near Infrared Irradiation. *Nanoscale Adv.* **2021**, *3* (22), 6490–6502. https://doi.org/10.1039/d1na00601k.

(76) Shao, Q.; Yang, Z.; Zhang, G.; Hu, Y.; Dong, Y.; Jiang, J. Multifunctional Lanthanide-Doped Core/Shell Nanoparticles: Integration of Upconversion Luminescence, Temperature Sensing, and Photothermal Conversion Properties. *ACS Omega* **2018**, *3* (January), 188–197. https://doi.org/10.1021/acsomega.7b01581.

(77) Bednarkiewicz, A.; Wawrzynczyk, D.; Nyk, M.; Strek, W. Optically Stimulated Heating Using Nd3+ Doped NaYF4 Colloidal near Infrared Nanophosphors. *Appl. Phys. B Lasers Opt.* **2011**, *103* (4), 847–852. https://doi.org/10.1007/s00340-010-4300-7.

(78) del Rosal, B.; Rocha, U.; Ximendes, E. C.; Martín Rodríguez, E.; Jaque, D.; Solé, J. G. Nd3+ions in Nanomedicine: Perspectives and Applications. *Opt. Mater. (Amst).* **2017**, *63*, 185–196. https://doi.org/10.1016/j.optmat.2016.06.004.

(79) Rocha, U.; Upendra Kumar, K.; Jacinto, C.; Ramiro, J.; Caamaño, A. J.; García Solé, J.; Jaque, D. Nd3+ Doped LaF3 Nanoparticles as Self-Monitored Photo-Thermal Agents. *Appl. Phys. Lett.* **2014**, *104* (5), 3–8. https://doi.org/10.1063/1.4862968.

(80) Ding, L.; Ren, F.; Liu, Z.; Jiang, Z.; Yun, B.; Sun, Q.; Li, Z. Size-Dependent Photothermal Conversion and Photoluminescence of Theranostic NaNdF4 Nanoparticles under Excitation of Different-Wavelength Lasers. *Bioconjug. Chem.* **2020**, *31* (2), 340–351. https://doi.org/10.1021/acs.bioconjchem.9b00700.

(81) L. Marciniak, K. Kniec, K. Elzbieciak, A. Bednarkiewicz, Non-plasmonic NIR-ac- tivated photothermal agents for photothermal therapy, in: A. Benayas, E. Hemmer, G. Hong, D. Jaque (Eds.), Near infrared-emitting nanoparticles for biomedical applications, Springer, 2020.

(82) Marciniak, L.; Pilch, A.; Arabasz, S.; Jin, D.; Bednarkiewicz, A.; Chen, M.; Sun, Y.; Li, F. Y.; Solé, J. G.; Jaque, D.; Palacio, F.; Carlos, L. D.; Millán, A.; Pedroni, M.; Speghini, A.; Hirata, G. A.; Martin, I. R.; Jaque, D. Heterogeneously Nd $^{3+}$ Doped Single Nanoparticles for NIR-Induced Heat

Conversion, Luminescence, and Thermometry. *Nanoscale* **2017**, *9* (24), 8288–8297. https://doi.org/10.1039/C7NR02630G.

(83) Shao, Q.; Li, X.; Hua, P.; Zhang, G.; Dong, Y.; Jiang, J. Enhancing the Upconversion Luminescence and Photothermal Conversion Properties of ~800 Nm Excitable Core/Shell Nanoparticles by Dye Molecule Sensitization. *J. Colloid Interface Sci.* **2017**, *486*, 121–127. https://doi.org/10.1016/j.jcis.2016.09.067.

(84) Romero-Aburto, R.; Narayanan, T. N.; Nagaoka, Y.; Hasumura, T.; Mitcham, T. M.; Fukuda, T.; Cox, P. J.; Bouchard, R. R.; Maekawa, T.; Kumar, D. S.; Torti, S. V.; Mani, S. A.; Ajayan, P. M. Fluorinated Graphene Oxide; A New Multimodal Material for Biological Applications. *Adv. Mater.* **2013**, *25* (39), 5632–5637. https://doi.org/10.1002/adma201301804.

(85) Sheng, Z.; Song, L.; Zheng, J.; Hu, D.; He, M.; Zheng, M.; Gao, G.; Gong, P.; Zhang, P.; Ma, Y.; Cai, L. Protein-Assisted Fabrication of Nano-Reduced Graphene Oxide for Combined Invivo Photoacoustic Imaging and Photothermal Therapy. *Biomaterials* **2013**, *34* (21), 5236–5243. https://doi.org/10.1016/j.biomaterials.2013.03.090.

(86) Xu, W.; Tamarov, K.; Fan, L.; Granroth, S.; Rantanen, J.; Nissinen, T.; Peräniemi, S.; Uski, O.; Hirvonen, M. R.; Lehto, V. P. Scalable Synthesis of Biodegradable Black Mesoporous Silicon Nanoparticles for Highly Efficient Photothermal Therapy. *ACS Appl. Mater. Interfaces* **2018**, *10* (28), 23529–23538. https://doi.org/10.1021/acsami.8b04557.

(87) Ou, G.; Li, Z.; Li, D.; Cheng, L.; Liu, Z.; Wu, H. Photothermal Therapy by Using Titanium Oxide Nanoparticles. *Nano Res.* **2016**, *9* (5), 1236–1243. https://doi.org/10.1007/s12274-016-1019-8.

(88) Jauffred, L.; Samadi, A.; Klingberg, H.; Bendix, P. M.; Oddershede, L. B. Plasmonic Heating of Nanostructures. *Chem. Rev.* **2019**, *119* (13), 8087–8130. https://doi.org/10.1021/acs.chemrev.8b00738.

(89) Mie, G. Beiträge Zur Optik Trüber Medien, Speziell Kolloidaler Metallösungen. *Ann. Phys.* **1908**, *330* (3), 377–445. https://doi.org/10.1002/andp.19083300302.

(90) Maestro, L. M.; Camarillo, E.; Sánchez-Gil, J. A.; Rodríguez-Oliveros, R.; Ramiro-Bargueño, J.; Caamaño, A. J.; Jaque, F.; Solé, J. G.; Jaque, D. Gold Nanorods for Optimized Photothermal Therapy: The Influence of Irradiating in the First and Second Biological Windows. *RSC Adv.* **2014**, *4* (96), 54122–54129. https://doi.org/10.1039/c4ra08956a.

(91) Wang, Y.; Meng, H. M.; Li, Z. Near-Infrared Inorganic Nanomaterial-Based Nanosystems for Photothermal Therapy. *Nanoscale* **2021**, *13* (19), 8751–8772. https://doi.org/10.1039/d1nr00323b.

(92) Regli, S.; Kelly, J. A.; Shukaliak, A. M.; Veinot, J. G. C. Photothermal Response of Photoluminescent Silicon Nanocrystals. *J. Phys. Chem. Lett.* **2012**, *3* (13), 1793–1797. https://doi.org/10.1021/jz3004766.

(93) Yong, K. T.; Law, W. C.; Hu, R.; Ye, L.; Liu, L.; Swihart, M. T.; Prasad, P. N. Nanotoxicity Assessment of Quantum Dots: From Cellular to Primate Studies. *Chem. Soc. Rev.* **2013**, *42* (3), 1236–1250. https://doi.org/10.1039/c2cs35392j.

(94) Li, J.; Zhang, W.; Ji, W.; Wang, J.; Wang, N.; Wu, W.; Wu, Q.; Hou, X.; Hu, W.; Li, L. Near Infrared Photothermal Conversion Materials: Mechanism, Preparation, and Photothermal Cancer Therapy Applications. *J. Mater. Chem. B* **2021**, *9* (38), 7909–7926. https://doi.org/10.1039/d1tb01310f.

(95) Liu, K.; Hong, X.; Choi, S.; Jin, C.; Capaz, R. B.; Kim, J.; Wang, W.; Bai, X.; Louie, S. G.; Wang, E.; Wang, F. Systematic Determination of Absolute Absorption Cross-Section of Individual Carbon Nanotubes. *Proc. Natl. Acad. Sci. U. S. A.* **2014**, *111* (21), 7564–7569. https://doi.org/10.1073/pnas.1318851111.

(96) Chen, Y. W.; Su, Y. L.; Hu, S. H.; Chen, S. Y. Functionalized Graphene Nanocomposites for Enhancing Photothermal Therapy in Tumor Treatment. *Adv. Drug Deliv. Rev.* **2016**, *105*, 190–204. https://doi.org/10.1016/j.addr.2016.05.022.

(97) Wang, Y. W.; Fu, Y. Y.; Peng, Q.; Guo, S. S.; Liu, G.; Li, J.; Yang, H. H.; Chen, G. N. Dye-Enhanced Graphene Oxide for Photothermal Therapy and Photoacoustic Imaging. *J. Mater. Chem. B* **2013**, *1* (42), 5762–5767. https://doi.org/10.1039/c3tb20986e.

(98) Wu, P.; Li, W.; Wu, Q.; Liu, Y.; Liu, S. Hydrothermal Synthesis of Nitrogen-Doped Carbon Quantum Dots from Microcrystalline Cellulose for the Detection of Fe3+ Ions in an Acidic Environment. *RSC Adv.* **2017**, *7* (70), 44144–44153. https://doi.org/10.1039/c7ra08400e.

(99) Yu, P.; Wen, X.; Toh, Y. R.; Tang, J. Temperature-Dependent Fluorescence in Carbon Dots. *J. Phys. Chem. C* **2012**, *116* (48), 25552–25557. https://doi.org/10.1021/jp307308z.

(100) Van De Walle, A.; Kolosnjaj-Tabi, J.; Lalatonne, Y.; Wilhelm, C. Ever-Evolving Identity of Magnetic Nanoparticles within Human Cells: The Interplay of Endosomal Confinement, Degradation, Storage, and Neocrystallization. *Acc. Chem. Res.* **2020**, *53* (10), 2212–2224. https://doi.org/10.1021/acs.accounts.0c00355.

(101) Zhang, L.; Yuan, M. Lanthanide Doped Lead-Free Double Perovskites as the Promising next Generation Ultra-Broadband Light Sources. *Light Sci. Appl.* **2022**, *11* (1), 10–12. https://doi.org/10.1038/s41377-022-00782-z.

(102) Bednarkiewicz, A.; Marciniak, L.; Carlos, L. D.; Jaque, D. Standardizing Luminescence Nanothermometry for Biomedical Applications. *Nanoscale* **2020**, *12* (27), 14405–14421. https://doi.org/10.1039/d0nr03568h.

(103) Runowski, M.; Woźny, P.; Martín, I. R. Optical Pressure Sensing in Vacuum and High-Pressure Ranges Using Lanthanide-Based Luminescent Thermometer-Manometer. *J. Mater. Chem. C* **2021**, *9* (13), 4643–4651.

https://doi.org/10.1039/d1tc00709b.

(104) Sun, L.-N.; Peng, H.; Stich, M. I. J.; Achatz, D.; Wolfbeis, O. S. PH Sensor Based on Upconverting Luminescent Lanthanide Nanorods. *Chem. Commun.* **2009**, No. 33, 5000. https://doi.org/10.1039/b907822c.

(105) Li, C.; Zeng, C.; Chen, Z.; Jiang, Y.; Yao, H.; Yang, Y.; Wong, W.-T. Luminescent Lanthanide Metal-Organic Framework Test Strip for Immediate Detection of Tetracycline Antibiotics in Water. *J. Hazard. Mater.* **2020**, *384*, 121498. https://doi.org/10.1016/j.jhazmat.2019.121498.

(106) Liu, Y.; Lu, Y.; Yang, X.; Zheng, X.; Wen, S.; Wang, F.; Vidal, X.; Zhao, J.; Liu, D.; Zhou, Z.; Ma, C.; Zhou, J.; Piper, J. A.; Xi, P.; Jin, D. Amplified Stimulated Emission in Upconversion Nanoparticles for Super-Resolution Nanoscopy. *Nature* **2017**, *543* (7644), 229–233. https://doi.org/10.1038/nature21366.

(107) Gargas, D. J.; Chan, E. M.; Ostrowski, A. D.; Aloni, S.; Altoe, M. V. P.; Barnard, E. S.; Sanii, B.; Urban, J. J.; Milliron, D. J.; Cohen, B. E.; Schuck, P. J. Engineering Bright Sub-10-Nm Upconverting Nanocrystals for Single-Molecule Imaging. *Nat. Nanotechnol.* **2014**, *9* (4), 300–305. https://doi.org/10.1038/nnano.2014.29.

(108) Liu, H.; Li, J.; Hu, P.; Sun, S.; Shi, L.; Sun, L. Facile Synthesis of Er3+/Tm3+ Co-Doped Magnetic/Luminescent Nanosystems for Possible Bioimaging and Therapy Applications. *J. Rare Earths* **2022**, *40* (1), 11–19. https://doi.org/10.1016/j.jre.2020.11.006.

(109) Lu, W.; Liao, Y.; Jiang, C.; Wang, R.; Shan, X.; Chen, Q.; Sun, G.; Liu, J. Polydopamine-Coated NaGdF4:Dy for: T 1/ T 2-Weighted MRI/CT Multimodal Imaging-Guided Photothermal Therapy. *New J. Chem.* **2019**, *43* (19), 7371–7378. https://doi.org/10.1039/c9nj00561g.

(110) Oliveira, H.; Bednarkiewicz, A.; Falk, A.; Fröhlich, E.; Lisjak, D.; Prina-Mello, A.; Resch, S.; Schimpel, C.; Vrček, I. V.; Wysokińska, E.; Gorris, H. H. Critical Considerations on the Clinical Translation of Upconversion Nanoparticles (UCNPs): Recommendations from the European Upconversion Network (COST Action CM1403). *Adv. Healthc. Mater.* **2019**, *8* (1). https://doi.org/10.1002/adhm.201801233.

(111) Guller, A. E.; Generalova, A. N.; Petersen, E. V.; Nechaev, A. V.; Trusova, I. A.; Landyshev, N. N.; Nadort, A.; Grebenik, E. A.; Deyev, S. M.; Shekhter, A. B.; Zvyagin, A. V. Cytotoxicity and Non-Specific Cellular Uptake of Bare and Surface-Modified Upconversion Nanoparticles in Human Skin Cells. *Nano Res.* **2015**, *8* (5), 1546–1562. https://doi.org/10.1007/s12274-014-0641-6.

(112) del Rosal, B.; Pérez-Delgado, A.; Carrasco, E.; Jovanović, D. J.; Dramićanin, M. D.; Dražić, G.; de la Fuente, Á. J.; Sanz-Rodriguez, F.; Jaque, D. Neodymium-Based Stoichiometric Ultrasmall Nanoparticles for Multifunctional Deep-Tissue Photothermal Therapy. *Adv. Opt. Mater.* **2016**,

4 (5), 782–789. https://doi.org/10.1002/adom.201500726.

(113) Chang, M.; Wang, M.; Shu, M.; Zhao, Y.; Ding, B.; Huang, S.; Hou, Z.; Han, G.; Lin, J. Enhanced Photoconversion Performance of NdVO4/Au Nanocrystals for Photothermal/Photoacoustic Imaging Guided and near Infrared Light-Triggered Anticancer Phototherapy. *Acta Biomater.* **2019**, *99*, 295–306. https://doi.org/10.1016/j.actbio.2019.08.026.

(114) Yu, Z.; Hu, W.; Zhao, H.; Miao, X.; Guan, Y.; Cai, W.; Zeng, Z.; Fan, Q.; Tan, T. T. Y. Generating New Cross-Relaxation Pathways by Coating Prussian Blue on NaNdF4 To Fabricate Enhanced Photothermal Agents. *Angew. Chemie* **2019**, *100871*, 8624–8628. https://doi.org/10.1002/ange.201904534.

(115) Xu, L.; Li, J.; Lu, K.; Wen, S.; Chen, H.; Shahzad, M. K.; Zhao, E.; Li, H.; Ren, J.; Zhang, J.; Liu, L. Sub-10 Nm NaNdF4 Nanoparticles as Near-Infrared Photothermal Probes with Self-Temperature Feedback. *ACS Appl. Nano Mater.* **2020**, *3* (3), 2517–2526. https://doi.org/10.1021/acsanm.9b02606.

(116) Wang, X.; Li, H.; Li, F.; Han, X.; Chen, G. Prussian Blue-Coated Lanthanide-Doped Core/Shell/Shell Nanocrystals for NIR-II Image-Guided Photothermal Therapy. *Nanoscale* **2019**, *11* (45), 22079–22088. https://doi.org/10.1039/c9nr07973d.

(117) Zhang, Y.; Chen, B.; Xu, S.; Li, X.; Zhang, J.; Sun, J.; Zheng, H.; Tong, L.; Sui, G.; Zhong, H.; Xia, H.; Hua, R. Dually Functioned Core-Shell NaYF4:Er3+ /Yb3+@NaYF4 :Tm3+/Yb3+ Nanoparticles as Nano-Calorifiers and Nano-Thermometers for Advanced Photothermal Therapy. *Sci. Rep.* **2017**, *7* (1), 1–13. https://doi.org/10.1038/s41598-017-11897-4.

(118) Li, A.; Li, X.; Wang, J.; Guo, Y.; Li, C.; Chen, W.; Wang, Z.; Tang, Y. Multifunctional α - NaYbF4: Tm3+ Nanocrystals with Intense Ultraviolet Self-Sensitized Upconversion Luminescence and Highly Efficient Optical Heating. *Ceram. Int.* **2022**, No. April. https://doi.org/10.1016/j.ceramint.2022.04.261.

(119) Li, H.; Zhao, Y.; Kolesnikov, I.; Xu, S.; Chen, L.; Bai, G. Multifunctional Rare Earth Ions-Doped Ba2LaF7 Nanocrystals for Simultaneous Temperature Sensing and Photothermal Therapy. *J. Alloys Compd.* **2023**, *931*, 167535. https://doi.org/10.1016/j.jallcom.2022.167535.

(120) Sobral, G. A.; Gomes, M. A.; Avila, J. F. M.; Rodrigues, J. J.; Macedo, Z. S.; Alencar, M. A. R. C. A Comparative Study of Er3+, Er3+-Eu3+, Er3+-Tb3+, and Er3+-Eu3+-Tb3+ Codoped Y2O3 Nanoparticles as Optical Heaters. *J. Nanomater.* **2015**, *2015*. https://doi.org/10.1155/2015/373675.

(121) Li, J.; Xu, L.; Lu, K.; Khuram Shahzad, M.; Ren, J.; Zhao, E.; Li, H.; Liu, L. Efficient Nanoheater Operated in a Biological Window for Photo-Hyperthermia Therapy. *Biomed. Opt. Express* **2019**, *10* (4), 1935–1941.

(122) Xu, M.; Ge, W.; Shi, J.; Li, Y. Near Infrared-Stimulated Heating Behaviors and Ultra-High Temperature Sensitivity in Bi2Ti2O7:Yb3+/Ho3+ Nanofibers. *J. Alloys Compd.* **2021**, *861*, 158622.

https://doi.org/10.1016/j.jallcom.2021.158622.

(123) Nexha, A.; Pujol, M. C.; Carvajal, J. J.; Díaz, F.; Aguiló, M. Effect of the Size and Shape of Ho, Tm:KLu(WO4)2 Nanoparticles on Their Self-Assessed Photothermal Properties. *Nanomaterials* **2021**, *11* (2), 485. https://doi.org/10.3390/nano11020485.

(124) Tong, L.; Li, X.; Zhang, J.; Xu, S.; Sun, J.; Zheng, H.; Zhang, Y.; Zhang, X.; Hua, R.; Xia, H.; Chen, B. NaYF4:Sm3+/Yb3+@NaYF4:Er3+/Yb3+ Core-Shell Structured Nanocalorifier with Optical Temperature Probe. *Opt. Express* **2017**, *25* (14), 16047. https://doi.org/10.1364/OE.25.016047.

(125) Zhou, S.; Jiao, X.; Jiang, Y.; Zhao, Y.; Xue, P.; Liu, Y.; Liu, J. Engineering Eu3+-Incorporated MoS2 Nanoflowers toward Efficient Photothermal/Photodynamic Combination Therapy of Breast Cancer. *Appl. Surf. Sci.* **2021**, *552* (November 2020), 149498. https://doi.org/10.1016/j.apsusc.2021.149498.

(126) Liu, Y.; Fan, H.; Guo, Q.; Jiang, A.; Du, X.; Zhou, J. Ultra-Small PH-Responsive Nd-Doped NaDyF4 Nanoagents for Enhanced Cancer Theranostic by in Situ Aggregation. *Theranostics* **2017**, *7* (17), 4217–4228. https://doi.org/10.7150/thno.21557.

(127) Tang, Z.; Liu, Q.; Li, J.; Wu, X.; Zhan, S.; Nie, G.; Hu, J.; Hu, S.; Xi, Z.; Wu, S.; Zhang, Y.; Shi, L.; Liu, Y. Tuning the Photothermal Effect of NaYF4: Yb3+, Er3+ Upconversion Luminescent Crystals through La3+ Ion Doping. *J. Lumin.* **2019**, *206* (October 2018), 21–26. https://doi.org/10.1016/j.jlumin.2018.10.063.

(128) Pu, X. Q.; Ju, X. J.; Zhang, L.; Cai, Q. W.; Liu, Y. Q.; Peng, H. Y.; Xie, R.; Wang, W.; Liu, Z.; Chu, L. Y. Novel Multifunctional Stimuli-Responsive Nanoparticles for Synergetic Chemo-Photothermal Therapy of Tumors. *ACS Appl. Mater. Interfaces* **2021**, *13* (24), 28802–28817. https://doi.org/10.1021/acsami.1c05330.

(129) Roper, D. K.; Ahn, W.; Hoepfner, M. Microscale Heat Transfer Transduced by Surface Plasmon Resonant Gold Nanoparticles. *J. Phys. Chem. C* **2007**, *111* (9), 3636–3641. https://doi.org/10.1021/jp064341w.

(130) Chen, H.; Shao, L.; Ming, T.; Sun, Z.; Zhao, C.; Yang, B.; Wang, J. Understanding the Photothermal Conversion Efficiency of Gold Nanocrystals. *Small* **2010**, *6* (20), 2272–2280. https://doi.org/10.1002/smll.201001109.

(131) Chiu, M. J.; Chu, L. K. Quantifying the Photothermal Efficiency of Gold Nanoparticles Using Tryptophan as an in Situ Fluorescent Thermometer. *Phys. Chem. Chem. Phys.* **2015**, *17* (26), 17090–17100. https://doi.org/10.1039/c5cp02620b.

(132) Chernov, G.; Ibarra-Valdez, J. L.; Carrillo-Torres, R. C.; Medrano-Pesqueira, T. C.; Chernov, V.; Barboza-Flores, M. Improved Method of Study on the Photothermal Effect of Plasmonic Nanoparticles by Dynamic

IR Thermography. *Plasmonics* **2018**, 935–944. https://doi.org/10.1007/s11468-018-0877-1.

(133) Pattani, V. P.; Tunnell, J. W. Nanoparticle-Mediated Photothermal Therapy: A Comparative Study of Heating for Different Particle Types. *Lasers Surg. Med.* **2012**, *44* (8), 675–684. https://doi.org/10.1002/lsm.22072.

(134) Espinosa, A.; Silva, A. K. A.; Sánchez-Iglesias, A.; Grzelczak, M.; Péchoux, C.; Desboeufs, K.; Liz-Marzán, L. M.; Wilhelm, C. Cancer Cell Internalization of Gold Nanostars Impacts Their Photothermal Efficiency In Vitro and In Vivo: Toward a Plasmonic Thermal Fingerprint in Tumoral Environment. *Adv. Healthc. Mater.* **2016**, *5* (9), 1040–1048. https://doi.org/10.1002/adhm.201501035.

(135) Xie, B.; Singh, R.; Torti, F. M.; Keblinski, P.; Torti, S. Heat Localization for Targeted Tumor Treatment with Nanoscale Near-Infrared Radiation Absorbers. *Phys. Med. Biol.* **2012**, *57* (18), 5765–5775. https://doi.org/10.1088/0031-9155/57/18/5765.

(136) Richardson, H. H.; Carlson, M. T.; Tandler, P. J.; Hernandez, P.; Govorov, A. O. Experimental and Theoretical Studies of Light-to-Heat Conversion and Collective Heating Effects in Metal Nanoparticle Solutions. *Nano Lett.* **2009**, *9* (3), 1139–1146. https://doi.org/10.1021/nl8036905.

(137) Li, R.; Zhang, L.; Shi, L.; Wang, P. MXene Ti3C2: An Effective 2D Light-to-Heat Conversion Material. *ACS Nano* **2017**, *11* (4), 3752–3759. https://doi.org/10.1021/acsnano.6b08415.

(138) Richardson, H. H.; Hickman, Z. N.; Thomas, A. C.; Kordesch, M. E.; Govorov, A. O. Thermo-Optical Properties of Nanoparticles and Nanoparticle Complexes Embedded in Ice: Characterization of Heat Generation and Actuation of Larger-Scale Effects. *Mater. Res. Soc. Symp. Proc.* **2006**, *964*, 1–6. https://doi.org/10.1557/proc-0964-r03-18.

(139) Han, H. S.; Choi, K. Y. Advances in Nanomaterial-mediated Photothermal Cancer Therapies: Toward Clinical Applications. *Biomedicines* **2021**, *9* (3), 1–16. https://doi.org/10.3390/biomedicines9030305.

(140) Cole, J. R.; Mirin, N. A.; Knight, M. W.; Goodrich, G. P.; Halas, N. J. Photothermal Efficiencies of Nanoshells and Nanorods for Clinical Therapeutic Applications. *J. Phys. Chem. C* **2009**, *113* (28), 12090–12094. https://doi.org/10.1021/jp9003592.

(141) Huang, P.; Lin, J.; Li, W.; Rong, P.; Wang, Z.; Wang, S.; Wang, X.; Sun, X.; Aronova, M.; Niu, G.; Leapman, R. D.; Nie, Z.; Chen, X. Biodegradable Gold Nanovesicles with an Ultrastrong Plasmonic Coupling Effect for Photoacoustic Imaging and Photothermal Therapy. *Angew. Chemie - Int. Ed.* **2013**, *52* (52), 13958–13964. https://doi.org/10.1002/anie.201308986.

(142) Yang, T.; Tang, Y.; Liu, L.; Lv, X.; Wang, Q.; Ke, H.; Deng, Y.; Yang, H.; Yang, X.; Liu, G.; Zhao, Y.; Chen, H. Size-Dependent Ag2S Nanodots for Second Near-Infrared Fluorescence/Photoacoustics Imaging and

Simultaneous Photothermal Therapy. *ACS Nano* **2017**, *11* (2), 1848–1857. https://doi.org/10.1021/acsnano.6b07866.

(143) Tian, Q.; Jiang, F.; Zou, R.; Liu, Q.; Chen, Z.; Zhu, M.; Yang, S.; Wang, J.; Wang, J.; Hu, J. Hydrophilic Cu9S5 Nanocrystals: A Photothermal Agent with a 25.7% Heat Conversion Efficiency for Photothermal Ablation of Cancer Cells in Vivo. *ACS Nano* **2011**, *5* (12), 9761–9771. https://doi.org/10.1021/nn203293t.

(144) Guo, B.; Feng, G.; Manghnani, P. N.; Cai, X.; Liu, J.; Wu, W.; Xu, S.; Cheng, X.; Teh, C.; Liu, B. A Porphyrin-Based Conjugated Polymer for Highly Efficient In Vitro and In Vivo Photothermal Therapy. *Small* **2016**, *12* (45), 6243–6254. https://doi.org/10.1002/smll.201602293.

(145) Liu, Y.; Ai, K.; Liu, J.; Deng, M.; He, Y.; Lu, L. Dopamine-Melanin Colloidal Nanospheres: An Efficient near-Infrared Photothermal Therapeutic Agent for in Vivo Cancer Therapy. *Adv. Mater.* **2013**, *25* (9), 1353–1359. https://doi.org/10.1002/adma.201204683.

(146) Chen, T.; Yao, T.; Peng, H.; Whittaker, A. K.; Li, Y.; Zhu, S.; Wang, Z. An Injectable Hydrogel for Simultaneous Photothermal Therapy and Photodynamic Therapy with Ultrahigh Efficiency Based on Carbon Dots and Modified Cellulose Nanocrystals. *Adv. Funct. Mater.* **2021**, *31* (45), 1–12. https://doi.org/10.1002/adfm.202106079.

(147) Li, D.; Han, D.; Qu, S. N.; Liu, L.; Jing, P. T.; Zhou, D.; Ji, W. Y.; Wang, X. Y.; Zhang, T. F.; Shen, D. Z. Supra-(Carbon Nanodots) with a Strong Visible to near-Infrared Absorption Band and Efficient Photothermal Conversion. *Light Sci. Appl.* **2016**, *5* (7), 1–9. https://doi.org/10.1038/lsa.2016.120.

(148) Ge, J.; Jia, Q.; Liu, W.; Lan, M.; Zhou, B.; Guo, L.; Zhou, H.; Zhang, H.; Wang, Y.; Gu, Y.; Meng, X.; Wang, P. Carbon Dots with Intrinsic Theranostic Properties for Bioimaging, Red-Light-Triggered Photodynamic/Photothermal Simultaneous Therapy In Vitro and In Vivo. *Adv. Healthc. Mater.* **2016**, *5* (6), 665–675. https://doi.org/10.1002/adhm.201500720.

(149) Miao, Z. H.; Wang, H.; Yang, H.; Li, Z.; Zhen, L.; Xu, C. Y. Glucose-Derived Carbonaceous Nanospheres for Photoacoustic Imaging and Photothermal Therapy. *ACS Appl. Mater. Interfaces* **2016**, *8* (25), 15904–15910. https://doi.org/10.1021/acsami.6b03652.

(150) Peng, H.; Tang, J.; Zheng, R.; Guo, G.; Dong, A.; Wang, Y.; Yang, W. Nuclear-Targeted Multifunctional Magnetic Nanoparticles for Photothermal Therapy. *Adv. Healthc. Mater.* **2017**, *6* (7). https://doi.org/10.1002/adhm.201601289.

(151) Huang, C. C.; Chang, P. Y.; Liu, C. L.; Xu, J. P.; Wu, S. P.; Kuo, W. C. New Insight on Optical and Magnetic Fe3O4 Nanoclusters Promising for near Infrared Theranostic Applications. *Nanoscale* **2015**, *7* (29), 12689–12697. https://doi.org/10.1039/c5nr03157e.

(152) Zhou, Z.; Sun, Y.; Shen, J.; Wei, J.; Yu, C.; Kong, B.; Liu, W.; Yang, H.; Yang, S.; Wang, W. Iron/Iron Oxide Core/Shell Nanoparticles for Magnetic Targeting MRI and near-Infrared Photothermal Therapy. *Biomaterials* **2014**, *35* (26), 7470–7478. https://doi.org/10.1016/j.biomaterials.2014.04.063.

(153) Liu, T.; Li, S.; Liu, Y.; Guo, Q.; Wang, L.; Liu, D.; Zhou, J. Mn-Complex Modified NaDyF4:Yb@NaLuF4:Yb,Er@polydopamine Core-Shell Nanocomposites for Multifunctional Imaging-Guided Photothermal Therapy. *J. Mater. Chem. B* **2016**, *4* (15), 2697–2705. https://doi.org/10.1039/c5tb02785c.

(154) Baffou, G.; Quidant, R.; Girard, C. Heat Generation in Plasmonic Nanostructures: Influence of Morphology. *Appl. Phys. Lett.* **2009**, *94* (15). https://doi.org/10.1063/1.3116645.

(155) Alrahili, M.; Peroor, R.; Savchuk, V.; McNear, K.; Pinchuk, A. Morphology Dependence in Photothermal Heating of Gold Nanomaterials with Near-Infrared Laser. *J. Phys. Chem. C* **2020**. https://doi.org/10.1021/acs.jpcc.9b11821.

(156) Deng, K.; Liu, D.; Wang, Z.; Zhou, Z.; Chen, Q.; Luo, J.; Zhang, Y.; Hou, Z.; Lin, J. Surface-Functionalized NdVO4:Gd3+ Nanoplates as Active Agents for Near-Infrared-Light-Triggered and Multimodal-Imaging-Guided Photothermal Therapy. *Pharmaceutics* **2022**, *14* (6), 1217. https://doi.org/10.3390/pharmaceutics14061217.

10 COPIES OF PUBLICATIONS CONSISTUTING THE CYCLE OF THE DOCTORAL DISSERTATION

ACS APPLIED MATERIALS & INTERFACES

www.acsami.org

Research Article

Standardization of Methodology of Light-to-Heat Conversion Efficiency Determination for Colloidal Nanoheaters

Agnieszka Paściak, Aleksandra Pilch-Wróbel, Łukasz Marciniak, P. James Schuck, and Artur Bednarkiewicz*

Cite This: *ACS Appl. Mater. Interfaces* 2021, 13, 44556–44567

Read Online

ACCESS | Metrics & More | Article Recommendations | Supporting Information

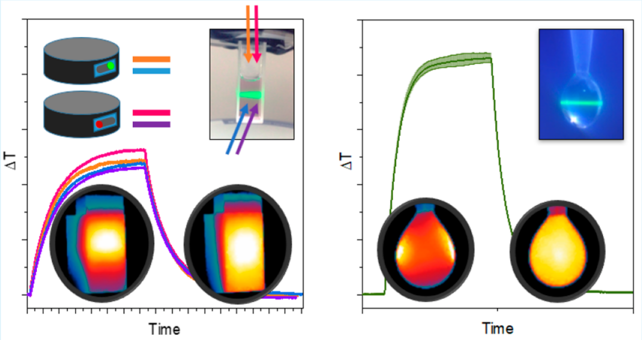

ABSTRACT: Localized photothermal therapy (PTT) has been demonstrated to be a promising method of combating cancer, that additionally synergistically enhances other treatment modalities such as photodynamic therapy or chemotherapy. PTT exploits nanoparticles (called nanoheaters), that upon proper biofunctionalization may target cancerous tissues, and under light stimulation may convert the energy of photons to heat, leading to local overheating and treatment of cancerous cells. Despite extensive work, there is, however, no agreement on how to accurately and quantitatively compare light-to-heat conversion efficiency (η_Q) and rank the nanoheating performances of various groups of nanomaterials. This disagreement is highly problematic because the obtained η_Q values, measured with various methods, differ significantly for similar nanomaterials. In this work, we experimentally review existing optical setups, methods, and physical models used to evaluate η_Q. In order to draw a binding conclusion, we cross-check and critically evaluate the same Au@SiO$_2$ sample in various experimental conditions. This critical study let us additionally compare and understand the influence of the other experimental factors, such as stirring, data recording and analysis, and assumptions on the effective mass of the system, in order to determine η_Q in a most straightforward and reproducible way. Our goal is therefore to contribute to the understanding, standardization, and reliable evaluation of η_Q measurements, aiming to accurately rank various nanoheater platforms.

KEYWORDS: *photothermal conversion efficiency, photothermal therapy, gold nanoparticles, standardization, nanoheaters*

1. INTRODUCTION

Photothermal therapy (PTT), alternatively named hyperthermia (HT), has been proposed to become adjuvant cancer treatment[1] to other well-known therapeutic methods such as photodynamic therapy[2] or chemotherapy.[3] This remote, minimally invasive (due to the need to inject exogenous functional nanomaterials) technique can not only combat cancer by itself, but has shown synergistic enhancement of therapeutic effects as compared to singular treatments. It is widely accepted that photothermal therapy exploits natural negative susceptibility of cancerous tissues to increased temperatures, as compared to normal tissues.[4] This can be explained on the basis of biochemistry and biophysics at the cellular level; for example, the research conducted on hepatoma cells has shown that at increased temperature (43 °C) in aerobic conditions, cellular respiration[5] and also protein synthesis[6] have been inhibited. Moreover, the difference in lability of cell membranes (surface or lysosomal) in healthy and cancerous cells has been raised.[5,6]

There are numerous ways cancerous tissues can be overheated above the physiological level (typically 39−45 °C).[7] Whole-body hyperthermia is highly exhausting for patients, and thus has been replaced with localized heat deposition methods exploiting hyperthermic nanoparticles (HTNPs). Such an approach requires further extensive studies and versatile chemical, physical, biochemical, and biological examination and evaluation of performance of various nanoparticles before they can be accepted for medical use in vivo. Among these features the chemistry (e.g., simple and cost-effective synthesis and the stability of colloidal NPs), biosafety (e.g., circulation time, deposition of HTNPs within organs and their clearance from the body,[8] lack of inherent primary or secondary toxicity), functionality (e.g., simple biofunctionalization and selective targeting of the cancerous tissues, heating and thermometry within a single nanoparticle for feedback controlled HT), and efficiency (i.e., light-to-heat conversion efficiency (η_Q) of HTNPs, and lethal light dose—

Received: July 1, 2021
Accepted: August 25, 2021
Published: September 9, 2021

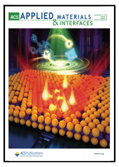

https://doi.org/10.1021/acsami.1c12409

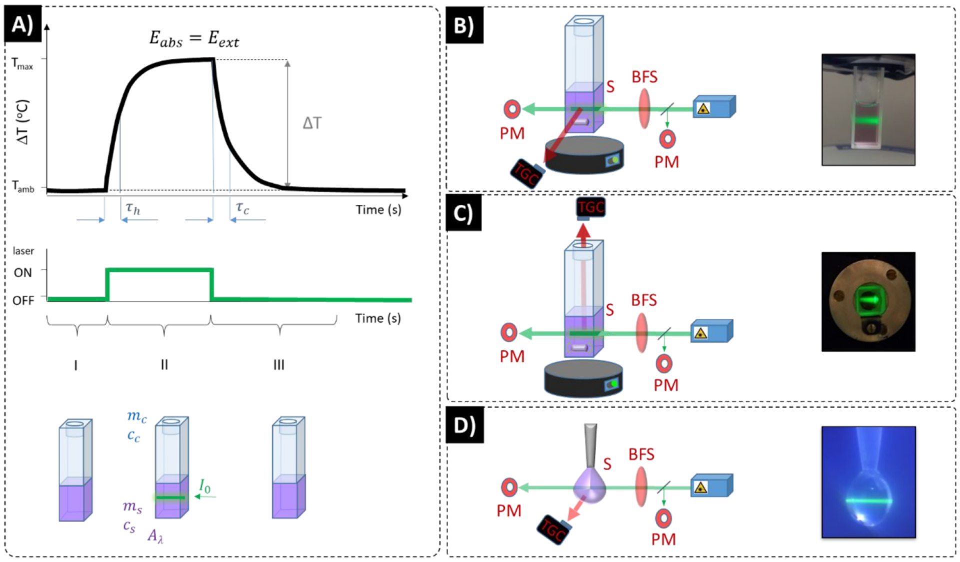

Figure 1. General scheme of methods and setups used to determine η_Q. (A) Schematic presentation of the elements and methods used in heat balance physical model (bottom row), photostimulation (middle row), and the exemplary results of typical η_Q measurements (top row); τ_h and τ_c denote inverse of heating and cooling rates, respectively, at saturation stage $E_{abs} = E_{ext}$, where E_{abs} and E_{ext} are absorbed and external energies, the ΔT is maximum temperature rise; m_x and c_x denote the mass and heat capacity of the cuvette (x = C) and of the sample (x = S), the sample is heated at stage II, while stabilizing at stage I and cooling down at stage III; schematic presentation and example photos of experimental setup variants: (B) Thermographic camera (TGC) records the temperature of side wall of the cuvette, (C) TGC records the temperature of colloidal nanoparticle solution directly from the top of the cuvette, (D) TGC records the temperature images of a small droplet of colloidal HTNPs. PM is optical power meter, BFS is a beam focusing system, S is a sample. Mild sample stirring may be applied in (B) and (C) setups.

response) are the most important parameters and methods to understand, optimize, or verify.

So far, numerous photothermal nanoheaters that fulfill most of the above-mentioned requirements have been proposed,[9] and their fundamental properties as well as feasibility for PTT has been demonstrated. In particular, these HTNPs include gold nanoparticles (AuNPs) in different shapes (nanospheres,[10] nanorods,[11] nanostars,[12] and others), as well as lanthanide doped nanoparticles,[13,14] quantum dots,[15] organic dyes,[16] transition metal dichalcogenides,[17] polymers,[18,19] and carbon-,[20,21] iron-,[22] and titanium-based[23] nanomaterials. In addition to these materials, semiconductor[24,25] and dielectric[26,27] materials have also shown very promising properties of converting light into heat, and even higher absorption coefficients were found as compared to plasmonic ones. The selection of the most appropriate NPs for PTT is not trivial because many features such as particle size, irradiation wavelength and time, η_Q, absorption cross-section, and shell surface are equally important for the potential adoption of particular NPs for PTT therapy. A small particle size and narrow size distribution is recommended to enable HTNPs to pass through the vascular system. For systemic administration, particle size should be smaller than 200 nm,[28] although there are studies that claimed that size under 50 nm provides fewer side effects.[29] Second, the specific interaction and accumulation of HTNPs in cancerous tissues require appropriate antibody-conjugation of the NPs,[30] while the nanoparticles should exhibit low inherent cytotoxicity, good biocompatibility and the possibility of fast clearance from the body after therapy. Third, the photoexcitation light wavelength (specifically for light induced heating) must fit one of the optical biological windows[31] to enable deep light penetration through the skin without excessive absorption and scattering, as well as without excessive heating and damaging of tissues by the light itself. Last, but not least, high η_Q values are required likewise high light-absorption cross section of given HTNPs, owing to restricted maximum permissible exposure (MPE) dose on the skin surface (according to the IEC-60825-1 and ANSI Z136.1 standards)[32,33] as well as unknown, and hypothetically low concentration of HTNPs in the targeted tissue.

The figure of merit for the PTT, which determines the feasibility of using a particular type of nanoparticles for HT and is comprehensively studied here, is light-to-heat conversion efficiency. However, due to the fact that in the literature on nanoheaters the efficiency of converting light into heat is not always determined,[9] it is difficult to quantitatively compare them in this respect. There have been many attempts to determine η_Q,[12,34−36] but the main objection is that the results obtained by most of them depend on the measurement conditions. Notably, many reports can be found that significantly differ in the evaluated η_Q for the same or very similar materials. We, therefore, see an urgent need to standardize the measurement techniques and experimental factors, which may ultimately affect the quantitative evaluation of η_Q between materials. A standardized η_Q measurement and analysis will in consequence enable proper comparison and ranking of various materials in different laboratories. Hence, we have critically assessed various existing light-to-heat conversion physical models, as well as built various optical setups (Figure 1) and evaluated many experimental factors using exactly the same batch of Au@SiO$_2$ NPs. We have chosen this HT nanomaterial as a prototypical example, because gold nanoparticles are one of the most common and intensively studied classes of HTNPs. The silica coating improves colloidal stability,[37] enhances biocompatibility, stabilizes NPs shape and surface, and enhances thermal stability.[38] Moreover, using NPs that are dispersible in water, which is a prerequisite for bioapplications, makes it easier to compare them with other agents and easier to further functionalize them.

It has been proposed and demonstrated that heat generated in nanoscale plasmonic particles may depend on the nanoparticle morphology, beam incidence orientation, and may display high nonuniformity around such singular objects or aggregates.[39] In our work, however, we adopt a simplified, but more general approach, by treating the colloidal nanoparticle solutions as homogeneous materials without entering into their nanoscale nature, which seems to be adequate for numerous types of other nonplasmonic nanoheaters, such as lanthanide doped NPs, quantum dots, and carbon based nanomaterials.

Almost all of the currently existing models are based on the analysis of experimentally measured temperature response kinetics resulting from heating the sample by a continuous wave laser beam. At first, ambient temperature is recorded (phase I in Figure 1A) and is followed by optical stimulation, which due to light-to-heat conversion increases the temperature of the sample (phase II in Figure 1A). Ultimately, saturated temperature is reached, and after switching the photostimulation off, the sample spontaneously cools down back to ambient temperature (phase III in Figure 1A). These heating−cooling kinetic profiles are key for evaluating the capability and efficiency of the water dispersed colloidal nanoparticle heaters to increase local temperature under photostimulation.

The starting point of η_Q calculations for the majority of existing models is the heat balance equation (eq 1), which describes the heating of the nanoparticle solution by continuous wave lasers. When ultrashort pulses of the excitation are applied, the equation should be expanded to take into account the average pumping power based on the energy, pulse duration, and pulse frequencies. Nevertheless, the major aim of our manuscript is to quantitatively investigate and compare light-to-heat conversion efficiency of the same batch of the sample with various optical setups, sample holders, and models, aiming to develop a most convenient and reliable quantification methodology.

$$\sum mc_p\frac{\mathrm{d}T}{\mathrm{d}t} = Q_L + Q_0 - Q_{\mathrm{ext}} \tag{1}$$

Σmc_p is a sum of products of mass and heat capacities of all system components, $\frac{\mathrm{d}T}{\mathrm{d}t}$is the rate of temperature increase, Q_{ext} is external heat flux, $Q_O + Q_L$ is heat produced by converting the absorbed light into heat, by either solvent (Q_O) or by the nanoparticles (Q_L). The Q_L is determined with the following equation:

$$Q_L = I(1 - 10^{-A_\lambda})\eta_Q \tag{2}$$

where I is a laser power, A_λ is the absorbance at irradiation wavelength λ and is measured experimentally using Lambert−Beer's law. In equilibrium conditions, $\sum mc_p\frac{\mathrm{d}T}{\mathrm{d}t} = 0$ in eq 1 and η_Q can be calculated as[34]

$$\begin{aligned}\eta_Q &= \frac{Q_{\mathrm{ext}} - Q_0}{I(1 - 10^{-A_\lambda})} = \frac{hA(T_{\max} - T_{\mathrm{amb}}) - Q_0}{I(1 - 10^{-A_\lambda})}\\ &= \frac{\Sigma_i m_i C_{p,i}(T_{\max} - T_{\mathrm{amb}})}{\tau_c * I(1 - 10^{-A_\lambda})} - \frac{Q_0}{I(1 - 10^{-A_\lambda})}\end{aligned} \tag{3}$$

In this model, Q_{ext} could be computed from experimental cooling kinetics, where h is the heat transfer coefficient, A is the surface area for heat transfer to surroundings, T_{amb} is the temperature of surroundings, and T is the current temperature. In equilibrium conditions, the actual temperature equals steady-state temperature $T = T_{\max} = T_{\mathrm{amb}} + \Delta T$. According to literature,[34] these parameters could be approximated by a sum of products of mass and heat capacities of all system components and cooling time coefficient τ_c. As we will discuss later, it is clear from eq 3 that there are a number of experimental factors which will ultimately affect the η_Q absolute value. For example, either the accuracy of τ_c determination, interpretation of which elements of the system should be considered in the sum of mass and heat capacity product $\Sigma_i m_i c_{p,i}$, or the method of actual temperature determination (Figure 1B−D) are all not trivial and may significantly affect the final results. For example, the results from the simulation presented by Marin et al.[40] differ from 63.8% to 91.4% for the same sample with different setup characterizing data. The τ_c is typically calculated as the exponential slope coefficient of the cooling part of heating−cooling kinetic profiles (Figure 1A). However, such an approach is not intuitive from the physics perspective, and it is noteworthy that the heating and the cooling time coefficients in all of our experiments differ. For instance, in the "top view" experiment (Figure 1C) with stirring, a cooling time coefficient was longer than the heating time coefficient. Although Richardson et al.[35] approximated the heating time rate for the cooling part of the profile, we suppose that the time rates may vary due to different heat propagation mechanisms, for example, collective heating and cooling by heat diffusion. It was found out that cooling rate is affected strongly by the material from which the holder (adjacent to the sample during the experiment) was made. The heater should be more effective if it heats the given volume faster, thus the heater's efficiency should be proven by the heating time rate.

As opposed to Roper's model, Wang's model[12] is also derived from the heat balance model (eq 1), but is converted into a different form:

$$\frac{d\Delta T}{dt} = a - b\Delta T \tag{4}$$

where

$$a = \frac{(1 - 10^{-A_\lambda})\eta_Q}{\Sigma_i m_i C_{p,i}},\quad b = \frac{hA}{\Sigma_i m_i C_{p,i}} \tag{5}$$

Based on that, the η_Q was calculated from equation:

$$\eta_Q = \frac{a\Sigma_i m_i C_{p,i}}{I(1 - 10^{-A_\lambda})} \tag{6}$$

where parameter a (K/s) describes how much of the incident power I (W/cm^2) can be effectively stored by the system of heat capacity C_p, that translates into how much the temperature changes per *unit time*. It must be underlined here that due to the different optical properties of nanomaterials at different wavelengths, η_Q depends on the excitation wavelength. Therefore, it is important to provide not only the η_Q, but wavelength specific η_Q (λ), which also means the η_Q cannot be directly compared in similar materials unless the excitation wavelength and absorption coefficient (at least) or spectra are provided. The a can be calculated from the rising part of the heating−cooling kinetic profiles:

$$T(t) = T_0 + \frac{a}{b}[1 - \mathrm{e}^{-bt}] \tag{7}$$

Theoretically, based on the assumption that the time constant of heating and cooling are identical[12,35] and assuming that the mass and heat capacities of the measuring system components are taken into account in the same way, both models should lead to similar results. However, this assumption may be wrong because Wang's model accounts for the mass of the system differently, that is, an effective mass of the measurement setup is considered instead of a simple sum of contributions from all the components. Moreover, as alluded to above, recent research shows that nanoparticles heat up more quickly than they cool down,[41] which raises new questions for the characterization of nanoheaters. Since the development of these phenomenological models and experimental methods, whose similarities and differences were presented above, many different materials have been characterized for their suitability for PTT. Nevertheless, the variability of experimental setups, measurement conditions, and assumptions used for data acquisition and analysis, make the conducted studies almost impossible to directly compare. Large discrepancies in experimentally obtained η_Q values can be found in the scientific literature for similar nanoheaters, and cannot be unequivocally ascribed to the actual differences in nanoparticles used.

2. RESULTS AND DISCUSSION

2.1. Light-to-Heat Conversion Efficiency: The Models. Because there is no agreement in the literature on which method of the η_Q determination is the most accurate, we were motivated to quantitatively compare the existing models and measurement setups. Not only did we evaluate the same batch of the sample, but also verified how variants of the experimental conditions (e.g., mechanical stirring or still colloid, side-wall or direct colloid temperature evaluation, the way the temperature is recorded, corrected, and analyzed, etc.) might affect the final η_Q result. A schematic comparison of all the experimental systems is presented in Figure 1B−D. We were also aiming to build an optical setup that is simple enough to be easily reproduced in any lab, with as few customized solutions or components as possible.

Most of the studies following the Roper's concept[34] exploit a standard 1 × 1 cm cuvette as a sample holder. A significant amount of sample (ca. 2 mL) is required, and the experiment itself is time-consuming (ca. 45 min for heating and 60 min for cooling to reach stable temperature). Simultaneously, it is technically challenging to eliminate long-time drift of light sources, detectors and external temperature. Moreover, it was supposed that the mass input of the cuvette itself, which is a relatively large heat receiver, might disrupt the results. This motivated us to test another setup, originally proposed by Richardson et al.[35] The cuvette with a colloidal sample was replaced by a droplet of the colloidal sample formed gently with a micropipette tip (Figure 1D). This technically simple approach requires much smaller volumes of colloid, and offers much faster temperature stabilization (<5 min vs >45 min required for the cuvette) during heating and cooling stages. However, because of the high surface-to-volume ratio of the droplet, solvent evaporation cannot be neglected and has proven to affect the actual temperature readout and consequently η_Q. To minimize evaporation, the humidity condition in the measurement chamber was intentionally increased by placing wet blankets inside and sealing the chamber with Parafilm to prevent humidity changes during measurement. A second way to reduce evaporation and also to minimize the impact of specific heat changes as a function of temperature is to intentionally avoid excessive heating, for example, by keeping the temperature rise below 10 degrees during the heating stage and keeping the measurement time as short as possible. Additionally, we paid special attention to keeping the dosing system airtight to avoid droplet regression. The droplet was dispensed with the pipet, and after its formation, a simple mechanical custom-made valve was used to prevent sucking it back. Other details of experimental setup performance are presented in the Materials and Methods and in the Supporting Information (Details of data analysis).

Finally, the calculation of η_Q requires prior characterization of the optical setup and knowledge of, among others, a mass of the components which stay in direct contact with the heating volume of the nanoparticles. Many reports assume a fixed mass of a whole cuvette for example, but actually Wang et al. proposed a simple and elegant solution for this ambiguous factor.[12] By using exactly the same optical setup, the optical heating of colloidal nanoparticles was replaced with a Joule resistance wire of known (measured) resistance. It was assumed that electricity is transformed into heat energy with 100% of efficiency, because the setup lacks elements in which energy could be transformed into other forms. Such an approach enabled determination of the product of mass and heat capacities of all system components using eq 8, where the a factor is a fitting parameter (in eq 7) achieved for electrical heating calibration, based on heating−cooling kinetic profiles.

$$\Sigma(m_i c_{p,i}) = \frac{P}{a} \tag{8}$$

From this equation it is possible to evaluate the effective mass of each component, but an assumption that some of them contribute fully in heat exchange is required. For measurements from the top view, it was assumed that colloidal sample mass contributes fully (temperature of sample is homogeneous or close to homogeneous). For the stirring experiments, the full mass of stirrer bar was included (because the stirrer is inside the colloidal sample), and for side-view experiments, the full mass of black tape of known emissivity (directly observed by TGC) was also included. The mass of the heating wire used in the calibration experiments was negligible because its mass of 5 mg and heat capacity equal to 460 J/kg·K (as compared to ∼2g of sample with heat capacity 4180 J/kg·K and ∼6.5 g weight of the cuvete with heat capacity 729 J/kg·K). Therefore, the remaining mass was assumed as an effective mass of cuvette m_{eff}. This approach also enabled one to minimize the impact of differences in mass of sample due to dosing imperfections (m = 2 g ± 0.007 g). Experiments were conducted with different input power (see Calibration Experimental Details in Materials and Methods), so the effective mass of the cuvette was obtained from each experiment independently and then averaged for each configuration. The measurement was carried out for each of the experimental variants separately for at least four different applied current values. The effective mass has been determined independently for each of the measurements to take into account small fluctuations in the mass between these repetitions. Then the obtained effective mass of the cuvette was averaged and these averaged m_{eff}, individually calculated for a given experimental configuration, were further used in calculations of η_Q for light induced heating experiments.

2.2. Light-to-Heat Conversion Efficiency: The Measurements. To evaluate how various measurement setups,

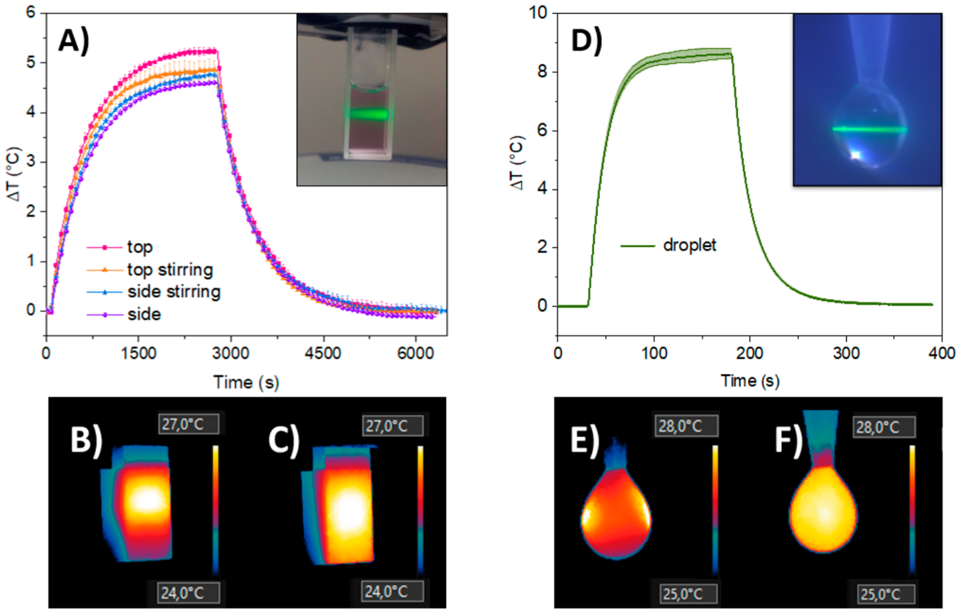

Figure 2. Heating and cooling of Au@SiO$_2$ sample in various experimental configurations. (A) Temperature curves in the "standard" setup with TGC in top and side view, with and without mechanical stirring. (B) Corresponding temperature images (obtained from the side view, in a setup without mechanical stirring) at heating (B) and cooling (C) stages. (D) Temperature heating−cooling curves obtained in a setup with droplet and corresponding temperature images of (E) heating and (F) cooling. Description of experimental variants is presented in Figure 1C, experimental parameters are described in SI Table S1.

preconditions, and technical or physical assumptions affect the value and accuracy of η_Q determination, we have decided to study the photothermal properties of gold nanoparticles. AuNPs are one of the most frequently examined light-to-heat converting nanoparticles for hyperthermia treatment because of ease of synthesis, stability in water, biocompatibility,[37] and high photoinduced heat generation efficiency.[35] The latter feature originates from localized surface plasmon resonances owing to cooperative oscillations of electrons.[42] Although the spectroscopic properties of plasmonic nanoparticles strongly depend on their size and shape asymmetry,[43,44] astonishingly, AuNPs of the same size and shape have demonstrated very different η_Q values in existing reports,[34,35] which inevitably means the final η_Q value depends on the experimental setups, specificities of synthesis made in various laboratories as well as a priori assumptions made during data evaluation. Therefore, the present, and ambiguous, status in photothermal conversion efficiency measurement techniques encouraged us to quantitatively compare the same batch of AuNPs@SiO$_2$ sample in different experimental conditions.

The η_Q evaluation (eq 3) requires accurate determination of the (i) absorption coefficient at the photostimulation wavelength, (ii) incident photoexcitation intensity, as well as the (iii) effective mass of the measurement setup, (iv) temperature rise ($T_{max} - T_{amb}$), and (v) the inverse cooling rate (i.e., cooling time coefficient, τ_c). While the first two parameters can be easily and precisely measured, the precision of η_Q determination requires the last three factors be accurately established as well, which is not trivial. For example, in Roper's experimental setup,[34] the thermocouple (TC) was located on a surface of a measurement cell directly behind the laser beam, which provides temperature readout close to maximum temperature in a measurement cell. However, the temperature determined in such a way could be underestimated due to the glass cell thickness. In the stationary state, the temperature of nanoparticles and the adjacent media are the same,[45] thus the temperature of nanoparticles should be measured at a location where the temperature of the colloidal sample is closest to an average temperature. Because of these issues, we have decided to use an alternative approach, by measuring temperature on a surface of the colloidal sample by a thermographic camera (TGC). Although much more costly, the ambiguities related to the positioning of the thermocouple can be neglected. Although the TGC was used before,[46] the related ambiguity is however associated with the way the T_{max} is determined, the highest versus averaged values, or the area of averaging temperature over the heated volume may significantly affect the ultimate η_Q calculations. This equivocality originates from the presence of temperature gradients (as shown in Figure 2). Our calculations show that considering local maximum temperature and the full mass of the sample in the model proposed by Roper et al.[34] leads to efficiencies exceeding 100% in some of the evaluated measurement setups (detailed discussion below). In the course of the performed evaluation and optimization, we found out that the most accurate results require averaging the temperature from the whole available sample surface, because the model actually treats the sample as a homogeneous material that naturally exchanges heat with the environment.

The photostimulation of colloidal nanoparticles by a collimated laser beam will always generate temperature gradients, which are impossible to resolve with a thermocouple having a size comparable to the droplet itself. Moreover, monitoring the temperature with the unsupervised orientation of a thermocouple against the position of the laser beam becomes a serious issue as the beam may accidentally hit and heat the TC directly. Additionally, the same photoexcitation intensity obtained with a Gaussian profile laser beam will generate more heat in the beam center as compared to top-hat profile, thus either conscious data correction must be

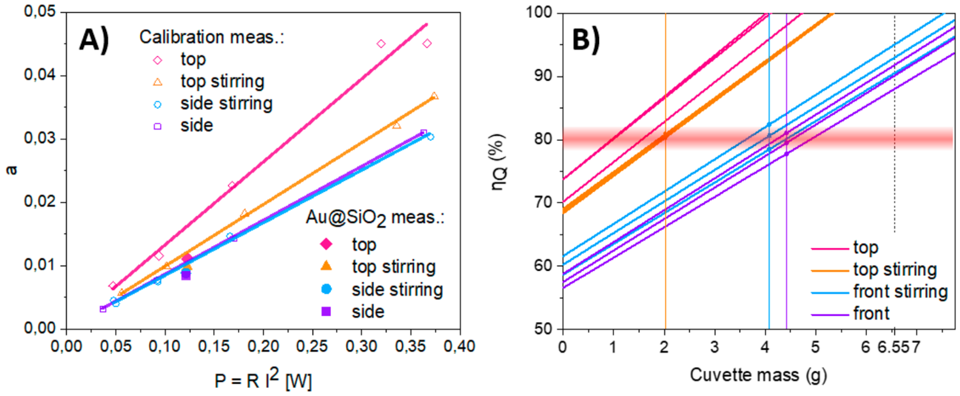

Figure 3. Calibration and experimental light-to-heat conversion data obtained in a spectrometric cuvette (10 mm optical path). (A) Calibration of the *a* factor (to ultimately derive the effective mass) versus power delivered in resistant wire (based on the method presented by Wang et al.[12]) various measurement setups (pure solvent - empty symbols; pink diamond - top view; orange triangle - top view with stirring; cyan circle - side view with stirring; purple rectangle - side view; the corresponding solid symbols represent Au@SiO2 sample). (B) η_Q in a function of cuvette mass included in calculations: the physical mass of cuvette is 6.55 g; other vertical lines represent calculated effective mass corresponding to particular experimental variants. By including an effective mass correction in data analysis from various setups (top view, pink; top view with stirring, orange; side view with stirring. cyan; side view, purple), coherent η_Q were found with an average value 80.2% ± 2% for all these presented setups (red diffused horizontal line represents mean value with 2% standard deviation, detailed data of individual experiments are presented in SI Tables S2 and S3). Multiple lines in (B) originate from a few repetitions of the same experiment.

performed, or temperature gradients must be diminished by mechanical stirring and temperature homogenization.[36,40] The stirring is additionally expected to speed up the cooling process through an increased dissipation surface, which is actually not included in the most popular Roper's model. Without stirring, the highest temperature increase is observed in the upper part of a sample due to the convection and heat flow. In general, the fluid convection depends on the system volume and geometry. This phenomenon is difficult to describe numerically in the context of light-to-heat conversion efficiency, but Wang's setup assumes taking into account the mean temperature of the stirred sample. As a matter of fact, the highest temperature increase is observed on the top of the sample when it is not stirred and when convection occurs (Figure 2A) and that is the reason for differences in calculated parameters *a* and η_Q when the same mass of system components is assumed for all variants (Figure 3). That makes the efficiency, calculated in conventional way, dependent on stirring.

These observations motivated further modification of the "standard" experimental setup, our aim was to make the measurement independent of convection in a way other than the mechanical stirring of the sample, which is originally not considered in the Roper's model. For that reason, we have decided to build and evaluate the setup proposed by Richardson et al.,[35] where the sample is confined to a hanging drop of colloidal nanoparticles, without any container (such as cuvette). However, unlike Richardson, we have measured the temperature increase by TGC with a magnifying germanium lens, instead of using a thermocouple positioned inside the droplet. Our approach increases the costs of the setup, but saves numerous technical and TC position adjustment difficulties, and additionally avoids errors caused by the heat transfer by thermocouple conduction. This last feature is especially appealing, as a small volume of nanoheaters purposely does not heat the sample (i.e., droplet) by more than 10 degrees. Moreover, various ways to derive T_{max} can be easily implemented and validated, such as finding the maximum value, or an averaged *T* value over part or the whole *T* image of the droplet. We learned that the most appropriate approach is to average the temperature across the entire observed surface of the droplet. Developing a standardized way to quantify light-to-heat conversion requires quite strict conditions and balancing between numerous factors and issues. The use of the droplet removes all issues related to the impact of sample holder on data acquisition and interpretation, and significantly shortens acquisition time (down to a few minutes per heating and cooling cycle). Another advantage of the droplet system is the fact it can be relatively easily reproduced in other laboratories. The obvious risk is the fact that the droplet evaporates at increased temperatures, thus care must be taken to keep the maximum temperature increase below 10 °C and control humidity within chamber. While the wet towel can be barely considered as a sophisticated scientific tool, in the course of numerous trials and experiments, we came to this simple, yet effective solution and find it most reliable. We have been monitoring the humidity within the sample chamber with a dedicated humidity digital reader, but this knowledge does not allow to correct variation of humidity post factum. In the course of experiments, we have been continuously visualizing the droplet and we noticed the droplet shrinks by ca. 16% after 10 min of the experiment in open humidity chamber, including 2 min of laser beam illumination (resulting at ca. 9 °C temperature increase), while in the same conditions, in increased humidity conditions droplet shrinks by ca. 9%. Intensive shrinkage ends up with shorter laser path within the droplet, increased concentration of colloidal NPs per droplet and other perturbations occurring to the temperature readout by the thermographic camera. And again, knowledge about the decreasing droplet size and the existing models do not allow to correct for this issue post measurement. Concluding, there are many technical challenges related to the optical system design, sample container, calibration, data reproducibility and accuracy, agreement with the model, capability to repeat measurements, etc. that we have verified and discussed in the paper. Our motivations for the research were therefore 4-fold: (1) to directly and quantitively evaluate and compare various setups using the same batch of the sample, (2) to evaluate setups that are sufficiently simple to reproduce in other laboratories without sophisticated, costly and complex optical setups, (3) to evaluate light-to-heat conversion nanoparticles that are dedicated for biomedical hyperthermia, (4) to enable fast and easily repeatable measurements with small volumes of NPs water colloids. Targeting specifically hyperthermia application means that temperature increase of 10 degrees from the initial temperature should be sufficiently broad operation temperature range. This apparent restriction has one another important advantage, namely, low thermal stability at high temperatures found in many of existing photothermal agents can be disregarded from analysis. In consequence of the assumptions we made, many other problems can be avoided, for example η_Q should be independent from the operating temperature range (the verification experiment of the temperature impact on η_Q is shown in SI Figures S1 and S2). Moreover, the potential specific rates of thermal decomposition of various PTT agents can be excluded from the analysis, which simplifies the interpretation and quantitative comparisons as well as disable the misestimation of the light-to-heat conversion efficiency for such thermally unstable photothermal agents. Hence, the estimations of the η_Q upon lower excitation power in standardized conditions, as presented in this manuscript, should enable reliable quantitative comparison between various nanoheaters. However, based on the calculated η_Q for given material and using the eq 6, one may easily extrapolate and predict the temperature rise at increased concentration of nanoheaters, or at increased pumping intensity, when higher temperatures must be obtained as during PTT. We therefore believe that the proposed method is a very simple and effective way of circumventing the above-discussed issues.

Besides the issues discussed above, there is still no agreement in the literature about which component masses of the measurement setup should be included in eq 3. According to the original Roper's model,[34] all elements should be incorporated (i.e., the whole colloidal solution of NPs, the cuvette and even the thermocouple itself) and this interpretation was further frequently reproduced in other works.[47,48] Some other approaches, like in the droplet model by Richardson,[35] included only the mass of the colloidal solution and excluded the cuvette mass from calculations.[44,49−51] Marin et al. evaluated light-to-heat conversion from a theoretical perspective, and concluded that excluding the cuvette mass from calculations resulted in experimental η_Q being closer to the calculated theoretical value.[40] The importance of this factor is evident, as the results from the simulation presented in this work differ by almost 30% for the same sample with different setup characterizing data. Alternatively, Lindley and Zhang[10] suggested that only the part of the cuvette in direct contact with the colloidal nanoheaters solution should be included in the evaluation to avoid overestimation of the η_Q value. Another alternative way of solving that issue was proposed by Wang et al.,[12] who proposed to experimentally establish the "effective" mass of a cuvette that participates in heat exchange and should actually be included in the calculations. The most important differences in existing measurement assumptions related to the various models are presented in Table 1 and SI Table S5. Additionally, details about the Chen's model are presented in the SI (Chen's model). All these above-described models are frequently referred to in publications that aim to present new nanomaterials or make a comparison of existing ones (e.g.,

Table 1. Features, Advantages, and Drawbacks of Existing Experimental Setups for η_Q Measurements[a]

reference	sample holder	stirring	external	T detector	issues/challenges	advantages
Roper et al[34]	specialized glass cell	no	yes	TC on the glass wall behind the laser beam	homemade small volume experimental cell; vacuum chamber	measurement in the vacuum eliminated heat exchange
Richardson et al[35]	bare droplet formed with syringe	no	no	TC above the laser beam	evaporation of the droplet; droplet retraction	small amount of sample required; short measurement time
Chen et al[36]	cuvette	yes	yes	TC inside the cuvette	large amount of sample required	homogeneous temperature distribution
Wang et al[12]	cuvette	yes	effective mass	TC inside the cuvette	the need of calibration of the system	homogeneous temperature distributioncalibration assures quantitative evaluation
this work (based on Richardson setup)	bare droplet formed with syringe	no	no	TGC		small amount of sample required; short measurement time; inhibited droplet evaporation
this work (based on Wang setup)	cuvette	yes/no	"effective mass"	TGC in "side" or "top" configuration	the need of calibration of the system	homogeneous temperature distribution; calibration assures quantitative evaluation

[a] TC, thermocouple; TGC, thermographic camera; the "external" column indicates whether the model includes the mass of external system components such as cuvette, stirring bar, etc.

Table 2. Comparison of η_Q Obtained for Various Diameter Spherical Au Nanoparticles[a]

material	NP size (nm)	λ_{EXC} (nm)	m_{EFF}	temperature detector	experimental setup comments	model	η_Q (%)
Au NPs[34]	20	514	whole glass cell	TC outside cell	small sample cell in a vacuum chamber	R	3.4−9.9
Au NPs[35]	20	532	droplet	TC inside droplet	sample is a droplet	R	100
Au NPs[50]	15	532	solvent only	TC inside cuvette	MS, open cuvette	R/C	78.4
Au nanospheres−theoretical abs/ext value[50]			−		−	−	99.6
$Au@SiO_2$ nanospheres [this work]	13 ± 2 (Au), ~ 140 ($Au@SiO_2$)	532	solvent only	TGC; through glass	MS on	R	57.5
					MS off		50.8
			solvent only	TGC; sample surface temperature	MS on	R	63.1
					MS off		67.5
			cuvette included	TGC: through glass	MS on	R	90.5
					MS off		80.8
			cuvette included	TGC sample surface temperature	MS on	R	98.4
					MS off		106.7
			"effective mass"	TGC through glass	MS on	W	**80.5**
				TGC sample surface		W	**80.6**
			droplet	TGC sample surface	sample is a droplet	R	66.8
						W	**81.1**

[a] The following abbreviations were used for the models: R, Roper's model; R/C, Roper's model with Chen's modification (stirring); W, Wang's model; TC, thermocouple; TGC, thermographic camera; MS, magnetic stirring; λ_{EXC}, irradiation wavelength; m_{EFF}, part of mass of a cuvette.

Roper,[15,47−49,51,52] Chen,[10,16] and Wang[53]). Replacing the colloidal nanoheaters by an electrically driven resistance wire phantom, Wang discovered that only, ca. 20% of the bona fide mass of the cuvette actually had to be included in the data analysis. This value may vary depending on a particular configuration, but (i) because the electrically driven wire phantom has a known resistance and efficiency, (ii) it is power supplied with easily measurable current, and (iii) because it is studied with exactly the same sample holders and detection setup configuration as in the light-to-heat conversion measurements, the calibration procedure is simple to implement and enables one to account for the effective mass of the sample holder. In our measurements, we applied a similar calibration procedure using the same experimental conditions as those further used to quantify light-to-heat conversion efficiency with nanoparticle heaters (Figure 3A), which enabled us to compare the efficiencies obtained by different methods for the same sample (Figure 3B). As expected, the calculated "effective mass" showed some degree of variability depending on the actual measurement configuration (Figure 3A). For "top" measurement variants, the heating rate is dependent mostly on convection or mechanical stirring of the sample, so the impact of the cuvette is lower than in "side" variants, in which the heat conduction through the wall of a quartz cuvette plays an important role. The comprehensive comparison of the above-described methods of light-to-heat efficiency, performed for the same batch of $AuNP@SiO_2$ is presented in Figure 3B. The obtained efficiencies are compared in Table 2 with other literature reports on ca. 20 nm diameter spherical Au nanoparticles. The comparison of efficiency of other plasmonic and nonplasmonic nanomaterials is presented in research works.[9,54] Detailed (not averaged) experimental data are presented in SI Tables S2−S4. The results obtained with the Roper's model vary considerably. The η_Q for the "top" configuration is the highest among all the obtained with this model. The most probable reason for η_Q to exceed 100% is generation of significant temperature gradients and the fact this is not the entire volume of the sample that gets heated homogeneously, but the heating is induced and monitored only in its top part. This result is closest to Richardson's result, however $Au@SiO_2$ NPs are expected to have lower light-to-heat conversion efficiency than Au NPs because the coating leads to higher scattering due to the increase in size. It is worth noting that results obtained with a modified Wang's model lead to the same η_Q value, independently from the measurement conditions. Only in the "top" variant, the η_Q is slightly lower, but this is probably caused by difficulties in reproducing the laser beam by a heating wire: cables connecting the heating wire with the current leads were attached from above, and thus can disturb the precise determination of the effective mass in this variant. This case indicates how important it is to correctly determine the effective mass in an irregular geometry system. On the other hand, the effective mass of the pipet tip, which served to create the droplet was found negligible, as expected.

3. CONCLUSION

Light-to-heat conversion efficiency is one of the most important figures-of-merit in the studies of materials dedicated to the photothermal therapy of cancer. The η_Q should enable one to quantitatively and reliably compare, and further optimize, various nanoheaters between various laboratories. Unfortunately, large discrepancies in η_Q are commonly found even for very similar nanoheaters, making this quantity unreliable for its purpose. Through careful evaluation of theoretical models, numerous assumptions and experimental setups made for the same batch of $AuNPs@SiO_2$ nanoheaters, we have critically evaluated existing systems and models, and thus contributed to the understanding and standardization of η_Q determination. More specifically, despite the fact that η_Q is nominally a material constant, its determined value was found to depend on numerous measurement conditions and assumptions, such as the mass of the system and its geometry, the presence of colloidal sample stirring, and the specifics of how and where the temperature was measured. Before a ranking of different HTNPs can be reliably made, a unified approach to η_Q is a prerequisite.

Our measurements confirm that (simple to implement) effective mass correction enables to obtain coherent and

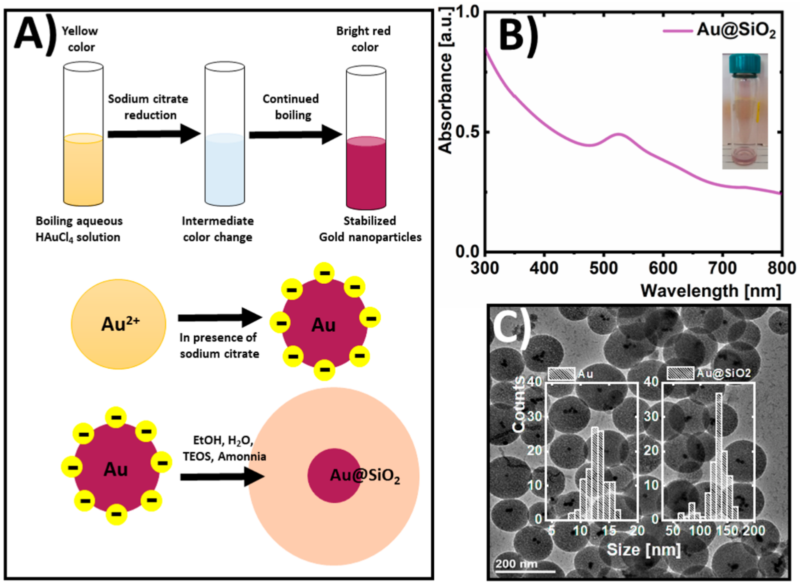

Figure 4. (A) Scheme of two-step synthesis of Au and Au@SiO$_2$ nanoparticles, (B) absorption spectra of the colloidal solution of Au@SiO$_2$ nanoparticles in water, (C) TEM images with size distribution of pristine and SiO$_2$ covered AuNPs.

directly comparable η_Q values even though significantly different measurement setups were applied. Alternatively, we have also critically evaluated and presented an improved measurement system exploiting the droplet based concept, which not only eliminated the need for effective mass correction, but most of all reduced the volume of the sample ca. 100-fold and reduced recording time up to 10-fold as compared to other conventional measurement systems. Additional modifications, aiming to reduce sample evaporation during measurements were proposed to further minimize artifacts and improve the reliability of the obtained efficiency values.

4. MATERIALS AND METHODS

Au@SiO$_2$ Preparation. Gold(III) chloride hydrate (99.995%), tetraethyl orthosilicate-TEOS (99%), ammonia solution (28−30%), were purchased from Sigma-Aldrich. Ethanol (96%) was purchased from Avantor and sodium citrate was purchased from MERCK. All chemical reagents were used without further purification.

Au NPs were prepared by reduction the gold salt with sodium citrate.[55,56] The freshly prepared water solution of sodium citrate was added to 9.95 mL of water solution of HAuCl$_4$ in constant temperature (80 °C) under vigorous stirring. The color of the mixture turned wine red after few minutes which indicates the production of Au nanoparticles. The protocol of synthesis is illustrated in Figure 4.

Then, Au NPs were coated with silica. The as-prepared Au nanoparticles were mixed with a proper amount of ethanol (12 mL), distilled water (500 μL), TEOS (20 μL), and ammonia (500 μL). The solution was maintained at room temperature for 24 h under vigorous stirring. Next, the mixture was centrifuged (10 000 rpm, 10 min) and the obtained pellet was purified by ethanol and dispersed in distilled water.

The photostability was checked independently (SI Figure S3). Four cycles of heating and cooling were performed on the same droplet of AuNPs from the same batch as previously. Sample was diluted before experiment to decrease maximum temperature and reduce evaporation. Results have shown that maximum temperature was not decreasing in the next cycles.

Experimental Details. The first experimental variant is based on the Roper's setup.[34] It consists of the activation light source−laser diode (532 nm, 1 W, Changchun New Industries Optoelectronics Technology Co. Ltd.), optical setup for photon beam collimation, fluorescence cuvette containing 2 mL solution of nanoparticles, thermographic camera (TGC) (FLIR T540, accuracy ±0.5 °C with a reference, thermal sensitivity <40 mK, 24° @ 30 °C) and thermohigrometer (ETI Ltd., type 6500). The cuvette was inserted into the holder which remained in minimal contact with the upper part of the cuvette to reduce heat transfer to other elements of the system. The cuvette entrance wall was set at the angle of 7° to the laser beam to avoid multiple reflections, and the exit wall was set at the angle of approximately 15° to the TGC to eliminate camera own reflections from the perpendicular wall of the cuvette. This wall of the cuvette was covered with piece of black tape of known emissivity ($E = 0.96$, $m = 0.15$ g, 3M, Poland) for accurate measurement with a TGC. The system was isolated from external light and heat by a 5 cm thick styrofoam cage. Measurements were conducted in an air-conditioned room at 23 °C and constant humidity conditions during all experiments. The laser power of 200 mW was set and mean power density was 1.6 W/cm^2. The laser beam (spot size 4 mm) was hitting the center of the entrance wall under 7° angle, to avoid multiple reflections in quartz cuvette.

Because significant heating can be expected for highly concentrated samples due to plasmonic effects, we measured our samples in diluted form (to keep heating of no more than 10 °C above RT) and indeed in the course of the experiments we did not observe any concentration dependent effects. In a typical measurement "side-view" procedure (Figure 1B), the sample was dispersed on the ultrasonic scrubber and inserted (2 mL, 2 cm height) into the cuvette, which was fixed into stable position by cuvette holder. The focus of the TGC was set to the side surface of the cuvette (90° angle to the laser beam axis) and was kept the same for all the measurements. Then the setup was left for approximately 20 min to reach stable temperature distribution in the field of view of the TGC. The laser diode was turned on at least 2 min before each experiment, but the beam was blocked by a mechanical shutter to prevent sample illumination before the actual experiment started. Recording temperature images by TGC and recording laser power with power meter (photodiode S120C head and PM100USB power meter, Thorlabs) started simultaneously. After 70 s the laser beam shutter was unlocked and heating curves were registered. Then, after 45 min laser was turned off and the cooling curve was registered for the next 60 min.

Data from the TGC was analyzed in FLIR Tools software. Temperature of sample was averaged from the whole cuvette surface area staying in direct contact with the colloid. The η_Q calculations derived from the cooling curve were based on equations presented by

Roper et al.,[34] while the ones derived from the heating curve, were using equations presented by Wang et al.[12] Other details of data analysis and well as error analysis are presented in SI (Details of data analysis). Because in the described setup significant gradients of temperature were noted in the initial phase of heating−cooling kinetic profiles, we verified the impact of gentle magnetic stirring on the output temperature profiles quality. For that purpose, the magnetic base was placed below the cuvette bottom (without direct contact), and a small magnet bar (3 × 1 × 1 mm) was dropped into the cuvette. The stirrer was turned on 1 h before the experiment started to obtain a stable temperature gradient in the sample environment.

Next the experimental setup was modified to provide direct colloidal surface measurements ("top view" variant, Figure 1C). TGC was positioned above the experimental setup with a 9° angle between objective axis and colloid surface. Black tape of known emissivity was removed from the cuvette because it was not required in this setup configuration (water emissivity is known, $E = 0.90$). In this case, the temperature recorded by the camera was acquired through the round neck of the cuvette, thus the temperature was averaged from ellipsoid part of the TVC image (whole available sample surface). Similarly to the "side view" experimental setup, the influence of magnetic stirring was verified.

Experiment with "droplet" configuration required similar optical setup, but it requires also independent sample dosing system (SI Figure S4). Also measurement procedure was more complicated in this case (see SI Droplet setup-detailed experimental procedure and issues).

Calibration Experimental Details. Instead of a laser beam, 0.3 mm kanthal resistance wire of known (measured) resistance was used. The current was supplied to the heating wire using silver-plated copper wire. The wire was carefully fixed at position, where photostimulating laser beam was heating the sample to keep the position of the TGC and all other components in the given configuration exactly the same as during photostimulation experiments. The heating element was welded to silver-plated copper wire to obtain a stable electrical connection. A current of 0.25−1.02 A was set on the regulated DC power supply (MCP M10-QS3020, Poland) and the voltage on the heating wire was recorded with a multimeter (attached to the wire slightly above the height of the cuvette). Based on this data, resistance (around 380 ohms) and supplied power (P) were determined.

ASSOCIATED CONTENT

Supporting Information

The Supporting Information is available free of charge at https://pubs.acs.org/doi/10.1021/acsami.1c12409.

> Standardization of light to heat conversion efficiency; The CAD drawing of the chamber (suitable for 3D printing) for the droplet setup is available from us upon request (PDF)

AUTHOR INFORMATION

Corresponding Author

Artur Bednarkiewicz − *Institute of Low Temperature and Structure Research, Polish Academy of Sciences, 50-422 Wrocław, Poland;* orcid.org/0000-0003-4113-0365; Email: a.bednarkiewicz@intibs.pl

Authors

Agnieszka Paściak − *Institute of Low Temperature and Structure Research, Polish Academy of Sciences, 50-422 Wrocław, Poland;* orcid.org/0000-0002-3206-360X

Aleksandra Pilch-Wróbel − *Institute of Low Temperature and Structure Research, Polish Academy of Sciences, 50-422 Wrocław, Poland;* orcid.org/0000-0003-1991-4008

Łukasz Marciniak − *Institute of Low Temperature and Structure Research, Polish Academy of Sciences, 50-422 Wrocław, Poland;* orcid.org/0000-0001-5181-5865

P. James Schuck − *Department of Mechanical Engineering, Columbia University, New York, New York 10027, United States;* orcid.org/0000-0001-9244-2671

Complete contact information is available at: https://pubs.acs.org/10.1021/acsami.1c12409

Author Contributions

The manuscript was written through contributions of all authors. All authors have given approval to the final version of the manuscript.

Funding

This work was funded by NanoTBTech-H2020-FETOPEN (801305) "Nanoparticle-based 2D thermal bioimaging technologies" project. P.J.S. acknowledges support from the Global Research Laboratory (GRL) Program through the National Research Foundation of Korea (NRF) that is funded by the Ministry of Science and ICT (2016911815), KRICT (KK2061-23, SKO1930-20).

Notes

The authors declare no competing financial interest.

REFERENCES

(1) Wang, S.; Ma, X.; Hong, X.; Cheng, Y.; Tian, Y.; Zhao, S.; Liu, W.; Tang, Y.; Zhao, R.; Song, L.; Teng, Z.; Lu, G. Adjuvant Photothermal Therapy Inhibits Local Recurrences after Breast-Conserving Surgery with Little Skin Damage. *ACS Nano* **2018**, *12* (1), 662−670.

(2) Hou, Z.; Deng, K.; Wang, M.; Liu, Y.; Chang, M.; Huang, S. Hydrogenated Titanium Oxide Decorated Upconversion Nanoparticles: Facile Laser Modified Synthesis and 808 Nm Near-Infrared Light Triggered Phototherapy. *Chem. Mater.* **2019**, *31*, 774−784.

(3) Liu, T.; Wang, C.; Gu, X.; Gong, H.; Cheng, L.; Shi, X.; Feng, L.; Sun, B.; Liu, Z. Drug Delivery with PEGylated MoS2 Nano-Sheets for Combined Photothermal and Chemotherapy of Cancer. *Adv. Mater.* **2014**, *26* (21), 3433−3440.

(4) Skitzki, J. J.; Repasky, E. A.; Evans, S. S. Hyperthermia as an Immunotherapy Strategy for Cancer. *Curr. Opin. Invest. Drugs* **2009**, *10* (6), 550−558.

(5) Mondovi, B.; Strom, R.; Rotilio, G.; Agro, A. F.; Cavaliere, R.; Rossi Fanelli, A. The Biochemical Mechanism of Selective Heat Sensitivity of Cancer Cells: I. Studies on Cellular Respiration. *Eur. J. Cancer* **1969**, *5* (2), 129−136.

(6) Mondovi, B.; Finazzi Agro, A.; Rotilio, G.; Strom, R.; Morrica, G.; Rossi Fanelli, A. The Biochemical Mechanism of Selective Heat Sensitivity of Cancer Cells: II. Studies on Nucleic Acids and Protein Synthesis. *Eur. J. Cancer* **1969**, *5* (2), 137−146.

(7) van der Zee, J.; Vujaskovic, Z.; Kondo, M.; Sugahara, T. The Kadota Fund International Forum 2004-Clinical Group Consensus. *Int. J. Hyperthermia* **2008**, *24* (2), 111−122.

(8) Gnach, A.; Lipinski, T.; Bednarkiewicz, A.; Rybka, J.; Capobianco, J. A. Upconverting Nanoparticles: Assessing the Toxicity. *Chem. Soc. Rev.* **2015**, *44* (6), 1561−1584.

(9) Marciniak, L.; Kniec, K.; Elzbieciak, K.; Bednarkiewicz, A. *Near Infrared-Emitting Nanoparticles for Biomedical Applications*; Benayas, A., Hemmer, E., Hong, G, Jaque, D., Ed.; Springer, 2020.

(10) Lindley, S. A.; Zhang, J. Z. Bumpy Hollow Gold Nanospheres for Theranostic Applications: Effect of Surface Morphology on Photothermal Conversion Efficiency. *ACS Appl. Nano Mater.* **2019**, *2* (2), 1072−1081.

(11) Liao, Y.-T.; Liu, C.-H.; Chin, Y.; Chen, S.-Y.; Liu, S. H.; Hsu, Y.-C.; Wu, K. C.-W. Biocompatible and Multifunctional Gold Nanorods for Effective Photothermal Therapy of Oral Squamous Cell Carcinoma. *J. Mater. Chem. B* **2019**, *7* (28), 4451−4460.

(12) Wang, X.; Li, G.; Ding, Y.; Sun, S. Understanding the Photothermal Effect of Gold Nanostars and Nanorods for Biomedical Applications. *RSC Adv.* **2014**, *4* (57), 30375−30383.

(13) Marciniak, L.; Pilch, A.; Arabasz, S.; Jin, D.; Bednarkiewicz, A. Heterogeneously Nd3+ Doped Single Nanoparticles for NIR-Induced Heat Conversion, Luminescence, and Thermometry. *Nanoscale* **2017**, *9* (24), 8288−8297.

(14) Shao, Q.; Li, X.; Hua, P.; Zhang, G.; Dong, Y.; Jiang, J. Enhancing the Upconversion Luminescence and Photothermal Conversion Properties of ∼ 800 Nm Excitable Core/Shell Nanoparticles by Dye Molecule Sensitization. *J. Colloid Interface Sci.* **2017**, *486*, 121−127.

(15) Li, S.; Zhou, S.; Li, Y.; Li, X.; Zhu, J.; Fan, L.; Yang, S. Exceptionally High Payload of the IR780 Iodide on Folic Acid-Functionalized Graphene Quantum Dots for Targeted Photothermal Therapy. *ACS Appl. Mater. Interfaces* **2017**, *9* (27), 22332−22341.

(16) Jiang, R.; Cheng, S.; Shao, L.; Ruan, Q.; Wang, J. Mass-Based Photothermal Comparison among Gold Nanocrystals, PbS Nanocrystals, Organic Dyes, and Carbon Black. *J. Phys. Chem. C* **2013**, *117* (17), 8909−8915.

(17) Chien, Y.; Chan, K. K.; Anderson, T.; Kong, K. V.; Ng, K. Advanced Near-Infrared Light-Responsive Nanomaterials as Therapeutic Platforms for Cancer Therapy. *Adv. Ther.* **2019**, *1800090*, 1−49.

(18) Guo, L.; Liu, W.; Niu, G.; Zhang, P.; Zheng, X.; Jia, Q.; Zhang, H.; Ge, J.; Wang, P. Polymer Nanoparticles with High Photothermal Conversion Efficiency as Robust Photoacoustic and Thermal Theranostics. *J. Mater. Chem. B* **2017**, *5* (15), 2832−2839.

(19) Geng, J.; Sun, C.; Liu, J.; Liao, L. De; Yuan, Y.; Thakor, N.; Wang, J.; Liu, B. Biocompatible Conjugated Polymer Nanoparticles for Efficient Photothermal Tumor Therapy. *Small* **2015**, *11* (13), 1603−1610.

(20) Sheng, Z.; Song, L.; Zheng, J.; Hu, D.; He, M.; Zheng, M.; Gao, G.; Gong, P.; Zhang, P.; Ma, Y.; Cai, L. Protein-Assisted Fabrication of Nano-Reduced Graphene Oxide for Combined Invivo Photoacoustic Imaging and Photothermal Therapy. *Biomaterials* **2013**, *34* (21), 5236−5243.

(21) Romero-Aburto, R.; Narayanan, T. N.; Nagaoka, Y.; Hasumura, T.; Mitcham, T. M.; Fukuda, T.; Cox, P. J.; Bouchard, R. R.; Maekawa, T.; Kumar, D. S.; Torti, S. V.; Mani, S. A.; Ajayan, P. M. Fluorinated Graphene Oxide; A New Multimodal Material for Biological Applications. *Adv. Mater.* **2013**, *25* (39), 5632−5637.

(22) Espinosa, A.; Di Corato, R.; Kolosnjaj-Tabi, J.; Flaud, P.; Pellegrino, T.; Wilhelm, C. Duality of Iron Oxide Nanoparticles in Cancer Therapy: Amplification of Heating Efficiency by Magnetic Hyperthermia and Photothermal Bimodal Treatment. *ACS Nano* **2016**, *10* (2), 2436−2446.

(23) Ou, G.; Li, Z.; Li, D.; Cheng, L.; Liu, Z.; Wu, H. Photothermal Therapy by Using Titanium Oxide Nanoparticles. *Nano Res.* **2016**, *9* (5), 1236−1243.

(24) Ishii, S.; Sugavaneshwar, R. P.; Chen, K.; Dao, T. D.; Nagao, T. Solar Water Heating and Vaporization with Silicon Nanoparticles at Mie Resonances. *Opt. Mater. Express* **2016**, *6* (2), 640.

(25) Ishii, S.; Sugavaneshwar, R. P.; Nagao, T. Titanium Nitride Nanoparticles as Plasmonic Solar Heat Transducers. *J. Phys. Chem. C* **2016**, *120* (4), 2343−2348.

(26) Zograf, G. P.; Timin, A. S.; Muslimov, A. R.; Shishkin, I. I.; Nominé, A.; Ghanbaja, J.; Ghosh, P.; Li, Q.; Zyuzin, M. V.; Makarov, S. V. All-Optical Nanoscale Heating and Thermometry with Resonant Dielectric Nanoparticles for Controllable Drug Release in Living Cells. *Laser Photonics Rev.* **2020**, *14* (3), 1−11.

(27) Zograf, G. P.; Petrov, M. I.; Makarov, S. V.; Kivshar, Y. S. All-dielectric thermonanophotonics https://arxiv.org/abs/2104.01964.

(28) Quarta, A.; Piccirillo, C.; Mandriota, G. Nanoheterostructures (NHS) and Their Applications in Nanomedicine: Focusing on In Vivo Studies. *Materials* **2019**, *12* (139), 1−37.

(29) Yan, L.; Zhao, F.; Wang, J.; Zu, Y.; Gu, Z.; Zhao, Y. A Safe-by-Design Strategy towards Safer Nanomaterials in Nanomedicines *Adv. Mater.* **2019**, 1805391.

(30) Farahavar, G.; Abolmaali, S. S.; Gholijani, N.; Nejatollahi, F. Antibody-Guided Nanomedicines as Novel Breakthrough Therapeutic, Diagnostic and Theranostic Tools. *Biomater. Sci.* **2019**, *7* (10), 4000−4016.

(31) Polo, E.; Navarro Poupard, M. F.; Guerrini, L.; Taboada, P.; Pelaz, B.; Alvarez-Puebla, R. A.; del Pino, P. Colloidal Bioplasmonics. *Nano Today* **2018**, *20*, 58−73.

(32) IEC. *Safety of Laser Products - Part1: Equipment Classification and Requirements (IEC 60825−1:2007)*; **2014**; Vol *3.0*.

(33) *ANSI Z136.1—2007, American National Standard for Safe Use of Lasers*, 2007.

(34) Roper, D. K.; Ahn, W.; Hoepfner, M. Microscale Heat Transfer Transduced by Surface Plasmon Resonant Gold Nanoparticles *J. Phys. Chem. C* **2007**. *111*3636.

(35) Richardson, H. H.; Carlson, M. T.; Tandler, P. J.; Hernandez, P.; Govorov, A. O. Experimental and Theoretical Studies of Light-to-Heat Conversion and Collective Heating Effects in Metal Nanoparticle Solutions. *Nano Lett.* **2009**, *9* (3), 1139−1146.

(36) Chen, H.; Shao, L.; Ming, T.; Sun, Z.; Zhao, C.; Yang, B.; Wang, J. Understanding the Photothermal Conversion Efficiency of Gold Nanocrystals. *Small* **2010**, *6* (20), 2272−2280.

(37) Wu, Z.; Liang, J.; Ji, X.; Yang, W. Preparation of Uniform Au@SiO2 Particles by Direct Silica Coating on Citrate-Capped Au Nanoparticles. *Colloids Surf., A* **2011**, *392* (1), 220−224.

(38) Chen, Y.-S.; Frey, W.; Kim, S.; Homan, K.; Kruizinga, P.; Sokolov, K.; Emelianov, S. Enhanced Thermal Stability of Silica-Coated Gold Nanorods for Photoacoustic Imaging and Image-Guided Therapy. *Opt. Express* **2010**, *18* (9), 8867.

(39) Baffou, G.; Quidant, R.; García De Abajo, F. J. Nanoscale Control of Optical Heating in Complex Plasmonic Systems. *ACS Nano* **2010**, *4* (2), 709−716.

(40) Marin, R.; Skripka, A.; Besteiro, L. V.; Benayas, A.; Wang, Z.; Govorov, A. O.; Canton, P.; Vetrone, F. Highly Efficient Copper Sulfide-Based Near-Infrared Photothermal Agents: Exploring the Limits of Macroscopic Heat Conversion. *Small* **2018**, *14* (49), 1−9.

(41) Lapolla, A.; Godec, A. Faster Uphill Relaxation in Thermodynamically Equidistant Temperature Quenches. *Phys. Rev. Lett.* **2020**, *125* (11), 110602.

(42) Norton, S. J.; Vo-Dinh, T. Photothermal Effects of Plasmonic Metal Nanoparticles in a Fluid *J. Appl. Phys.* **2016**, *119* (8). 083105.

(43) Baffou, G.; Quidant, R.; Girard, C. Heat Generation in Plasmonic Nanostructures: Influence of Morphology. *Appl. Phys. Lett.* **2009**, *94* (15), 2009−2011.

(44) Alrahili, M.; Peroor, R.; Savchuk, V.; McNear, K.; Pinchuk, A. Morphology Dependence in Photothermal Heating of Gold Nanomaterials with Near-Infrared Laser *J. Phys. Chem. C* **2020**. *124*4755.

(45) Bastos, A. R. N.; Brites, C. D. S.; Rojas-Gutierrez, P. A.; DeWolf, C.; Ferreira, R. A. S.; Capobianco, J. A.; Carlos, L. D. Thermal Properties of Lipid Bilayers Determined Using Upconversion Nanothermometry. *Adv. Funct. Mater.* **2019**, *29* (48), 1−10.

(46) Chernov, G.; Ibarra-Valdez, J. L.; Carrillo-Torres, R. C.; Medrano-Pesqueira, T. C.; Chernov, V.; Barboza-Flores, M. Improved Method of Study on the Photothermal Effect of Plasmonic Nanoparticles by Dynamic IR Thermography. *Plasmonics* **2019**, *14*, 935−944.

(47) Ayala-Orozco, C.; Urban, C.; Knight, M. W.; Urban, A. S.; Neumann, O.; Bishnoi, S. W.; Mukherjee, S.; Goodman, A. M.; Charron, H.; Mitchell, T.; Shea, M.; Roy, R.; Nanda, S.; Schiff, R.; Halas, N. J.; Joshi, A. Au Nanomatryoshkas as Efficient Near-Infrared Photothermal Transducers for Cancer Treatment: Benchmarking against Nanoshells. *ACS Nano* **2014**, *8* (6), 6372−6381.

(48) Almada, M.; Leal-Martínez, B. H.; Hassan, N.; Kogan, M. J.; Burboa, M. G.; Topete, A.; Valdez, M. A.; Juárez, J. Photothermal Conversion Efficiency and Cytotoxic Effect of Gold Nanorods Stabilized with Chitosan, Alginate and Poly(Vinyl Alcohol). *Mater. Sci. Eng., C* **2017**, *77*, 583−593.

(49) Li, D.; Han, D.; Qu, S. N.; Liu, L.; Jing, P. T.; Zhou, D.; Ji, W. Y.; Wang, X. Y.; Zhang, T. F.; Shen, D. Z. Supra-(Carbon Nanodots)

with a Strong Visible to near-Infrared Absorption Band and Efficient Photothermal Conversion. *Light: Sci. Appl.* **2016**, *5* (7), 1−8.

(50) Jiang, K.; Smith, D. A.; Pinchuk, A. Size-Dependent Photothermal Conversion Efficiencies of Plasmonically Heated Gold Nanoparticles. *J. Phys. Chem. C* **2013**, *117* (51), 27073−27080.

(51) Bi, C.; Chen, J.; Chen, Y.; Song, Y.; Li, A.; Li, S.; Mao, Z.; Gao, C.; Wang, D.; Möhwald, H.; Xia, H. Realizing a Record Photothermal Conversion Efficiency of Spiky Gold Nanoparticles in the Second Near-Infrared Window by Structure-Based Rational Design. *Chem. Mater.* **2018**, *30* (8), 2709−2718.

(52) Cole, J. R.; Mirin, N. A.; Knight, M. W.; Goodrich, G. P.; Halas, N. J. Photothermal Efficiencies of Nanoshells and Nanorods for Clinical Therapeutic Applications. *J. Phys. Chem. C* **2009**, *113* (28), 12090−12094.

(53) Qin, Z.; Wang, Y.; Randrianalisoa, J.; Raeesi, V.; Chan, W. C. W.; Lipiński, W.; Bischof, J. C. Quantitative Comparison of Photothermal Heat Generation between Gold Nanospheres and Nanorods. *Sci. Rep.* **2016**, *6* (1), 29836.

(54) Wei, W.; Zhang, X.; Zhang, S.; Wei, G.; Su, Z. Biomedical and Bioactive Engineered Nanomaterials for Targeted Tumor Photothermal Therapy: A Review. *Mater. Sci. Eng., C* **2019**, *104* (June), 109891.

(55) Kobayashi, Y.; Inose, H.; Nakagawa, T.; Gonda, K.; Takeda, M.; Ohuchi, N.; Kasuya, A. Control of Shell Thickness in Silica-Coating of Au Nanoparticles and Their X-Ray Imaging Properties. *J. Colloid Interface Sci.* **2011**, *358* (2), 329−333.

(56) Haiss, W.; Thanh, N. T. K.; Aveyard, J.; Fernig, D. G. Determination of Size and Concentration of Gold Nanoparticles from UV−Vis Spectra. *Anal. Chem.***2007**. 794215.

https://doi.org/10.1021/acsami.1c12409
ACS Appl. Mater. Interfaces 2021, 13, 44556−44567

Supporting Information

Standardization of Methodology of Light-to-Heat Conversion Efficiency Determination for Colloidal Nanoheaters

Agnieszka Paściak[1], *Aleksandra Pilch-Wróbel*[1], *Łukasz Marciniak*[1], *Peter James Schuck*[2],

*Artur Bednarkiewicz**[1]

[1] Institute of Low Temperature and Structure Research, Polish Academy of Sciences, Okólna 2, 50-422 Wroclaw, Poland
[2] Department of Mechanical Engineering, Columbia University, New York, NY, United States

* Author to whom correspondence should be addressed: a.bednarkiewicz@intibs.pl

Details of data analysis

Droplet size was determined from thermographic camera data in TGC camera FLIR Tools software: the number of pixels forming a drop was determined and based on the scale (i.e. plastic tip end diameter) the real droplet volume was calculated. Temperature was averaged from the whole available droplet surface excluding edges (pixels in temperature range between temperature of droplet and temperature of background). Due to the fact that the thermographic camera accuracy is 2 °C, we made efforts to improve this value by concurrently taking the reference measurement of a background, which remained at a constant temperature and we have subtracted the noisy background signal. As we have checked, this operation did not introduce any additional measurement errors, and allowed to eliminate artifacts, such as imperfections of the thermographic camera. In the case of a droplet, wet tissues placed nearby the droplet were chosen as background measurement area, to include the temperature difference between droplet and environment caused by water evaporation. In case of measurements in cuvette, the background signal originated from black tape above the cuvette (black tape was also placed on the cuvette to minimize reflections from quartz glass cuvette). Data from FLIR Tools and Thorlabs optical power meters was exported, and then analyzed in Origin 2019 software.

Droplet setup – detailed experimental procedure and issues

The optical power calibration measurement was carried out to determine the ratio between reference and measurement optical power. The dosing system was sealed and refilled with water to avoid uncontrollable droplet regression or ejection. Thermographic camera was set perpendicular to the droplet dispensing system. Humidity chamber was also optimized – a vessel with water has been placed below the droplet and tissues soaked with water were placed nearby. Water reference measurements were conducted before and after sample measurements. Before experiment, sample was dispersed on the ultrasonic scrubber. After dropping, the position of droplet was adjusted and the chamber was isolated with Parafilm. Beam shutter was set in OFF position and the whole setup was covered by Styrofoam and black fabric. Power meters were zero adjusted and the setup was left alone until the temperature difference between the droplet and surroundings was less than 0.2 degree, which indicated that the humidity inside the chamber was stabilized. Then the laser was turned on and after 2 minutes the measurement by thermographic camera and power meters started. Initial 30 s were "dark" measurement, then the shutter was removed and the sample was heated by laser irradiation. After 3 minutes, when the temperature of the droplet became stable, the laser was turned off, and sample was cooling down. After 7 minutes when temperature turned back into initial state, the measurements were stopped. All further data analysis was performed off-line.

We have made effort to make the system possibly reliable. We have resolved many experimental issues:

1. We found out that various nanomaterials might have different contact angles, so the maximum droplet size may differs. It also may depend on surface charge of the pipette tip. The system has to include droplet position regulation (we have built simplified system which allows for that, but we recommend to use XYZ stage).

2. Droplet acts like a lens, so its position has to be fixed in the way that enables light transmission measurements throughout the exact Z-axis of the setup.

3. We found out, that our pipette itself is not tight enough to preserve droplet from retraction. To solve that, firstly we have tried to use solenoid valve, but it generated significant amount of heat which disrupted measurements. From that reason we have decided to use a mechanical valve (home-made one, commercially available ones should also work). We found out that the system is tight when all connections are filled with water.

4. Droplet is relatively small object (no more than 3 mm in diameter), so to register distinct picture of it, thermographic camera (FLIR T540) with a macro IR lens should be located close enough. Because the power supply electronics of the camera generates heat which through specular reflection from flat gall surfaces may affect the measurements, we have decided to use magnifying germanium lens (Ø=1”, F=50 mm, Thorlabs) with transmission matching the transmission of the TGC camera lens.

5. We have discovered that humidity plays significant role in temperature measurements, especially when the amount of sample is small: we have built a humidity chamber to minimize the evaporation.

Power dependence of Au@SiO$_2$ nanoparticles light-to-heat conversion efficiency

The measurement of light-to-heat conversion efficiency as a function of laser power was carried out in the droplet system using originally synthesized NPs about 1.5 years after the sample synthesis. Some changes were observed in samples properties (Figure S1) such as: smoothing of the peak at approx. 600 nm, reduced scattering (these changes are probably due to sedimentation of synthesis residues or aggregates on the bottom of the sample) and a relatively higher peak height corresponding to the maximum of plasmon resonance (which could be caused by sample evaporation). During experiments (Figure S2) the temperature increased by no more than 9 °C above room temperature for pump laser power in the 9 to 118 mW range. The obtained results display very similar values, which stay within measurement accuracy and neither a rising nor falling trend could be observed. High standard deviations for several points are mainly caused by the dispersion of droplet sizes, which was monitored during the experiments with the calibrated thermographic camera.

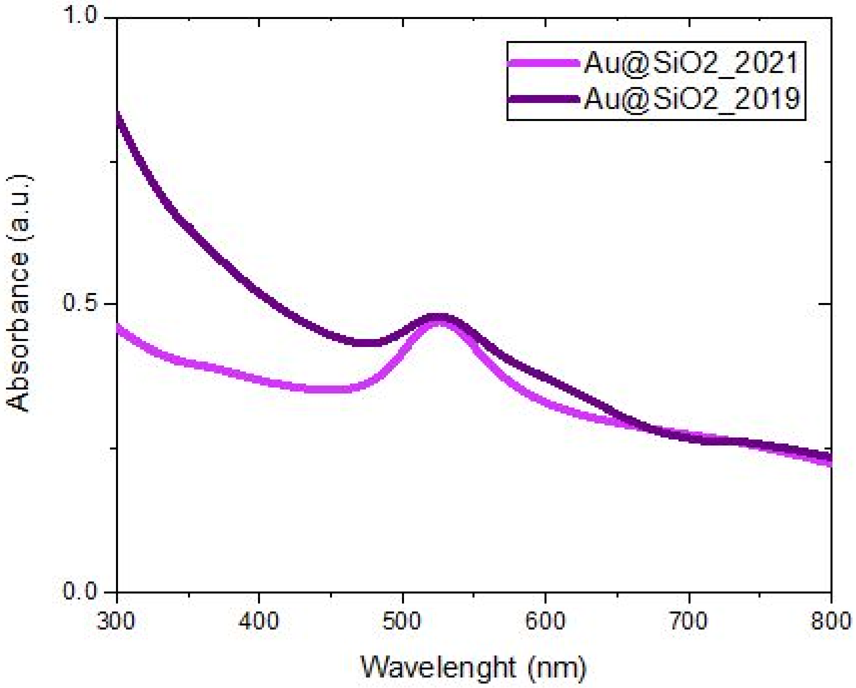

Figure S1. Absorption spectra of the sample used for power dependent η_Q experiment: original and freshly measured (dark purple) and 1.5 years old (light pink) samples.

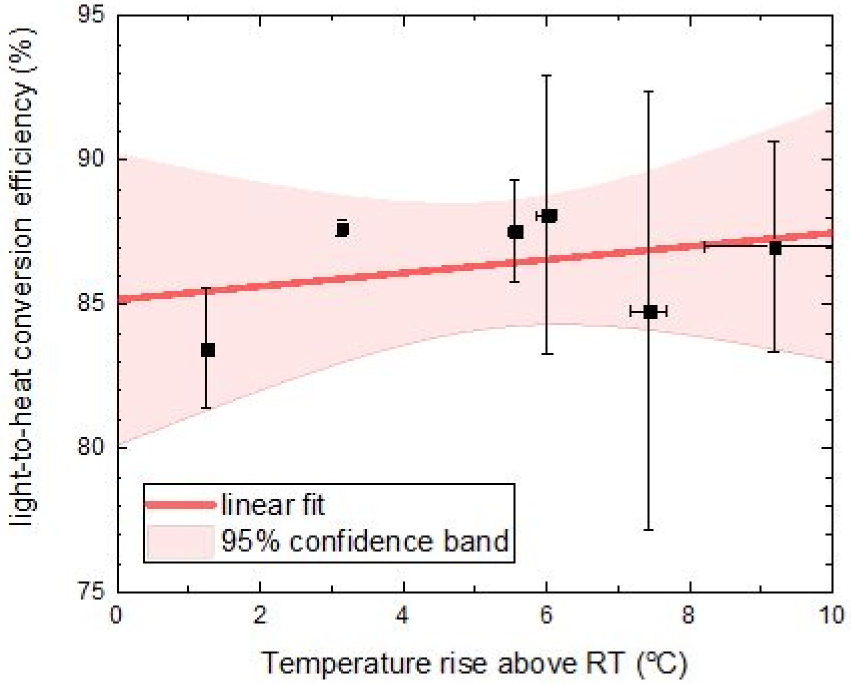

Figure S2. Dependence of the light-to-heat conversion efficiency on self-generated temperature for the Au@SiO_2 sample. The error bars show standard deviation calculated from at least 3 measurements.

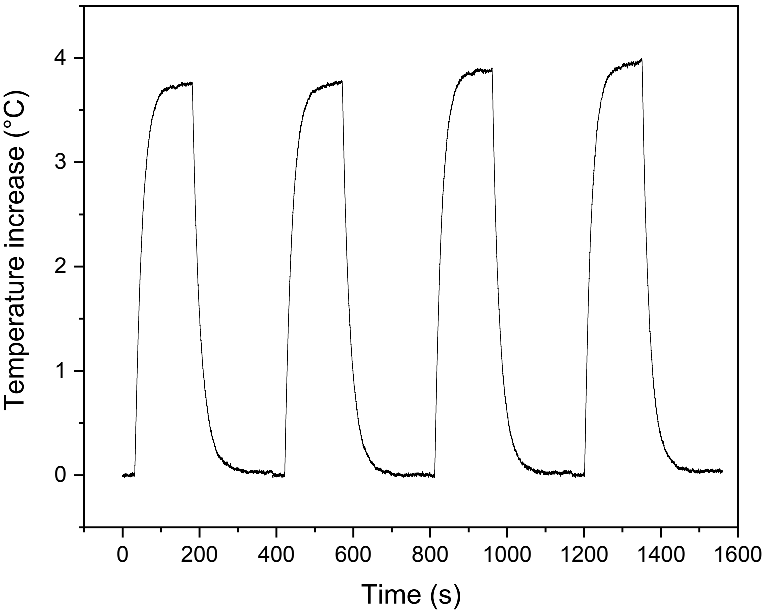

Figure S3. Heating and cooling curves of diluted Au@SiO_2 sample: laser power: 116.9 mW, sample absorbance: 0.054, sample mass: 10.8 µg

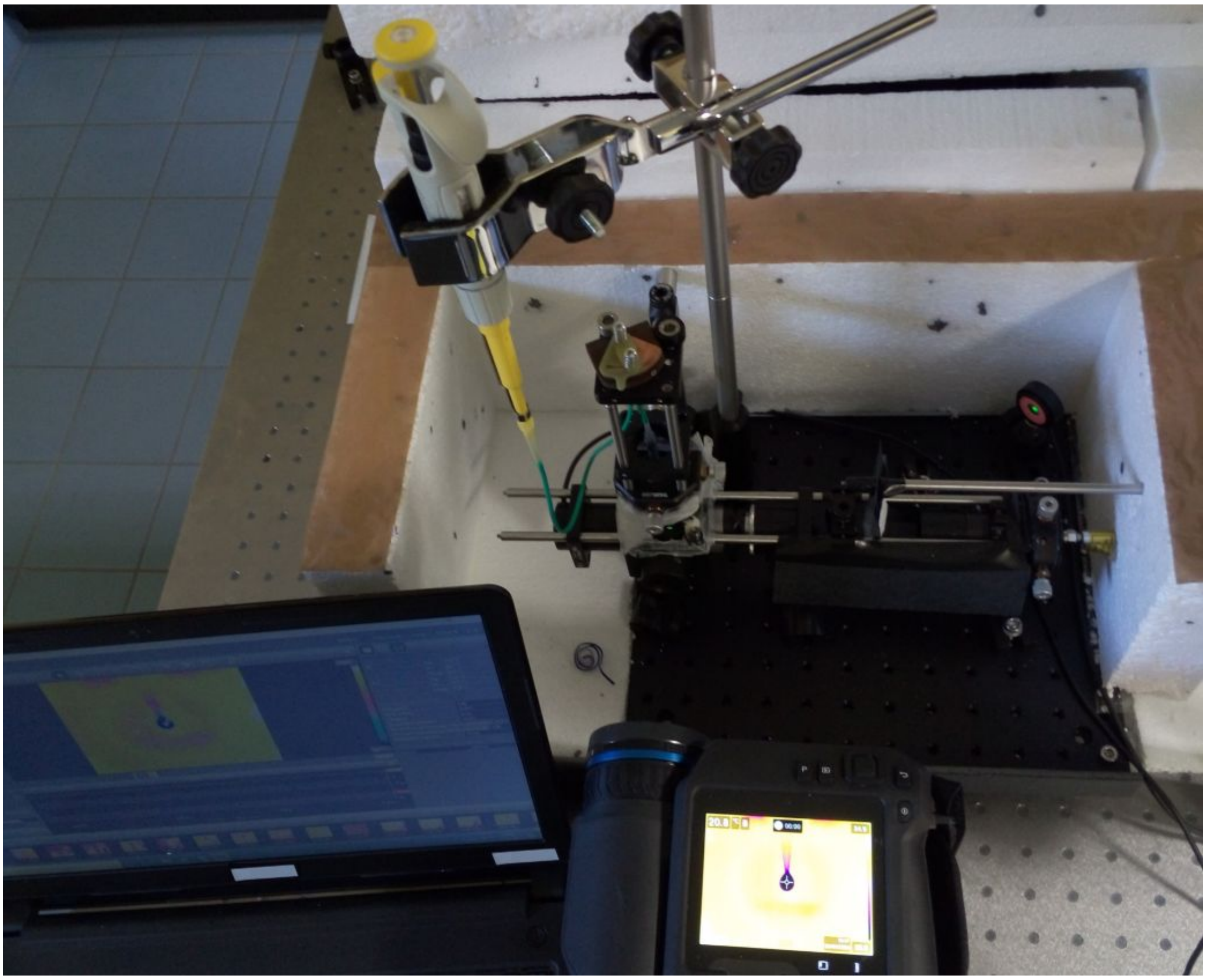

Figure S4. Droplet experimental setup photography

Table S1. Experimental parameters

Experiments in cuvette:

Main parameters	
Type of excitation	Continuous wave
Laser power (mW)	~200
Power density ($\frac{W}{cm^2}$)	~1.6
Laser contact surface (mm^2)	~12.6 (FWHM=4mm)
Q_0 ($\frac{J}{s}$)	0
C_{sample} ($\frac{J}{kg*K}$)	4190

Thermovision parameters	
Emissivity (-)	0.90 / 0.96
Camera angle (°)	7
Distance (m)	0.2
Humidity (%) (laboratory)	~50
Air temperature (°C)	23
Reflected temperature (°C)	23

Droplet experiment:

Main parameters	
Type of excitation	Continuous wave
Laser power (mW)	~115
Density power ($\frac{W}{cm^2}$)	235
Laser contact surface (mm^2)	0.049
Q_0 ($\frac{J}{s}$)	0
C_{sample} ($\frac{J}{kg*K}$)	4190

Thermovision parameters	
Emissivity (-)	0.9
Camera angle (°)	0
Distance (m)	0.1
Humidity (%) (chamber)	~80
Air temperature (°C)	23
Reflected temperature (°C)	23

Table S2 Detailed data of experiments performed in cuvette, the ± values are standard deviation of the obtained results.

Exp.	dT	Abs [-]	I [mW]	Tau decay [s]	Tau rise [s]	Sample mass [g]	a (Wang)	Efficiency – Roper (m=mass of sample + stirrer bar if used)		Effective mass of the cuvette [g]	Efficiency – Wang (effective mass)	
Side 1	4.62	0.417	198.9	613.5	579.8	2.02	0.00808	51.8	50.8 ± 1.6	4.42 ± 0.25	77.8	79.4 ± 1.7
Side 2	4.65	0.417	197.6	617.3	558.6	2.00	0.00842	51.7			81.0	
Side 3	4.56	0.417	197.1	632.9	551.9	1.98	0.00830	49.0			79.5	
Top 1	5.87	0.421	199.7	591.7	545.7	2.01	0.01088	67.3	67.6 ± 0.4	-1.16 ± 0.77	66.3	65.1 ± 2.0
Top 2	5.98	0.421	199.9	584.8	544.9	1.97	0.01111	67.9			66.2	
Top 3	6.04	0.421	198.6	588.2	568.0	1.94	0.01067	67.5			62.9	
Side Stirring 1	4.83	0.402	201.0	574.7	598.6	2.01	0.00808	59.8	57.5 ± 2.3	4.08 ± 1.05	78.5	80.5 ± 2.0
Side Stirring 2	4.67	0.402	200.4	581.4	552.7	2.01	0.00846	57.3			82.4	
Side Stirring 3	4.70	0.402	203.9	595.2	561.8	2.01	0.00842	55.3			80.6	
Top Stirring 1	5.08	0.421	201.2	546.4	512.6	2.01	0.00999	64.2	63.1 ± 1.2	2.02 ± 0.36	80.9	80.6 ± 0.3
Top Stirring 2	4.96	0.421	197.2	549.5	506.3	1.99	0.00985	63.1			80.6	
Top Stirring 3	4.99	0.421	197.7	552.5	505.7	1.96	0.00996	62.0			80.3	

Table S3. Detailed results of Wang's effective mass calibration experiment. For all experiments the same cuvette (6.5g) has been used. Values of specific heat capacity included in calculations were: c (H_2O)= 4180 $\frac{J}{kg*K}$; c (quartz glass) = 729 $\frac{J}{kg*K}$; c (PCV - tape) = 1172 $\frac{J}{kg*K}$. Resistance was evaluated as a product of voltage and current minus input wire resistance, ± values are standard deviation of obtained results.

Exp.	I [A]	R [ohm]	P = RI^2 [W]	Sample mass [g]	Tape mass [g]	Stirrer bar mass [g]	a (Wang)	Effective mass of the cuvette [g]	Effective mass of the cuvette [g]
Side 1	0.32	0.35863	0.03672	2.020	0.171	0	0.00312	4.26	4.42 ± 0.25
Side 2	0.69	0.35749	0.17020	2.001	0.171	0	0.01437	4.47	
Side 3	1.00	0.36300	0.36300	2.018	0.171	0	0.03098	4.20	
Side 4	0.50	0.36900	0.09225	2.013	0.171	0	0.00763	4.74	
Side Stirring 1	1.01	0.36280	0.37009	2.016	0.171	0.197	0.03033	4.56	4.08 ± 1.05
Side Stirring 2	0.50	0.37100	0.09275	2.009	0	0.197	0.00747	5.17	
Side Stirring 3	0.67	0.36987	0.16603	2.008	0.171	0.197	0.01468	3.38	
Side Stirring 4	0.50	0.36900	0.09225	2.014	0.171	0.197	0.00775	4.16	
Side Stirring 5	0.36	0.38744	0.05021	2.025	0.168	0.197	0.00403	4.85	
Side Stirring 6	0.35	0.39014	0.04779	2.012	0.168	0.197	0.00452	2.35	
Top Stirring 1	0.93	0.38816	0.33572	2.012	0	0.197	0.03204	2.49	2.02 ± 0.36
Top Stirring 2	0.99	0.38138	0.37379	2.008	0	0.197	0.03672	2.11	
Top Stirring 3	0.68	0.39153	0.18104	2.013	0	0.197	0.01823	1.74	
Top Stirring 4	0.51	0.39006	0.10145	2.019	0	0.197	0.00990	2.14	
Top Stirring 5	0.38	0.38774	0.05599	2.013	0	0.197	0.00569	1.61	
Top 1	0.91	0.38586	0.31953	2.006	0	0	0.04502	-1.79	-1.16 ± 0.77
Top 2	0.50	0.37500	0.09375	2.008	0	0	0.01156	-0.42	
Top 3	0.66	0.38694	0.16855	1.998	0	0	0.02266	-1.28	
Top 4	0.35	0.38586	0.04727	2.008	0	0	0.00679	-1.99	
Top 5	0.98	0.38178	0.36666	1.998	0	0	0.04508	-0.33	

Table S4. Detailed data of experiment performed in droplet setup; the ± values are standard deviation of the obtained results.

Exp.	**dT**	**Abs [-]**	**I [mW]**	**Tau decay [s]**	**Tau rise [s]**	**Sample mass [µg]**	**a (Wang)**	**Efficiency – Wang [%]**	**Efficiency – Roper [%]**
Drop 1	8.41	0.167	115.6	21.2	17.0	13.7	0.493	85.9	69.3
Drop 2	8.86	0.180	117.5	21.1	17.4	14.1	0.509	83.1	68.5
Drop 3	8.62	0.175	117.2	21.5	17.5	14.4	0.492	80.4	65.6
Drop 4	8.44	0.182	113.3	21.6	18.4	14.4	0.456	76.7	65.7
Drop 5	8.66	0.182	118.0	21.8	17.8	14.1	0.484	79.5	65.1
mean	8.60 ±0.19	0.177 ±0.007	116.3 ±2.0	21.4 ±0.3	17.6 ±0.6	14.1 ±0.3	0.487 ±0.020	81.1 ±3.6	66.8 ±2.0

Elaboration of experimental errors on calculations of light to heat conversion efficiency in the droplet configuration

Equation (6), which is used to determine light-to-heat conversion efficiency, was supplemented with Q_0 - heat flow induced by absorption of light by solvent:

$$\eta = \frac{a \sum mc_p - Q_0}{I\left(1 - 10^{-A_\lambda}\right)} \tag{S1}$$

The measurement error was estimated using the total differential method:

$$\Delta\eta = \left|\frac{d\eta}{da}\right| \Delta a + \left|\frac{d\eta}{d\sum mc_p}\right| \Delta \sum mc_p + \left|\frac{d\eta}{d\mathrm{Q}_0}\right| \Delta \dot{Q}_0 + \left|\frac{d\eta}{dI}\right| \Delta I + \left|\frac{d\eta}{dA_\lambda}\right| \Delta A_\lambda \tag{S2}$$

$$\frac{d\eta}{da} = \frac{\sum mc_p}{I\left(1 - 10^{-A_\lambda}\right)} \tag{S3}$$

$$\frac{d\eta}{d\sum mc_p} = \frac{a}{I\left(1 - 10^{-A_\lambda}\right)} \tag{S4}$$

$$\frac{d\eta}{d\mathrm{Q}_0} = -\frac{1}{I\left(1 - 10^{-A_\lambda}\right)} \tag{S5}$$

$$\frac{d\eta}{dI} = -\frac{a \sum mc_p - \dot{\mathrm{Q}}_0}{\left(1 - 10^{-A_\lambda}\right) * I^2} \tag{S6}$$

$$\frac{d\eta}{dA_\lambda} = \frac{\left(a \sum mc_p - \dot{\mathrm{Q}}_0\right) * 10^{A_\lambda} * \log 10}{I * \left(10^{A_\lambda} - 1\right)^2} \tag{S7}$$

The uncertainty of determination of the components of the equation was estimated based on the following considerations:

- Δa – standard error from fitting curve (Δa_{SE}) plus uncertainty of temperature determination (Equation S9); Equation S8 was transformed into a form:

  $$a = \frac{b(T(t) - T_0)}{1 - e^{-bt}} = \frac{bT}{1 - e^{-bt}} \tag{S8}$$

  $$\Delta a = \Delta a_{SE} + \left|\frac{da}{db}\right| \Delta b_{SE} + \left|\frac{da}{dT}\right| \Delta T + \left|\frac{da}{dt}\right| \Delta t \tag{S9}$$

  Here, also time of conducting experiment is included, meaning for *t* heading to infinity, the temperature difference should be established with greatest accuracy, but it is reasonable to conduct measurement by up to $4\tau = 4/b$, to minimize its impact.

$$\frac{da}{db}=\frac{T*e^{bt}\left(-1+e^{bt}-bt\right)}{\left(e^{bt}-1\right)^{2}}\cong T \tag{S10}$$

$$\frac{da}{dT}=\frac{b}{1-e^{-bt}}\cong b \tag{S11}$$

$$\Delta t\cong 0 \tag{S12}$$

Due to the high temporal resolution (Δt = 0.03s), this part of equation could be also neglected.

$$\Delta a=\Delta a_{SE}+T*\Delta b_{SE}+b*\Delta T \tag{S13}$$

- $\Delta\sum mc_p$

$$\Delta\sum mc_p=m_{drop}*\Delta c_{p,drop}+c_{p,drop}*\Delta m_{drop} \tag{S14}$$

- $\Delta\dot{Q}_0$

$$\dot{Q}_0=a_0\sum mc_p \tag{S15}$$

$$\Delta\dot{Q}_0=a_0*\Delta\sum mc_p+\sum mc_p*\Delta a_0 \tag{S16}$$

- ΔI=0,03*I

  Measurement error of laser power is mostly governed by the optical power meter accuracy (3%).

- ΔA_λ – Absorbance measurement error

  From Lambert-Beer's law:

$$A_\lambda=\log\frac{I_w}{I_s} \tag{S17}$$

  where I_w and I_s are light transmission of water and sample,

$$\Delta A_\lambda=\frac{\Delta I_w}{I_w*\ln(10)}+\frac{\Delta I_s}{I_s*\ln(10)}=\frac{I_w*0{,}03}{I_w*\ln(10)}+\frac{I_s*0{,}03}{I_s*\ln(10)}=0{,}026 \tag{S18}$$

Estimating the experimental parameters

- $Q_0=0, a_0=0, \Delta a_0=\Delta a$

  We did not observe heating of water while irradiating with a 532 nm beam

- $\Delta m_{drop}=6\ \mu g$

  Estimated resolution of determining the mass of droplet by thermal imaging camera visualization with improved edge determination (fitting the droplet edge data with a logistic curve)

- ΔT = 0.1 ^{0}C

  Estimated resolution of temperature differential measurements by thermal imaging camera with improved accuracy (artefacts eliminated by subtracting the background signal)

$$\Delta\eta = \left|\frac{d\eta}{da}\right|\Delta a + \left|\frac{d\eta}{d\sum mc_p}\right|\Delta\sum mc_p + \left|\frac{d\eta}{d\mathrm{Q}_0}\right|\Delta\dot{\mathrm{Q}}_0 + \left|\frac{d\eta}{dI}\right|\Delta I + \left|\frac{d\eta}{dA_\lambda}\right|\Delta A_\lambda \cong 39.5\%$$

$$\Delta\eta = 1.1\% \quad + \quad 31.4\% \qquad + \quad 1.0\% \quad + \quad 2.2\% \; + \; 3.8\% \qquad \cong 39.5\%$$

The analysis of errors, shows that the precision of the drop weight estimation based on its image has the greatest impact on the precision of the droplet volume determination. The reason for such a high value is the fact that the end of the tip with a diameter of 0.9 + 0.1 mm is used as a scale for determining the drop volume. The accuracy of the measurement can be therefore increased by using an independent, more accurate scale placed in the field of view.

Chen's model

Chen et al [1] firstly proposed an easy to reproduce experimental setup: a sample is in a spectrophotometric cuvette and the temperature of the sample is homogenous because of a use of a magnetic stirrer during experiments. Energy balance is the same as in equation (1), only the heat connected with solution was included in Q_L:

$$Q_L = I(1-\xi)(1-10^{-A_\lambda})\eta \tag{S19}$$

In opposite to I from Roper's model[2], here I is a is the reflection-corrected laser power, ξ is a fraction of energy absorbed by surroundings (cuvette and water) and A_λ is extinction value, Energy dissipated from the system was modeled by a Taylor series of ΔT:

$$Q_{ext} = B\Delta T + C\Delta T^{2} \tag{S20}$$

B and C were evaluated from cooling data (when $Q_L = 0$), similarly than in Roper's model,

$$\left(m_s c_{p,s} + m_c c_{p,c}\right)\frac{d\Delta T}{dt} = -B\Delta T - C(\Delta T)^2 \tag{S21}$$

Finally, light to heat conversion efficiency is:

$$\eta = \frac{B(T_{max} - T_{amb}) + C(T_{max} - T_{amb})^2 - I\xi}{I(1-\xi)\left(1-10^{-E_\lambda}\right)} \tag{S22}$$

Table S5. Comparison of existing physical models

	Roper [2] (cuvette)	**Richardson [3] (droplet)**	**Wang [4] (cuvette + stirring + "mass calibration")**
Standard setup description	Sample inside the sealed glass cell/cuvette	Droplet on the syringe	Stirred sample inside the sealed glass cell/cuvette
Efficiency equation	$\frac{\sum_i m_i C_{p,i}(T_{max} - T_{amb})}{\tau_c * I(1 - 10^{-A_\lambda})} - \frac{Q_0}{I(1 - 10^{-A_\lambda})}$	$\frac{m_w C_{p,w}(T_{max} - T_{amb})}{\tau_c * I(1 - 10^{-A_\lambda})}$	$\frac{a \sum_i m_i C_{p,i}}{I(1 - 10^{-A_\lambda})}$
Heat transfer processes included in model	Convection and conduction (no geometry included)	Convection of a sample	Convection (spontaneous) and conduction
Most important physical processes in the setup	Sample – convection Glass – conduction Glass-air – convection (eliminated when measured in a vacuum)	Sample – convection Syringe – conduction	Sample – forced convection Glass – conduction Glass-air - convection
Additional problems	Geometry of a system is not included in the model	Evaporation of a sample	Stirring not included in the model

(1) Chen, H.; Shao, L.; Ming, T.; Sun, Z.; Zhao, C.; Yang, B.; Wang, J. Understanding the Photothermal Conversion Efficiency of Gold Nanocrystals. *Small* **2010**, *6* (20), 2272–2280. https://doi.org/10.1002/smll.201001109.

(2) Roper, D. K.; Ahn, W.; Hoepfner, M. Microscale Heat Transfer Transduced by Surface Plasmon Resonant Gold Nanoparticles. *J. Phys. Chem. C* **2007**, *111* (9), 3636–3641. https://doi.org/10.1021/jp064341w.

(3) Richardson, H. H.; Carlson, M. T.; Tandler, P. J.; Hernandez, P.; Govorov, A. O. Experimental and Theoretical Studies of Light-to-Heat Conversion and Collective Heating Effects in Metal Nanoparticle Solutions. *Nano Lett.* **2009**, *9* (3), 1139–1146. https://doi.org/10.1021/nl8036905.

(4) Wang, X.; Li, G.; Ding, Y.; Sun, S. Understanding the Photothermal Effect of Gold Nanostars and Nanorods for Biomedical Applications. *RSC Adv.* **2014**, *4* (57), 30375–30383. https://doi.org/10.1039/C4RA02978J.

URZĄD PATENTOWY
RZECZYPOSPOLITEJ POLSKIEJ

al. Niepodległości 188/192
00-950 Warszawa, skr. poczt. 203
tel.: (+48) 22 579 05 55 | fax: (+48) 22 579 00 01
e-mail: kontakt@uprp.gov.pl | www.uprp.gov.pl

Departament Biotechnologii i Chemii

Warszawa, 18.10.2022r.

Nasz znak: DB.P.437330.6.jgaj
Wasz znak: 47580/20

DECYZJA

Na podstawie art. 24 i art. 52 ustawy z dnia 30 czerwca 2000r. Prawo własności przemysłowej (Dz. U. z 2021 r. poz. 324) Urząd Patentowy RP po rozpatrzeniu zgłoszenia oznaczonego numerem **P.437330** dokonanego w dniu **2021-03-17** udziela na rzecz:
INSTYTUT NISKICH TEMPERATUR I BADAŃ STRUKTURALNYCH IM. WŁODZIMIERZA TRZEBIATOWSKIEGO POLSKIEJ AKADEMII NAUK, Wrocław, Polska

PATENTU

na wynalazek(i) pt.:
Układ pomiarowy oraz sposób do wyznaczania sprawności konwersji światła z zakresu VIS i NIR na ciepło w nanomateriałach koloidalnych

pod warunkiem uiszczenia opłaty w wysokości **480zł**. za I okres ochrony wynalazku(ów) rozpoczynający się w dniu **2021-03-17** i obejmujący 1-3 rok ochrony*.

Podstawa prawna: art. 224 ust. 1 ustawy Prawo własności przemysłowej oraz pkt II ppkt 1 tabeli opłat stanowiącej załącznik nr 1 do rozporządzenia Rady Ministrów z 8 września 2016 r. zmieniającego rozporządzenie w sprawie opłat związanych z ochroną wynalazków, wzorów użytkowych, wzorów przemysłowych, znaków towarowych, oznaczeń geograficznych i topografii układów scalonych (Dz. U. z 2001 r. Nr 90, poz. 1000, z 2004 r. Nr 35, poz. 309, z 2008 r. Nr 41, poz. 241 oraz z 2016 r. poz. 1623).

Urząd Patentowy RP wzywa do wniesienia tej opłaty **w ciągu trzech miesięcy od dnia doręczenia decyzji**.

W razie nieuiszczenia wskazanej opłaty w wyznaczonym terminie Urząd Patentowy RP, na podstawie art. 52 ust. 2 ustawy Prawo własności przemysłowej stwierdzi wygaśnięcie decyzji o udzieleniu patentu.

Od niniejszej decyzji stronie przysługuje wniosek o ponowne rozpatrzenie sprawy przez Urząd Patentowy RP w terminie dwóch miesięcy od dnia jej doręczenia. Opłata za wniosek o ponowne rozpatrzenie sprawy wynosi 100 złotych i jest uiszczana na konto Urzędu. Jeżeli strona nie chce skorzystać z prawa do wniesienia wniosku o ponowne rozpatrzenie sprawy, może wnieść za pośrednictwem Urzędu skargę do Wojewódzkiego Sądu Administracyjnego w Warszawie w terminie 30 dni od dnia doręczenia stronie przedmiotowej decyzji. Opłata za wpis od skargi wynosi 1000 złotych i jest uiszczana na konto Sądu. Strona może ubiegać się na podstawie przepisów ustawy Prawo o postępowaniu przed sądami administracyjnymi o zwolnienie od kosztów sądowych albo o przyznanie prawa pomocy.

Na podstawie art. 227 ustawy Prawo własności przemysłowej oraz pkt I ppkt 12 powołanej tabeli opłat Urząd Patentowy RP wzywa do wniesienia w terminie trzech miesięcy opłaty w wysokości **220zł** za publikację o udzieleniu patentu.

Otrzymuje(ą):
rzecz. pat. Iwona Płodzich-Hennig
JWP RZECZNICY PATENTOWI
DOROTA RZĄŻEWSKA SP. K.
ul. Żelazna 28/30
00-833 Warszawa

Jolanta Gajewska
Ekspert
/podpisano kwalifikowanym podpisem elektronicznym/

Pismo wydane w formie dokumentu elektronicznego

*** Pouczenie**
Jeżeli w chwili wydania decyzji rozpoczął się kolejny okres ochrony wynalazku (kolejne lata), a Zgłaszający chce przedłużyć ochronę na te okresy (te lata), powinien łącznie z opłatą za I okres ochrony, wymienioną wyżej, wnieść opłatę za następne okresy - art. 224 ust. 1 ustawy Prawo własności przemysłowej.

INFORMACJA

1. Patent trwa 20 lat od daty zgłoszenia.

2. Opłatę za okres ochrony wskazany w decyzji oraz opłaty za następne okresy ochrony wynalazku należy uiszczać przelewem, przekazem pocztowym lub gotówką na rachunek Urzędu Patentowego RP:

URZĄD PATENTOWY RP NBP O/O Warszawa Nr 93 1010 1010 0025 8322 3100 0000

Przy uiszczaniu opłaty niezbędne jest wyraźne wskazanie jej tytułu (numeru zgłoszenia lub patentu, tytułu wynalazku(ów), okresu(ów) ochrony). Opłaty dotyczące poszczególnych zgłoszeń lub patentu(ów) uiszcza się oddzielnymi przekazami lub przelewami.

3. Opłaty za następne okresy ochrony należy wnieść najpóźniej w ostatnim dniu upływającego okresu ochrony.

4. Opłaty okresowe, o których mowa w punkcie 3, mogą być uiszczone w ciągu jednego roku przed terminem określonym w punkcie 3. Opłaty te można również uiszczać w terminie sześciu miesięcy po upływie terminu określonego w punkcie 3, przy jednoczesnym uiszczeniu opłaty dodatkowej w wysokości 30% opłaty należnej. **Termin ten nie podlega przywróceniu.**

5. Pełnomocnikiem w postępowaniu przed Urzędem Patentowym może być tylko rzecznik patentowy. Pełnomocnikiem osoby fizycznej (z wyjątkiem osób, które nie mają miejsca zamieszkania na obszarze Rzeczypospolitej Polskiej) może być również współuprawniony, a także rodzice, małżonek, rodzeństwo lub zstępni strony oraz osoby pozostające ze stroną w stosunku przysposobienia.

6. Podstawą do dokonania opłaty jest niniejszy dokument – Urząd nie wystawia rachunków (faktur).

7. Aktualnie obowiązujące stawki opłat za ochronę wynalazków (Dz.U. z 2016 r. poz. 1623)

Za pierwszy okres ochrony obejmujący 1,2 i 3 rok ochrony – 480,00 zł.
Za 4 rok ochrony wynalazku - 250,00 zł.
Za 5 rok ochrony wynalazku – 300,00 zł.
Za 6 rok ochrony wynalazku – 350,00 zł.
Za 7 rok ochrony wynalazku – 400,00 zł.
Za 8 rok ochrony wynalazku – 450,00 zł.
Za 9 rok ochrony wynalazku – 550,00 zł.
Za 10 rok ochrony wynalazku – 650,00 zł.
Za 11 rok ochrony wynalazku – 750,00 zł.
Za 12 rok ochrony wynalazku – 800,00 zł.
Za 13 rok ochrony wynalazku – 900,00 zł.
Za 14 rok ochrony wynalazku – 950,00 zł.
Za 15 rok ochrony wynalazku – 1050,00 zł.
Za 16 rok ochrony wynalazku – 1150,00 zł.
Za 17 rok ochrony wynalazku – 1250,00 zł.
Za 18 rok ochrony wynalazku – 1350,00 zł.
Za 19 rok ochrony wynalazku – 1450,00 zł.
Za 20 rok ochrony wynalazku – 1550,00 zł.

8. Art. 41 § 1 Kodeksu postępowania administracyjnego stanowi, iż w toku postępowania strony oraz ich przedstawiciele i pełnomocnicy mają **obowiązek zawiadomić** organ administracji publicznej **o każdej zmianie swego adresu**. W razie **zaniedbania** obowiązku określonego wyżej **doręczenie** pisma pod dotychczasowym adresem **ma skutek prawny**, tzn. że z przepisu art. 41 § 2 kpa wynika domniemanie prawidłowego doręczenia pisma.

W celu weryfikacji autentyczności korespondencji zeskanuj podany kod QR lub przejdź na stronę weryfikacji korespondencji Urzędu Patentowego RP dostępnej pod adresem **https://eprofil.pue.uprp.gov.pl/public/stamp/verify** i przepisz kod stempla.

Kod stempla: 84c-96c6-96a

DZIAŁ G

FIZYKA

A1 (21) **437330** (22) 2021 03 17

(51) *G01N 21/17* (2006.01)
G01K 11/00 (2006.01)
B01L 3/00 (2006.01)

(71) INSTYTUT NISKICH TEMPERATUR
I BADAŃ STRUKTURALNYCH
IM. WŁODZIMIERZA TRZEBIATOWSKIEGO
POLSKIEJ AKADEMII NAUK, Wrocław

(72) PAŚCIAK AGNIESZKA; BEDNARKIEWICZ ARTUR;
MARCINIAK ŁUKASZ

(54) **Układ pomiarowy oraz sposób do wyznaczania sprawności konwersji światła z zakresu VIS i NIR na ciepło w nanomateriałach koloidalnych**

(57) Przedmiotem zgłoszenia jest układ pomiarowy do pomiarów efektywności konwersji światła na ciepło w materiałach koloidalnych posiadający układ optyczny zawierający źródło światła, układ soczewek do formowania skupionej wiązki światła, element półprzepuszczalny, miernik mocy optycznej wiązki światła, komorę z próbką formowaną do postaci kropli, miernik referencyjnej mocy optycznej i kamerę termowizyjną charakteryzujący się tym, że komora (10) ma umieszczony centralnie system dozowania próbki SD przyjmującej formę kropli (8) składający się z wymiennej końcówki (9), uchwytu XYZ (12), dozowników (14, 15) i zaworu (16), gdzie wymienna końcówka (9) połączona jest od góry z uchwytem XYZ (12), przy czym przestrzeń między komorą (10) a uchwytem XYZ (12) ma uszczelnienie (11) oraz w płaszczyźnie obrazowania kropli jest umieszczona skala (13), gdzie system dozowania próbki SD wytwarza krople o zadanej objętości i pozycji względem układu optycznego obejmującego elementy zgłoszenia od (1) do (7) i kamery termowizyjnej (18). Przedmiotem zgłoszenia jest także sposób pomiaru konwersji światła na ciepło realizowany przy pomocy wspomnianego układu pomiarowego.

(9 zastrzeżeń)

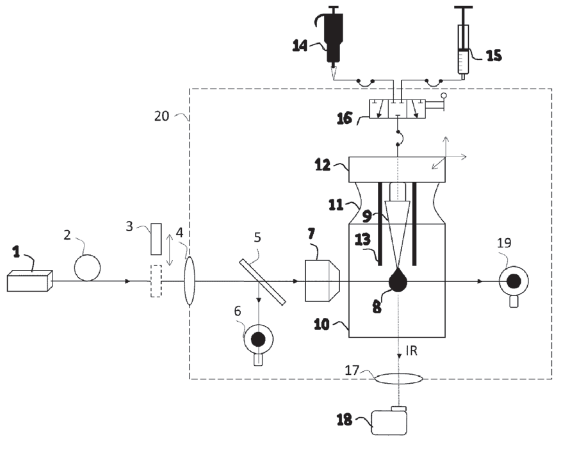

A1 (21) **437283** (22) 2021 03 12

(51) *G01N 33/569* (2006.01)
G01N 21/45 (2006.01)

(71) POLITECHNIKA GDAŃSKA, Gdańsk

(72) MAJCHROWICZ DARIA; WITYK PAWEŁ;
SZCZERSKA MAŁGORZATA; LISTEWNIK PAULINA;
TEREBIENIEC AGATA

(54) **Zestaw do wykrywania wirusa SARS-CoV-2 i sposób funkcjonalizacji głowicy pomiarowej**

(57) Przedmiotem wynalazku jest zestaw do wykrywania wirusa SARS-CoV-2 zawierający głowicę pomiarową sprzężoną z sprzęgaczem światłowodowym, korzystnie jednomodowym, do którego na wejściu przyłączone jest źródło światła poprzez światłowód, korzystnie jednomodowy, a na wyjściu przyłączony jest układ detekcji w postaci analizatora widma optycznego, a źródłem światła jest źródło szerokopasmowe o krótkiej drodze koherencji, charakteryzujący się tym, że układ pomiarowy stanowi głowica pomiarowa będąca mikrosferą optyczną (5) ze sfunkcjonalizowaną powierzchnią, natomiast w głowicy pomiarowej (5) powierzchnie odbijające promieniowanie optyczne stanowią granice ośrodków: rdzeń (6) światłowodu zakończonego mikrosferą - płaszcz (7) światłowodu zakończonego mikrosferą oraz płaszcz (7) światłowodu zakończonego mikrosferą - badane medium otaczające mikrosferę, gdzie generowany jest sygnał interferencyjny. Przedmiotem wynalazku jest również sposób funkcjonalizacji głowicy pomiarowej, którą jest mikrosfera (5), charakteryzujący się tym, że mikrosfera (5) poddana jest kolejno chemisorpcji, utworzeniu warstwy SAM, dalej biotynylacji, w roztworze NHS-LC-biotyny w dimetylosulfotlenku (DMSO). W kolejnym etapie mikrosferę (5) umieszcza się w roztworze białka S wirusa SARS-CoV-2 znakowanego awidyną.

(2 zastrzeżenia)

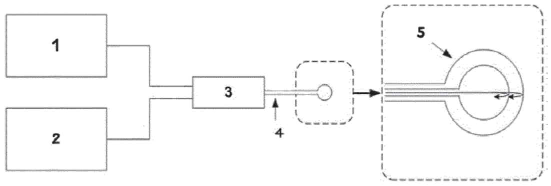

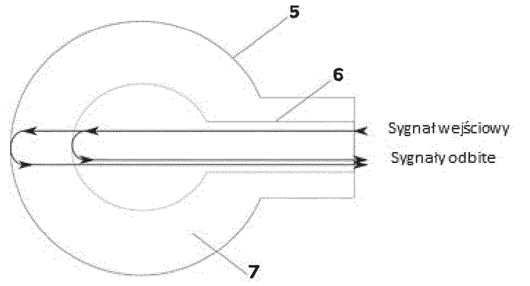

A1 (21) **437284** (22) 2021 03 12

(51) *G01N 33/569* (2006.01)
G01N 21/45 (2006.01)

(71) POLITECHNIKA GDAŃSKA, Gdańsk

(72) SZCZERSKA MAŁGORZATA; TEREBIENIEC AGATA;
LISTEWNIK PAULINA; MAJCHROWICZ DARIA;
WITYK PAWEŁ

(54) **Zestaw do wykrywania wirusa SARS-CoV-2 i sposób funkcjonalizacji głowicy pomiarowej**

(57) Przedmiotem wynalazku jest zestaw do wykrywania wirusa SARS-CoV-2 zawierający głowicę pomiarową sprzężoną z sprzęgaczem światłowodowym, korzystnie jednomodowym, do którego na wejściu przyłączone jest źródło światła poprzez światłowód, korzystnie jednomodowy, a na wyjściu przyłączony jest układ detekcji w postaci analizatora widma optycmego, a źródłem światła jest źródło szerokopasmowe o krótkiej drodze koherencji, charakteryzujący się tym, że układ pomiarowy stanowi głowica pomiarowa interferometru Fabry-Perot (5) ze sfunkcjonalizowaną powierzchnią czoła światłowodu (4), natomiast w głowicy pomiarowej (5) powierzchnie odbijające promieniowanie optyczne stanowią granice ośrodków: sfunkcjonalizowane czoło światłowodu (4) – badane medium otaczające oraz badane medium otaczające - warstwa odbijająca (8), którą jest lustro, gdzie generowany jest sygnał interferencyjny. Przedmiotem wynalazku jest również sposób funkcjonalizacji głowicy pomiarowej, charakteryzujący się tym, że czoło światłowodu (4) poddane jest kolejno chemisorpcji, utworzeniu warstwy SAM,

ACS APPLIED MATERIALS & INTERFACES

www.acsami.org

Research Article

Quantitative Comparison of the Light-to-Heat Conversion Efficiency in Nanomaterials Suitable for Photothermal Therapy

Agnieszka Paściak, Riccardo Marin, Lise Abiven, Aleksandra Pilch-Wróbel, Małgorzata Misiak, Wujun Xu, Katarzyna Prorok, Oleksii Bezkrovnyi, Łukasz Marciniak, Corinne Chanéac, Florence Gazeau, Rana Bazzi, Stéphane Roux, Bruno Viana, Vesa-Pekka Lehto, Daniel Jaque, and Artur Bednarkiewicz*

Cite This: *ACS Appl. Mater. Interfaces* 2022, 14, 33555−33566

Read Online

ACCESS | Metrics & More | Article Recommendations | Supporting Information

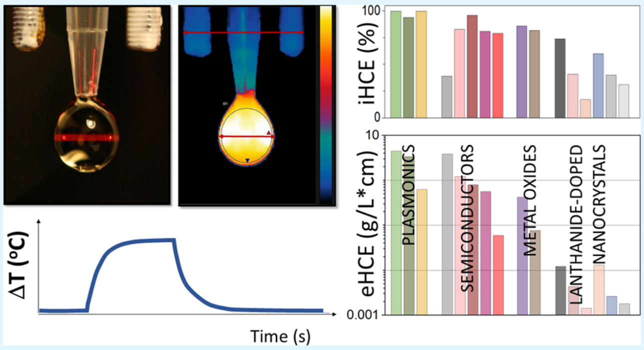

ABSTRACT: Functional colloidal nanoparticles capable of converting between various energy types are finding an increasing number of applications. One of the relevant examples concerns light-to-heat-converting colloidal nanoparticles that may be useful for localized photothermal therapy of cancers. Unfortunately, quantitative comparison and ranking of nanoheaters are not straightforward as materials of different compositions and structures have different photophysical and chemical properties and may interact differently with the biological environment. In terms of photophysical properties, the most relevant information to rank these nanoheaters is the light-to-heat conversion efficiency, which, along with information on the absorption capacity of the material, can be used to directly compare materials. In this work, we evaluate the light-to-heat conversion properties of 17 different nanoheaters belonging to different groups (plasmonic, semiconductor, lanthanide-doped nanocrystals, carbon nanocrystals, and metal oxides). We conclude that the light-to-heat conversion efficiency alone is not meaningful enough as many materials have similar conversion efficiencies—in the range of 80−99%—while they significantly differ in their extinction coefficient. We therefore constructed their qualitative ranking based on the external conversion efficiency, which takes into account the conventionally defined light-to-heat conversion efficiency and its absorption capacity. This ranking demonstrated the differences between the samples more meaningfully. Among the studied systems, the top-ranking materials were black porous silicon and CuS nanocrystals. These results allow us to select the most favorable materials for photo-based theranostics and set a new standard in the characterization of nanoheaters.

KEYWORDS: *photothermal conversion efficiency, nanoheaters, photothermal treatment, gold nanoparticles, lanthanide-doped nanomaterials, porous silicon, semiconductor nanocrystals*

1. INTRODUCTION

Photothermal conversion nanoparticles, referred to as nanoheaters (NHs), allow one to increase the temperature of their surroundings in a spatially localized and contactless manner, which opens new opportunities in many areas. For example, optical NHs can be applied in technology areas such as solar light energy harvesting, photocatalysts or photoactuators,[1] as well as in biotechnology in the treatment of dentin hypersensitivity[2] or antibacterial therapy.[3,4] Additionally, NHs have shown great prospects in cancer photothermal therapy (PTT),[5] especially after the first report of the successful application of NHs in clinical trials for the treatment of prostate cancer.[6] Depending on the temperature range, the PTT takes advantage of the fact that, unlike healthy cells, cancer cells are specifically more sensitive to overheating beyond 41 °C (hyperthermia range), or the affected cells are damaged by thermal ablation (temperatures above 48 °C).[7]

Despite the great interest and significant progress in the field of optically stimulated heating nanomaterials, there are numerous factors, materials, and methods to be optimized to enable practical applications of PTT in clinics. First of all, as for any nanomaterial-based therapeutic and diagnostic approach, the NH's cytotoxicity must be verified before it could be considered for clinical trials.[8−10] Also, NHs should accumulate and reside in targeted tissues long enough to enable conducting efficient therapy. Moreover, the suitable NHs for PTT should ideally be biodegradable or excretable,

Received: May 6, 2022
Accepted: July 1, 2022
Published: July 18, 2022

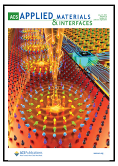

https://doi.org/10.1021/acsami.2c08013

which would ensure better biosafety.[11] Moreover, the safety of stimulus must be assured—in particular, a light dose and appropriate wavelength must ensure safe and deep treatment. For example, to overcome the absorption of water and tissue components, the most appropriate approach is to select NHs whose absorption lies in one of the biological spectral windows (e.g., NIR-I: 700−980 nm, NIR-II: 1000−1400 nm).[7] Among them, the first biological window, NIR-I, is preferable due to the significantly lower absorption of water at the PTT photoexcitation wavelengths. From the photophysics and materials science perspective, NHs should exhibit a high absorption coefficient at the irradiation wavelength and high light-to-heat conversion efficiency (i.e., internal light-to-heat conversion efficiency; iHCE), which is defined as the capability to convert the absorbed energy specifically into heat. Moreover, their size should not exceed 200 nm to avoid undesired effects, which might appear after injection, such as thrombus, occlusions, or kidney blocks.[12] Knowledge of these physical parameters allows for an initial assessment of the suitability of the material as a PTT NH before conducting critical experiments on animals and clinical trials.

Different classes of NHs have been already proposed, including organic (e.g., dyes,[13−15] polymers[16,17]) and inorganic systems. In the latter class, typical materials are plasmonic nanoparticles (e.g., AuNPs,[18−20] Ag NPs,[21] $Cu_{2-x}S$[22]), semiconductors (e.g., quantum dots,[23] silicon-based nanoparticles,[24] or titanium-based nanoparticles[25]), and lanthanide-doped nanoparticles,[26,27] along with carbon[13,28,29] and metal oxide[11,30] NHs. Given the differences in their physicochemical properties, there is an urgent need for a comparison of various nanomaterials in view of their different morphologies, sizes, surface chemistries as well as physical and chemical compositions or properties such as iHCE.

iHCE conventionally determines how much of the absorbed ultraviolet, visible, or near-infrared (UV/vis/NIR) radiation will be converted into heat. Typically, Roper's model is used for that purpose, which is based on the spontaneous cooling profile.[31] However, in our previous work,[32] we proved that the analysis of the heating profile (Wang's model[20]) leads to more consistent results for various measurement configurations. In Wang's model, in the case of negligible heating of the solvent, the iHCE is determined from the equation

$$\text{iHCE} = \frac{a \cdot \sum m_i \cdot C_{p,i}}{P \cdot (1 - 10^{-A_\lambda})} \tag{1}$$

where $\sum m_i \cdot C_{p,i}$ is a sum of the product of the effective mass and heat capacity of sample and experimental system components, $P[W]$ is the power of the laser beam illuminating the sample, and A_λ is the absorbance of the sample. The parameter $a[K/s]$ describes how the temperature of a sample changes per unit time under the influence of absorbed energy, and the parameter $b[1/s]$ is the rate constant. These parameters are determined by fitting the growing part of the heating−cooling kinetic profiles with the equation

$$T(t) = T_0 + \frac{a}{b}[1 - e^{-bt}] \tag{2}$$

Because iHCE is often determined with arbitrary and not justified assumptions (e.g., considering the mass of a sample holder instead of the effective mass of the NH), which leads to disparate results for the same material,[32] it is necessary to be able to qualitatively compare the available materials using a standardized method. We demonstrated that the droplet-based measuring system not only requires a small amount of sample but also offers time-efficient measurement unlike most other conventional systems. Using the setup and methods developed previously,[32] in this work, we performed a systematic and quantitative comparison of colloidal, light-to-heat-converting NHs belonging to different classes aiming to rank them according to their iHCE. It must be clearly stated that these various NHs convert the delivered photoexcitation energy to heat, exploiting various physical mechanisms (discussed in Section 3). In particular, we have examined various classes of NH colloidal nanoparticles:

(i) Plasmonic: gold nanorods (AuNRs) and copper sulfide coated by glutathione (CuS@GSH) and by citrate (CuS@cit);
(ii) Lanthanide-doped nanoparticles: Nd, Nd/Sm, and Nd/Dy codoped $NaYF_4$ nanoparticles;
(iii) Semiconductor: silver sulfide NHs covered by polyethylene glycol (Ag_2S@PEG), dithiolated diethylenetriamine pentaacetic acid (Ag_2S@DTDTPA), mercaptoundecanoic acid (Ag_2S@MUA), Ag-Ag_2S dimers, and black porous silicon (BPSi);
(iv) Carbon: carbon dots (CDs); and
(v) Metal oxide: maghemite γ-Fe_2O_3 and maghemite nanoflowers decorated with gold nanoparticles Au: γ-Fe_2O_3-Au.

In the course of the study, we realized that the iHCE, which is an internal heating efficiency, is not sufficient to rank the NH materials for practical applications in PTT. Therefore, an external heating efficiency (eHCE) figure of merit was proposed, similar to the brightness in photoluminescence metrology. Moreover, to understand which factors can affect the efficiency of light-to-heat conversion for selected NHs, we examined different coatings and codoping in the case of rare earth ions. For materials with broad absorption bands, we have systematically determined how the iHCE and eHCE depend on wavelength, which may enhance the understanding of their physical properties and will also allow for optimal wavelength selection for therapy purposes.

2. MATERIALS AND METHODS

2.1. Synthesis Procedures. Since an extensive range of materials is presented in this paper, descriptions of the synthesis and a list of the reactants used are included in the Supporting Information (Descriptions S1 and S2).

2.2. Material Characterization. The morphology of the samples, AuNRs, $NaNdF_4$:Dy@PAA, and carbon dots, on the one hand, and Ag_2S, γ-Fe_2O_3, and of γ-Fe_2O_3-Au, on the other hand, was determined by transmission electron microscopy (TEM), using a Philips CM-20 Super-Twin instrument operating at 160 kV and an FEI Tecnai Spirit G2 instrument at an acceleration voltage of 120.0 kV, respectively. Before the measurement, samples were diluted with a suitable solvent and dispersed in an ultrasonic bath; then, a droplet of the suspension was deposited on a copper grid coated with a carbon film. BPSi was imaged with high-resolution transmission electron microscopy (HR-TEM) (JEOL JEM2100F). The morphologies of samples CuS and Ag-Ag_2S were investigated using a transmission electron microscope (TEM, JEOL JEM1400 Flash) operating at 100 kV. For TEM observations, the particles were precipitated with isopropanol (iPrOH), recovered by means of centrifugation (30,000*g* for 20 min at 4 °C), and washed once with a mixture of water and iPrOH, before being redispersed in water.

Powder diffraction data of AuNRs, $NaNdF_4$:Dy@PAA, and C-dots were collected on an X'Pert PRO X-ray diffractometer equipped with

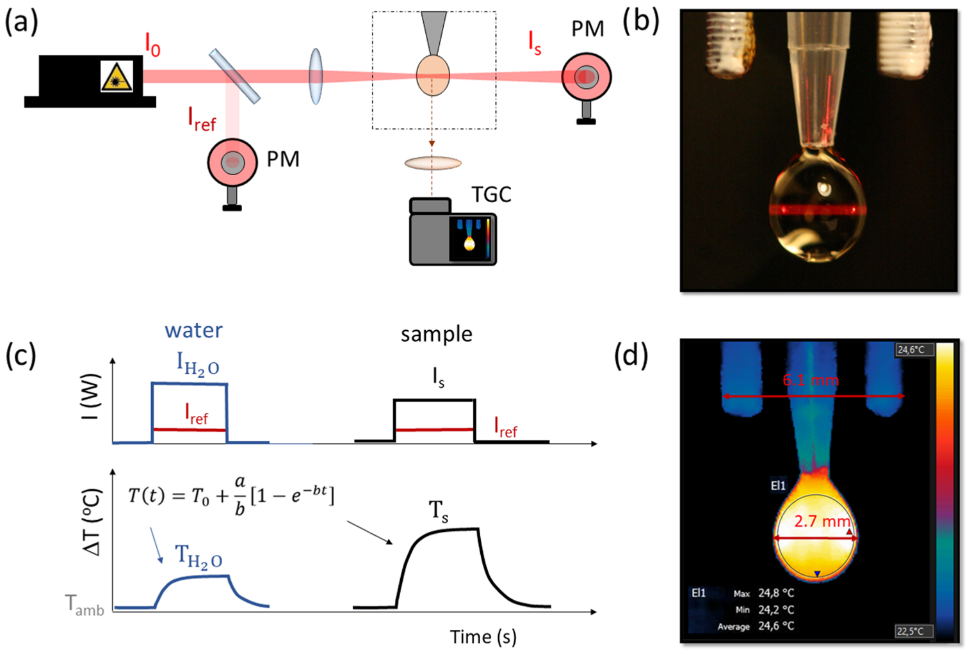

Figure 1. Schematic setup and methodology for measuring the efficiency of light-to-heat conversion of colloidal nanomaterials. (a) Experimental "droplet" setup (PM, power meter; TGC, thermographic camera). (b) Photography of a typical droplet irradiated by a 668 nm laser beam. (c) Exemplary data analysis. The graph above shows the optical power behind a drop of sample (I_s) or water I_{H_2O} and the reference power (I_{ref}) measured simultaneously. The temperature rise (graph below) in the sample (T_s) water colloid and the solvent itself (T_{H2O}) must be known to evaluate the light-to-heat conversion efficiency. (d) Typical image of a droplet during heating; a scale is visible above the droplet—elements with a measured distance of 6.1 mm.

a PIXcel ultrafast line detector, a focusing mirror, and soller slits for Cu Kα radiation. The XRD profiles of BPSi and γ-Fe_2O_3 were measured using Cu Kα radiation on a Bruker D8 Advance; in the case of BPSi, measurements were performed with a zero-background sample holder. For Ag_2S diffractometer Bruker D8 discover equipped with a EIGER2 R 500K 2D detector was used. For CuS and Ag-Ag_2S nanoparticles, X-ray powder diffraction (XRPD) measurements were performed on a Rigaku D/max-γB diffractometer working in the Bragg–Brentano geometry (θ–2θ) with a step of 0.03° in the 20–60° range. A filtered Cu Kα radiation (λ = 1.5418 Å) was used.

Absorption spectra were obtained in the transmission mode using a Cary Varian 5E UV–vis–NIR spectrometer. In the UV region and the vis/NIR region, a deuterium and a halogen lamp were, respectively, used as excitation sources. In the UV and visible ranges, the R928 photomultiplier was used as a detector, and a cooled PbS detector was used for the NIR region. For CuS and Ag-Ag_2S nanoparticles, optical extinction spectra were recorded at room temperature with a UV–vis–NIR spectrophotometer (Perkin Elmer Lambda1050) using a 3 nm step.

Sample concentration was estimated by synthesis conditions when it was possible (in the case of Ln^{3+}-doped materials, CDs, CuS, γ-Fe_2O_3-Au), by redox titration of Fe^{3+} using $Cr_2O_7^{2-}$ for γ-Fe_2O_3, or by evaporating and weighing the material (AuNRs, BPSi, Ag_2S, Ag-Ag_2S).

2.2.1. Light-to-Heat Conversion Efficiency Measurements: Procedure. The iHCE (calculated as will be defined in chapter 2.3) was evaluated in a miniaturized setup,[32] shown schematically in Figure 1a, which requires only approximately 10 μL of sample. Droplet (Figure 1b,d) volumes within different experiments were typically within the 12–15 μL range and were smaller (6–9 μL) if the surface tension of the sample was less than that of water. However, within one experiment, care was taken to ensure that the difference between the volume of the sample droplet and the volume of the water droplet (reference) was less than 0.5 μL. The photoexcitation beam spot diameter was approximately 1 mm^2, and the optical path (droplet diameter) was up to 3 mm. The following continuous-wave laser diodes were used (all from Changchun New Industries Optoelectronics Technology Co., Ltd.): 400 nm (100 mW), 445 nm (1.5 W), 532 nm (1 W), 668 nm (1 W), 793 nm (3 W), 808 nm (2 W), 940 nm (2 W), 980 nm (10 W), and 1060 nm (2 W). The kinetic, time-resolved temperature profiles were registered by a thermographic camera (FLIR T540, accuracy ±0.5 °C with a reference, thermal sensitivity <40 mK, 24° @ 30 °C). Optical power behind the sample and the reference power were evaluated with two power meters (photodiode S120C head and PM100USB power meter, Thorlabs). The radiation power was 90 mW or less (above 40 mW) for wavelengths >900 nm to minimize overheating of the water in this range. Samples were diluted to obtain a temperature rise in the 1–5 °C range. The selected power is an experimentally determined optimum value (see Figure S1: power dependence of internal HCE and eHCE). The 120 mW and higher illumination power iHCEs are poorly reproducible (due to the dilution of the sample causing small and hard-to-determine absorbance value), while measurements at lower powers mean that the sample must be concentrated, which may affect the droplet density and result in the inability to maintain a stable droplet at the tip.

Measurements were conducted in a humidity chamber to minimize evaporation of the droplet. The humidity was found to be critically important to keep the volume of the droplet constant over ca. 8 min of experiment under laser illumination and heat generation. To prove it, we conducted an experiment in which we illuminated water drops of the same volume with a 980 nm laser beam at 90 mW for a time corresponding to standard measurements, but one measurement was carried out in a humidity chamber and the other in the external humidity conditions of the laboratory room (about 65%). In the first case, the droplet shrunk by less than 2%, while in the second case, the droplet volume was 7% lower at the end of the experiment. In addition, at low humidity, the temperature of the droplet (visualized by a thermal imaging camera) is lower than the ambient temperature, which is due to its evaporation and can lead to an incorrect temperature reading and ultimately to incorrect result evaluations (Figure S2).

The procedure of setup alignment and droplet formation has been described in our previous report.[32] Briefly, the droplet was formed,

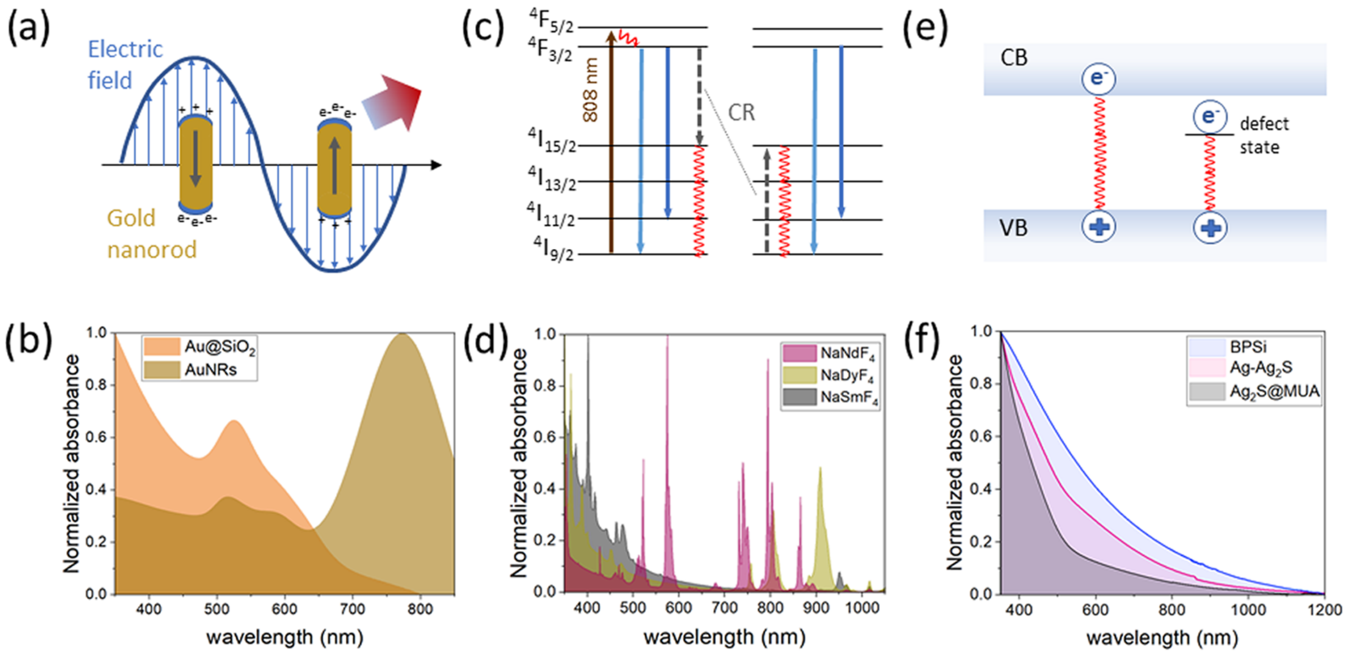

Figure 2. Mechanisms of heat generation and absorption spectra in different classes of NHs. (a) Localized surface plasmon resonance in plasmonic NHs. (b) Absorption spectra of gold nanospheres and gold nanorods. (c) Cross-relaxation in Nd^{3+} ions, which is the heat generation explanation for Nd^{3+} ions. (d) Absorption spectra of $NaNdF_4$, $NaDyF_4$, and $NaSmF_4$ nanoparticles dispersed in chloroform. (e) Mechanism of heat generation in semiconductors. (f) Absorption spectra of semiconductor nanocrystals investigated in this study.

positioned, and photographed on a contrasting background to precisely determine its size. Afterward, it was sealed inside a humidity chamber and left to stabilize its temperature for 5 min. Simultaneously, the laser was turned on to stabilize, but the beam was still blocked. Then, recordings by a thermographic camera and power meters were started. After 30 s, the laser beam was uncovered and the heating profile was registered during 2 min (Figure 1c). Then, the laser was turned off and the cooling curve profile was registered for up to 3 min. At the end of the recording of the thermal transient, an additional photograph was acquired to confirm the initial measurement of the droplet size.

2.2.2. Data Analysis. The droplet size was determined from thermographic camera data in thermographic camera FLIR Tools software: the number of pixels forming a drop was determined by home-made software (i.e., height and variable diameter), and based on the scale bar (visible in the field of view), the real droplet volume was calculated. The temperature was averaged from the whole available droplet surface excluding edges (pixels in the temperature range between the real temperature of the droplet and the temperature of the background). Since the inherent thermographic camera accuracy is 2 °C, we made efforts to improve this value by concurrently taking the reference measurement of a background, which remained at a constant temperature. We have subtracted this reference value, captured on the same picture, to minimize artifacts originating from the electronic noise of the camera. As we have verified, this operation allowed one to increase the accuracy of the temperature measurement with the thermal imaging camera to less than about 0.5 °C. Data from FLIR Tools and Thorlabs optical power meters were exported and then analyzed in Origin 2019 software. A similar example of data analysis using Microsoft Excel and ImageJ software is shown in the Supporting file.

2.3. Methodology of Light-to-Heat Conversion Efficiency Evaluation. The calculations were performed based on the Wang model[20] under the assumption that in a droplet system the effective mass of the system was the mass of the droplet (it has been shown that results obtained in this way correspond to the results of measurements in a cuvette with an independently determined effective mass).[32] When the heating of the solvent is not negligible, it is necessary to subtract the associated term ($\dot{Q}_0$). If the heat from heating the solvent itself is not subtracted, the efficiency in that case could exceed 100%, since the denominator of eq 1 takes into account the absorbance, which is measured with a water reference. Because of this consideration, we have calculated the iHCE from the following equation

$$\mathrm{HCE} = \frac{a\cdot m_{\mathrm{d}}\cdot C_{p,\mathrm{d}} - \dot{Q}_0}{P(1-10^{-A_\lambda})} = \frac{(a_{\mathrm{s}}-a_0)\cdot m_{\mathrm{d}}\cdot C_{p,\mathrm{d}}}{P(1-10^{-A_\lambda})} \tag{3}$$

The parameters a_0 and a_s were both evaluated in the same way from the heating profile of the sample and the solvent, respectively, whereas the mass of the droplets of the dispersion or the solvent alone was considered equal. Care was taken to obtain the solvent droplets as close in size as possible to the sample drops.

The iHCE, by itself, does not give information on how much of the supplied energy was converted into heat (i.e., external conversion efficiency) but provides information on only how much of the absorbed energy has been converted into heat (i.e., internal conversion efficiency). Laser radiation can not only be absorbed but also be scattered, reflected, or refracted by the material. In laboratory practice, the extinction coefficient is used, which is the sum of the absorption and scattering coefficients

$$\mu = \mu_{\mathrm{abs}} + \mu_{\mathrm{sca}} \tag{4}$$

If the scattering coefficient of the material has a large contribution, this introduces an additional error that results in a reduction of the calculated iHCE. The photons that are actually scattered could be erroneously included, while only the absorbed ones should be considered. Second, the light energy absorbed by some materials can be naturally emitted as photons. The presence of a finite value of photoluminescence quantum yield (PLQY) intrinsically limits the capability of the material to convert absorbed photons into heat. However, from a practical point of view, it is also necessary to consider the absorption properties to determine the required material concentration and to select the radiation dose. For this reason, we propose a new efficiency measure for NHs, external HCE, which takes into account both the iHCE determined so far and the mass absorption coefficient a, which allows for quantitative characterization of the material. eHCE represents how much of the incident pump power is transformed into heat.

$$\mathrm{eHCE} = \mathrm{HCE}\cdot a \tag{5}$$

The mass absorption coefficient can be determined from Lambert–Beer's law written in the mass form

$$a_\lambda = \frac{A_\lambda}{\rho L} \tag{6}$$

where A_λ is the absorbance at a given wavelength, ρ is the mass concentration (mg/mL), and L is the optical path (cm). The absorbed pump power could be underestimated for highly scattering samples, which however we were avoiding by proper surface modifications (to form stable colloids). We chose the mass coefficient instead of the molar coefficient because in the case of nanoparticles, the accurate determination of the molar concentration is challenging due to the presence of a finite size distribution and possible inhomogeneity in the particle composition (as is the case for the Ag-Ag_2S dimers herein studied). Moreover, when biomedical applications such as PTT are sought after, mass concentrations are usually preferred over molar ones.

3. LIGHT-TO-HEAT CONVERSION MECHANISMS

The most common mechanism of light-to-heat conversion relies on multiphonon relaxation of the excited states (Figure 2). After irradiation of the material, excitation from the ground state to the excited state occurs, which is followed by relaxation via internal conversion and vibrational relaxation to the lowest excited singlet state (for organic molecules), valence band (in semiconductors), or ground state (in lanthanides). This former mechanism may be preceded by singlet → triplet energy intersystem crossing or energy/charge exchange, which are competitive to radiative processes responsible for the reemission of the delivered energy in the form of photons. There is also a possibility of heat generation via the surface plasmon resonance process, which is typical for metallic NHs.

Plasmonic NHs are generally metallic nanomaterials that convert electromagnetic energy into heat through the surface plasmon resonance process. More specifically, heating is caused by a joule dissipation of oscillating electrons (Figure 2a). Surface plasmon resonance depends on the size and morphology of the nanoparticles.[18,20,33] These differences are evident in the extinction spectra; for example, gold nanoparticles in the form of nanospheres have one absorption peak between 500 and 600 nm, whereas for larger nanoparticles, the maximum is red-shifted.[33] Position of the peak far from NIR-I makes it of limited use in photothermal therapy. In contrast, gold nanorods have two absorption peaks (Figure 2b), one in a similar range as nanospheres, corresponding to the transverse mode, and a second, stronger absorption peak located in the near-infrared, corresponding to the longitudinal mode. Gold NHs in other shapes, such as nanostars, nanoshells, bipyramids, hexapods, and others, have also been designed to achieve absorption in a different range or to improve the iHCE.[34] It was demonstrated that the efficiency is higher for nanorods than for nanostars[20] and that the iHCE decreases with increasing nanoparticle size, which can be explained by the increased scattering of incident photons on these nanostructures. Lindley and Zhang have shown that smooth hollow gold nanospheres show a slightly higher efficiency than bumpy ones.[18] In addition to gold and silver NHs, $Cu_{2-x}S$s,[22] despite being semiconductors, also exhibit plasmonic properties due to free charge carriers. However, in this case, in place of free electrons in the conduction band, free vacancies occur at the top of the valence band. The plasmonic materials we have included in our study are AuNRs, CuS@GSH, and CuS@cit.

Lanthanide-ion-doped NHs have been primarily exploited for bioimaging and luminescence thermometry due to their rich energy-level diagrams, nonblinking and nonbleaching luminescence, long luminescence lifetimes, and narrowband absorption (Figure 2d) and emission, but they also show some promise for heat generation.[35−40] Lanthanide-doped nanocrystals in general show high stability and low toxicity and can be easily functionalized;[35] however, their absorption cross section is typically low, and because of that, it is debatable if they are suitable for PTT. Strategies to address the issues related to poor absorption cross sections by, e.g., conjugating them to "antennas" (plasmonic, dyes, etc.) are still under development.[41] An important example of materials that meet the requirements necessary in biomedicine is NHs doped with neodymium ions.[36,37] The advantageous feature of this ion is the location of its excitation band in NIR-I (i.e., ~808 nm) and emission in both NIR-I and NIR-II (ca. 860, 1060, and 1300 nm). Pioneering work in the use of neodymium-doped nanomaterial not only as an excellent emitter but also as an NH was performed in 2010 by Bednarkiewicz et al.[36] On the other hand, the first team to use neodymium for ex vivo studies was Rocha et al. in 2014.[38] Since then, many attempts have been made to use rare-earth-doped nanocrystals as heaters, including studies on animals.[39,42−44] In the case of the Nd^{3+} ion, the mechanism causing heat generation is the concentration quenching of $\{^4F_{3/2}, {}^4I_{9/2}\} \leftrightarrow \{^4I_{15/2}, {}^4I_{15/2}\}$ through cross-relaxation transitions and through a subsequent series of nonradiative multiphonon depopulation steps of higher excited states (Figure 2c).[40] This mechanism is probably responsible for the conversion of light to heat in the $NaYF_4$-based materials we studied.

For semiconductor nanocrystals, heat generation is due to the nonradiative recombination of free electrons and holes (Figure 2e)[45] and intraband nonradiative deexcitations. For NHs in the quantum dot regime, absorption and emission strictly depend on NH size, which is due to the quantum confinement.[46] Even though quantum dots have a good long-term photostability and chemical stability,[23] some of them display photoblinking and certain compositions can be cytotoxic.[10] In this work, we study Ag_2S, which is in the quantum dot regime. However, the biosafety risks could be reduced by surface passivation and its biofunctionalization[47] or by selecting Pb- or Cd-free compositions (e.g., $CuInS_2$, Ag_2S, etc.). Among the semiconductors, porous silicon deserves special attention because silicon is commonly found in tissues as a trace element and is present in, e.g., drinking water; thus, it can be simply absorbed and excreted safely.[48] Moreover, porous silicon has a large specific area and its surface could be easily biofunctionalized[40] for drug loading and biotargeting.[49] Herein, we included black porous silicon for which the proposed heat conversion mechanism is nonradiative carrier recombination.[50]

Carbon NHs are used primarily in solar energy applications. For photothermal therapy, carbon dots (CDs) deserve special attention due to their small size; moreover, CDs are characterized by their easy surface functionalization and good dispersibility and, importantly, for their biomedical applications, low toxicity, and good biocompatibility.[51] Due to the numerous mobile π-electrons, strong electron−electron scattering and weak electron−phonon interactions occur. It was speculated that π-electrons act similarly to the free

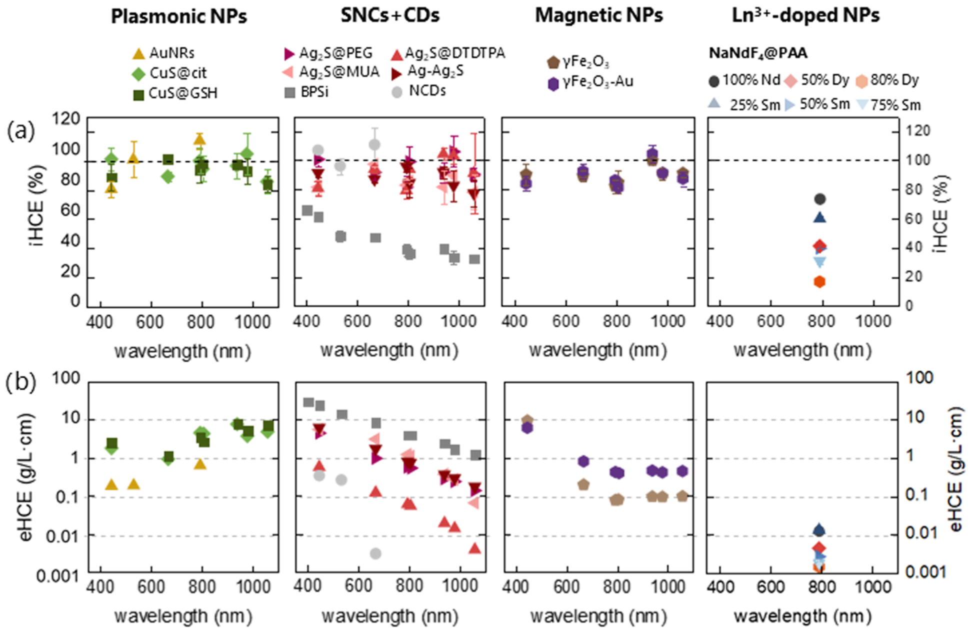

Figure 3. Ranking of the nanoheaters studied in this work. (a) Light-to-heat conversion efficiency as a function of wavelength. (b) External light-to-heat conversion efficiency as a function of wavelength.

electrons in metallic nanoclusters rather than semiconductor QDs.[52] However, CDs typically have absorption in the UV/vis range, and research is ongoing to develop techniques to shift the absorption toward the NIR. In our research, we included conventional CDs absorbing in UV and vis ranges.

Among the various metal oxide nanoparticles, those based on iron oxides are the most widely used for numerous applications. Iron oxide NHs are primarily known for their ability to generate heat under magnetic field stimulation, making them suitable for use in magnetic hyperthermia. However, these materials also exhibit high absorption capacities, making their use in photothermal therapy possible. Moreover, it has been shown that the therapy with optical excitation leads to better results for iron oxides, magnetite and maghemite.[53] There have also been reports of successful combinations of these two therapies, which synergistically improved the effectiveness of the therapy.[30] Iron oxide NHs are characterized by good biocompatibility and biodegradability.[54] For these NHs, the heat generation mechanism is not yet well understood.[55] Among the investigated NHs, the γ-Fe_2O_3-Au and γ-Fe_2O_3 belong to this group.

To quantitatively compare various colloidal nanoparticles for their suitability in PTT, we versatilely characterized their structural and spectroscopic properties and finally exploited a single optimized optical setup to measure iHCE.[32] Herein, iHCE and eHCE results obtained for each material and their wavelength dependence are presented, and the best NHs are discussed.

4. RESULTS AND DISCUSSION

4.1. Results by Materials. Plasmonic NHs are one of the most well-studied classes of NHs. We have determined the iHCE of 28.8 nm × 8.0 nm gold nanorods to be close to 100% (Figure 3 and Table S1) at 794 nm, which is similar to 94% for 63.8 nm × 24.5 nm nanorods measured by Wang et al.[20] AuNRs can therefore be regarded as one of the most effective light-to-heat-converting materials. Although for 532 and 794 nm the measured iHCE values exceed 100%, the material was stabilized by CTAB, which increased the viscosity of the sample and thus the droplet size needed to be reduced, which increased the measurement error. The different viscosity can affect the geometrical properties of the droplet, which translates into a change in optical properties and hence possibly introducing additional systematic error. To minimize this impact, the sample was diluted and a water droplet with a matching optical path was chosen as a reference.

For ca. 7−9 nm round-shaped CuS samples, which feature plasmonic properties similar to those of AuNRs, close to 100% iHCE was obtained. To understand whether the type of coating affects the iHCE, CuS coated with glutathione and citrate ions was studied at different excitation wavelengths. No significant difference between samples covered with glutathione and citrate was observed in the vis and NIR ranges, which is in agreement with the result obtained by Marin et al. at 806 nm.[22] Although the exact iHCE values differ (94−100 vs 71%), the discrepancy may be caused by varying assumptions about the effective mass of the measurement system, as well as differences in the optical path, since in the case of drops the optical path is shorter and therefore the influence of scattering is reduced.[22]

In our research on lanthanide NHs, we focused on the Nd^{3+} ion due to its well-understood and easily controllable photophysical properties of nanomaterials based on such an ion. Although neodymium-containing materials have already been published by many authors, the obtained results in the efficiency of converting light to heat have either not been quantified or simply significantly differ between different studies, from 9[44] to 85%[56] (see Table S2). As shown in the literature, the efficiency can be influenced by the size of the nanoparticle as well as the thickness and the type of coating,[56] and these also differ in various studies. The effect of coating is important because it functions as a thermal impedance.[57] Our results show an iHCE of 74% for the $NaNdF_4$ covered by PAA. To further progress with the understanding and optimization of Ln^{3+}-doped nanoheaters, we hypothesized that adding dysprosium or samarium ions could increase the iHCE because these ions have a dense ladder of energy levels through which nonradiative relaxation could occur. To verify this hypothesis, we conducted a series of measurements for $NaNdF_4$ materials doped with samarium and dysprosium ions (which were replacing Nd^{3+} ions in the pristine composition), coated with PAA for greater stability. As it turned out, the addition of a dopant did not have a positive effect: on the contrary, it caused a reduction in iHCE (Figure S3). The possible explanation is that the presence of samarium or dysprosium introduces additional energy diffusion that is unfavorable for heat generation, which occurs through cross-relaxation. Furthermore, by increasing the amount of Sm^{3+}/Dy^{3+} ions replacing Nd^{3+}, the Nd^{3+} ions are more distant from each other, reducing the possibility of cross-relaxation between them. Moreover, if the dopant replaces the dominant ion and does not absorb itself at the radiation wavelength, it reduces the absorption capacity of the NH designed in this way, which is undesirable.

Our results show that the attempt of adding a dopant instead of Nd^{3+} ions did not allow increasing the iHCE above 80%. This may partially explain the nonzero quantum yield, but it is not a complete explanation, as for highly doped NHs (25% Nd^{3+}), it is less than 5%.[58] Xu et al. recently showed that the iHCE decreases as the size of the nanoparticle increases (due to less surface quenching), and the effect is even more pronounced as the size increases after applying an inert coating due to better surface protection.[56] However, the coating of the PAA material was necessary to obtain the time-stable and reproducible materials.

Ag_2S nanoparticles are of increasing interest due to their large absorption cross section (3.46×10^{-22} cm^2 at 800 nm) and iHCE of 93%, according to the literature (Ag_2S with PEG coating).[59] In our work, we have investigated ca. 3−9 nm dot-shaped Ag_2S with different coatings: poly(ethylene glycol) (PEG), dithiolated diethylenetriamine pentaacetic acid (DTDTPA), mercaptoundecanoic acid (MUA), and Ag-Ag_2S dimers. We have observed that in all of these NHs, the iHCE is higher than 75%. We observed that at 794 nm the excitation iHCE is the highest for Ag_2S@MUA and the lowest for Ag_2S@DTDTPA. This difference could be partially explained by PLQY (Table S3): for Ag_2S@DTDPTA, the highest (0.66%) PLQY was observed. In addition, the coating can create impedance and induce differences between the temperature of the medium and the temperature of the nanoparticles;[57] hence, it can differentially affect the iHCE.

In our comparison, we include a representative of silicon materials as well, i.e., BPSi, which has an irregular shape with a diameter of around 190 nm (Figure S4). Similar conversion efficiencies to those of Xu et al.[24] at 806 nm (34% in the mentioned work and 36% on our measurement system) were obtained. We also proved that higher efficiencies could be obtained for shorter wavelengths, which suggests that this material can be useful in sunlight-based devices.[1]

To broaden the range of materials, we examined ca. 8 nm N-doped CDs. Their absorption (Figure S5) allowed us to measure iHCE only in the visible range. Our results have shown iHCE close to 100%. If the material does not exhibit luminescence and scatters poorly, a high (close to 100%) iHCE can be expected. Typically, the PLQY of CDs is on the order of a few percentage points[60] unless special efforts (e.g., doping) are taken to improve it, so the preferable pathways are nonradiative relaxations. Due to the large discrepancy in the literature regarding the PLQY of CDs, and the observation that our CDs also show some luminescence, we performed a PLQY measurement (Figure S6) and obtained a PLQY of 3.2% for 445 nm excitation. This means that in this case it can be assumed that almost all of the absorbed light energy is converted into heat and the artifacts from scattering are practically absent. An example of a work in which red light was used to excite CD nanoparticles was demonstrated by Ge et al.,[61] who obtained 38.5% iHCE and demonstrated in vivo studies on mice.[62] Similarly, Geng et al. presented nitrogen and oxygen codoped CDs with 38.3% iHCE at 808 nm.[63] Higher iHCE was obtained for supra-carbon nanodots: 52% for 732 nm and 53% for 808 nm.[64]

Our results for materials belonging to the iron oxide class show that both spherical γ-Fe_2O_3 and maghemite nanoflowers decorated with ultrasmall gold nanoparticles are characterized by high (>80%) iHCE. Diverse iHCEs for iron oxide NHs mentioned in the literature were obtained. Lozano-Pedraza et al.[55] presented that for iron oxides with a dominant maghemite phase, the NH size (in the range of 9−18 nm) does not significantly influence the iHCE, but different shapes result in different iHCEs. In contrast, Sadat et al.[65] showed a graph presenting the size dependence of different Fe_2O_3 NHs, where the iHCE decreased with the rise in NH size from ∼80% iHCE for 10 nm NHs covered by PAA to ∼30% for ∼100 nm NHs covered by PS to ∼18% for Fe_2O_3 beads.

A direct comparison of iHCE values with literature values is difficult because, first, iHCE is not always determined as an exact value and, second, when it is determined, it is often influenced by factors such as the position of the temperature sensor and assumptions considering the mass of the sample.[32] Furthermore, previous literature results were often obtained for other wavelengths and for materials that differ in morphology.

4.2. Selection of Therapeutic Wavelength.

It is preferable to perform PTT with absorption wavelengths falling into the biological windows. The reason for this choice stems from the lower absorption coefficient of water and of other components of biological tissues. Moreover, reduced light scattering occurs at longer wavelengths. Doing so, the light penetration depth can be extended significantly as compared to that achievable with shorter wavelengths. Usually, the excitation wavelengths are selected also depending on the NH absorption maxima because by using such wavelengths the greatest part of the excitation light can be absorbed. This is critically important for PTT because increasing the photoexcitation intensity is not possible beyond the permitted light dose exposure for a given tissue or skin; typically, under normal conditions, a maximum excitation power density of 330 mW/cm^2 is commonly accepted for tissue examination, but values of up to 2 W/cm^2 are used for PTT.[9] However, apart from the absorption capacity, it is also necessary to know the iHCE, which, as we show for some materials, strongly depends on the wavelength (Figure 3a).

The determination of such a correlation was only possible for materials with a broad absorption band. Although only NIR is primarily used for therapeutic purposes, knowing how efficiently photons of different energies are converted to heat can be useful also to understand the mechanisms of light-to-heat conversion. The most glaring example is BPSi, for which the iHCE is the highest at shorter wavelengths and follows a similar trend of the absorption spectrum. Thus, although the material converts absorbed ∼800 nm photons with iHCE close to 35%, for visible light, the iHCE is almost doubled while the absorption capability also increases. A similar effect was observed for silicon nanoparticles by Regli et al.[50] In that work, 488, 514, and 647 nm photoexcitation wavelengths were investigated and the iHCE decreased from 64 to 51%, which was explained by carrier thermalization contribution to photothermal effects. They also observed that photoluminescence intensity in this spectral range is higher at a longer wavelength; however, in the case of BPSi, no luminescence was observed.

In contrast, for the CuS, the iHCE as a function of wavelength does not change significantly. For this NH particle type, we can assume that the quantum yield is close to zero at all explored wavelengths. Similarly, for Ag_2S, Ag-Ag_2S dimers, AuNRs, γ-Fe_2O_3, and γ-Fe_2O_3-Au, no obvious wavelength dependence was observed. Different results were presented on the work on maghemite,[55] which showed wavelength dependence in the range of 700−1280 nm, and the iHCE almost doubled at the longest wavelength; however, these results were obtained for a material with different morphology and size. There are very few publications illustrating iHCE as a function of wavelength, while for materials that show no luminescence and where the impact of scattering on the results is negligible, we expect a constant value of iHCE.

4.3. Selection of the Most Effective Materials and Further Perspectives.

Selection of the best material is not a trivial task. Although Figure 3a shows that for most materials there is no wavelength dependence of iHCE, this is not always the case and providing the iHCE value requires specifying at which wavelength the value was determined. Moreover, because of the wavelength dependence of the absorption coefficient, eHCE is also strongly affected by the wavelength (Figure 3b). In Figure 4, we decided to limit the presentation of the iHCE and eHCE to 794 nm, which is generally considered an optimal wavelength for PTT. The numerical data are given in Table S1.

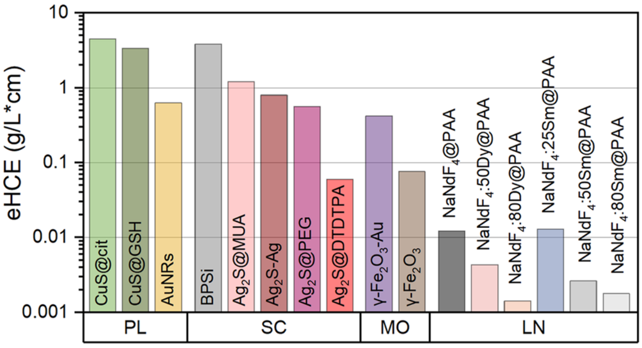

Figure 4. External light-to-heat conversion efficiency at 794 nm: ranking of nanoheaters investigated in this study.

From the eHCE results (Figure 3b), it can be seen that the vast majority of the materials studied shows the best properties for shorter wavelengths, in the visible range. This observation defines the first challenge for NHs dedicated to PTT, namely, to design new materials that provide a sufficiently high absorption coefficient for the NIR-I. Furthermore, as the wavelength increases, the absorption of water also increases, making heating no longer selective. The evidence for this may be the heating of a water droplet at the same power, which is negligible in the first optical window and significant above 900 nm (Figure S7). This obstacle defined the next challenge to search for NHs absorbing efficiently in the optical windows, e.g., at 800 nm. The importance of the absorption coefficient is clearly seen for BPSi, which, despite its relatively low iHCE, has the highest eHCE coefficient in the vis range. The probable reason for such outstanding absorption capacities is the porous structure of the material, which translates into its relatively lower mass at a similar volume. The highest eHCEs at NIR-I and NIR-II are observed for CuS. The reason for the increasing eHCE at longer wavelengths is the position of the maximum of absorption at 926/1037 nm (citrate/GSH coating). Ag_2S and Ag-Ag_2S dimers also reach high eHCEs in NIR-I. In the case of Ag_2S, the eHCE strongly depends on the coating; the value found for the DTDTPA coating is one order of magnitude lower than for MUA and PEG, and the highest values are observed for MUA. The discrepancies in the values observed for the different Ag_2S might stem from the following reasons: different size (hence different surface-to-volume ratio), different vibrational energy of the attached molecules, and different relative weight of the ligand shell vs the total weight of the sample (including the inorganic Ag_2S core and the ligand shell). The high eHCE of γ-Fe_2O_3-Au (0.420 L/(g·cm)) with regard to γ-Fe_2O_3 (0.076 L/(g·cm)) could be explained by the higher intensity of plasmonic coupling between the gold nanoparticles. For instance, it was reported that the optical specific absorption rate (SAR) values (see[30]) increase from 2940 W/g for γ-Fe_2O_3 up to 4581 W/g in γ-Fe_2O_3-Au,[66] and the value can be further controlled by linkers. In the present case, indeed, the plasmonic effect in gold nanoparticles enhanced the heat generation by enhancing the absorption capacity. The photothermal conversion depends on several material parameters such as size, shape, surface, aggregation status, etc., which can affect light absorption and scattering properties, which in turn can affect the heat generation or conversion efficiency. This creates additional difficulties in quantitatively comparing materials with different properties. Our intention was to select NHs with a variety of compositions and morphologies to show a comparison of as many materials as possible on the standardized experimental system. However, this is only a fraction of the numerous NHs already known.[1,7,12,40] We also speculate that many of the materials presented in numerous publications can achieve high iHCE scores and even higher eHCE values than the ones presented in this work. Moreover, the approach and methodology described in this work can also be used to compare other materials, including organic materials such as supramolecular assemblies,[67,68] amino acids,[69] and dyes, which are used in clinics (e.g., ICG;[14] or next-generation dyes, e.g., croconium dye[15]). In this case, scattering is unlikely to have a significant impact on iHCE. The only limitations of the proposed method relate to photobleaching, which makes it impossible to record a temperature rise curve consistent with the model, as well as the solvents' wetting angle must allow the forming of a droplet.

The proposed ways of comparing the NHs and the observed relative trends are envisaged to inform the design of NHs with the potential to be translated to the bedside as they allow us to unambiguously rank all of those different materials. Such a ranking should be supplemented in the future by studies of cytotoxicity, clearance kinetics, and biological interaction studies so that a reliable and versatile comparison of various NHs can help select the most appropriate candidate nanoheaters for PTT in vivo.

5. CONCLUSIONS

Advanced inorganic nanomaterials belonging to five different classes of materials were synthesized, and their iHCE values were measured using optimized and standardized experimental setups (with different laser diode light sources of the same light beam output). Most of the studied nanomaterials were found to display a high (>75%) light-to-heat conversion efficiency, which can be easily related to the low or absent luminescence. No significant effect of the laser wavelength on the iHCE was observed if the sample did not show scattering. Although one may claim that scattering leads to an underestimation of the iHCE, such materials will be less suitable for photothermal therapy due to the high risk of healthy tissues overheating and their lower absorptivity.

In contrast to expectations, for the $NaNdF_4$ nanoparticles codoped with rare earth ions (Sm^{3+}, Dy^{3+}), we found that the cross-relaxations and multiphonon relaxations within the Nd^{3+} network are nevertheless more efficient that quenching at those additional ions. For this class of materials, increasing their suitability for photothermal therapy by improving their absorption cross section still remains a challenge. The progress in augmenting the absorption in combination with the feasible single bifunctional (heating and local thermometry using core−shell compositional architectures) lanthanide-doped nanoparticles promises further development of functional PTT nanoplatforms.

Although much attention has been given to the determination of the iHCE of NHs, from the perspective of ranking different materials, it should be complemented by knowledge of the mass absorption coefficient because iHCE alone is not sufficient to select the optimal dose of material and optical power. Of all of the materials measured, BPSi has the best absorption capacity in the VIS spectral range, while in the NIR range, the most suitable for PTT, CuS shows the most promising properties, and their application would require the lowest NH and irradiation dose.

■ ASSOCIATED CONTENT

Supporting Information

The Supporting Information is available free of charge at https://pubs.acs.org/doi/10.1021/acsami.2c08013.

List of chemical reagents; description of syntheses; power dependence of internal HCE and eHCE; thermal images of droplets at/without increased humidity conditions; calculated iHCE and eHCE of measured samples at 794 nm; HCE of Nd^{3+}-doped nanomaterials (literature results' comparison); iHCE of $NaNdF_4$ as a function of the Sm^{3+}/Dy^{3+} dopant concentration; emission QY under 808 nm CW laser irradiation at distinct laser power densities; morphology of the NHs; absorption spectra of CDs, $NaNdF_4$ doped with Dy^{3+} and Sm^{3+}, Ag_2S, and γ-Fe_2O_3; QY measurement of CDs; temperature rise curves of a 13 μL water droplet for different wavelengths measured at constant irradiance power (90 mW); XRDs of the NHs; and a tutorial of data analysis using excel and ImageJ software (PDF)

Example analysis solver (XLSX)

■ AUTHOR INFORMATION

Corresponding Author

Artur Bednarkiewicz − *Institute of Low Temperature and Structure Research, Polish Academy of Sciences, 50-422 Wroclaw, Poland;* orcid.org/0000-0003-4113-0365; Email: a.bednarkiewicz@intibs.pl

Authors

Agnieszka Paściak − *Institute of Low Temperature and Structure Research, Polish Academy of Sciences, 50-422 Wroclaw, Poland;* orcid.org/0000-0002-3206-360X

Riccardo Marin − *Nanomaterials for Bioimaging Group (nanoBIG), Departamento de Física de Materiales, Facultad de Ciencias, Universidad Autónoma de Madrid, Madrid 28049, Spain;* orcid.org/0000-0003-3270-892X

Lise Abiven − *Sorbonne Université, CNRS, Laboratoire de Chimie de la Matière Condensée de Paris, UMR 7574, F-75005 Paris, France;* orcid.org/0000-0002-5467-2107

Aleksandra Pilch-Wróbel − *Institute of Low Temperature and Structure Research, Polish Academy of Sciences, 50-422 Wroclaw, Poland;* orcid.org/0000-0003-1991-4008

Małgorzata Misiak − *Institute of Low Temperature and Structure Research, Polish Academy of Sciences, 50-422 Wroclaw, Poland;* orcid.org/0000-0001-6163-1795

Wujun Xu − *Department of Applied Physics, University of Eastern Finland, 70211 Kuopio, Finland;* orcid.org/0000-0002-3177-4709

Katarzyna Prorok − *Institute of Low Temperature and Structure Research, Polish Academy of Sciences, 50-422 Wroclaw, Poland;* orcid.org/0000-0002-7444-796X

Oleksii Bezkrovnyi − *Institute of Low Temperature and Structure Research, Polish Academy of Sciences, 50-422 Wroclaw, Poland;* orcid.org/0000-0002-7069-9748

Łukasz Marciniak − *Institute of Low Temperature and Structure Research, Polish Academy of Sciences, 50-422 Wroclaw, Poland;* orcid.org/0000-0001-5181-5865

Corinne Chanéac − *Sorbonne Université, CNRS, Laboratoire de Chimie de la Matière Condensée de Paris, UMR 7574, F-75005 Paris, France;* orcid.org/0000-0001-9785-1052

Florence Gazeau − *Université Paris Cité, CNRS, F75006 Paris, France;* orcid.org/0000-0002-6482-3597

Rana Bazzi − *Institut UTINAM, UMR 6213 CNRS-UBFC, Université Bourgogne Franche-Comté, 25030 Besançon, France;* orcid.org/0000-0001-7274-6694

Stéphane Roux − *Institut UTINAM, UMR 6213 CNRS-UBFC, Université Bourgogne Franche-Comté, 25030 Besançon, France;* orcid.org/0000-0002-5198-1916

Bruno Viana − *Chimie ParisTech, CNRS, Institut de Recherche de Chimie Paris, PSL Research University, F-75231 Paris, France;* orcid.org/0000-0002-2959-862X

Vesa-Pekka Lehto − *Department of Applied Physics, University of Eastern Finland, 70211 Kuopio, Finland;* orcid.org/0000-0001-8153-1070

Daniel Jaque − *Nanomaterials for Bioimaging Group (nanoBIG), Departamento de Física de Materiales, Facultad de Ciencias, Universidad Autónoma de Madrid, Madrid 28049, Spain;* orcid.org/0000-0002-3225-0667

Complete contact information is available at: https://pubs.acs.org/10.1021/acsami.2c08013

Notes

The authors declare no competing financial interest.

■ ACKNOWLEDGMENTS

A.P., L.A., A.P.-W., M.M. C.C., F.G., L.M., B.V., and A.B. acknowledge the financial support from the FET OPEN 801305 project. K.P. acknowledges financial support from NCN, Poland, grant number 2018/31/D/ST5/01328. W.X. and V.L. acknowledge the funding support from the Academy of Finland (Grant No. 314412). R.B and S.R acknowledge financial support from the ISITE-BFC project (contract ANR-15-IDEX-0003, BIONANOCAR). This work was supported by the Ministerio de Ciencia e Innovación de España under grant PID2019-106211RB-I00 (R.M. and D.J.). The authors are also very grateful to Carlos Brites and Miguel Hernandez from Aveiro Institute of Materials (Aveiro University) for PLQY measurements of Ag_2S.

■ REFERENCES

(1) Kim, J. U.; Lee, S.; Kang, S. J.; Kim, T. Il. Materials and Design of Nanostructured Broadband Light Absorbers for Advanced Light-to-Heat Conversion. *Nanoscale* **2018**, *10*, 21555−21574.

(2) Gao, H.; Zhang, L.; Lian, X.; Wang, Y.; Jiang, S.; Wang, G.; Dai, X.; Zou, H.; Ding, D. A Dentin Hypersensitivity Treatment Using Highly Stable Photothermal Conversion Nanoparticles. *Mater. Chem. Front.* **2021**, *5*, 3388−3395.

(3) Zhang, S.; Lu, Q.; Wang, F.; Xiao, Z.; He, L.; He, D.; Deng, L. Gold-Platinum Nanodots with High-Peroxidase-like Activity and Photothermal Conversion Efficiency for Antibacterial Therapy. *ACS Appl. Mater. Interfaces* **2021**, *13*, 37535−37544.

(4) Xiao, Y.; Xu, M.; Lv, N.; Cheng, C.; Huang, P.; Li, J.; Hu, Y.; Sun, M. Dual Stimuli-Responsive Metal-Organic Framework-Based Nanosystem for Synergistic Photothermal/Pharmacological Antibacterial Therapy. *Acta Biomater.* **2021**, *122*, 291−305.

(5) Wang, S.; Ma, X.; Hong, X.; Cheng, Y.; Tian, Y.; Zhao, S.; Liu, W.; Tang, Y.; Zhao, R.; Song, L.; Teng, Z.; Lu, G. Adjuvant Photothermal Therapy Inhibits Local Recurrences after Breast-Conserving Surgery with Little Skin Damage. *ACS Nano* **2018**, *12*, 662−670.

(6) Rastinehad, A. R.; Anastos, H.; Wajswol, E.; Winoker, J. S.; Sfakianos, J. P.; Doppalapudi, S. K.; Carrick, M. R.; Knauer, C. J.; Taouli, B.; Lewis, S. C.; Tewari, A. K.; Schwartz, J. A.; Canfield, S. E.; George, A. K.; West, J. L.; Halas, N. J. Gold Nanoshell-Localized Photothermal Ablation of Prostate Tumors in a Clinical Pilot Device Study. *Proc. Natl. Acad. Sci. U.S.A.* **2019**, *116*, 18590−18596.

(7) Jaque, D.; Martínez Maestro, L.; del Rosal, B.; Haro-Gonzalez, P.; Benayas, A.; Plaza, J. L.; Martín Rodríguez, E.; García Solé, J. Nanoparticles for Photothermal Therapies. *Nanoscale* **2014**, *6*, 9494−9530.

(8) Gnach, A.; Lipinski, T.; Bednarkiewicz, A.; Rybka, J.; Capobianco, J. A. Upconverting Nanoparticles: Assessing the Toxicity. *Chem. Soc. Rev.* **2015**, *44*, 1561−1584.

(9) Ximendes, E.; Benayas, A.; Jaque, D.; Marin, R. Quo Vadis, Nanoparticle-Enabled in Vivo Fluorescence Imaging? *ACS Nano* **2021**, *15*, 1917−1941.

(10) Hardman, R. A Toxicologic Review of Quantum Dots: Toxicity Depends on Physicochemical and Environmental Factors. *Environ. Health Perspect.* **2006**, *114*, 165−172.

(11) Zhou, Z.; Wang, X.; Zhang, H.; Huang, H.; Sun, L.; Ma, L.; Du, Y.; Pei, C.; Zhang, Q.; Li, H.; Ma, L.; Gu, L.; Liu, Z.; Cheng, L.; Tan, C. Activating Layered Metal Oxide Nanomaterials via Structural Engineering as Biodegradable Nanoagents for Photothermal Cancer Therapy. *Small* **2021**, *17*, No. 2007486.

(12) Quarta, A.; Piccirillo, C.; Mandriota, G.; Di Corato, R. Nanoheterostructures (NHS) and Their Applications in Nanomedicine: Focusing on In Vivo Studies. *Materials* **2019**, *12*, No. 139.

(13) Jiang, R.; Cheng, S.; Shao, L.; Ruan, Q.; Wang, J. Mass-Based Photothermal Comparison among Gold Nanocrystals, PbS Nanocrystals, Organic Dyes, and Carbon Black. *J. Phys. Chem. C* **2013**, *117*, 8909−8915.

(14) Shirata, C.; Kaneko, J.; Inagaki, Y.; Kokudo, T.; Sato, M.; Kiritani, S.; Akamatsu, N.; Arita, J.; Sakamoto, Y.; Hasegawa, K.; Kokudo, N. Near-Infrared Photothermal/Photodynamic Therapy with Indocyanine Green Induces Apoptosis of Hepatocellular Carcinoma Cells through Oxidative Stress. *Sci. Rep.* **2017**, *7*, No. 13958.

(15) Gao, X.; Jiang, S.; Li, C.; Chen, Y.; Zhang, Y.; Huang, P.; Lin, J. Highly Photostable Croconium Dye-Anchored Cell Membrane Vesicle for Tumor PH-Responsive Duplex Imaging-Guided Photothermal Therapy. *Biomaterials* **2021**, *267*, No. 120454.

(16) Guo, L.; Liu, W.; Niu, G.; Zhang, P.; Zheng, X.; Jia, Q.; Zhang, H.; Ge, J.; Wang, P. Polymer Nanoparticles with High Photothermal Conversion Efficiency as Robust Photoacoustic and Thermal Theranostics. *J. Mater. Chem. B* **2017**, *5*, 2832−2839.

(17) Tas, C. E.; Berksun, E.; Koken, D.; Unal, S.; Unal, H. Photothermal Waterborne Polydopamine/Polyurethanes with Light-to-Heat Conversion Properties. *ACS Appl. Polym. Mater.* **2021**, *3*, 3929−3940.

(18) Lindley, S. A.; Zhang, J. Z. Bumpy Hollow Gold Nanospheres for Theranostic Applications: Effect of Surface Morphology on Photothermal Conversion Efficiency. *ACS Appl. Nano Mater.* **2019**, *2*, 1072−1081.

(19) Liao, Y.-T.; Liu, C.-H.; Chin, Y.; Chen, S.-Y.; Liu, S. H.; Hsu, Y.-C.; Wu, K. C.-W. Biocompatible and Multifunctional Gold Nanorods for Effective Photothermal Therapy of Oral Squamous Cell Carcinoma. *J. Mater. Chem. B* **2019**, *7*, 4451−4460.

(20) Wang, X.; Li, G.; Ding, Y.; Sun, S. Understanding the Photothermal Effect of Gold Nanostars and Nanorods for Biomedical Applications. *RSC Adv.* **2014**, *4*, 30375−30383.

(21) Wei, L.; Lu, J.; Xu, H.; Patel, A.; Chen, Z. S.; Chen, G. Silver Nanoparticles: Synthesis, Properties, and Therapeutic Applications. *Drug Discovery Today* **2015**, *20*, 595−601.

(22) Marin, R.; Skripka, A.; Besteiro, L. V.; Benayas, A.; Wang, Z.; Govorov, A. O.; Canton, P.; Vetrone, F. Highly Efficient Copper Sulfide-Based Near-Infrared Photothermal Agents: Exploring the Limits of Macroscopic Heat Conversion. *Small* **2018**, *14*, No. 1803282.

(23) Yang, J. M.; Yang, H.; Lin, L. Quantum Dot Nano Thermometers Reveal Heterogeneous Local Thermogenesis in Living Cells. *ACS Nano* **2011**, *5*, 5067−5071.

(24) Xu, W.; Tamarov, K.; Fan, L.; Granroth, S.; Rantanen, J.; Nissinen, T.; Peräniemi, S.; Uski, O.; Hirvonen, M. R.; Lehto, V. P. Scalable Synthesis of Biodegradable Black Mesoporous Silicon Nanoparticles for Highly Efficient Photothermal Therapy. *ACS Appl. Mater. Interfaces* **2018**, *10*, 23529−23538.

(25) Ou, G.; Li, Z.; Li, D.; Cheng, L.; Liu, Z.; Wu, H. Photothermal Therapy by Using Titanium Oxide Nanoparticles. *Nano Res.* **2016**, *9*, 1236−1243.

(26) Marciniak, L.; Pilch, A.; Arabasz, S.; Jin, D.; Bednarkiewicz, A. Heterogeneously Nd3+doped Single Nanoparticles for NIR-Induced Heat Conversion, Luminescence, and Thermometry. *Nanoscale* **2017**, *9*, 8288−8297.

(27) Shao, Q.; Li, X.; Hua, P.; Zhang, G.; Dong, Y.; Jiang, J. Enhancing the Upconversion Luminescence and Photothermal Conversion Properties of ∼800 Nm Excitable Core/Shell Nanoparticles by Dye Molecule Sensitization. *J. Colloid Interface Sci.* **2017**, *486*, 121−127.

(28) Romero-Aburto, R.; Narayanan, T. N.; Nagaoka, Y.; Hasumura, T.; Mitcham, T. M.; Fukuda, T.; Cox, P. J.; Bouchard, R. R.; Maekawa, T.; Kumar, D. S.; Torti, S. V.; Mani, S. A.; Ajayan, P. M. Fluorinated Graphene Oxide; A New Multimodal Material for Biological Applications. *Adv. Mater.* **2013**, *25*, 5632−5637.

(29) Sheng, Z.; Song, L.; Zheng, J.; Hu, D.; He, M.; Zheng, M.; Gao, G.; Gong, P.; Zhang, P.; Ma, Y.; Cai, L. Protein-Assisted Fabrication of Nano-Reduced Graphene Oxide for Combined Invivo Photoacoustic Imaging and Photothermal Therapy. *Biomaterials* **2013**, *34*, 5236−5243.

(30) Espinosa, A.; Di Corato, R.; Kolosnjaj-Tabi, J.; Flaud, P.; Pellegrino, T.; Wilhelm, C. Duality of Iron Oxide Nanoparticles in Cancer Therapy: Amplification of Heating Efficiency by Magnetic Hyperthermia and Photothermal Bimodal Treatment. *ACS Nano* **2016**, *10*, 2436−2446.

(31) Roper, D. K.; Ahn, W.; Hoepfner, M. Microscale Heat Transfer Transduced by Surface Plasmon Resonant Gold Nanoparticles. *J. Phys. Chem. C* **2007**, *111*, 3636−3641.

(32) Paściak, A.; Pilch-Wróbel, A.; Marciniak, Ł.; Schuck, P. J.; Bednarkiewicz, A. Standardization of Methodology of Light-to-Heat Conversion Efficiency Determination for Colloidal Nanoheaters. *ACS Appl. Mater. Interfaces* **2021**, *13*, 44556−44567.

(33) Jiang, K.; Smith, D. A.; Pinchuk, A. Size-Dependent Photothermal Conversion Efficiencies of Plasmonically Heated Gold Nanoparticles. *J. Phys. Chem. C* **2013**, *117*, 27073−27080.

(34) Abadeer, N. S.; Murphy, C. J. Recent Progress in Cancer Thermal Therapy Using Gold Nanoparticles. *J. Phys. Chem. C* **2016**, *120*, 4691−4716.

(35) Shao, Q.; Yang, Z.; Zhang, G.; Hu, Y.; Dong, Y.; Jiang, J. Multifunctional Lanthanide-Doped Core/Shell Nanoparticles: Integration of Upconversion Luminescence, Temperature Sensing, and Photothermal Conversion Properties. *ACS Omega* **2018**, *3*, 188−197.

(36) Bednarkiewicz, A.; Wawrzynczyk, D.; Nyk, M.; Strek, W. Optically Stimulated Heating Using Nd3+ Doped NaYF4 Colloidal near Infrared Nanophosphors. *Appl. Phys. B* **2011**, *103*, 847−852.

(37) del Rosal, B.; Rocha, U.; Ximendes, E. C.; Martín Rodríguez, E.; Jaque, D.; Solé, J. G. Nd3+ions in Nanomedicine: Perspectives and Applications. *Opt. Mater.* **2017**, *63*, 185−196.

(38) Rocha, U.; Upendra Kumar, K.; Jacinto, C.; Ramiro, J.; Caamaño, A. J.; García Solé, J.; Jaque, D. Nd3+ Doped LaF3 Nanoparticles as Self-Monitored Photo-Thermal Agents. *Appl. Phys. Lett.* **2014**, *104*, No. 053703.

(39) Ding, L.; Ren, F.; Liu, Z.; Jiang, Z.; Yun, B.; Sun, Q.; Li, Z. Size-Dependent Photothermal Conversion and Photoluminescence of Theranostic NaNdF4 Nanoparticles under Excitation of Different-Wavelength Lasers. *Bioconjugate Chem.* **2020**, *31*, 340−351.

(40) Marciniak, L.; Kniec, K.; Elzbieciak, K.; Bednarkiewicz, A. Non-plasmonic NIR-Activated Photothermal Agents for Photothermal Therapy. In *Near Infrared-Emitting Nanoparticles for Biomedical Applications*, Benayas, A.; Hemmer, E.; Hong, G.; J, D., Eds.; Springer, 2020; pp 305−347.

(41) Marin, R.; Jaque, D.; Benayas, A. Switching to the Brighter Lane: Pathways to Boost the Absorption of Lanthanide-Doped Nanoparticles. *Nanoscale Horiz.* **2021**, *6*, 209−230.

(42) del Rosal, B.; Pérez-Delgado, A.; Carrasco, E.; Jovanović, D. J.; Dramićanin, M. D.; Dražić, G.; de la Fuente, ÁJ.; Sanz-Rodriguez, F.; Jaque, D. Neodymium-Based Stoichiometric Ultrasmall Nanoparticles for Multifunctional Deep-Tissue Photothermal Therapy. *Adv. Opt. Mater.* **2016**, *4*, 782−789.

(43) Chang, M.; Wang, M.; Shu, M.; Zhao, Y.; Ding, B.; Huang, S.; Hou, Z.; Han, G.; Lin, J. Enhanced Photoconversion Performance of NdVO4/Au Nanocrystals for Photothermal/Photoacoustic Imaging Guided and near Infrared Light-Triggered Anticancer Phototherapy. *Acta Biomater.* **2019**, *99*, 295−306.

(44) Yu, Z.; Hu, W.; Zhao, H.; Miao, X.; Guan, Y.; Cai, W.; Zeng, Z.; Fan, Q.; Tan, T. T. Y. Generating New Cross-Relaxation Pathways by Coating Prussian Blue on NaNdF 4 To Fabricate Enhanced Photothermal Agents. *Angew. Chem.* **2019**, *100871*, 8624−8628.

(45) Marin, R.; Jaque, D. Doping Lanthanide Ions in Colloidal Semiconductor Nanocrystals for Brighter Photoluminescence. *Chem. Rev.* **2021**, *121*, 1425−1462.

(46) Bera, D.; Qian, L.; Tseng, T. K.; Holloway, P. H. Quantum Dots and Their Multimodal Applications: A Review. *Materials* **2010**, *3*, 2260−2345.

(47) Yong, K. T.; Law, W. C.; Hu, R.; Ye, L.; Liu, L.; Swihart, M. T.; Prasad, P. N. Nanotoxicity Assessment of Quantum Dots: From Cellular to Primate Studies. *Chem. Soc. Rev.* **2013**, *42*, 1236−1250.

(48) Jugdaohsingh, R. Silicon and Bone Health. *J. Nutr. Heal. Aging* **2007**, *11*, 99−110.

(49) Xu, W.; Rytkönen, J.; Rönkkö, S.; Nissinen, T.; Kinnunen, T.; Suvanto, M.; Närvänen, A.; Lehto, V. P. A Nanostopper Approach to Selectively Engineer the Surfaces of Mesoporous Silicon. *Chem. Mater.* **2014**, *26*, 6734−6742.

(50) Regli, S.; Kelly, J. A.; Shukaliak, A. M.; Veinot, J. G. C. Photothermal Response of Photoluminescent Silicon Nanocrystals. *J. Phys. Chem. Lett.* **2012**, *3*, 1793−1797.

(51) Wu, P.; Li, W.; Wu, Q.; Liu, Y.; Liu, S. Hydrothermal Synthesis of Nitrogen-Doped Carbon Quantum Dots from Microcrystalline Cellulose for the Detection of Fe3+ Ions in an Acidic Environment. *RSC Adv.* **2017**, *7*, 44144−44153.

(52) Hassan, M.; Gomes, V. G.; Dehghani, A.; Ardekani, S. M. Engineering Carbon Quantum Dots for Photomediated Theranostics. *Nano Res.* **2018**, *11*, 1−41.

(53) Cabana, S.; Curcio, A.; Michel, A.; Wilhelm, C.; Abou-Hassan, A. Iron Oxide Mediated Photothermal Therapy in the Second Biological Window: A Comparative Study between Magnetite/Maghemite Nanospheres and Nanoflowers. *Nanomaterials* **2020**, *10*, No. 1548.

(54) Van De Walle, A.; Kolosnjaj-Tabi, J.; Lalatonne, Y.; Wilhelm, C. Ever-Evolving Identity of Magnetic Nanoparticles within Human Cells: The Interplay of Endosomal Confinement, Degradation, Storage, and Neocrystallization. *Acc. Chem. Res.* **2020**, *53*, 2212−2224.

(55) Lozano-Pedraza, C.; Plaza-Mayoral, E.; Espinosa, A.; Sot, B.; Serrano, A.; Salas, G.; Blanco-Andujar, C.; Cotin, G.; Felder-Flesch, D.; Begin-Colin, S.; Teran, F. J. Assessing the Parameters Modulating Optical Losses of Iron Oxide Nanoparticles under near Infrared Irradiation. *Nanoscale Adv.* **2021**, *3*, 6490−6502.

(56) Xu, L.; Li, J.; Lu, K.; Wen, S.; Chen, H.; Shahzad, M. K.; Zhao, E.; Li, H.; Ren, J.; Zhang, J.; Liu, L. Sub-10 Nm NaNdF 4 Nanoparticles as Near-Infrared Photothermal Probes with Self-Temperature Feedback. *ACS Appl. Nano Mater.* **2020**, *3*, 2517−2526.

(57) Bastos, A. R. N.; Brites, C. D. S.; Rojas-Gutierrez, P. A.; DeWolf, C.; Ferreira, R. A. S.; Capobianco, J. A.; Carlos, L. D. Thermal Properties of Lipid Bilayers Determined Using Upconversion Nanothermometry. *Adv. Funct. Mater.* **2019**, *29*, No. 1905474.

(58) Skripka, A.; Benayas, A.; Brites, C. D. S.; Martín, I. R.; Carlos, L. D.; Vetrone, F. Inert Shell Effect on the Quantum Yield of Neodymium-Doped Near-Infrared Nanoparticles: The Necessary Shield in an Aqueous Dispersion. *Nano Lett.* **2020**, *20*, 7648−7654.

(59) Shen, Y.; Santos, H. D. A.; Ximendes, E. C.; Lifante, J.; Sanz-Portilla, A.; Monge, L.; Fernández, N.; Coria, I. C.; Jacinto, C.; Brites, C. D. S.; Carlos, L. D.; Benayas, A.; Iglesias-de la Cruz, M. C.; Jaque, D. Ag2S Nanoheaters with Multiparameter Sensing for Reliable Thermal Feedback during In Vivo Tumor Therapy. *Adv. Funct. Mater.* **2020**, *30*, No. 2002730.

(60) Sahadev, N.; Anappara, A. A. Photo-to-Thermal Conversion: Effective Utilization of Futile Solid-State Carbon Quantum Dots (CQDs) for Energy Harvesting Applications. *New J. Chem.* **2020**, *44*, 10662−10670.

(61) Ge, J.; Jia, Q.; Liu, W.; Guo, L.; Liu, Q.; Lan, M.; Zhang, H.; Meng, X.; Wang, P. Red-Emissive Carbon Dots for Fluorescent, Photoacoustic, and Thermal Theranostics in Living Mice. *Adv. Mater.* **2015**, *27*, 4169−4177.

(62) Kim, D.; Jo, G.; Chae, Y.; Subramani, S.; Lee, B. Y.; Kim, E. J.; Ji, M. K.; Sim, U.; Hyun, H. Bioinspired: Camellia Japonica Carbon Dots with High near-Infrared Absorbance for Efficient Photothermal Cancer Therapy. *Nanoscale* **2021**, *13*, 14426−14434.

(63) Geng, B.; Yang, D.; Pan, D.; et al. NIR-Responsive Carbon Dots for Efficient Photothermal Cancer Therapy at Low Power Densities. *Carbon N. Y.* **2018**, *134*, 153−162.

(64) Li, D.; Han, D.; Qu, S. N.; et al. Supra-(Carbon Nanodots) with a Strong Visible to near-Infrared Absorption Band and Efficient Photothermal Conversion. *Light Sci. Appl.* **2016**, *5* (7), No. e1018.

(65) Sadat, M. E.; Kaveh Baghbador, M.; Dunn, A. W.; Wagner, H. P.; Ewing, R. C.; Zhang, J.; Xu, H.; Pauletti, G. M.; Mast, D. B.; Shi, D. Photoluminescence and Photothermal Effect of Fe3O4 nanoparticles for Medical Imaging and Therapy. *Appl. Phys. Lett.* **2014**, *105*, No. 091903.

(66) Nicolás-Boluda, A.; Vaquero, J.; Laurent, G.; Renault, G.; Bazzi, R.; Donnadieu, E.; Roux, S.; Fouassier, L.; Gazeau, F. Photothermal Depletion of Cancer-Associated Fibroblasts Normalizes Tumor Stiffness in Desmoplastic Cholangiocarcinoma. *ACS Nano* **2020**, *14*, 5738−5753.

(67) Liu, Y.; Shen, G.; Zhao, L.; Zou, Q.; Jiao, T.; Yan, X. Robust Photothermal Nanodrugs Based on Covalent Assembly of Non-

pigmented Biomolecules for Antitumor Therapy. *ACS Appl. Mater. Interfaces* **2019**, *11*, 41898−41905.

(68) Zhao, L.; Liu, Y.; Xing, R.; Yan, X. Supramolecular Photothermal Effects: A Promising Mechanism for Efficient Thermal Conversion. *Angew. Chem., Int. Ed.* **2020**, *59*, 3793−3801.

(69) Chang, R.; Zou, Q.; Zhao, L.; Liu, Y.; Xing, R.; Yan, X. Amino-Acid-Encoded Supramolecular Photothermal Nanomedicine for Enhanced Cancer Therapy. *Adv. Mater.* **2022**, *34*, No. 2200139.

Supporting Information

Quantitative comparison of the light-to-heat conversion efficiency in nanomaterials suitable for photothermal therapy

*Agnieszka Paściak, Riccardo Marin, Lise Abiven, Aleksandra Pilch-Wróbel, Małgorzata Misiak, Wujun Xu, Katarzyna Prorok, Oleksii Bezkrovnyi, Łukasz Marciniak, Corinne Chaneac, Florence Gazeau, Rana Bazzi, Stéphane Roux, Bruno Viana, Vesa-Pekka Lehto, Daniel Jaque, Artur Bednarkiewicz**

*E-mail: a.bednarkiewicz@intibs.pl

List of figures and contents

Description S1 Chemical reagents

All of the chemical reagents in this experiment were used as received without further purification. Hexadecyltrimethylammonium bromide (CTAB, 99.0%), ammonium bromide (NH_4Br), sodium bromide (NaBr), hydrogen tetrachloroaurate trihydrate ($HAuCl_4 \cdot 3H_2O$, 99.9%), silver nitrate ($AgNO_3$, 99.9%), iron(III) chloride hexahydrate ($FeCl_3 \cdot 6H_2O$, 98%), iron(II) chloride tetrahydrate ($FeCl_2 \cdot 4H_2O$, > 98%), sodium sulfide nonahydrate ($Na_2S \cdot 9H_2O$, 99.99%), 11-mercaptoundecanoic acid (95%), poly(ethylene glycol) methyl ether thiol (6kDa), L-ascorbic acid (99%), sodium borohydride ($NaBH_4$, 99%), samarium oxide (99.99%), neodymium oxide (99.99%), dysprosium oxide (99.99%), acetic acid (99%), diethylene glycol (99%), N-Methyldiethanolamine (NMDEA, ≥99%), pure oleic acid, citric acid (99%), sodium hydroxide (NaOH, ≥ 98%), and 1-octadecene (90%) were purchased from Sigma Aldrich Chemistry. Copper chloride dihydrate ($CuCl_2 \cdot 2H_2O$, 99%), glutathione reduced (GSH, 98+%), sodium sulfide nonahydrate ($Na_2S \cdot 9H_2O$, 98%) were purchased from Alfa Aesar. Silver nitrate ($AgNO_3$, 99.85%) and trisodium citrate (Na_3(cit), 98% were purchased from Acros Organics. Sodium silicide (NaSi) was provided by SiGNa Chemistry Inc. HCl and HF were bought from Merck, $HClO_4$ (65%) from Carlo Erba, ethanol (96% pure p.a.), n-hexane (95%), acetone (pure p.a.), and chloroform were purchased from POCH S.A (Poland). Urea (pure p.a.) was purchased from Chempur (Poland). Isopropyl alcohol was purchased from Fisher, roasted coffee powder was purchased from Hacendado, Mercadona. DTDTPA is a non commercial product and was prepared as previously reported [1].

Description S2. Synthesis procedures

2.1.1 Synthesis of gold nanorods

Gold nanorods (AuNRs) were synthesized by a modified seed-mediated method [2]. Au seeds are small nuclei made of gold, which serve as the starting point for the development of a more complex structure. The synthesis was performed in a water bath at 30 °C.

Seed solution: 25 µL of 50 mM $HAuCl_4$ was added to 4.7 mL of 0.1M CTAB solution, the mixture was slowly stirred until a completely clear solution was obtained (about 5 min). Then, 300 µL of 10 mM $NaBH_4$ (freshly prepared) was added under vigorous stirring. The color of the solution changed from yellow to brownish yellow. The seed solution was stored at 30 °C (gently stirred). Obtained seeds were used for the synthesis of single crystal Au nanorods.

The growth solution was prepared by adding 100 µL of 50 mM $HAuCl_4$ to 10 mL of 100 mM CTAB solution. The mixture was kept for 10 min in water bath (30°C) to ensure complexation between gold salt and CTAB. Then, 75 µL of 100 mM ascorbic acid was added to the mixture, which was gently stirred (the solution became colorless). To the grown solution, 80 µL of 5 mM $AgNO_3$ was added. Finally, 120 µL seeds solution was added to the mixture. Obtained solution was vigorously stirred and the left undisturbed at 30°C for 30 min in water bath. Next, the solution of as-prepared nanorods was centrifuged at 8000 rpm for 30 min. The precipitate containing nanorods was dissolved in 3 mL hot (50 ºC) of 300 mM CTAB solution and transferred into a glass tube. Upon cooling at room temperature, a brown precipitate at the tube bottom was observed. The precipitate containing nanorods was separated carefully from the supernatant, finally dispersed in water (5 ml) and stored at room temperature.

2.1.2. CuS

The synthesis of copper sulfide (CuS) nanoparticles was performed slightly modifying the reported procedure [3]. In brief, 1 mL of a 0.1 M aqueous solution of $Na_2S\cdot 9H_2O$ was swiftly injected into 20 mL of an aqueous solution of the selected ligand (trisodium citrate, Na_3cit, 0.06 mmol, 17.6 mg; L-glutathione, GSH, 0.1 mmol, 30.7 mg) and $CuCl_2\cdot 2H_2O$ (0.1 mmol, 17 mg) in a 50-mL round-bottomed flask. After 5 min of stirring at room temperature, the flask was transferred to an oil bath pre-heated at 90 °C and the mixture was kept under stirring at that temperature for a preselected amount of time (30 min for Na_3cit and 20 min for GSH). Subsequently, the reaction mixture was quickly cooled down to room temperature in a cold-water bath and transferred to a 20-mL vial. For TEM observations, the particles were precipitated with isopropanol (iPrOH), recovered by means of centrifugation (30,000 g for 20 min at 4 °C), and washed once with a mixture of water and iPrOH, before being redispersed in water. The sample was stored at 8 ºC for further use. Assuming 100% synthesis efficiency, the estimated material concentration was approximately 0.5 mg/mL (disregarding the contribution from the ligands).

2.1.3. $NaY_{1-x}Ln_xF_4$

Preparation of precursor: The 2 mmol of acetate precursors ($(CH_3COO)_3Ln$) were prepared by mixing lanthanide oxides (Nd_2O_3, Sm_2O_3, Dy_2O_3 — 1 mmol) with 50% aqueous acetic acid. Prepared mixture was heated to 200 °C for 120 min in Teflon-lined autoclave. The final precursor was obtained by evaporation of solvents in vacuum and further drying (130 °C for 12 h).

Preparation of differently doped $NaYF_4$ material: The synthesis was analogous to procedure described before [4]. The given amount (2 mmol Ln^{3+}) of $(CH_3COO)_3Ln$ precursors were mixed in three-neck flask with oleic acid (12 mL) and octadecene (30 mL). The solution was stirred and heated to 140 ^oC under vacuum for 30 min to form a $Ln(oleate)_3$ complex and remove oxygen and water. Subsequently, the reaction temperature was decreased to 50 °C, and 8 mmol ammonium fluoride (NH_4F) and 5 mmol sodium hydroxide (NaOH) dissolved in 20 mL of methanol were added to the reaction flask. The reaction atmosphere was changed to nitrogen and maintained till the end of the synthesis. After that, the temperature was increased to 80 °C to evaporate methanol. This process took approximately 30 min. Finally, the reaction temperature was quickly increased to 300 °C and the solution was stirred at this temperature for 60 min. After the synthesis, the solution was cooled to room temperature. The obtained nanoparticles were precipitated with an excess of ethanol and centrifuged (18 000 g for 10 min). The obtained pellet was purified by washing with *n*-hexane and ethanol. The final product was dispersed in 5 mL of chloroform. Based on the synthesis conditions, assuming 100% synthesis efficiency the estimated material concentration was 20 mg/mL.

Polyacrylic acid (PAA) coating: To obtain water-dispersible samples, a ligand exchange method was applied. First, to remove the oleate ligands from the NP surface, 10 mg of NPs was transferred to an Eppendorf tube and centrifuged (20 min, 20000 g). The obtained pellet was redispersed in 500 μL of n-hexane. The mixture was sonicated as long as the pellet had been suspended. After that, 400 μL of acetonitrile and 100 μL of $NOBF_4$ dissolved in acetonitrile (0.16 M) were added to the tube, and solution was mixed for 10 minutes. In the next step the oleic stripped nanoparticles were precipitated by adding 500 μL of toluene to the Eppendorf tube and centrifuged. Finally, the BF_4^- capped nanoparticles were dispersed in 100 μL dry DMF. Next, 64 μL of PAA solution in water (80 mg/mL) was added to the reaction tube, and vigorously stirred for 20 minutes. After this time, and centrifugation (14 000 g, 15 min) the obtained pellet was dispersed in 500 μL of distilled water.

2.1.4. Ag-Ag_2S dimers

The synthesis of the Ag-Ag_2S dimers was performed according to the procedure reported in [5]. First, an aqueous coffee extract was prepared soaking 15 g of a roasted coffee powder (Hacendado, Mercadona, Spain) in 100 mL of de-ionized water for 2 h, followed by filtration, and dilution to a final volume of 120 mL. Subsequently, water (6.5 mL), coffee extract (3.5 mL), and a magnetic stir bar were added to a 20-mL vial. The initial pH of the solution was 5.5 and was later adjusted to 9.0-9.5 by addition of NaOH 0.5 M. In the meantime, $AgNO_3$ (0.1 mmol, 17 mg) was dissolved in deionized water (1 mL) and swiftly added to the diluted coffee extract. Upon addition of the Ag^+ solution, Ag NPs started forming immediately (as denoted by a marked darkening of the mixture) and the pH dropped. The pH was quickly readjusted between 9.0-9.5 with $NaOH_{aq}$ 0.5 M, and then 0.5 mL of a 0.1 M Na_2S solution in water was swiftly introduced in the reaction mixture. The color shifted almost immediately from dark orange to dark brown, indicating the formation of Ag_2S. Stirring was continued for 2 min and finally the reaction mixture was quenched in 15 mL of iPrOH. After centrifugation at 3,820 g for 20 min, the reaction product was collected as a pellet and the slightly orange supernatant discarded. Finally, the dispersion was filtered through a 200-nm cellulose filter and stored at 8 ºC for further use.

2.1.5. Ag_2S

Ag_2S nanocrystals were prepared using a hydrothermal method assisted by microwave heating [6]. Crystallization of silver sulphide from silver nitrate ($AgNO_3$, 5 mM, 2 eq.) and sodium sulphide ($Na_2S\cdot 9H_2O$, 1eq.) in water solution at pH 8, is induced on a monomodal microwave cavity at 100 °C (300 W) during 5 min under magnetic stirring. Nanoparticle growth is controled by adding complexing ligands (CL) in the previous reactant's water solution before heating. Three different ligands have been used for this study, mercaptoundecanoic acid (MUA), polyethylene glycol (PEG) and dithiolated diethylenetriamine pentaacetic acid (DTDTPA) with a stoichiometry of 3 eq., 2 eq. and 1.5 eq. per silver atom respectively. After the microwave heating program, Ag_2S nanoparticles decorated with CL (Ag_2S@CL) were washed with absolute ethanol and finally, dispersed in water.

2.1.6. BPSi

BPSi was prepared according to a previously published protocol [7,8]. The reactants of NaSi, ammonium salt (NH_4Br), and NaBr were mixed with the mass ratio of 1:4:4. Then, they reacted in a tube oven under a N_2 atmosphere at 240 °C for 5 h. After cooling to room temperature, the raw product was washed with 2.0 M HCl and then further purified with 1% HF solution. The obtained product was washed with H_2O and ball-milled in ethanol (1000 rpm, 30 min). The

BPSi NHs with desired mean diameter around 200 nm were obtained via the removal of big particles with 1500 RCF centrifugation for 5 min.

2.1.7. γFe_2O_3

Maghemite, γFe_2O_3, were synthesized by coprecipitation of iron(II) and iron (III) cations as previously reported [9]. Magnetite spinel iron oxide Fe_3O_4 is first precipitated by addition of aqueous solution of ferrous and ferric ions (Fe(II)/Fe(III)=0.5) at pH 9 using a METROHM 3D Combititreur device. All solutions were carefully deaerated with nitrogen, which was continuously bubbled during the precipitation. After 1 hour of ageing, magnetite is centrifugated during 15 min at 8000 rpm and then, a perchloric acid solution (3 M) is added to magnetite for a fully oxidation step into maghemite γ-Fe_2O_3 [10]. The estimated obtained concentration is 42 mg/mL.

2.1.8. γ Fe_2O_3 decorated with Au

The synthesis of spinel iron oxide nanoflowers decorated with gold nanoparticles have been synthesized as previously reported [11]. Briefly, γ-Fe_2O_3 NFs were obtained from coprecipitation of $FeCl_3 \cdot 6H_2O$ (2.164 g; 8 mmol) and $FeCl_2 \cdot 4H_2O$ (0.796 g; 4 mmol) in 75 mL of diethylene glycol (DEG). After 1 hour of stirring, 75 mL of a solution of NMDEA is first added to the mixture and then, 80 mL of an alkaline solution of both DEG and NMDEA (1:1, v/v). The resulting mixture was stirred for 3 h, and then heated during 4 h at 220 °C. The black solid is washed with a mixture of ethanol, ethyl acetate and nitric acid (10%). At this stage, 20 mL of $Fe(NO_3)_3 \cdot 9H_2O$ ($4.951.10^{-3}$ mol) is added to the nanoparticles. The mixture is heated to 80 °C for 45 min to achieve a complete oxidation of magnetite in maghemite. After nitric acid treatment and washing with acetone and diethyl ether, γ-Fe_2O_3 NFs are redispersed in water.

In same time, gold nanoparticles stabilized with DTDTPA were synthesised by reduction of $HAuCl_4 \cdot 3H_2O$ ($5.1 \cdot 10^{-6}$ mol) in DTDTPA ($5.1 \cdot 10^{-6}$ mol) solution with an excess of $NaBH_4$ as described by Alric et al. [12]. After 1 h of vigourous stirring, 5 mL of aqueous hydrochloric acid solution (1 M) were added. Gold@DTDTPA nanoparticles were then precipitated and washed thoroughly and successively with 0.01 M HCl, water and diethyl ether. The resulting black powder was dispersed in 10 mL of 0.01 M NaOH solution.

Finally, as-prepared suspension of gold@DTDTPA are modified by dopamine and mixed with the suspension of maghemite nanoflowers (γ-Fe_2O_3 NFs, 6 mL, 35 g Fe/L). The mixture with a pH of 5.5 was heated at 50 °C for 24 h. After washing with ultrapure water, acetone, and diethyl ether, an aqueous suspension of γ-Fe_2O_3 NFs-Au is obtained with an iron and gold concentration of 25 and 5 mg/mL respectively.

2.1.9. CDs

N-doped carbon dots were synthesized according to the previously described method [13]. Briefly, 1 mmol of citric acid and 3 mmol urea were dissolved in 40 mL H_2O and stirred until a clear solution was formed. The solution was then transferred to a 100 mL Teflon-lined autoclave and the reaction was carried out at 180 ^{0}C for 12 h. The solution was then cooled naturally to room temperature. The product was used for characterization and measurements without additional purification. Based on the synthesis conditions, the estimated material concentration is 9.3 mg/mL.

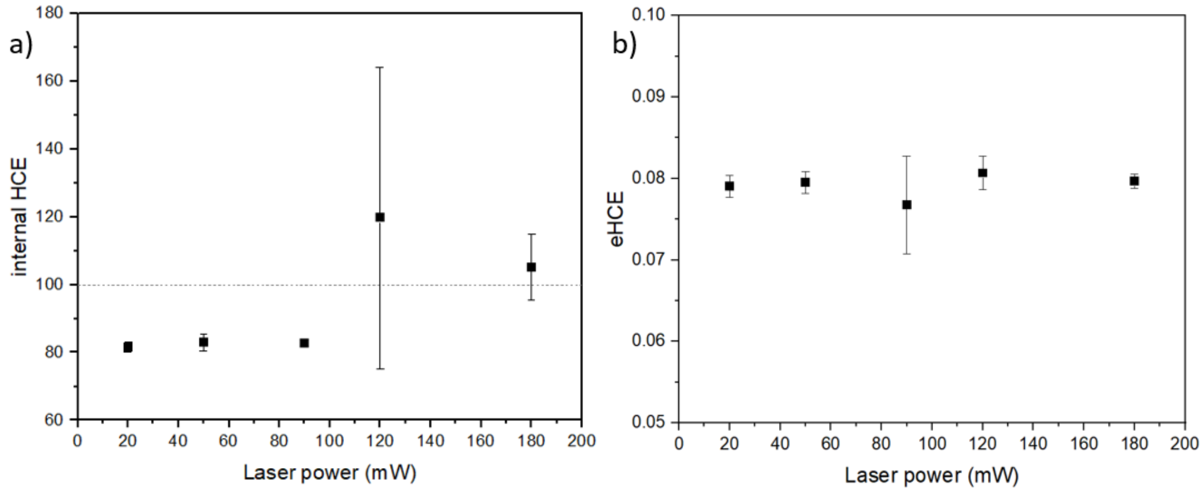

Figure S1. Power dependence of internal HCE and eHCE. Measurements were performed for γ-Fe_2O_3 sample at 806 nm. Error bars are standard deviation from 3 measurements.

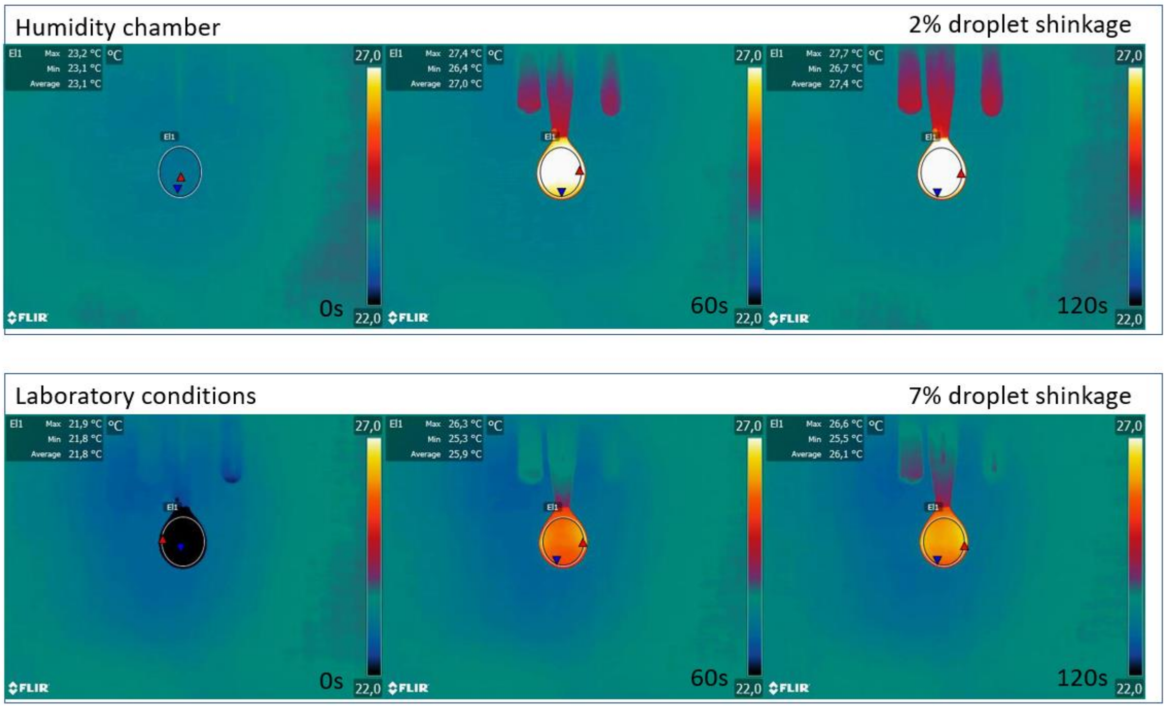

Figure S2. Thermal images of droplets registered at increased (top) and ambient (bottom) humidity conditions at 0 (left), 60 (middle) and 120 (right) seconds of irradiation at 980 nm, 90 mW.

Table S1. Comparison of the possibilities of using different materials in photothermal therapy. Data provided for 794 nm excitation (except for CDs which occurred at 445 nm).

NH class	**NH**	**λ with max. of Abs.**	**α (L/(g·cm))**	**iHCE 794 nm (%)**	**eHCE 794 nm (L/(g·cm))**
plasmonic	AuNRs	~780	0.627	~100	0.627
	CuS@citrate	926	4.49	~100	4.49
	CuS@glutathione	1037	3.60	94	3.38
lanthanide-based	$NaNdF_4$@PAA	794	0.0166	74	0.0122
	$NaNdF_4$:50%Dy @PAA	794	0.0106	41	0.0044
	$NaNdF_4$:80%Dy @PAA	794	0.0086	17	0.0014
	$NaNdF_4$:25%Sm @PAA	794	0.0217	60	0.0130
	$NaNdF_4$:50%Sm @PAA	794	0.0067	40	0.0027
	$NaNdF_4$:75%Sm @PAA	794	0.0058	31	0.0017
semiconductors	Black porous silicon	UV	9.92	39	3.84
	Ag-Ag_2S	UV	0.832	96	0.798
	Ag2S@PEG	UV	0.695	81	0.566
	Ag2S@MUA	UV	1.46	83	1.21
	Ag2S@DTDTPA	UV	0.0753	79	0.0598
iron oxide	γ-Fe_2O_3	UV	0.0927	82	0.0763
	γ-Fe_2O_3@Au	UV	0.487	86	0.420
carbon	carbon nanodots	UV	0.338 (445 nm)	~100 (445 nm)	0.338 (445 nm)

Table S2 iHCE of Nd^{3+} doped nanomaterials

Material, diameter	**diameter**	**λ [nm]**	**iHCE [%]**	**Ref**
$NaNdF_4$	9-25 nm	800	85-74	[14]
$NaNdF_4$@$NaYF_4$@$NaYF_4$:1%Nd	25 nm	808	72	[15]
$NaNdF_4$@prussian blue	29 nm	808	60.8	[16]
$NaNdF_4$	19 nm	808	8.7	[16]
$NdVO_4$,	2.4 nm	808	72	[17]
$NaErF_4$@$NaYF_4$@$NaNdF_4$ – prussian blue	51.1 nm (without PB), 164 nm	808	50.5	[18]
$NaYF_4$:Yb,Er@$NaYF_4$:Yb @$NaYF_4$:Yb,Nd @$mSiO_2$/IR806@PAH-PEG-FA	41 nm	793	46	[19]
$NdVO_4$/Au	21 nm	808	32.2	[20]

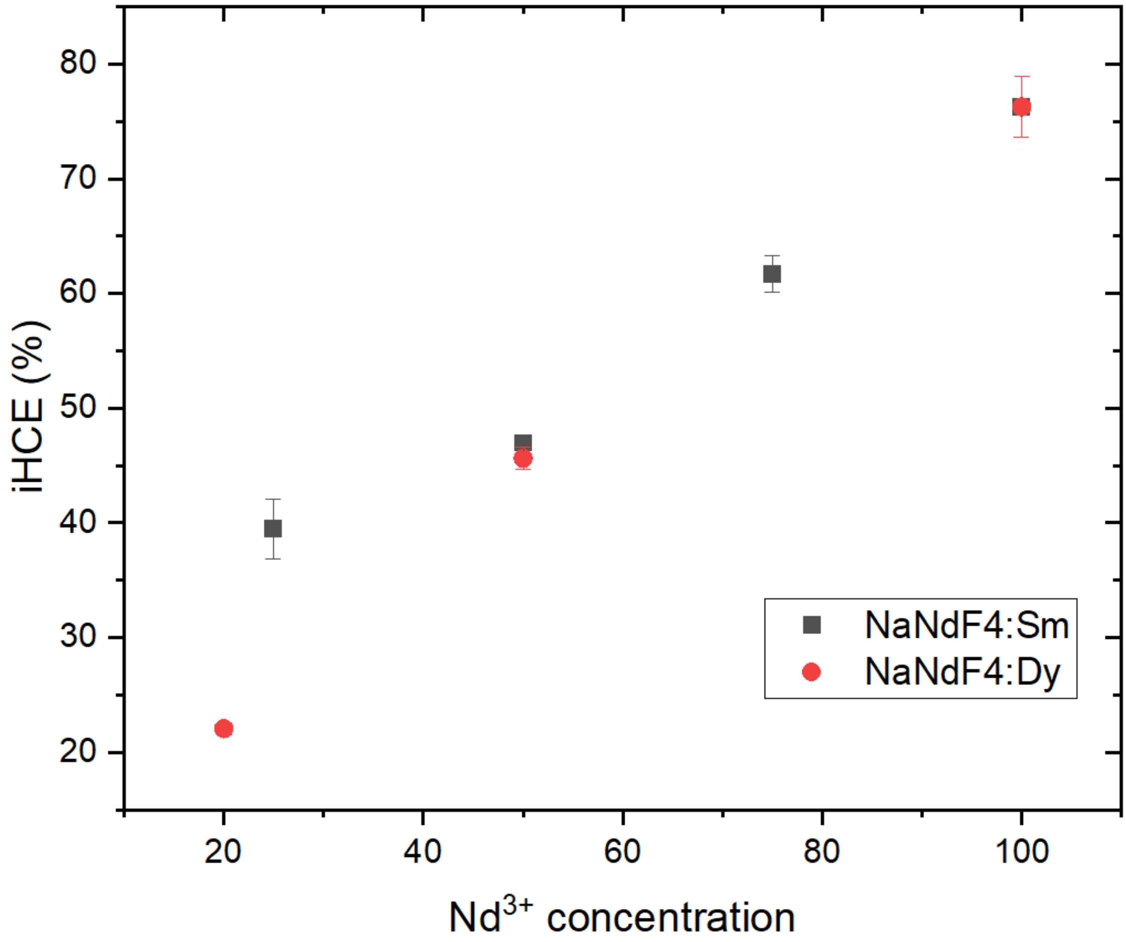

Figure S3. Internal light-to-heat conversion efficiency of $NaNdF_4$ in function of Sm^{3+}/Dy^{3+} dopant concentration.

Table S3. Emission quantum yield under 808 nm CW laser irradiation at distinct laser power densities. The emission quantum yield values were obtained integrating the emission in the range 947.92-1451.33 nm.

Identifier	Power Density ($W.cm^{-2}$)	QY (%)
Ag_2S@PEG	532	$<1\times10^{-5}$
Ag_2S@11MUA	532	0.064±0.006
Ag_2S@DPDPA	532	0.66±0.07

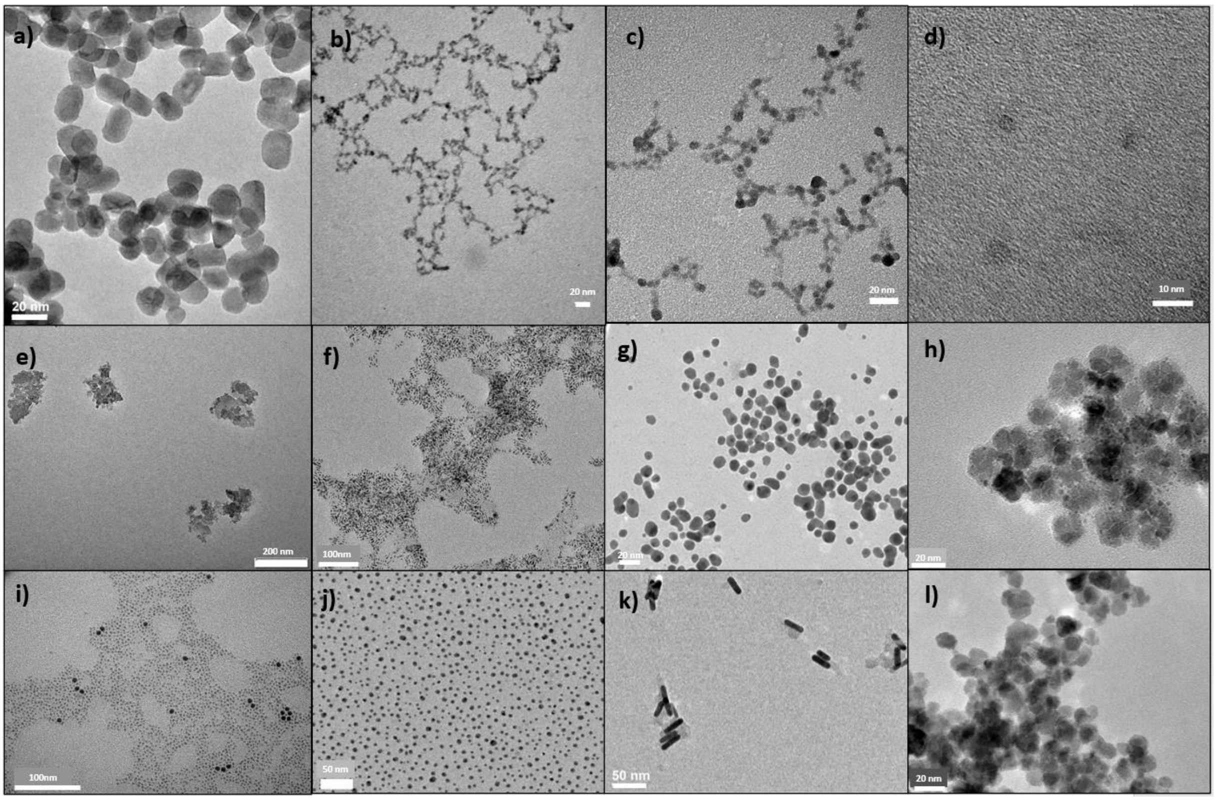

Figure S4 Morphology of the materials compared in this work: a) $NaNdF_4$: 50Sm, b) CuS covered by GSH c) CuS covered by citrate, d) carbon dots, e) black porous silicon, f) Ag_2S@MUA, g) Ag-Ag_2S dimers, h) γ-Fe_2O_3 decorated with gold nanoparticles,

i) Ag_2S@DTDTPA, j) Ag_2S decorated with PEG, k) colloidal gold in the form of nanorods, l) γ-Fe_2O_3

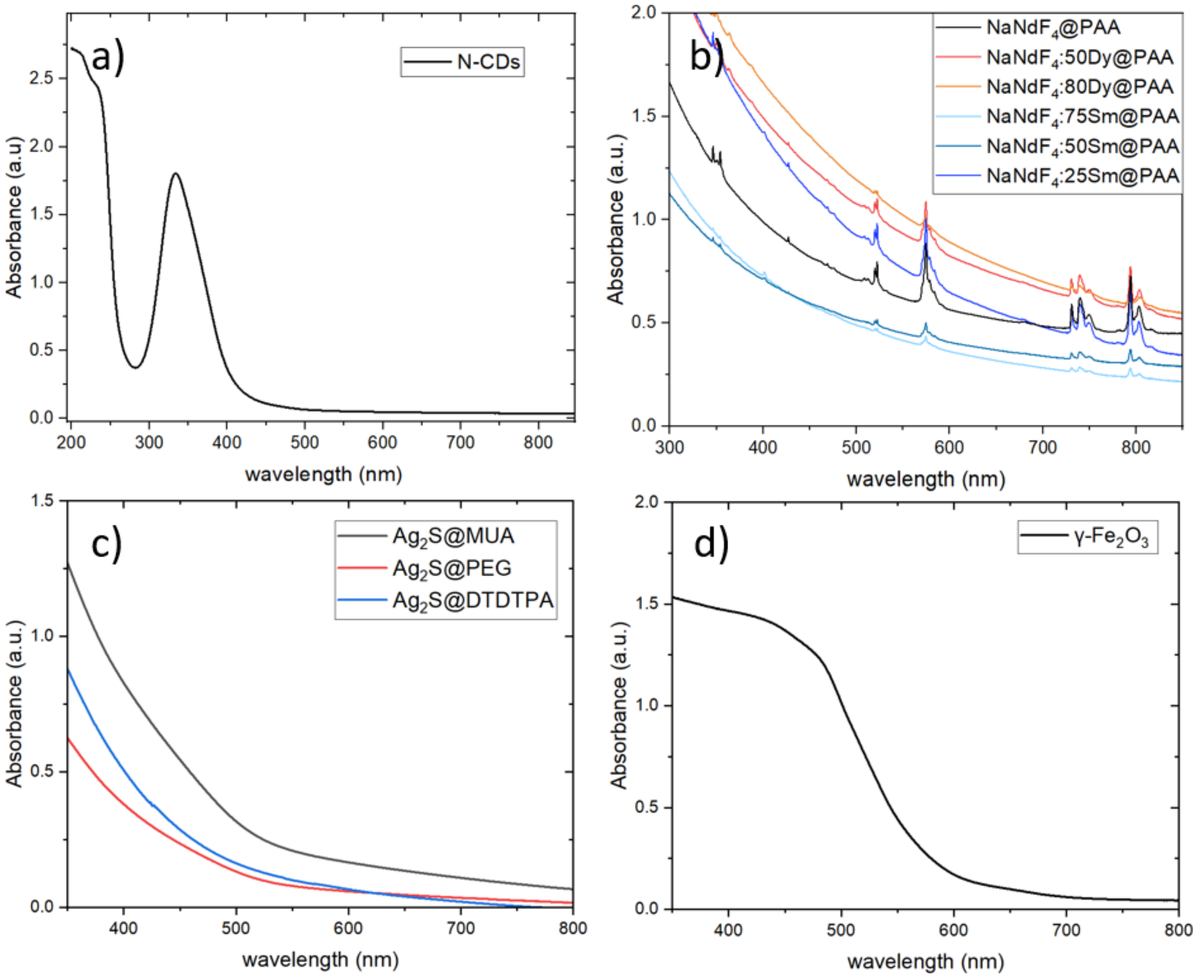

Figure S5. Absorption spectra of a) CQDs, b) NaNdF$_4$ doped with Dy^{3+} and Sm^{3+}, c) Ag$_2$S, d) γ-Fe$_2$O$_3$. Absorption spectra for γ-Fe$_2$O$_3$ decorated with gold nanoparticles, are given in ref of the following article in SI: [11].

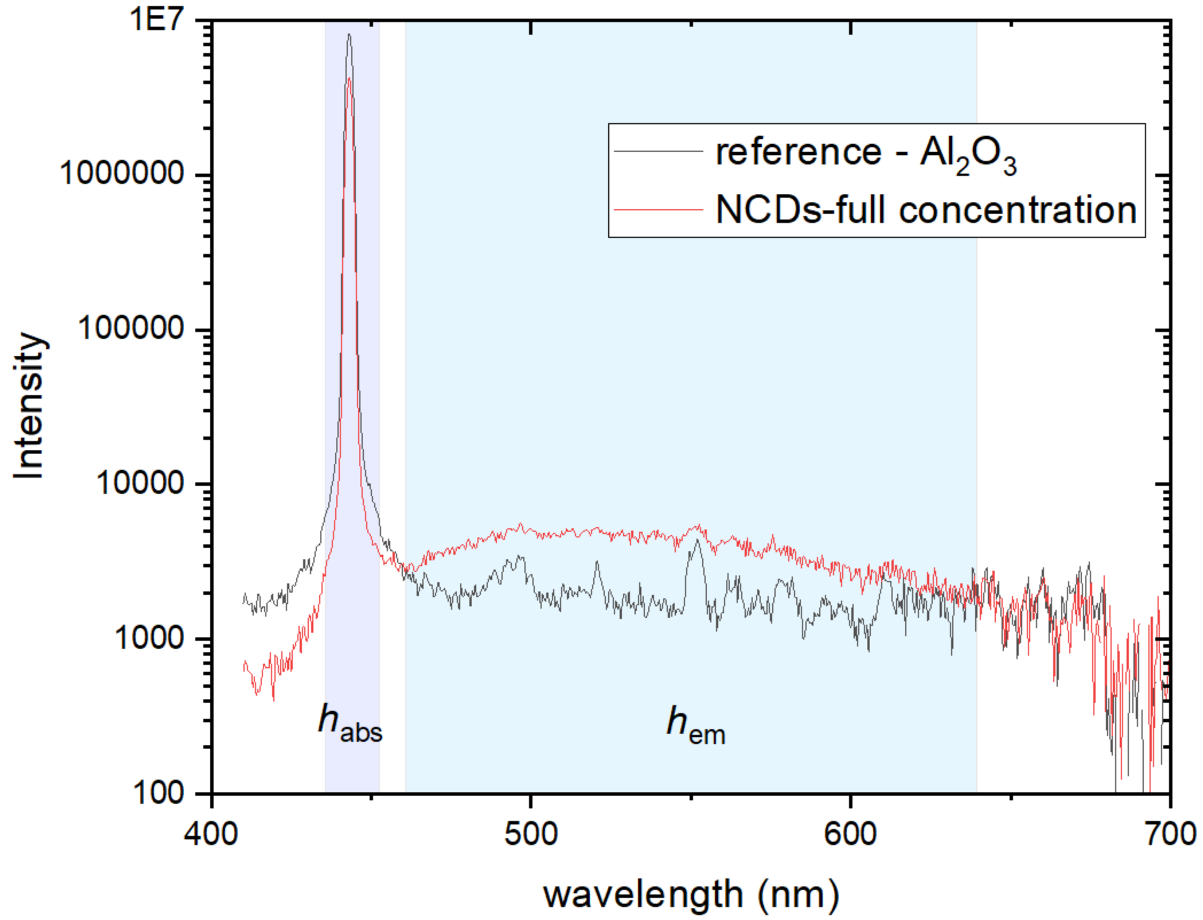

Figure S6. Photoluminescence quantum yield (QY) measurement of CDs. QY was calculated basing on Equation SE1:

$$QY = \frac{h_{em}}{h_{abs}} = \frac{I_{CDs} - I_{ref}}{I_{ref} - I_{CDs}} \tag{SE1}$$

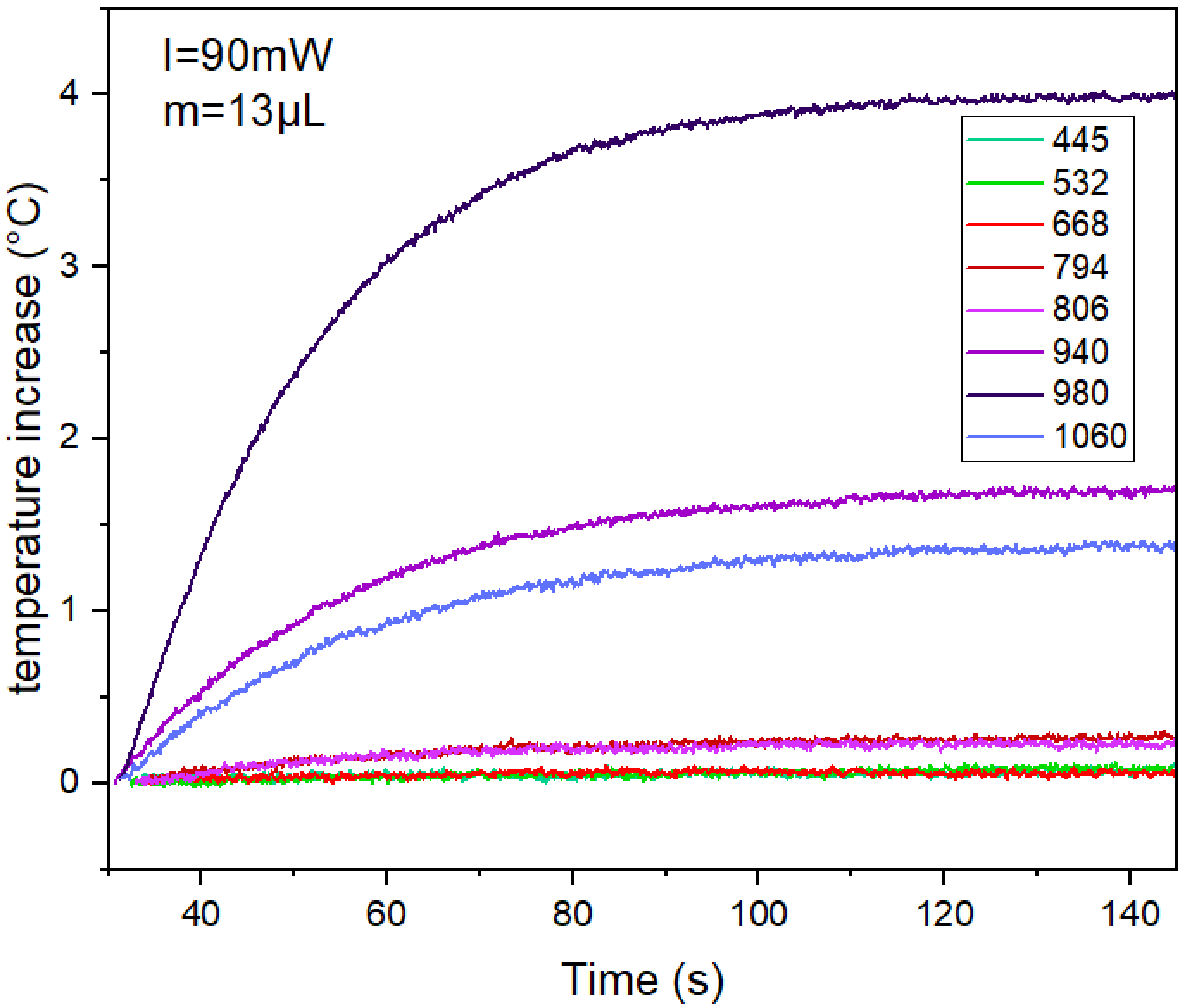

Figure S7. Temperature rise curves of a 13 uL water droplet for different wavelengths measured at constant irradiance power (90 mW).

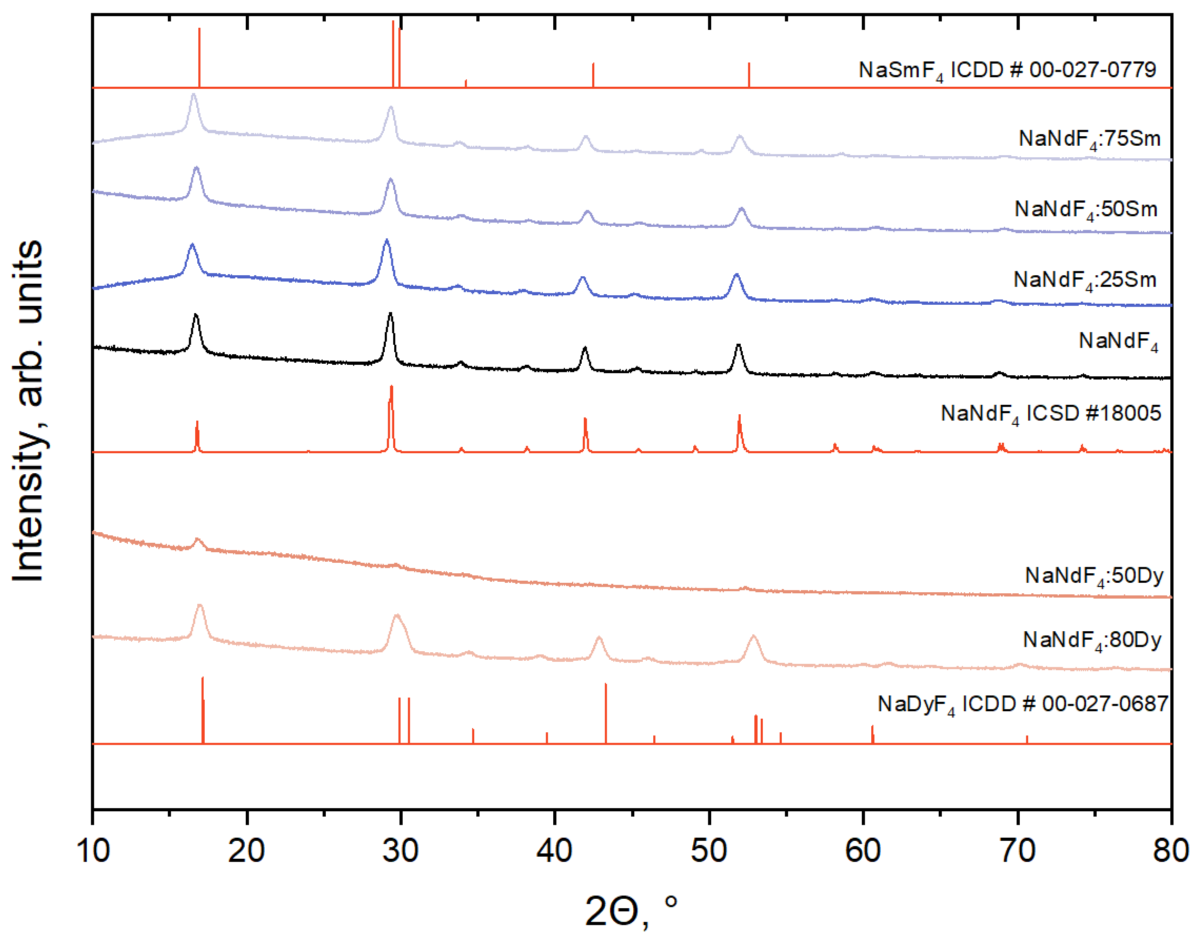

Figure S8 XRD of NaNdF$_4$ samples doped with Dy^{3+} and Sm^{3+}.

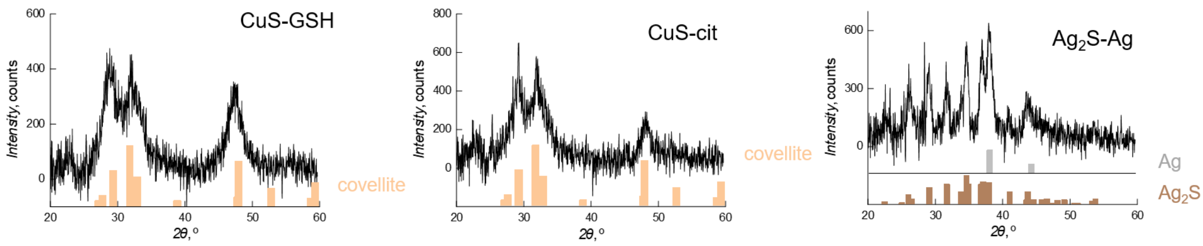

Figure S9 XRD of CuS@GSH, CuS@cit and Ag-Ag$_2$S samples

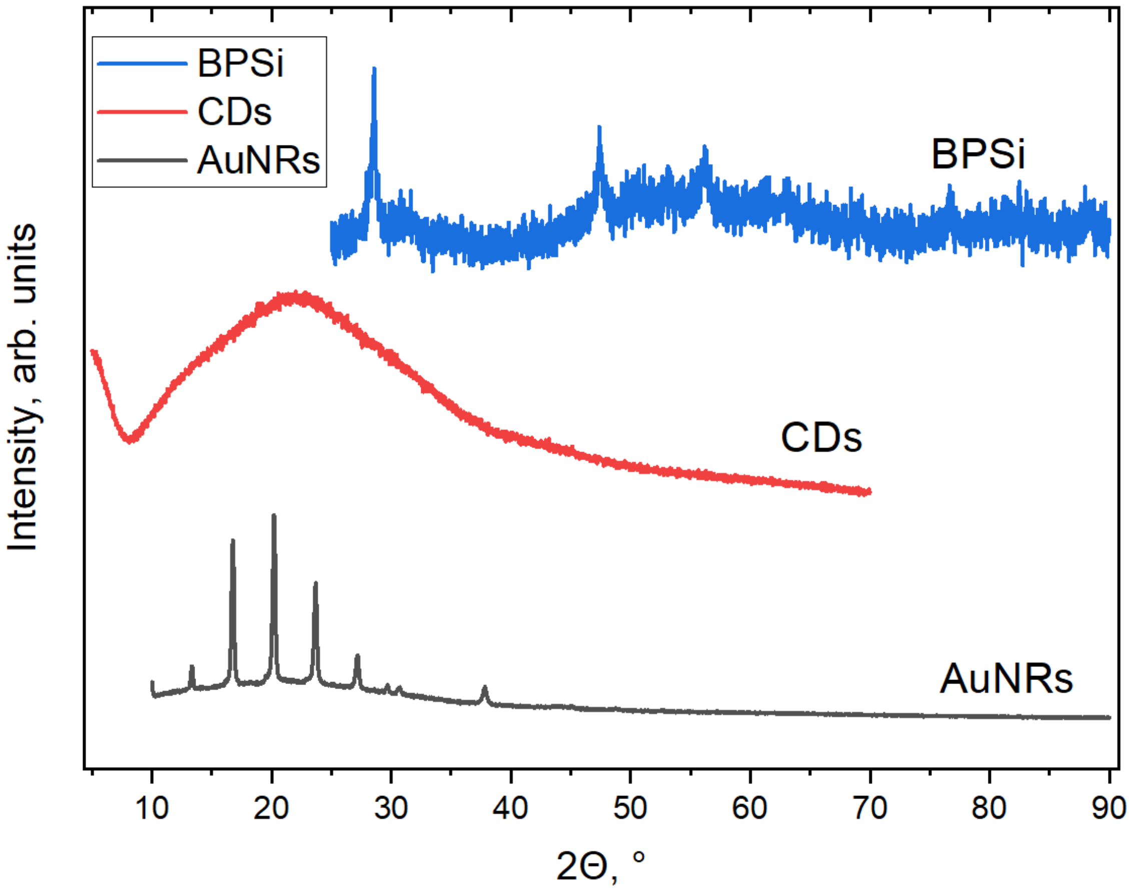

Figure S10 XRD of BPSi, CDs and AuNRs samples

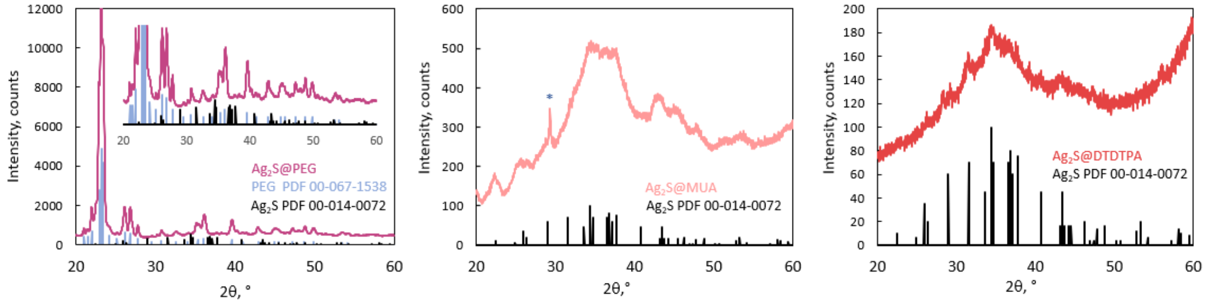

Figure S11 XRD of Ag_2S samples, * is a peak from sample holder.

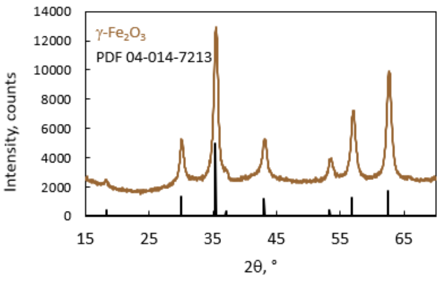

Figure S12 XRD of $\gamma\text{-}Fe_2O_3$ sample

References:

(1) Arifin, D. R.; Long, C. M.; Gilad, A. A.; Alric, C.; Roux, S.; Tillement, O.; Link, T. W.; Arepally, A.; Bulte, J. W. M. Trimodal Gadolinium-Gold Microcapsules Containing Pancreatic Islet Cells Restore Normoglycemia in Diabetic Mice and Can Be Tracked by Using US, CT, and Positive-Contrast MR Imaging. *Radiology* **2011**, *260* (3), 790–798. https://doi.org/10.1148/radiol.11101608.

(2) Scarabelli, L.; Sánchez-Iglesias, A.; Pérez-Juste, J.; Liz-Marzán, L. M. A “Tips and Tricks” Practical Guide to the Synthesis of Gold Nanorods. *J. Phys. Chem. Lett.* **2015**, *6* (21), 4270–4279. https://doi.org/10.1021/acs.jpclett.5b02123.

(3) Marin, R.; Lifante, J.; Besteiro, L. V.; Wang, Z.; Govorov, A. O.; Rivero, F.; Alfonso, F.; Sanz-Rodríguez, F.; Jaque, D. Plasmonic Copper Sulfide Nanoparticles Enable Dark Contrast in Optical Coherence Tomography. *Adv. Healthc. Mater.* **2020**, *9* (5). https://doi.org/10.1002/adhm.201901627.

(4) Marciniak, L.; Pilch, A.; Arabasz, S.; Jin, D.; Bednarkiewicz, A.; Chen, M.; Sun, Y.; Li, F. Y.; Solé, J. G.; Jaque, D.; Palacio, F.; Carlos, L. D.; Millán, A.; Pedroni, M.; Speghini, A.; Hirata, G. A.; Martin, I. R.; Jaque, D. Heterogeneously Nd $^{3+}$ Doped Single Nanoparticles for NIR-Induced Heat Conversion, Luminescence, and Thermometry. *Nanoscale* **2017**, *9* (24), 8288–8297. https://doi.org/10.1039/C7NR02630G.

(5) Marin, R.; Benayas, A.; García-Carillo, N.; Lifante, J.; Yao, J.; Mendez-Gonzalez, D.; Sanz-Rodríguez, F.; Rubio-Retama, J.; Besteiro, L. V.; Jaque, D. Nanoprobes for Biomedical Imaging with Tunable Near-Infrared Optical Properties Obtained via Green Synthesis. *Adv. Photonics Res.* **2021**, *2100260*, 2100260. https://doi.org/10.1002/adpr.202100260.

(6) Glais, E.; Pellerin, M.; Castaing, V.; Alloyeau, D.; Touati, N.; Viana, B.; Chanéac, C. Luminescence Properties of ZnGa 2 O 4 :Cr 3+ ,Bi 3+ Nanophosphors for Thermometry Applications. *RSC Adv.* **2018**, *8* (73), 41767–41774. https://doi.org/10.1039/c8ra08182d.

(7) Xu, W.; Tamarov, K.; Fan, L.; Granroth, S.; Rantanen, J.; Nissinen, T.; Peräniemi, S.; Uski, O.; Hirvonen, M. R.; Lehto, V. P. Scalable Synthesis of Biodegradable Black Mesoporous Silicon Nanoparticles for Highly Efficient Photothermal Therapy. *ACS Appl. Mater. Interfaces* **2018**, *10* (28), 23529–23538. https://doi.org/10.1021/acsami.8b04557.

(8) Xu, W.; Leskinen, J.; Tick, J.; Happonen, E.; Tarvainen, T.; Lehto, V. P. Black Mesoporous Silicon as a Contrast Agent for LED-Based 3D Photoacoustic Tomography. *ACS Appl. Mater. Interfaces* **2020**, *12* (5), 5456–5461. https://doi.org/10.1021/acsami.9b18844.

(9) Vayssières, L.; Chanéac, C.; Tronc, E.; Jolivet, J. P. Size Tailoring of Magnetite Particles Formed by Aqueous Precipitation: An Example of Thermodynamic Stability of Nanometric Oxide Particles. *J. Colloid Interface Sci.* **1998**, *205* (2), 205–212. https://doi.org/10.1006/jcis.1998.5614.

(10) Jolivet, J. P.; Chanéac, C.; Tronc, E. Iron Oxide Chemistry. From Molecular Clusters to Extended Solid Networks. *Chem. Commun.* **2004**, *4* (5), 477–483. https://doi.org/10.1039/b304532n.

(11) Nicolás-Boluda, A.; Vaquero, J.; Laurent, G.; Renault, G.; Bazzi, R.; Donnadieu, E.; Roux, S.; Fouassier, L.; Gazeau, F. Photothermal Depletion of Cancer-Associated Fibroblasts Normalizes Tumor Stiffness in Desmoplastic Cholangiocarcinoma. *ACS Nano* **2020**, *14* (5), 5738–5753. https://doi.org/10.1021/acsnano.0c00417.

(12) Alric, C.; Miladi, I.; Kryza, D.; Taleb, J.; Lux, F.; Bazzi, R.; Billotey, C.; Janier, M.; Perriat, P.; Roux,

S.; Tillement, O. The Biodistribution of Gold Nanoparticles Designed for Renal Clearance. *Nanoscale* **2013**, *5* (13), 5930–5939. https://doi.org/10.1039/c3nr00012e.

(13) Zhang, X.; Qin, X.; Zhang, W. NaYF4:Yb, Er with N-GQDs Mixture: One-Pot Hydrothermal Synthesis and Its Luminescent Film. *Opt. Mater. (Amst).* **2021**, *114* (February), 110910. https://doi.org/10.1016/j.optmat.2021.110910.

(14) Xu, L.; Li, J.; Lu, K.; Wen, S.; Chen, H.; Shahzad, M. K.; Zhao, E.; Li, H.; Ren, J.; Zhang, J.; Liu, L. Sub-10 Nm NaNdF 4 Nanoparticles as Near-Infrared Photothermal Probes with Self-Temperature Feedback . *ACS Appl. Nano Mater.* **2020**, *3* (3), 2517–2526. https://doi.org/10.1021/acsanm.9b02606.

(15) Marciniak, L.; Pilch, A.; Arabasz, S.; Jin, D.; Bednarkiewicz, A. Heterogeneously Nd3+doped Single Nanoparticles for NIR-Induced Heat Conversion, Luminescence, and Thermometry. *Nanoscale* **2017**, *9* (24), 8288–8297. https://doi.org/10.1039/c7nr02630g.

(16) Yu, Z.; Hu, W.; Zhao, H.; Miao, X.; Guan, Y.; Cai, W.; Zeng, Z.; Fan, Q.; Tan, T. T. Y. Generating New Cross-Relaxation Pathways by Coating Prussian Blue on NaNdF 4 To Fabricate Enhanced Photothermal Agents . *Angew. Chemie* **2019**, *100871*, 8624–8628. https://doi.org/10.1002/ange.201904534.

(17) del Rosal, B.; Pérez-Delgado, A.; Carrasco, E.; Jovanović, D. J.; Dramićanin, M. D.; Dražić, G.; de la Fuente, Á. J.; Sanz-Rodriguez, F.; Jaque, D. Neodymium-Based Stoichiometric Ultrasmall Nanoparticles for Multifunctional Deep-Tissue Photothermal Therapy. *Adv. Opt. Mater.* **2016**, *4* (5), 782–789. https://doi.org/10.1002/adom.201500726.

(18) Wang, X.; Li, H.; Li, F.; Han, X.; Chen, G. Prussian Blue-Coated Lanthanide-Doped Core/Shell/Shell Nanocrystals for NIR-II Image-Guided Photothermal Therapy. *Nanoscale* **2019**, *11* (45), 22079–22088. https://doi.org/10.1039/c9nr07973d.

(19) Lin, S. L.; Chen, Z. R.; Chang, C. A. Nd3+ Sensitized Core-Shell-Shell Nanocomposites Loaded with Ir806 Dye for Photothermal Therapy and up-Conversion Luminescence Imaging by a Single Wavelength Nir Light Irradiation. *Nanotheranostics* **2018**, *2* (3), 243–257. https://doi.org/10.7150/ntno.25901.

(20) Chang, M.; Wang, M.; Shu, M.; Zhao, Y.; Ding, B.; Huang, S.; Hou, Z.; Han, G.; Lin, J. Enhanced Photoconversion Performance of NdVO4/Au Nanocrystals for Photothermal/Photoacoustic Imaging Guided and near Infrared Light-Triggered Anticancer Phototherapy. *Acta Biomater.* **2019**, *99*, 295–306. https://doi.org/10.1016/j.actbio.2019.08.026.

Journal of Alloys and Compounds 934 (2023) 167900

Contents lists available at ScienceDirect

Journal of Alloys and Compounds

journal homepage: www.elsevier.com/locate/jalcom

Highly-doped lanthanide nanomaterials for efficient photothermal conversion – selection of the most promising ions and matrices

Agnieszka Paściak, Małgorzata Misiak, Karolina Trejgis, Karolina Elżbieciak-Piecka, Oleksii Bezkrovnyi, Łukasz Marciniak, Artur Bednarkiewicz *,1

Institute of Low Temperature and Structure Research, Polish Academy of Sciences, Okólna 2, 50–422 Wroclaw, Poland

ARTICLE INFO

Article history:
Received 2 August 2022
Received in revised form 1 November 2022
Accepted 2 November 2022
Available online 3 November 2022

Keywords:
Photothermal conversion efficiency
Nanoheaters
Lanthanide-doped nanomaterials
Neodymium

ABSTRACT

Materials doped with rare earth ions are widely used in luminescence applications. However, alternative uses of these materials, such as photothermal conversion, have not yet been systematically investigated. In this work, we systematically and quantitatively compare internal and external photothermal conversion efficiency of materials doped with neodymium, thulium and ytterbium ions, and co-doped with samarium and dysprosium ions. Furthermore, we investigate influence of various matrix materials on photothermal conversion efficiency. These include fluoride, oxide, vanadate and perovskite materials. This was done to determine if photothermal conversion efficiency is dependent on dopant and matrix selection. Our research indicates that the highest internal and external photothermal conversion efficiency is achieved with neodymium ions. Moreover, $NdVO_4$ was found to be the most promising host for future applications. Although the internal photothermal conversion efficiency was relatively low (19%), $NdVO_4$ exhibited significant external photothermal conversion efficiency of 0.08 L/g·cm at 806 nm, which is ca. 14 times higher than that of $NaNdF_4$ at the same wavelength.

1. Introduction

Hyperthermic methods are efficient and minimally invasive cancer treatment methods [1]. However, systemic heat deposition can be exhausting for patients and may cause severe side effects [2]. Photothermal therapy (PTT) using nanoheaters (NHs) allows for high selectivity, thus mitigating typical side effects of hyperthermia treatment [3,4]. These NHs utilize light-to-heat conversion nanomaterials illuminated with NIR light to produce heat. NHs are also applicable in antibacterial treatments [5] and the treatment of dentin hypersensitivity [6]. Typically, near infrared radiation (NIR) and biological spectral windows (NIR-I: 700–980 nm, NIR-II: 1000–1400 nm) [1] are preferred due to lower water and tissue absorption. This allows light to penetrate deep into the tissue and reduce the irradiation dose. Since NIR-I and NIR-II ranges are optimal for these applications, it is necessary to use nanoparticles that can effectively absorb and weakly scatter light within this range. Various materials belonging to different classes are known to meet these criteria [7,8]. Among others, various plasmonic [4,9], semiconducting [10] and hybrid [11] nanomaterials are characterized as having high absorption cross-section in the NIR range. However, these materials have broad absorption bands, which makes luminescence based temperature feedback control challenging. This makes it impossible to remotely (by analysis of spectral fingerprints [12–14]) evaluate local temperature without simultaneous heating of the material. In this aspect, materials doped with rare earth ions perform better as a result of their narrow absorption bands (to address some functions with light of appropriate wavelength), multi-band emission (to ratiometrically read temperature) and long luminescence lifetimes (that enable lifetime based thermometry [15]). Additionally, these luminophores exhibit very efficient anti-Stokes emission which helps diminish sample/tissue autofluorescence or other artifacts. Lanthanide doped materials, especially core-shell nanoparticles, enable the combination of multiple different functionalities within a single nanoparticle, e.g. photothermal heating with nanothermometry [12–14], bioimaging [16], chemotherapy [17], or bone fracture repair capabilities [18] which are becoming increasingly studied in the most recent literature. Moreover, lanthanide-doped nanomaterials (Ln-NMs) can be easily synthesized, are stable in different chemical environment and exhibit high photostability [19]. Furthermore, they have low inherent cytotoxicity [20]. This is promising for intravenous administration and future applications in PTT.

---

* Corresponding author.
E-mail address: a.bednarkiewicz@intibs.pl (A. Bednarkiewicz).

[1] ORCID Bednarkiewicz: 0000–0003-4113–0365

https://doi.org/10.1016/j.jallcom.2022.167900

Nevertheless, the research on the biological effects of lanthanide-doped nanoparticles is still in progress [21]. Recently, there has been advanced research regarding methods of delivering nanomaterials to tumor tissues, as well as their bio-excretion [22]. These studies are not only interesting for future therapies and theranostics, but may also help answer fundamental questions about cancer development and its susceptibility to various drugs and treatment modalities.

Lanthanide ion doped NH materials have been known since at least 2010 [23], and there have been numerous reports on their potential use in PTT. The absorption in lanthanide doped matrices is relatively low due to the forbidden nature of the optical *f-f* transitions. Therefore, recent studies do not utilize lanthanide ions as absorbers, and alternative absorbers have been tested such as highly absorbing dyes [24], polymers [25], catecholamines [26] or metals [27]. Among various rare earth ions, Nd^{3+} [12,24,28–32] and Yb^{3+} [13,33–38] doped materials are particularly common for PTT applications. Heating effect was also observed in materials doped with erbium [39], holmium [40] and thulium ions [41]. Other ions, like Sm^{3+} [36], Eu^{3+} [42], Dy^{3+} [43], and La^{3+} [44] were also investigated, but their role was not directly connected with absorption of light due to the lack of strong absorption bands in the biological windows. Ln-NMs are more often used for luminescence generation than for PTT applications. Since different selection rules apply relative to the rare earth ions performing as NHs, current studies on their use as NHs is incomplete.

The heat generation in the Ln-NMs occurs due to numerous energy levels which, along with the long luminescence decay times, increase the probability that ions will interact and exchange energy. This often leads to multiphonon relaxation, which ultimately manifests as an increase in local temperature. Usually these non-radiative relaxation processes are intentionally minimized (by selection of low-phonon matrices, lowering of the material temperature, designing materials with low ion dopant content [45]) in order to improve the luminescence properties. For PTT applications, however, maximization of these non-radiative process is desirable. Therefore, dopant concentration should be increased to promote cross-relaxation and multiphonon transitions. Furthermore, oxide matrices with high cut-off energies should be utilized to enhance the performance of Ln-NHs. In more advanced nanomaterials, e.g. core-shell structure materials, non-radiative transitions are often preceded by numerous energy transfers between ions [12,28]. This implies that the internal light-to-heat conversion efficiency (iHCE) can be affected by dopant ion type, dopant ion concentration, and the material structure as well as the surface-to-volume ratio of the nanocrystal.

The efficiency of the NHs can be qualitatively evaluated by measuring the increase in temperature generated by colloidal nanoheaters under a given laser illumination [40]. As a result, a direct comparison of materials requires strictly identical measurement conditions. In order to compare materials in differing experimental systems, a more reliable measurement quantity is needed. This figure must not only indicate how much of the absorbed energy is converted into heat, but also account for the amount of NHs present as well as the absorption coefficient of the NHs at the prescribed excitation wavelength. Such a figure of merit was proposed in our previous work [8], where we determined the external light-to-heat conversion efficiency for each material as:

$$eHCE = iHCE \cdot a \tag{1}$$

Where a is a mass absorption coefficient, and iHCE is determined using methods similar to those proposed in work [9] with consideration of the heating of the solvent [8]:

$$iHCE = \frac{(a_s - a_0) m_d \cdot C_{p,d}}{P \cdot (1 - 10^{-A_\lambda})} \tag{2}$$

Where $m_d \cdot C_{p,d}$ is a product of the effective mass and heat capacity of sample, P is the laser beam power, A_λ is the absorbance of the sample, and parameter a [K / s] is evaluated from the heating profile (of solvent (a_s) and water (a_0)) represented by Eq. (3).

$$T(t) = T_0 + \frac{a}{b}[1 - e^{-bt}] \tag{3}$$

In our previous work, we compared heating efficiency of different material classes such as semiconductors, plasmonic, a select rare-earth ions, quantum dots and metal oxides. In this paper, we focus exclusively on various dielectric materials doped with various rare earth ions. To the best of our knowledge, this influence has not yet been systematically investigated. Direct comparisons of results obtained on different measuring systems using different models and setups is unreliable and infeasible. Moreover, there are only few studies in which iHCE was determined for NHs doped with lanthanide ions [12,24,28–32,34,46,47]. For this reason we have quantitatively evaluated the iHCE and eHCE of different lanthanide dopants (neodymium, thulium and ytterbium ions, co-doped with samarium and dysprosium ions) and different host materials (fluorides, oxide, vanadate and perovskite) aiming to identify the most important factors that impact iHCE and select the best possible candidates for PTT.

2. Materials and methods

2.1. Synthesis procedures

Nanocrystals were prepared using commercially available reagents without any further purification. Neodymium oxide (99.99%), neodymium(III) acetate hydrate ($(CH_3CO_2)_3Nd \cdot xH_2O$ (99.9%), 1-octadecene (90%), oleic acid (90%), oleylamine (OAm, 70%), trifluoroacetic acid (Reagent Plus, 99%), sodium fluoride (99%), aluminum isopropoxide (≥99.99%), hexadecyltrimethylammonium bromide (≥98%), ammonium fluoride NH_4F (≥98.0%) and yttrium(III) acetate hydrate ($(CH_3CO_2)_3Y \cdot 3\,H_2O$ 99.9%) were purchased from Sigma Aldrich. Lithium hydroxide monohydrate (56.5%) and ammonium metavanadate (99%) were purchased from Alfa Aesar. Ethanol (96% pure p.a.), methanol (pure p.a.), n-hexane (95%), chloroform (pure p.a.), hydrochloric acid (35–38%), acetic acid (99.5%) and sodium hydroxide (99.8%) were purchased from POCH S.A.(Poland). Thulium oxide (99.99%), dysprosium oxide (99.99%), ytterbium oxide (99.9%), samarium oxide (99.9%), neodymium oxide (99.95%) were purchased from Stanford Materials. 1,4-butanediol (99 +%) was purchased from POL-AURA.

2.1.1. $NaY_{1-x}Ln_xF_4$ nanocrystals

The materials were synthesized by thermal decomposition method in oleic acid and 1-octadecene solvents [48].

Preparation of the lanthanide acetates: For the preparation of 1.5 mmol of acetates, 0.75 mmol of respective lanthanide oxides (Yb_2O_3, Sm_2O_3, Dy_2O_3, Tm_2O_3) were used in combination with 50% acetic acid solution. The mixture was then heated to 200 °C for 120 min in a Teflon-lined autoclave. The final product was obtained by evaporation of the solvents under vacuum and final drying at 145 °C for 12 h.

Preparation of the colloidal fluoride nanoparticles: Appropriate amounts of yttrium acetate and particular lanthanide (Ln) acetates, depending on the synthesized host, were placed in a 250 mL three-neck round-bottom flask with 22.5 mL octadecene and 9 mL oleic acid. The solution was then magnetically stirred and heated to 140 °C under vacuum conditions. Once the solution reached 140 °C, it was stirred for an additional 30 min to form $Y(oleate)_3$ and $Ln(oleate)_3$ complexes and to remove residual water and oxygen. In parallel, 0.2222 g (6 mmol, molar ratio F^-: RE^{3+} = 4) of ammonium fluoride and 0.1500 g (3.75 mmol; molar ratio Na^+: RE^{3+} = 2.5) of sodium hydroxide were weighed and placed into another vessel. 10 mL methanol was then added and the mixture magnetically stirred.

Next, the temperature of oleates was reduced to 50 °C and a gentle flow of nitrogen was introduced. When the temperature of the solution reached 50 °C, a methanol solution of NaOH and NH_4F was quickly added to the flask and stirred for 30 min. After 30 min of stirring, the temperature was increased to 85 °C and the flow of nitrogen was ceased, leaving the solution in a vacuum environment. This was done to completely evaporate the methanol from the reaction mixture. After the methanol evaporated, the reaction temperature was increased to 300 °C with a minimum temperature rise rate of about 15 °C/min. Temperature was held at 300 °C for 60 min under the nitrogen flow. The final transparent dispersion was then cooled to room temperature. Ethanol was added to the solution, causing NPs to precipitate. NPs were then isolated from the solution by centrifugation at 10,000 rpm (22,360.0 rcf) for 10 min. For purification, the resulting pellet was dispersed in a minimal amount of *n*-hexane. An additional precipitation was performed through addition of more ethanol. The NPs were again isolated by centrifugation at 14,000 rpm (43,825.6 rcf) for 10 min. The final product stabilized with OA ligands, was dispersed in 3.75 cm^3 of chloroform.

2.1.2. *NdF_3 nanocrystals - thermal decomposition*

NdF_3 nanocrystals were synthesized by thermal decomposition of trifluoroacetate precursor in high boiling point solvents according to a previously published protocol [49]. Prior to synthesis, the Nd $(CF_3COO)_3$ precursor was prepared by initial dissolution of 2.5 mmol Nd_2O_3 in trifluoroacetic acid and water (v/v 1:1). Excess acid was then evaporated, and the precursor was dried in a three-necked round bottom flask on a hot plate for 12 h at 125 °C. Next, 35 mL oleic acid and 35 mL 1-octadecene were added to the flask. The residual water and acid were removed under vacuum at 120 °C. The temperature was then increased to 300 °C, and the solution was stirred for 30 min in a dry N_2 atmosphere. The solution was then cooled to room temperature and nanocrystals were precipitated through the addition of 20 mL ethanol. Nanocrystals were then separated by centrifugation (22, 360 rcf 10 min) and washed with n-hexane and ethanol (4 mL and 16 mL respectively). Nanocrystals were centrifuged again and redispersed in 10 mL chloroform.

2.1.3. *NdF_3 nanocrystals - in aqueous solution*

Water dispersible NdF_3 nanocrystals were synthesized by precipitation from $NdCl_3$ and NaF solution according to previously published protocol with some modifications [50]. First, 0.1 mmol $NdCl_3{\cdot}6\,H_2O$ (prepared earlier from Nd_2O_3) was dissolved in 10 mL deionized water (solution A). In the second flask, 0.3 mmol NaF was dissolved in 10 mL deionized water (solution B). Then, the solution B was added dropwise to the solution A and stirred 1 h at 75 °C. The nanocrystals were then separated by centrifugation (22, 360 rcf 10 min), washed with deionized water and ethanol, centrifuged and redispersed in 2 mL deionized water. The opalescent colloidal solution was stored at 4 °C.

2.1.4. *$NdAlO_3$ nanocrystals - in aqueous solution*

The synthesis of $NdAlO_3$ perovskite was performed in a Novoclave reactor (type 3/100 mL, 400 bar, 500 °C from Büchi AG Switzerland) according to a modified version of the protocol described in the literature [51]. Stoichiometric amounts of acetate hydrate and aluminum isopropoxide were dissolved in 35 mL of 1,4-butanediol. In order to ensure homogeneous dispersion of the substrates within the solvent, the solution was stirred and ultrasonicated for 30 min. Subsequently, the as prepared solution was poured into a reactor vessel and stirring commenced immediately. The reactor was heated up to 285 °C and kept at this temperature for 3 h under constant mechanical stirring (400 rpm). Afterwards, the reactor was left to cool down and to reach room temperature. The $NdAlO_3$ suspension was centrifuged and precipitates were washed with water and ethanol several times. The final product was dispersed in water and partially dried for further investigation.

2.1.5. *$NdVO_4$ nanocrystals*

The $NdVO_4$ nanocrystals were synthesized according to a modified procedure described in literature [32,52]. To synthesize neodymium nitrate, Nd_2O_3 was dissolved in deionized water with diluted hot ultrapure nitric acid. This was followed by triple recrystallization process. Since ammonium metavanadate (NH_4VO_3) is insoluble in water, a 16 mL, 0.6 M solution of NaOH was prepared. 0.3743 g NH_4VO_3 was added to this solution under constant, vigorous stirring. Subsequently, 8 mL of 0.4 M $Nd(NO_3)_3{\cdot}6H_2O$ aqueous solution was added to the solution dropwise. The suspension was stirred for 20 min followed by a pH adjustment to 4.5–5. The solution was then transferred to a 100 mL stainless steel autoclave and maintained at 180 °C for 24 h. The $NdVO_4$ precipitates were separated via a centrifuge and washed several times with deionized water and ethanol. The final product was dispersed in water for further investigation.

2.1.6. *Nd_2O_3 nanocrystals*

The synthesis was performed according to the previously published protocol used for Gd_2O_3 nanoparticles synthesis [53]. Prior to synthesis, acetate precursors were prepared by dissolution of 6 mmol LiOH and 1.5 mmol Nd_2O_3 in acetic acid and water (1:1 v/v). Excess acid was evaporated and the precursors were dried on a hotplate at 145 °C. Then, 12 mL oleic acid, 18 mL oleylamine and 30 mL 1-octadecene were added to three necked flask with dried acetate precursors. The solution was then stirred under vacuum at 140 °C for 1 h before being heated to 320 °C in a N_2 atmosphere. The solution was stirred at this temperature for 1 h. The solution was then cooled to room temperature and nanocrystals were precipitated by the addition of methanol. Nanocrystals were then centrifuged (22 360 rcf 10 min) and washed four times with n-hexane and methanol. The washed nanocrystals were then redispersed in 6 mL $CHCl_3$.

2.1.7. *Transfer of nanocrystals to water*

The oleate capped hydrophobic nanocrystals dispersed in nonpolar solvent were transferred to water by first removing hydrophobic ligand from their surface via hydrochloric acid treatment (0.2 M or 2 M HCl) [54]. The procedure was modified to obtain transparent colloids. 10 mg of nanocrystals in $CHCl_3$ (from 100 to 300 µL depending on the sample concentration) were transferred to the Eppendorf tube and 1 mL of 0.2 M HCl (2 M HCl in case of $NaYF_4$:50%Yb sample) was added. The solution was vortexed for 20 min and the chloroform fraction was removed. The nanocrystals were separated from water fraction by centrifuging (21 000 rcf 10 min) and redispersed in 0.5 mL H_2O for further experiments.

Nd_2O_3 nanocrystals cannot be transferred to water by simple acid treatment due to their fast dissolution. As a result, transfer was supported by CTAB (Hexadecyltrimethylammonium bromide) [55]. 100 µL of Nd_2O_3 (~ 5 mg) in $CHCl_3$ was added to 5 mL 0.05 M CTAB. The solution was then stirred in an open vial for ~1 h at 75 °C until the solution become more transparent. After evaporation of chloroform, the nanocrystals were separated by centrifugation, washed with distilled water two times, and then redispersed in 250 µL H_2O.

2.2. *Characterization of materials*

The morphology of the samples ($NaNdF_4$, $NaYF_4:Yb^{3+}$, $NaYF_4:Yb^{3+},Sm^{3+}$, NdF_3 (synthesized in water and in $CHCl_3$,) Nd_2O_3, $NdVO_4$, $NdAlO_3$) was determined by Titan G2 (S)TEM 60–300 instrument at an acceleration voltage of 80 kV. The morphology of the samples ($NaYF_4:Nd^{3+}$, $NaYF_4:Nd^{3+},Sm^{3+}$, $NaYF_4:Tm^{3+}$, $NaYF_4:Tm^{3+}$,

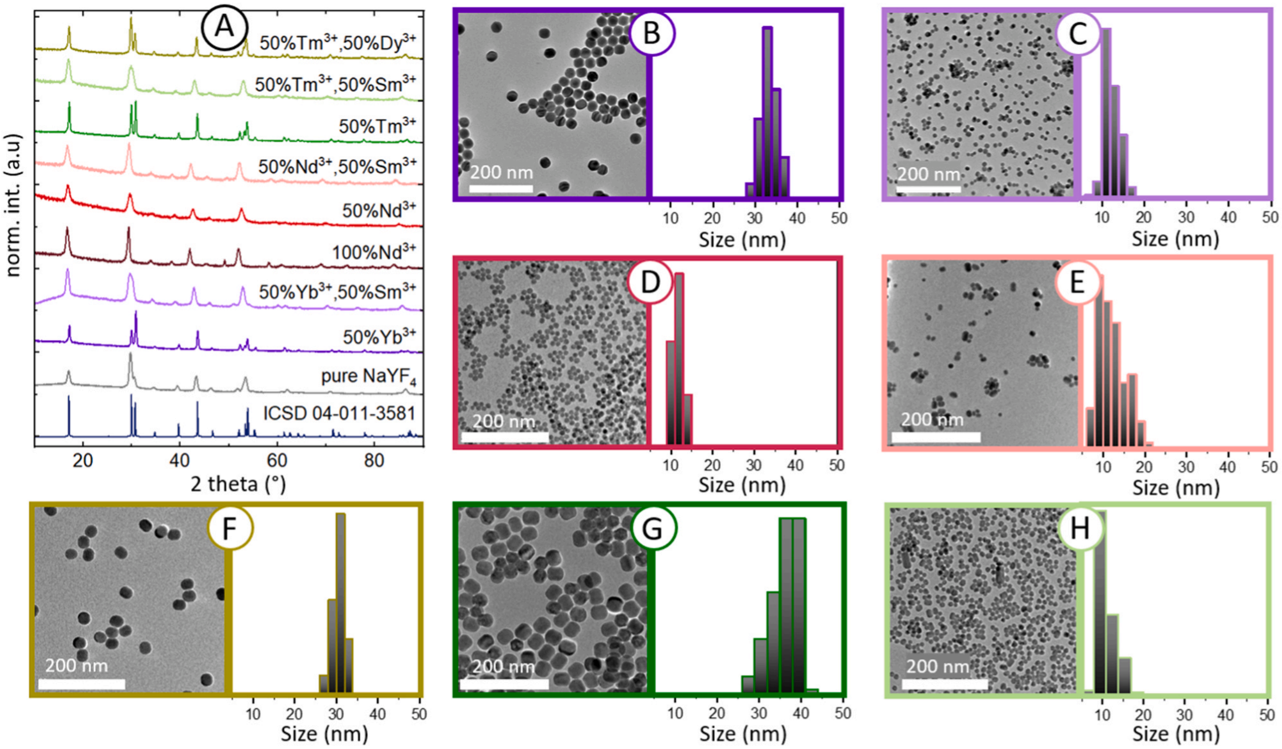

Fig. 1. Structural characterisation of $NaYF_4$ colloidal nanoparticles doped with RE ions: A) X-ray diffraction spectra, B-H) morphology and size distribution of samples: B) 50%Yb, C) 50%Yb, 50%Sm D) 50%Nd, E) 50%Nd, 50%Sm, F) 50%Tm, 50%Dy, G) 50%Tm, H) 50%Tm, 50%Sm.

Sm^{3+}, $NaYF_4$:Tm^{3+},Dy^{3+}) was determined using a Philips CM-20 SuperTwin instrument operating at 160 kV. Prior to measurement, samples were diluted with a suitable solvent, dispersed in an ultrasonic bath, then a droplet of the suspension was deposited on a copper grid coated with a carbon film.

Powder diffraction data were collected on an X′Pert PRO X-ray diffractometer equipped with PIXcel ultrafast line detector, focusing mirror and Soller slits for Cu Kα radiation.

Absorption spectra were obtained in the transmission mode using a Cary Varian 5E UV-Vis-NIR spectrometer. A halogen lamp was used as excitation source. A R928 photomultiplier was used as a detector for the VIS range, and a cooled PbS detector was used for the NIR region.

Concentration of samples was estimated as dry remnants residue from unit volume of colloidal solution.

2.2.1. Light-to-heat conversion efficiency evaluation

iHCE was evaluated in a droplet-based experimental system used in previous investigations [56]. The sampling volumes for individual measurements were 11–14 µL and ca. 9 µL in case of Nd_2O_3 stabilized with CTAB. The photoexcitation beam spot diameter was approximately 0.2 mm, and the actual optical path in the sample was measured for individual samples as droplet diameter (typically less than 3 mm). The following continuous wave laser diodes were used: 793 nm (Changchun New Industries Optoelectronics Technology Co. Ltd., 3 W), 808 nm (Changchun New Industries Optoelectronics Technology Co. Ltd., 2 W), 980 nm (Changchun New Industries Optoelectronics Technology Co. Ltd., 10 W). The experimentally measured wavelengths of the laser diodes at the set excitation power were 794, 806 and 970 nm. The kinetic, time resolved temperature profiles were registered by thermographic camera (TGC) (FLIR T540, accuracy ± 0.5 °C with a reference, thermal sensitivity < 40 mK, 24° @ 30 °C). Optical power illuminating the sample and reference power were evaluated with two power meters (photodiode S120C head and PM100USB power meter, Thorlabs). The radiation power was 90 mW or 40 mW at 970 nm to minimize overheating of the water. The samples were diluted to obtain a temperature increase of no more than 5 °C in order to minimize droplet evaporation. The measurement procedure was described in detail in our previous work [56].

3. Results and discussion

In order to select the most effective NH we prepared two series of nanomaterials: $NaYF_4$ matrix doped with Yb^{3+}, Nd^{3+} and Tm^{3+} ions and additionally co-doped with Sm^{3+} and Dy^{3+} ions. Moreover, we compared different Nd^{3+} doped matrices, such as $NaNdF_4$, NdF_3, Nd_2O_3, $NdVO_4$, $NdAlO_3$. These results are presented and discussed in the following paragraphs.

3.1. Selection of rare-earth ion for photothermal conversion

As mentioned in the introduction, only the NHs characterized by strong absorption bands in the optical biological windows are investigated for PTT. Only three ions fulfil these requirements: Yb^{3+}, Nd^{3+}, Tm^{3+}. Even though Dy^{3+} ions also have an absorption band in the NIR-I (~808 nm), its molar absorption coefficient is too low for a reliable measurement. In order to verify which of the aforementioned three Ln^{3+} ions are most suitable for PTT, a series of colloidal $NaYF_4$ fluorides doped with 50% of the absorber ion was prepared. Further co-doping of these samples was performed to further understand the potential impact of additional energy transfer channels on the ability to increase iHCE. This was done by substituting 50% of the doped Y^{3+} ions with samarium, dysprosium or yttrium itself, which do not absorb significantly at the provided excitation wavelength. A 793 nm laser beam was selected for Nd^{3+} and Tm^{3+} excitation and a 980 nm was chosen for Yb^{3+}. We did not observe measurable luminescence of these samples, and therefore were not capable to determine their emission quantum yields.

The morphology analysis confirmed that non-aggregated, homogeneous nanocrystals with narrow size distributions were

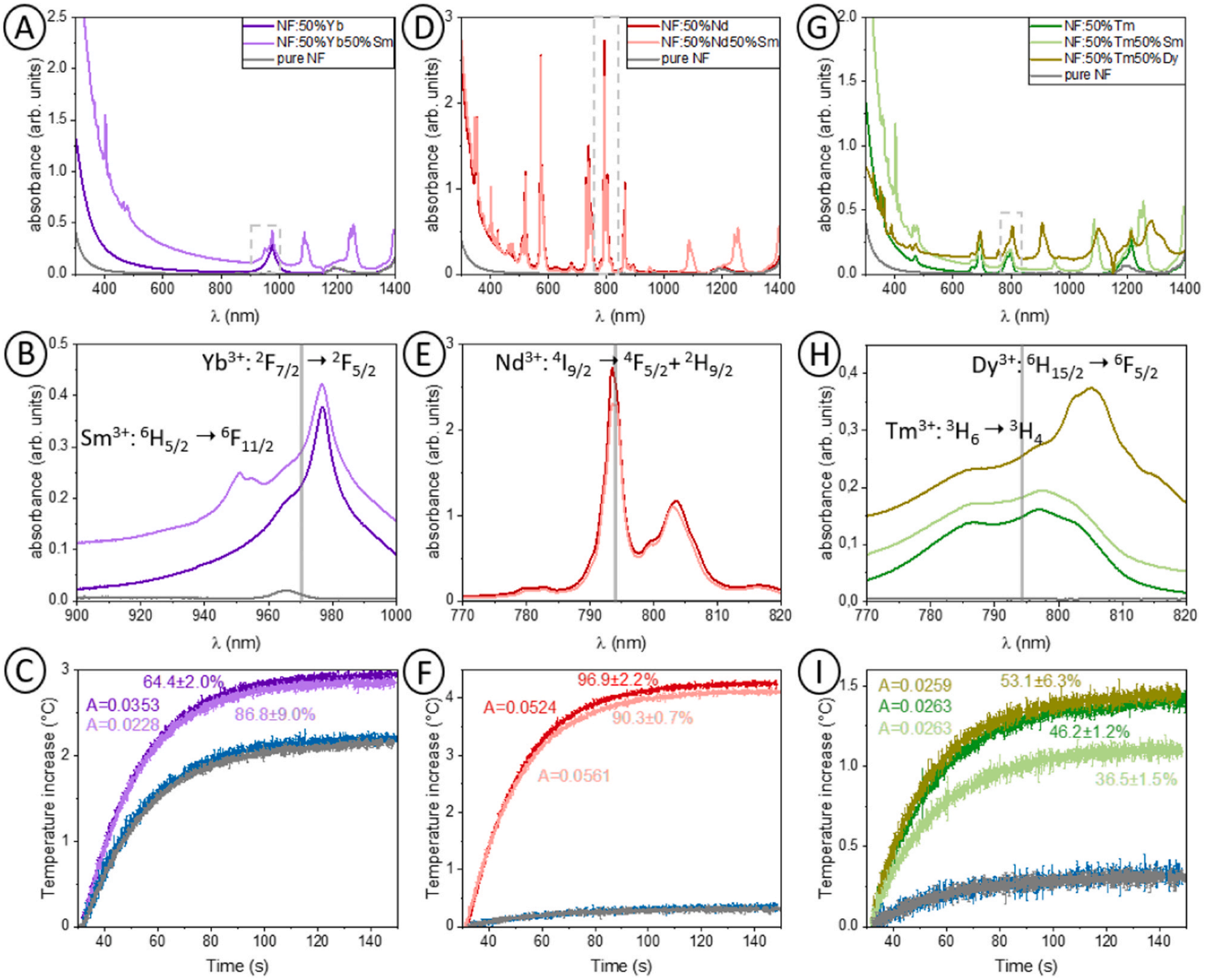

Fig. 2. Absorption spectra in chloroform (A, B, D, E, G, H) and temperature increase as a function of illumination time for samples dispersed in water and for the solvent itself (water - blue curve and pure $NaYF_4$ - grey curve: $NaYF_4$:Yb,Sm measured at 970 nm (C), $NaYF_4$:Nd,Sm measured at 794 nm (F), $NaYF_4$:Tm,Dy,Sm measured at 794 nm (I). The *A* parameter is the measured absorbance and numbers given in % are iHCEs with standard deviation.

synthesized. Although all samples were synthesized under exactly the same conditions, and their shapes are spherical, these is some variation in average size across samples (Fig. 1). We ascribe this variation to the impact lanthanide dopants have on the crystallization process. In particular, materials co-doped with Sm^{3+} ions were significantly smaller in size. Regardless of the co-dopant type, the average size of the Sm^{3+} co-doped samples is below 15 nm. Spherical samples containing Nd^{3+} ions also exhibit a diameter of the order of 12 nm ($NaYF_4$:50%Nd), and $NaNdF_4$ nanorods, have a width of less than 20 nm. Counterparts not containing these ions were typically twice the size of ions doped with Sm^{3+} and Nd^{3+}. These samples were 30–40 nm in diameter or thickness. The significantly smaller size of the nanocrystals doped with Sm^{3+} and Nd^{3+} ions is also reflected in the broadening of the diffraction peaks [57–59] (Fig. 1A). This smaller nanocrystal size can be attributed to the atomic number and considerably larger ionic radius of these two ions, which for Sm^{3+} is 0.958 Å [60], for Nd^{3+} 0.983 Å [60]. Larger nanocrystals were achieved for ions with higher atomic number, such as Yb^{3+} or Tm^{3+}, whose ionic radii are 0.868 Å [60] and 0.880 Å [60], respectively. Additionally, the larger ionic radius of Nd^{3+} and Sm^{3+} relative to Y^{3+} ions (ionic radius 0.900 Å [60]) causes a broadening of the unit cell volume, resulting in a shift of the diffraction peaks of nanocrystals containing these ions towards lower angles compared to the reference pattern (ICSD 04–011–3581). According to data from the literature, the atomic number and ionic radius of RE^{3+} ions, also impact the free energy of the system, which further influences the shape of the nanoparticles [61–63]. As shown in other investigations, nanoparticles heavily doped with Nd^{3+} ions have a characteristically elongated shape. Our synthesized $NaNdF_4$ particles also present an elongated shape, consistent with observations in these previous works.

Heating of Yb^{3+} doped materials at 980 nm has been observed many times [13,33–38]. This is often observed simultaneously with radiative emission for thermometric purpose. However, the iHCE was not evaluated in those studies. For $NaYF_4$ doped with 50%Yb^{3+} and for samples co-doped with 50%Yb^{3+} and 50%Sm^{3+}, there is an observed increase in temperature and a measured iHCE of 64% and 87%, respectively. (Fig. 2C). Samarium co-doping results in a smaller size, and smaller NHs show higher iHCEs. This has also been observed in other studies [29,38]. Moreover, bare (without a passive shell) and heavily (50%) Yb^{3+} doped nanoparticles are relatively efficient absorbers (Fig. 2A), and they are prone to energy migration within Yb^{3+} network (Fig. 3A) toward the surface, where, the O-H vibrations effectively depopulate Yb^{3+} ions and further contribute to enhanced heating [64,65]. Although the sample co-doped with samarium ions shows higher iHCE, it exhibits lower absorption at 970 nm. After accounting for this phenomenon, we can conclude that these samples do not have significantly different eHCEs

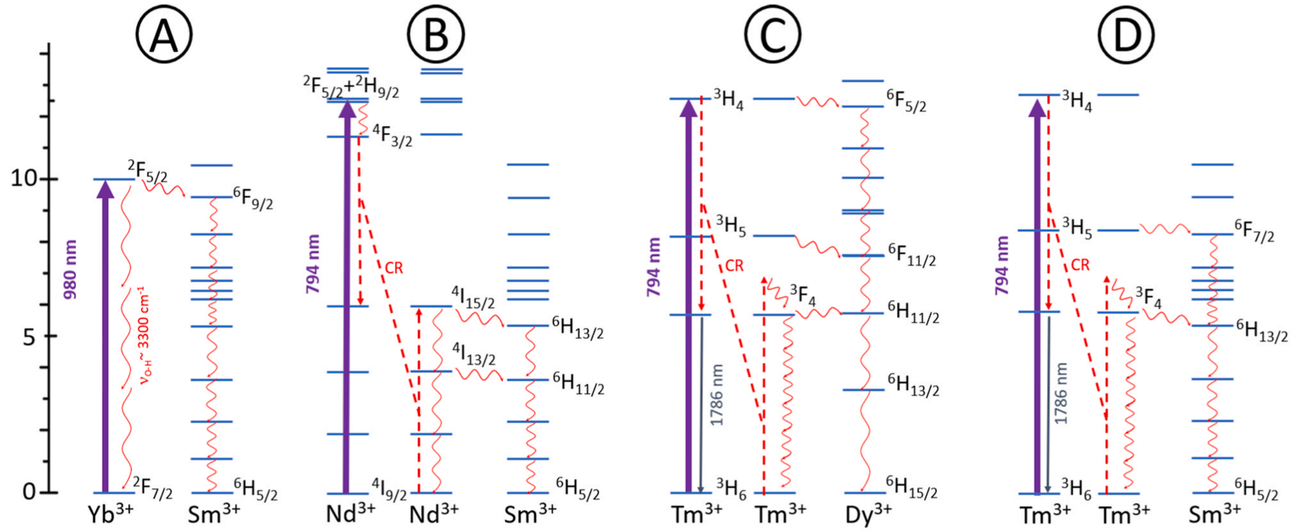

Fig. 3. Energy diagrams and possible non-radiative transitions within nanocrystals consisting of: a) Yb^{3+} and Sm^{3+}, b) Nd^{3+} and Sm^{3+}, c) Tm^{3+} and Dy^{3+}, d) Tm^{3+} and Sm^{3+} ions. The indicated energy transfer consider energy matching only, but do not consider the actual oscillator strengths and the probabilities of these various transitions which differ between various hosts.

($2.39·10^{-3}$ vs $2.14·10^{-3}$ L/g·cm). Therefore, the addition of samarium is not practical in this case. It is also worth noting that at 970 nm, strong absorption band of water exists which results in substantial heating of water, thus rendering this excitation wavelength inadequate for biomedical applications. The temperature curves for the sample containing pure $NaYF_4$ matrix coincide with those obtained for water. The small absorption peak visible at 965 nm (Fig. 2B) corresponds to oleic acid present on the surface of nanocrystals [66].

The co-doping of samarium to a sample containing 50% of Nd^{3+} (Fig. 2D-E) did not increase temperature nor enhanced the iHCE (Fig. 2F). This result opposes the results obtained by Xu et al. [67] for $NaY(WO_4)_2$ microstructures. Those samples containing 1% Nd^{3+} ions doped with increasing concentrations of samarium (0.1–5%) exhibited an increase in temperature corresponding to increasing dopant concentrations. This was explained by cross-relaxation between neodymium and samarium ions. However, for highly doped samples we expect that cross-relaxation solely between neodymium ions is more likely (Fig. 3B). As a result, one observes a higher iHCE for samples without samarium ion doping.

For Tm^{3+} doped NHs, only ~50% iHCE was achieved (Fig. 2I), which is less efficient light-to-heat conversion relative to those doped with Nd^{3+} or Yb^{3+}. The efficient $^3F_4 \rightarrow {}^3H_6$ emission in NIR (at ca. 5600 cm^{-1}) may be responsible for this observation. Slightly better heating performance was measured for the sample doped with 50% Tm^{3+} and co-doped with Dy^{3+}. We speculate the $^3H_4(Tm^{3+}) \rightarrow {}^6F_{5/2}$ (Dy^{3+}) energy transfer is more efficient and Dy^{3+}, having more energy levels, can exploit multiphonon relaxation and help to convert the absorbed energy into heat (Fig. 3C). The absorption spectra of Tm^{3+} and Dy^{3+} at ca. 800 nm (Fig. 2G-H) show significant absorption coefficient for both ions as well as significant spectral overlap. This shows that Dy^{3+} can potentially absorb 794 nm radiation or participate in energy exchange from Tm^{3+}. This would ultimately lead to enhanced heating. A smaller temperature increase was measured for the Sm^{3+} co-doped sample, and no Sm^{3+} absorption can be observed in the 12550 cm^{-1} spectral range, preventing direct absorption of ca. 800 nm radiation by Sm^{3+}. The energy can be transferred from excited Tm^{3+} ions ($^3H_5$ (Tm^{3+}) to $^6F_{7/2}(Sm^{3+})$), but the population mechanism of $^3H_5$ level of Tm^{3+} is hindered by efficient cross-relaxation ($^3H_4$;$^3H_6$)→($^3F_4$;$^3F_4$) + ca. 1350 cm^{-1}. This disables the population of the $^3H_5$ level (Fig. 3D).

Different lanthanides have different tendencies regarding location in the nanoparticle. Specific ions can be located either inside the nanoparticle grain or at its boundary [68]. For example, Li et al. [69] demonstrated that in $NaGdF_4$:Yb,Er sample the highest concentration of Yb^{3+} ions was in the inner layer of the nanoparticles. This mechanism could explain lower iHCE for 50%Tm 50%Sm samples as compared to 50%Tm sample. If Sm^{3+} are located mostly in the outer shell, it could act as an effective passive layer, thus decreasing the possibility of heat exchange at the surface. This would require additional extensive research and is beyond the scope of this work.

Comparison of the obtained data with the literature data is difficult, as there are limited papers covering lanthanide ions contribution to the temperature gain (Table 1), and the iHCE was not determined in numerous papers covering this phenomenon [13,14,33,43,70–73]. Furthermore, iHCE depends on the morphology, size, coating and concentration of the dopant. These features of nanomaterials are not easily reproduced. For example, a very high (close to 100%) iHCE was measured for the $NaNdF_4$ sample. The results are not consistent with the literature possibly due to differences in methodology. Different assumptions made in the commonly used Roper model can lead to divergent results [56]. However, our results of high iHCE of $NaNdF_4$ are similar to those of Xu et al. [29]. The magnitude of eHCE for samples doped with Nd^{3+} is an order of magnitude higher than that of fluorides doped with Yb^{3+} and Tm^{3+} ions. Therefore, Nd^{3+} was selected for the further investigation.

3.2. Impact of matrix on photothermal conversion

Dopant ion is not the only factor to consider when selecting the most efficient NHs. To determine how the host material impacts the iHCE and eHCE, a series of fully-concentrated Nd^{3+} samples were prepared (Fig. 4).

NdF_3 samples were prepared in two ways. Synthesis of NdF_3 in water produced c.a. ~90 nm large nanoflowers, while synthesis involving thermal decomposition of trifluoroacetates in high boiling

Table 1
HCEs of lanthanide-doped NHs.

Material	Diameter (nm)	λ_{EXC} (nm)	iHCE (%)	eHCE (L/g·cm)·10^{-3}	Ref
$NaNdF_4$	9–25	800	85–74	–	[29]
$NaNdF_4$ @$NaYF_4$ @$NaYF_4$:1%Nd	25	808	72.7	–	[28]
Er@ 70Yb@ 60Nd	18–21	800	40	–	[12]
$NaNdF_4$	19	808	8.7	–	[24]
$NaErF_4$ @$NaYF_4$ @$NaNdF_4$ @citric acid	51 (without citric acid)	808	18.6	–	[30]
$NdVO_{4,}$	2.4	808	72.0	–	[31]
$NdVO_4$	~60	808	23.5	–	[32]
$NaErF_4$	11	1530	75.0	–	[46]
$NaErF_4$	11	980	39.0	–	[46]
MoS_2:5%Eu^{3+} nanoflowers	~150	808	49.0	–	[42]
Prussian blue-Yb	~150	808	55.0	–	[47]
$BaLa_2(MoO_4)_4$:Er^{3+}/Yb^{3+}	50–300	980	46.7	–	[34]
SrF_2:Yb,Er	10–41	980	32.0–11.5	–	[38]
$NaYF_4$:50%Yb	33	970	64.4	2.39	This work
$NaYF_4$:50%Yb50%Sm	11	970	86.8	2.14	
$NaYF_4$:50%Nd	12	794	96.9	21.1	
$NaYF_4$:50%Nd50%Sm	12	794	90.3	20.7	
$NaYF_4$:50%Tm	36	794	46.2	2.52	
$NaYF_4$:50%Tm50%Dy	31	794	53.1	2.88	
$NaYF_4$:50%Tm50%Sm	11	794	36.5	1.97	

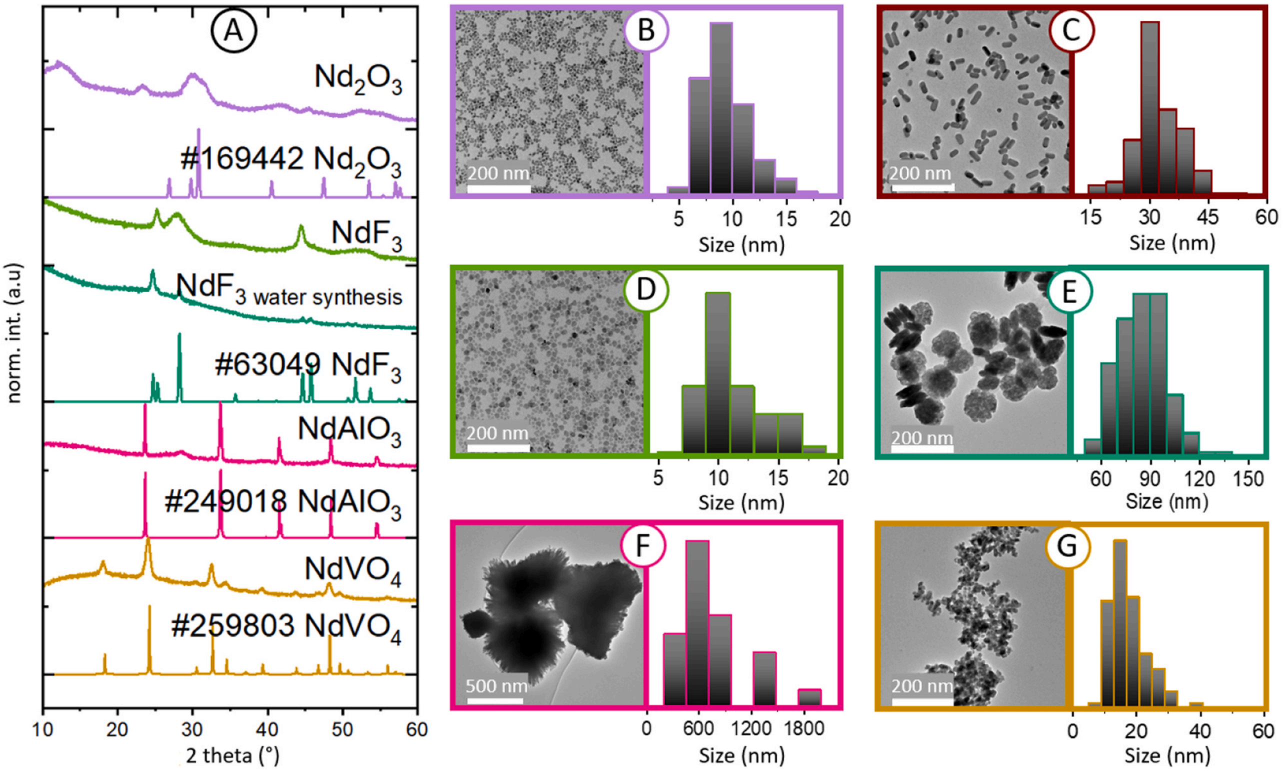

Fig. 4. Structural characterisation A) X-ray diffraction spectra and morphology and size distribution of B) Nd_2O_3, C) $NaNdF_4$, D) NdF_3, synthesised in $CHCl_3$, E) NdF_3, synthesised in water, F) $NdAlO_3$ and G) $NdVO_4$.

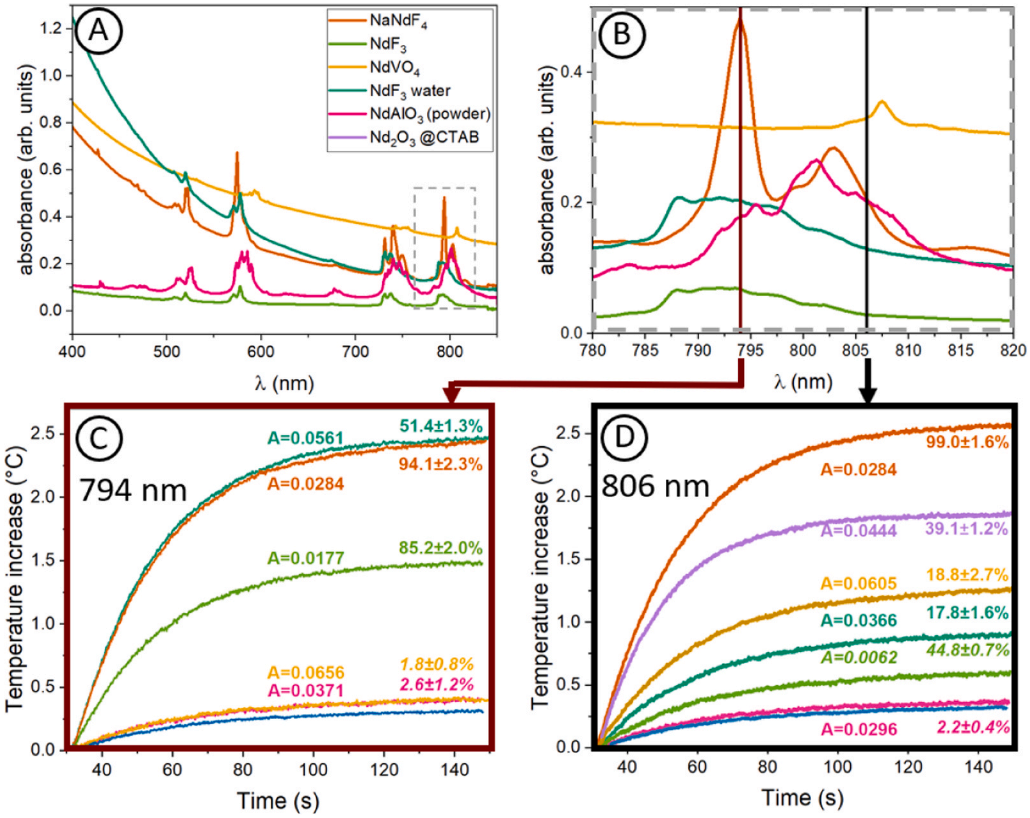

Fig. 5. Absorption spectra (A,B) and temperature increase curves of fully concentrated Nd^{3+} doped samples under 794 (C), and 806 nm (D) laser beam excitation (90 mW), *A* is the measured absorbance and numbers given in % are iHCEs values with standard deviation.

solvents yielded ~10 nm NHs with non-uniform morphology. Nd_2O_3 synthesized in high boiling organic solvents could not be directly transferred into water by acid treatment due to rapid dissolution of these nanoparticles, generating a $NdCl_3$ solution. Therefore, CTAB surfactant was used to obtain stable colloidal solution of Nd_2O_3 @ OA,OAm/CTAB nanocrystals in water. Unfortunately, the presence of organic ligands and CTAB can alter the thermal properties of the sample. They form a layer that can act as a thermal insulator and can change the wetting angle of the droplet.

$NdVO_4$ synthesized in water is characterized by its small size (~15 nm) and varied morphology. $NdAlO_3$, however, formed large aggregates larger than 500 nm.

The absorption spectra of neodymium in different matrices (Fig. 5A,B) are similar to the excitation spectra presented by del Rosal et al. [74]. The only notable difference concerns $NaNdF_4$. The peak maxima at ~800 nm are shifted and have different relative intensities.

Measurements were performed at 794 and 806 excitation wavelengths (Fig. 5C,D). It was anticipated that the samples with matrices of high phonon energy would exhibit the highest iHCE. However, results show this effect is not as strong as expected (Table 2). The highest iHCE at 794 nm was seen in 30 × 17 nm $NaNdF_4$ nanorods. This can be explained by the small size and relatively low scattering of the nanorods. iHCE indicates how much of the absorbed energy will be converted into heat. An iHCE less than 100% indicates that either the sample is emitting or scattering is occurring. The size of the nanoparticles has a notable impact on the iHCE. For example, Xu et al. showed the iHCE size-dependence of $NaNdF_4$ nanocrystals: a decrease in the iHCE was observed with increasing nanocrystal size [29]. Our results confirm this dependence for 90 nm NdF_3 synthesized in water. The efficiency is significantly lower (51%) than in 10 nm NdF_3 synthesized in $CHCl_3$ (85%). The vanadate sample also features a low iHCE. Although the grain sizes are small, this sample had a tendency to aggregate into larger structures (as confirmed by an enhancement on the UV absorption spectrum). This may have contributed to increased scattering. Perovskite samples exhibit both small absorption and small temperature rise. Unfortunately, it was not possible to obtain stable colloidal perovskite nanomaterial. As a result, it is difficult to accurately evaluate the iHCE. The high iHCE values measured for $NaNdF_4$, affirms that nanoparticle transfer to water by acid treatment produces stable nanocolloids. Furthermore, no visual changes were observed in samples transferred to water by this method.

Due to issues obtaining colloidal solution of Nd_2O_3 in water, we investigated the Nd_2O_3 stabilized by CTAB. In this case, we observed a low iHCE, likely due to a high degree of scattering. This most probably results from the presence of OA,OAm/CTAB layer on the nanocrystal surfaces. This sample was more turbid than the samples prepared with HCl.

The eHCE parameter is more meaningful than the iHCE with respect to PTT applications. Despite the scattering and the relatively lower iHCE for $NdVO_4$ at 806 nm, this material exhibited the best performance. $NdVO_4$ has already been tested for cytotoxicity and examined under in vivo conditions in mice [31,32] and in human cell lines [79]. The material we examined exhibited a tendency to form agglomerates which slightly compromised its stability in water. However, there is a possibility to improve its stability and biocompatibility by, for example, coating it with additional layers, such as poly(vinyl pyrrolidone) [32], or polydopamine and bovine serum albumin [79]. At 794 nm, $NaNdF_4$ nanorods demonstrated the highest eHCE of the examined materials. eHCE is highly wavelength dependent since, in the case of LnNMs, the absorption capacity strongly relies on how close the excitation wavelength is to the absorption band maximum.

Table 2
The iHCE and eHCE of Nd^{3+} doped NHs. Results marked (*) are uncertain as they are based on values below the threshold for reliable measurement (A < 0.01, ΔT < 0.5). Reference number are in square bracket.

Material	Matrix cut-off phonon energy (cm^{-1})	Size (~)	Water conversion approach	iHCE at 794 nm (%)	Mass abs coefficient (L/g·cm)·10^{-3}	eHCE (794 nm) (L/g·cm)·10^{-3}	iHCE at 806 nm (%)	Mass abs coefficient (L/g·cm)·10^{-3}	eHCE (806 nm) (L/g·cm)·10^{-3}
$NdVO_4$	890 [75]	10–20 nm, aggregate	Water synthesis	1.8 *	461	8.26	19	428	80.5
Nd_2O_3	600 [76]	8 nm	CTAB stabilization	–	–	–	39	18.6	7.29
$NdAlO_3$	570 [76]	300 nm – 900 nm	Water synthesis	2.6 *	156	4.00	2.2 *	123	2.67
NdF_3	514 [77]	90 nm	Water synthesis	51	11.2	5.73	18	7.20	1.29
NdF_3	514 [77]	10 nm	Removing organic ligand by HCl treatment	85	3.14	2.67	45 *	1.12	0.50
$NaNdF_4$	300–400 [78]	30 × 17 nm	Removing organic ligand by HCl treatment	94	45.0	42.3	99	5.64	5.59

4. Conclusion

The influence of various lanthanide ions on iHCE and eHCE was investigated in this study. Among Yb^{3+}, Nd^{3+} and Tm^{3+} ions, the highest iHCE was obtained by Nd^{3+} ion doping. The additional dopant of Sm^{3+} did not improve the samples' iHCE. Dy^{3+} doped sample containing Tm^{3+} ions exhibited slightly improved iHCE, however, it has no significant effect on the external HCE. The impact of matrix type on iHCE and eHCE of samples was investigated. It was found that, contrary to expectations, the iHCE is not directly related to phonon energy of the matrix Most notably, we observed that particle size has a very strong impact on the obtained results. The most promising results were found for the smallest materials due to their low scattering. Among the investigated materials, $NdVO_4$ was observed to be the best for future PTT use regarding external photothermal conversion efficiency (eHCE (806 nm)= 80.5·10^{-3} L/g·cm). Moreover, the vanadate matrix is known as a non-toxic material and can be easily biofunctionalized making them an excellent candidate for photothermal therapy. Among the other samples, fluorides ($NaNdF_4$, NdF_3) demonstrated good stability, and $NaNdF_4$ exhibited high external HCE at 794 nm (42.3·10^{-3} L/g·cm).

Funding

This work was supported by the European Commission H2020-FETOPEN (801305-NanoTBTech) "Nanoparticle-based 2D thermal bioimaging technologies" project.

CRediT authorship contribution statement

Agnieszka Paściak: Conceptualization, HCE measurements, data analysis, writing – original draft, **Małgorzata Misiak:** Synthesis of materials, discussion, Review & editing, **Karolina Trejgis:** Synthesis of materials, **Karolina Elżbieciak-Piecka:** Synthesis of materials, **Oleksii Bezkrovnyi**: TEM measurements, **Łukasz Marciniak:** Review & editing, **Artur Bednarkiewicz:** Conceptualization, supervision, discussion, review & editing, funding acquisition.

Data availability

Data will be made available on request.

Declaration of Competing Interest

The authors declare that they have no known competing financial interests or personal relationships that could have appeared to influence the work reported in this paper.

Acknowledgements

We would like to express our sincere thanks to John Reeks for language proofreading the publication.

References

[1] D. Jaque, L. Martínez Maestro, B. Del Rosal, P. Haro-Gonzalez, A. Benayas, J.L. Plaza, E. Martín Rodríguez, J. García Solé, Nanoparticles for photothermal therapies, Nanoscale 6 (2014) 9494–9530, https://doi.org/10.1039/c4nr00708e

[2] J. van der Zee, Z. Vujaskovic, M. Kondo, T. Sugahara, The Kadota Fund International Forum 2004-Clinical group consensus, Int. J. Hyperth. 24 (2008) 111–122, https://doi.org/10.1038/jid.2014.371

[3] S. Wang, X. Ma, X. Hong, Y. Cheng, Y. Tian, S. Zhao, W. Liu, Y. Tang, R. Zhao, L. Song, Z. Teng, G. Lu, Adjuvant photothermal therapy inhibits local recurrences after breast-conserving surgery with little skin damage, ACS Nano 12 (2018) 662–670, https://doi.org/10.1021/acsnano.7b07757

[4] A.R. Rastinehad, H. Anastos, E. Wajswol, J.S. Winoker, J.P. Sfakianos, S.K. Doppalapudi, M.R. Carrick, C.J. Knauer, B. Taouli, S.C. Lewis, A.K. Tewari, J.A. Schwartz, S.E. Canfield, A.K. George, J.L. West, N.J. Halas, Gold nanoshell-localized photothermal ablation of prostate tumors in a clinical pilot device

study, Proc. Natl. Acad. Sci. U. S. A. 116 (2019) 18590–18596, https://doi.org/10.1073/pnas.1906929116

[5] T. Ma, X. Zhai, Y. Huang, M. Zhang, X. Zhao, Y. Du, C. Yan, A smart nanoplatform with photothermal antibacterial capability and antioxidant activity for chronic wound healing, Adv. Healthc. Mater. 10 (2021) 1–9, https://doi.org/10.1002/adhm.202100033

[6] H. Gao, L. Zhang, X. Lian, Y. Wang, S. Jiang, G. Wang, X. Dai, H. Zou, D. Ding, A dentin hypersensitivity treatment using highly stable photothermal conversion nanoparticles, Mater. Chem. Front. 5 (2021) 3388–3395, https://doi.org/10.1039/d0qm01006e

[7] L. Marciniak, K. Kniec, K. Elzbieciak, A. Bednarkiewicz, Non-plasmonic NIR-activated photothermal agents for photothermal therapy, in: A. Benayas, E. Hemmer, G. Hong, D. Jaque (Eds.), Near infrared-emitting nanoparticles for biomedical applications, Springer, 2020.

[8] A. Paściak, R. Marin, L. Abiven, A. Pilch-Wróbel, M. Misiak, W. Xu, K. Prorok, O. Bezkrovnyi, C. Marciniak, F. Chanéac, R. Gazeau, S. Bazzi, B. Roux, V. Viana, D. Lehto, Jaque, A. Bednarkiewicz, Quantitative Comparison of the Light-to-Heat Conversion Efficiency in Nanomaterials Suitable for Photothermal Therapy, ACS Appl. Mater. Interfaces 14 (2022) 33555–33566, https://doi.org/10.1021/acsami.2c08013

[9] X. Wang, G. Li, Y. Ding, S. Sun, Understanding the photothermal effect of gold nanostars and nanorods for biomedical applications, RSC Adv. 4 (2014) 30375–30383, https://doi.org/10.1039/C4RA02978J

[10] Y. Shen, H.D.A. Santos, E.C. Ximendes, J. Lifante, A. Sanz-Portilla, L. Monge, N. Fernández, I. Chaves-Coira, C. Jacinto, C.D.S. Brites, L.D. Carlos, A. Benayas, M.C. Iglesias-de la Cruz, D. Jaque, Ag2S nanoheaters with multiparameter sensing for reliable thermal feedback during in vivo tumor therapy, Adv. Funct. Mater. 30 (2020), https://doi.org/10.1002/adfm.202002730

[11] A. Pradyasti, H. Thi Hoang, K.T. Lim, M.H. Kim, Synthesis of porous Ag–Ag2S@Ag–Au hybrid nanostructures with broadband absorption properties and their photothermal conversion application, J. Alloy. Compd. 896 (2022) 163062, https://doi.org/10.1016/j.jallcom.2021.163062

[12] K. Lu, X. Sun, L. Xu, B. Jiang, J. Ren, J.J. Carvajal, E. Zhao, L. Liu, J. Zhang, Self-monitored biological nanoheaters operating in the first biological window based on single-band red upconversion nanoparticles fabricated through architectural design, J. Alloy. Compd. 842 (2020), https://doi.org/10.1016/j.jallcom.2020.155602

[13] A. Li, Z. Li, L. Pan, Z. Wang, W. Chen, Q. Shao, B. Wu, Y. Tang, Upconversion luminescent nanoheater based on NaGd(MoO4)2: Yb3+/Tm3+ nanocrystals: Surfactant-free solvothermal synthesis, upconversion photoluminescence and photothermal conversion, J. Alloy. Compd. 904 (2022) 164087, https://doi.org/10.1016/j.jallcom.2022.164087

[14] H. Li, Y. Zhao, I. Kolesnikov, S. Xu, L. Chen, G. Bai, Multifunctional rare earth ions-doped Ba2LaF7 nanocrystals for simultaneous temperature sensing and photothermal therapy, J. Alloy. Compd. 931 (2023) 167535, https://doi.org/10.1016/j.jallcom.2022.167535

[15] K. Maciejewska, A. Bednarkiewicz, L. Marciniak, NIR luminescence lifetime nanothermometry based on phonon assisted Yb3+-Nd3+energy transfer, Nanoscale Adv. 3 (2021) 4918–4925, https://doi.org/10.1039/d1na00285f

[16] S. Pei, J.B. Li, Z. Wang, Y. Xie, J. Chen, H. Wang, L. Sun, A. CORM, loaded nanoplatform for single NIR light-activated bioimaging, gas therapy, and photothermal therapy: In vitro, J. Mater. Chem. B 9 (2021) 9213–9220, https://doi.org/10.1039/d1tb01561c

[17] Q. Jia, X. Han, Y. Liu, X. Liao, J. Zhou, Tumor–microenvironment activated programmable synergistic cancer therapy by bioresponsive rare-earth nanocomposite, J. Rare Earths. 40 (2022) 1399–1406, https://doi.org/10.1016/j.jre.2021.09.022

[18] B. Liu, X. Gu, Q. Sun, S. Jiang, J. Sun, K. Liu, F. Wang, Y. Wei, Injectable in situ induced robust hydrogel for photothermal therapy and bone fracture repair, Adv. Funct. Mater. 31 (2021), https://doi.org/10.1002/adfm.202010779

[19] B. del Rosal, U. Rocha, E.C. Ximendes, E. Martín Rodríguez, D. Jaque, J.G. Solé, Nd3+ions in nanomedicine: Perspectives and applications, Opt. Mater. (Amst.). 63 (2017) 185–196, https://doi.org/10.1016/j.optmat.2016.06.004

[20] A. Gnach, T. Lipinski, A. Bednarkiewicz, J. Rybka, J.A. Capobianco, Upconverting nanoparticles: assessing the toxicity, Chem. Soc. Rev. 44 (2015) 1561–1584, https://doi.org/10.1039/c4cs00177j

[21] H. Oliveira, A. Bednarkiewicz, A. Falk, E. Fröhlich, D. Lisjak, A. Prina-Mello, S. Resch, C. Schimpel, I.V. Vrček, E. Wysokińska, H.H. Gorris, Critical considerations on the clinical translation of upconversion nanoparticles (UCNPs): recommendations from the european upconversion network (COST Action CM1403), Adv. Healthc. Mater. 8 (2019), https://doi.org/10.1002/adhm.201801233

[22] Y. Li, X. Fan, Y. Li, L. Zhu, R. Chen, Y. Zhang, H. Ni, Q. Xia, Z. Feng, B.Z. Tang, J. Qian, H. Lin, Biologically excretable AIE nanoparticles wear tumor cell-derived “exosome caps” for efficient NIR-II fluorescence imaging-guided photothermal therapy, Nano Today 41 (2021) 101333, https://doi.org/10.1016/j.nantod.2021.101333

[23] A. Bednarkiewicz, D. Wawrzynczyk, M. Nyk, W. Strek, Optically stimulated heating using Nd3+ doped NaYF4 colloidal near infrared nanophosphors, Appl. Phys. B Lasers Opt. 103 (2011) 847–852, https://doi.org/10.1007/s00340-010-4300-7

[24] Z. Yu, W. Hu, H. Zhao, X. Miao, Y. Guan, W. Cai, Z. Zeng, Q. Fan, T.T.Y. Tan, Generating new cross-relaxation pathways by coating prussian blue on NaNdF 4 to fabricate enhanced photothermal agents, Angew. Chem. 100871 (2019) 8624–8628, https://doi.org/10.1002/ange.201904534

[25] J. Li, S. Xu, Y. Yu, K. Liu, Y. Gao, B. Chen, 808 nm triggered multifunctional UCNPs@PDA nanocomposites for temperature sensing and photothermal conversion, J. Mater. Sci. Mater. Electron. 33 (2022) 6563–6575, https://doi.org/10.1007/s10854-022-07831-8

[26] H. Liu, J. Li, P. Hu, S. Sun, L. Shi, L. Sun, Facile synthesis of Er3+/Tm3+ co-doped magnetic/luminescent nanosystems for possible bioimaging and therapy applications, J. Rare Earths 40 (2022) 11–19, https://doi.org/10.1016/j.jre.2020.11.006

[27] C. Wang, C. Xu, L. Xu, C. Sun, D. Yang, J. Xu, F. He, S. Gai, P. Yang, A novel core-shell structured upconversion nanorod as a multimodal bioimaging and photothermal ablation agent for cancer theranostics, J. Mater. Chem. B 6 (2018) 2597–2607, https://doi.org/10.1039/c7tb02842c

[28] L. Marciniak, A. Pilch, S. Arabasz, D. Jin, A. Bednarkiewicz, Heterogeneously Nd3+doped single nanoparticles for NIR-induced heat conversion, luminescence, and thermometry, Nanoscale 9 (2017) 8288–8297, https://doi.org/10.1039/c7nr02630g

[29] L. Xu, J. Li, K. Lu, S. Wen, H. Chen, M.K. Shahzad, E. Zhao, H. Li, J. Ren, J. Zhang, L. Liu, Sub-10 nm NaNdF4 nanoparticles as near-infrared photothermal probes with self-temperature, Feedback, ACS Appl. Nano Mater. 3 (2020) 2517–2526, https://doi.org/10.1021/acsanm.9b02606

[30] X. Wang, H. Li, F. Li, X. Han, G. Chen, Prussian blue-coated lanthanide-doped core/shell/shell nanocrystals for NIR-II image-guided photothermal therapy, Nanoscale 11 (2019) 22079–22088, https://doi.org/10.1039/c9nr07973d

[31] B. del Rosal, A. Pérez-Delgado, E. Carrasco, D.J. Jovanović, M.D. Dramićanin, G. Dražić, Á.J. de la Fuente, F. Sanz-Rodriguez, D. Jaque, Neodymium-based stoichiometric ultrasmall nanoparticles for multifunctional deep-tissue photothermal therapy, Adv. Opt. Mater. 4 (2016) 782–789, https://doi.org/10.1002/adom.201500726

[32] M. Chang, M. Wang, M. Shu, Y. Zhao, B. Ding, S. Huang, Z. Hou, G. Han, J. Lin, Enhanced photoconversion performance of NdVO4/Au nanocrystals for photothermal/photoacoustic imaging guided and near infrared light-triggered anticancer phototherapy, Acta Biomater. 99 (2019) 295–306, https://doi.org/10.1016/j.actbio.2019.08.026

[33] A. Li, X. Li, J. Wang, Y. Guo, C. Li, W. Chen, Z. Wang, Y. Tang, Multifunctional α-NaYbF4: Tm3+ nanocrystals with intense ultraviolet self-sensitized upconversion luminescence and highly efficient optical heating, Ceram. Int (2022), https://doi.org/10.1016/j.ceramint.2022.04.261

[34] S. Sinha, K. Kumar, Studies on up/down-conversion emission of Yb3+ sensitized Er3+ doped MLa2(MoO4)4 (M = Ba, Sr and Ca) phosphors for thermometry and optical heating, Opt. Mater. (Amst.). 75 (2018) 770–780, https://doi.org/10.1016/j.optmat.2017.10.036

[35] Y. Zhang, B. Chen, S. Xu, X. Li, J. Zhang, J. Sun, H. Zheng, L. Tong, G. Sui, H. Zhong, H. Xia, R. Hua, Dually functioned core-shell NaYF4:Er3+/Yb3+@NaYF4:Tm3+/Yb3+nanoparticles as nano-calorifiers and nano-thermometers for advanced photothermal therapy, Sci. Rep. 7 (2017) 1–13, https://doi.org/10.1038/s41598-017-11897-4

[36] L. Tong, X. Li, J. Zhang, S. Xu, J. Sun, H. Zheng, Y. Zhang, X. Zhang, R. Hua, H. Xia, B. Chen, NaYF4:Sm3+/Yb3+@NaYF4:Er3+/Yb3+ core-shell structured nanocalorifier with optical temperature probe, Opt. Express 25 (2017) 477–482, https://doi.org/10.1364/OE.25.016047

[37] H. Zheng, B. Chen, H. Yu, X. Li, J. Zhang, J. Sun, L. Tong, Z. Wu, H. Zhong, R. Hua, H. Xia, Rod-shaped NaY(MoO4)2:Sm3+/Yb3+ nanoheaters for photothermal conversion: Influence of doping concentration and excitation power density, Sens. Actuators, B Chem. 234 (2016) 286–293, https://doi.org/10.1016/j.snb.2016.04.162

[38] S. Balabhadra, M.L. Debasu, C.D.S. Brites, R.A.S. Ferreira, L.D. Carlos, Radiation-to-heat conversion efficiency in SrF2:Yb3+/Er3+ upconverting nanoparticles, Opt. Mater. (Amst.). 83 (2018) 1–6, https://doi.org/10.1016/j.optmat.2018.05.069

[39] T. Wei, F. Yang, B. Jia, C. Zhao, M. Wang, M. Du, Q. Zhou, Y. Guo, Z. Li, High performance temperature sensing and optical heating of Tm3+- and Yb3+- co-doped SrBi4Ti4O15 up-conversion luminescence nanoparticles, Ceram. Int. 45 (2019) 18084–18090, https://doi.org/10.1016/j.ceramint.2019.06.030

[40] M. Xu, W. Ge, J. Shi, Y. Li, Near infrared-stimulated heating behaviors and ultra-high temperature sensitivity in Bi2Ti2O7:Yb3+/Ho3+ nanofibers, J. Alloy. Compd. 861 (2021) 158622, https://doi.org/10.1016/j.jallcom.2021.158622

[41] A. Nexha, M.C. Pujol, J.J. Carvajal, F. Díaz, M. Aguiló, Effect of the Size and Shape of Ho, Tm:KLu(WO4)2 Nanoparticles on Their Self-Assessed Photothermal Properties, Nanomaterials 11 (2021) 485, https://doi.org/10.3390/nano11020485

[42] S. Zhou, X. Jiao, Y. Jiang, Y. Zhao, P. Xue, Y. Liu, J. Liu, Engineering Eu3+-incorporated MoS2 nanoflowers toward efficient photothermal/photodynamic combination therapy of breast cancer, Appl. Surf. Sci. 552 (2021) 149498, https://doi.org/10.1016/j.apsusc.2021.149498

[43] Y. Liu, H. Fan, Q. Guo, A. Jiang, X. Du, J. Zhou, Ultra-small pH-responsive Nd-doped NaDyF4 nanoagents for enhanced cancer theranostic by in situ aggregation, Theranostics 7 (2017) 4217–4228, https://doi.org/10.7150/thno.21557

[44] Z. Tang, Q. Liu, J. Li, X. Wu, S. Zhan, G. Nie, J. Hu, S. Hu, Z. Xi, S. Wu, Y. Zhang, L. Shi, Y. Liu, Tuning the photothermal effect of NaYF4:Yb3+,Er3+ upconversion luminescent crystals through La3+ ion doping, J. Lumin. 206 (2019) 21–26, https://doi.org/10.1016/j.jlumin.2018.10.063

[45] S. Wen, J. Zhou, K. Zheng, A. Bednarkiewicz, X. Liu, D. Jin, Advances in highly doped upconversion nanoparticles, Nat. Commun. 9 (2018), https://doi.org/10.1038/s41467-018-04813-5

[46] J. Li, L. Xu, K. Lu, M. Khuram Shahzad, J. Ren, E. Zhao, H. Li, L. Liu, Efficient nanoheater operated in a biological window for photo-hyperthermia therapy, Biomed. Opt. Express 10 (2019) 1935–1941, https://doi.org/10.1364/BOE.10.001935

[47] X. Chen, G. Wu, J. Tang, L. Zhou, S. Wei, Ytterbium – Doped Prussian blue: Fabrication, photothermal performance and antibacterial activity, Inorg. Chem. Commun. 114 (2020) 107821, https://doi.org/10.1016/j.inoche.2020.107821

[48] D. Li, Q. Shao, Y. Dong, J. Jiang, Phase-, shape- and size-controlled synthesis of NaYF4:Yb3+,Er3+ nanoparticles using rare-earth acetate precursors, J. Rare Earths 32 (2014) 1032–1036, https://doi.org/10.1016/S1002-0721(14)60179-4

[49] X. Sun, Y.W. Zhang, Y.P. Du, Z.G. Yan, R. Si, L.P. You, C.H. Yan, From trifluoroacetate complex precursors to monodisperse rare-earth fluoride and oxyfluoride nanocrystals with diverse shapes through controlled fluorination in solution phase, Chem. - A Eur. J. 13 (2007) 2320–2332, https://doi.org/10.1002/chem.200601072

[50] X.F. Yu, L.D. Chen, M. Li, M.Y. Xie, L. Zhou, Y. Li, Q.Q. Wang, Highly efficient fluorescence of NdF3/SiO2 core/shell nanoparticles and the applications for in vivo NIR detection, Adv. Mater. 20 (2008) 4118–4123, https://doi.org/10.1002/adma.200801224

[51] M. Odziomek, F. Chaput, F. Lerouge, M. Sitarz, S. Parola, Highly luminescent YAG:Ce ultra-small nanocrystals, from stable dispersions to thin films, J. Mater. Chem. C. 5 (2017) 12561–12570, https://doi.org/10.1039/c7tc03504g

[52] W. Fan, W. Zhao, L. You, X. Song, W. Zhang, H. Yu, S. Sun, A simple method to synthesize single-crystalline lanthanide orthovanadate nanorods, J. Solid State Chem. 177 (2004) 4399–4403, https://doi.org/10.1016/j.jssc.2004.08.027

[53] T. Paik, T.R. Gordon, A.M. Prantner, H. Yun, C.B. Murray, Designing tripodal and triangular gadolinium oxide nanoplates and self-assembled nanofibrils as potential multimodal bioimaging probes, ACS Nano 7 (2013) 2850–2859, https://doi.org/10.1021/nn4004583

[54] N. Bogdan, F. Vetrone, G.A. Ozin, J.A. Capobianco, Synthesis of ligand-free colloidally stable water dispersible brightly luminescent lanthanide-doped upconverting nanoparticles, Nano Lett. 11 (2011) 835–840, https://doi.org/10.1021/nl1041929

[55] J. Cichos, M. Karbowiak, A general and versatile procedure for coating of hydrophobic nanocrystals with a thin silica layer enabling facile biofunctionalization and dye incorporation, J. Mater. Chem. B. 2 (2014) 556–568, https://doi.org/10.1039/c3tb21442g

[56] A. Paściak, A. Pilch-Wróbel, P.J. Marciniak, Schuck, A. Bednarkiewicz, Standardization of methodology of light-to-heat conversion efficiency determination for colloidal nanoheaters, ACS Appl. Mater. Interfaces (2021), https://doi.org/10.1021/acsami.1c12409

[57] P. Scardi, M. Ermrich, A. Fitch, E.W. Huang, R. Jardin, R. Kuzel, A. Leineweber, A. Mendoza Cuevas, S.T. Misture, L. Rebuffi, C. Schimpf, Size–strain separation in diffraction line profile analysis, J. Appl. Crystallogr 51 (2018) 831–843, https://doi.org/10.1107/S1600576718005411

[58] J.I. Langford, A.J.C. Wilson, Scherrer after sixty years: A survey and some new results in the determination of crystallite size, J. Appl. Crystallogr 11 (1978) 102–113, https://doi.org/10.1107/s0021889878012844

[59] D. Balzar, N. Audebrand, M.R. Daymond, A. Fitch, A. Hewat, J.I. Langford, A. Le Bail, D. Louër, O. Masson, C.N. McCowan, N.C. Popa, P.W. Stephens, B.H. Toby, Size-strain line-broadening analysis of the ceria round-robin sample, J. Appl. Crystallogr 37 (2004) 911–924, https://doi.org/10.1107/S0021889804022551

[60] R.D. Shannon, Revised effective ionic radii and systematic studies of interatomie distances in halides and chaleogenides, Acta Crystallogr. Sect. B Struct. Sci. A 32 (1976) 751–767, https://doi.org/10.1023/A:1018927109487

[61] F. Wang, Y. Han, C.S. Lim, Y. Lu, J. Wang, J. Xu, H. Chen, C. Zhang, M. Hong, X. Liu, Simultaneous phase and size control of upconversion nanocrystals through lanthanide doping, Nature 463 (2010) 1061–1065, https://doi.org/10.1038/nature08777

[62] S. Zeng, G. Ren, C. Xu, Q. Yang, High uniformity and monodispersity of sodium rare-earth fluoride nanocrystals: Controllable synthesis, shape evolution and optical properties, CrystEngComm 13 (2011) 1384–1390, https://doi.org/10.1039/c0ce00325e

[63] K. Trejgis, K. Ledwa, K. Maciejewska, L. Li, L. Marciniak, Modulation of thermometric performance of single-band-ratiometric luminescent thermometers based on luminescence of Nd3+ activated tetrafluorides by size modification, Sci. Rep. 12 (2022) 1–14, https://doi.org/10.1038/s41598-022-09912-4

[64] F. Wang, J. Wang, X. Liu, Direct evidence of a surface quenching effect on size-dependent luminescence of upconversion nanoparticles, Angew. Chem. - Int. Ed. 49 (2010) 7456–7460, https://doi.org/10.1002/anie.201003959

[65] Q. Su, S. Han, X. Xie, H. Zhu, H. Chen, C.-K. Chen, R.-S. Liu, X. Chen, F. Wang, X. Liu, The effect of surface coating on energy migration-mediated upconversion, J. Am. Chem. Soc. 134 (2012) 20849–20857, https://doi.org/10.1021/ja3111048

[66] T. Sago, H. Ishii, H. Hagihara, N. Takada, H. Suda, Analysis of chemiluminescence spectra in oxidative degradation of oleic acid, Chem. Phys. Lett. 565 (2013) 138–142, https://doi.org/10.1016/j.cplett.2013.02.035

[67] S. Xu, S. Xiang, Y. Zhang, J. Zhang, X. Li, J. Sun, L. Cheng, B. Chen, 808 nm laser induced photothermal effect on Sm3+/Nd3+ doped NaY(WO4)2 microstructures, Sens. Actuators, B Chem. 240 (2017) 386–391, https://doi.org/10.1016/j.snb.2016.08.176

[68] D.N.F. Muche, A.L. da Silva, K. Nakajima, D. Gouvêa, R.H.R. Castro, Simultaneous segregation of lanthanum to surfaces and grain boundaries in MgAl2O4 nanocrystals, Appl. Surf. Sci. 529 (2020) 147145, https://doi.org/10.1016/j.apsusc.2020.147145

[69] X. Li, R. Wang, F. Zhang, D. Zhao, Engineering homogeneous doping in single nanoparticle to enhance upconversion efficiency, Nano Lett. 14 (2014) 3634–3639, https://doi.org/10.1021/nl501366x

[70] A. Li, D. Xu, Y. Tang, Z. Wang, Z. Li, Y. Zhang, Solid solution Na(Gd/La)(MoO4)2:Yb3+/Er3+ upconversion nanocrystals with simultaneously enhanced photothermal conversion efficiency and luminescence intensity, J. Lumin. 239 (2021) 118356, https://doi.org/10.1016/j.jlumin.2021.118356

[71] E.C. Ximendes, U. Rocha, C. Jacinto, K.U. Kumar, D. Bravo, F.J. López, E.M. Rodríguez, J. García-Solé, D. Jaque, Self-monitored photothermal nanoparticles based on core-shell engineering, Nanoscale 8 (2016) 3057–3066, https://doi.org/10.1039/c5nr08904b

[72] Y. Yu, S. Xu, M. Jiang, R. Song, J. Li, Y. Gao, X. Zhang, X. Li, H. Yu, B. Chen, Near infrared triggered dual-functional NaYF4:Yb3+/Tm3+@NaYF4:Yb3+/Sm3+ core-shell UCNPs for temperature sensing and photothermal conversion, Phys. B Condens. Matter 622 (2021) 413340, https://doi.org/10.1016/j.physb.2021.413340

[73] A.R. Hong, J.Y. Byun, K. Lee, H.S. Jang, Sub-20 nm LiErF4-Based Upconversion Nanophosphors for Simultaneous Imaging and Photothermal Therapeutics, ACS Appl. Nano Mater. 3 (2020) 8662–8671, https://doi.org/10.1021/acsanm.0c01383

[74] B. Del Rosal, A. Pérez-Delgado, M. Misiak, A. Bednarkiewicz, A.S. Vanetsev, Y. Orlovskii, D.J. Jovanović, M.D. Dramićanin, U. Rocha, K. Upendra Kumar, C. Jacinto, E. Navarro, E. Martín Rodríguez, M. Pedroni, A. Speghini, G.A. Hirata, I.R. Martín, D. Jaque, Neodymium-doped nanoparticles for infrared fluorescence bioimaging: The role of the host, J. Appl. Phys. 118 (2015) 1–11, https://doi.org/10.1063/1.4932669

[75] I.E. Kolesnikov, D.V. Tolstikova, A.V. Kurochkin, S.A. Pulkin, A.A. Manshina, M.D. Mikhailov, Concentration effect on photoluminescence of Eu3+-doped nanocrystalline YVO4, J. Lumin. 158 (2015) 469–474, https://doi.org/10.1016/j.jlumin.2014.10.024

[76] H. Kawahara, K. Fujioka, H. Furuse, Synthesis of YAlO3 up-conversion powder using a co-precipitation technique, Jpn. J. Appl. Phys. 59 (2020), https://doi.org/10.35848/1347-4065/abc1ab

[77] M.M. Lage, A. Righi, F.M. Matinaga, J.Y. Gesland, R.L. Moreira, Raman-spectroscopic study of lanthanide trifluorides with the β-YF3 structure, J. Phys. Condens. Matter 16 (2004) 3207–3218, https://doi.org/10.1088/0953-8984/16/18/021

[78] J.F. Suyver, J. Grimm, M.K. Van Veen, D. Biner, K.W. Krämer, H.U. Güdel, Upconversion spectroscopy and properties of NaYF4 doped with Er3+, Tm3+ and/or Yb3+, J. Lumin. 117 (2006) 1–12, https://doi.org/10.1016/j.jlumin.2005.03.011

[79] K. Deng, D. Liu, Z. Wang, Z. Zhou, Q. Chen, J. Luo, Y. Zhang, Z. Hou, J. Lin, Surface-functionalized NdVO4:Gd3+ nanoplates as active agents for near-infrared-light-triggered and multimodal-imaging-guided photothermal therapy, Pharmaceutics 14 (2022) 1217, https://doi.org/10.3390/pharmaceutics14061217